Scanning Tunneling Microscopy of Metal-Organic Complexes

Dissertation

zur Erlangung des Doktorgrades
der Mathematisch-Naturwissenschaftlichen Fakultät
der Christian-Albrechts-Universität zu Kiel

vorgelegt von

Sven Johannsen

Kiel, 2024

Erster Gutachter: Prof. Dr. Richard Berndt

Zweiter Gutachter: Prof. Dr. Olaf Magnussen

Tag der mündlichen Prüfung: 25.3.2024

Eidesstattliche Erklärung

Hiermit erkläre ich, dass ich die vorliegende Arbeit eigenständig mit der Hilfe meiner wissenschaftlichen Betreuer angefertigt habe und nur die in dieser Arbeit angegebenen Hilfsmittel benutzt habe, sowie die gängigen Nachschlagwerke der Naturwissenschaften. Die hier vorliegende Arbeit wurde nicht ganz und auch nicht in Teilen an anderer Stelle im Rahmen eines Prüfungsverfahrens vorgelegt. Damit wurde diese Arbeit auch nicht in einem solchen Zusammenhang veröffentlicht oder zur Veröffentlichung eingereicht. Ich habe keine früheren Promotionsversuche vorgenommen. Bis zu diesem Zeitpunkt wurde mir kein akademischer Grad entzogen und es geht auch kein solches Verfahren vonstatten. Diese Arbeit wurde unter Einhaltung der Regeln guter wissenschaftlicher Praxis der Deutschen Forschungsgemeinschaft angefertigt.

Die im folgenden aufgeführten Kapitel dieser Arbeit basieren auf Veröffentlichungen in wissenschaftlichen Fachzeitschriften:

- Kapitel 4.1:
  S. Johannsen et al., "Electron-Induced Spin-Crossover in Self-Assembled Tetramers", ACS Nano **15**, 11770–11778 (2021)
- Kapitel 4.2:
  S. Johannsen et al., "Three-State Switching of an Fe Spin Crossover Complex", J. Phys. Chem. C **126**, 7238–7244 (2022)
- Kapitel 4.3:
  S. Johannsen et al., "Spin Crossover in a Co Complex on Ag(111)", Angew. Chem. Int. Ed. **61**, e202115892 (2022)
- Kapitel 5:
  S. Johannsen et al., "Spin-Crossover and Fragmentation of Fe(neoim)$_2$ on Silver and Gold", J. Phys. Chem. Lett. **14**, 7814–7823 (2023)

Kapitel 6 dieser Arbeit basiert auf einem Manuskript mit ergänzenden Informationen, welches für die Veröffentlichung vorbereitet wird.

Kiel, den

_____

Sven Johannsen

Zusammenfassung

Im Rahmen dieser Dissertationsschrift wurden organometallische Komplexe, genauer spin-crossover-Komplexe, in direktem Kontakt mit Metalloberflächen mit Hilfe von Tieftemperatur-Rastertunnelmikroskopie im Ultrahochvakuum untersucht. Verschiedene Komplexe wurden durch Sublimation auf metallische Einkristalle aufgebracht. Strukturelle, elektronische und magnetische Eigenschaften wurden auf der Einzelmolekül-Skala untersucht. Die in dieser Dissertation untersuchten Molekülsysteme werden in den folgenden Abschnitten kurz zusammengefasst.

Die erste Untersuchung befasst sich mit Fe(H_2B(pyrazole)(pyridylpyrazole))$_2$ adsorbiert auf einer Ag(111)-Oberfläche. Für Submonolagen-Bedeckung kondensieren die meisten Komplexe in gitterförmige Tetramere auf der Silberoberfläche. Zwei Komplexe pro Tetramer können durch Injektion von elektrischem Strom zwischen zwei Zuständen geschaltet werden. Schalten von strukturell analogen Zn(H_2B(pyrazole)(pyridylpyrazole))$_2$-Komplexen auf Ag(111), wo aufgrund der vollbesetzten $3d$-Schale kein Spinübergang erwartet wird, war nicht möglich. Aus diesem Grund ordnen wir dem Schalten einzelner Fe(H_2B(pyrazole)(pyridylpyrazole))$_2$-Komplexe einem Spinübergang zwischen low-spin- (LS) und high-spin- (HS) Zustand zu. Einzelne Komplexe wurden tausende Male ohne Anzeichen von Abnutzung geschaltet. Eine Vielzahl von Schaltereignissen wurde in Zeitreihen des Tunnelstroms aufgenommen, welche Zwei-Niveau-Fluktuationen bei höheren elektrischen Spannungen aufwiesen. Hierbei entsprach jedem Niveau einem Spinzustand. Schaltraten und Schaltausbeuten konnten aus diesen Messungen ermittelt und analysiert werden. Die Schaltausbeuten liegen zwei Größenordnungen höher als bei anderen Spin-Crossover-Systemen.
Durch Stromfluss in die übrigen nicht schaltbaren Komplexe in einem Tetramer kann fernausgelöstes Schalten der schaltbaren Nachbarkomplexe verursacht werden. Der Zustand des schaltbaren Nachbarkomplexes beeinflusst geringfügig die scheinbare Höhe des nicht schaltbaren Komplexes. Aufgrund dieser Tatsache kann das fernausgelöste Schalten mit recht hoher Zeitauflösung detektiert werden. Die Schaltrate des fernausgelösten Schaltens ist lediglich eine Größenordnung kleiner im Vergleich zur Schaltrate des durch direkte Anregung ausgelösten Schaltens.

Wir präsentieren ein Modell für die im Experiment beobachteten Tetramere, welches aufgrund von sterischer Abstoßung erklären kann, warum zwei Moleküle reversibel geschaltet werden können und zwei nicht. Berechnungen auf der Basis von Dichtefunktionaltheorie unterstützen unser vorgeschlagenes Modell. Ein vorläufiges Modell eines Mechanismus basierend auf Elektronentransfer zwischen benachbarten Komplexen kann in guter Näherung die Effizienz des fernausgelösten Schaltens reproduzieren.

Das Schaltverhalten von Fe(H_2B(pyrazole)(pyridylpyrazole))$_2$-Molekülen bei angelegter negativer Probenspannung ist komplizierter und beinhaltet einen dritten Schaltzustand. Dieser dritte Zustand kann in Strom-Spannungs-Kurven, gemessen an schaltbaren Komplexen, beobachtet werden. Desweiteren ist dieser Zustand bei geringem Tunnelstrom und geringer Probenspannung in aufgenommenen Topographien sichtbar. In einem spezifischen Spannungsintervall ist der Zustand stabil, wohingegen er bei erhöhten positiven Spannungen in den HS-Zustand übergeht. Wir erarbeiteten eine Routine, die es ermöglichte, diesen dritten Zustand gezielt an einem schaltbaren Komplex zu präparieren. Hierdurch konnten wir die Dynamik des Übergangs in den HS-Zustand bei verschiedenen Spannungen und Strömen untersuchen. Experimente an den strukturell analogen Co(H_2B(pyrazole)(pyridylpyrazole))$_2$-Komplexen auf Ag(111), zeigten in den aufgenommenen Topographien ähnlichen intermolekularen Bildkontrast. Wir interpretieren den neuen dritten Zustand als negativ geladenen HS-Zustand, welcher die gleiche elektronische 3*d*-Konfiguration besitzt wie die Co-Komplexe.

Experimente an spin-schaltbaren Co(H_2B(pyrazole)(pyridylpyrazole))$_2$-Komplexen auf Ag(111) führten zum tieferen Verständnis des Schaltmechanismus ausgelöst durch Injektion von Elektronen. Die Co(H_2B(pyrazole)(pyridylpyrazole))$_2$-Komplexe ordnen sich in Tetrameren auf der Oberfläche an, ähnlich den Tetrameren, welche Fe-Komplexe beinhalten. Sowohl bei positiver als auch bei negativer Probenspannung sind jeweils zwei Komplexe in einem Tetramer zwischen zwei Zuständen schaltbar. Die Schaltrate ist linear vom Tunnelstrom abhängig. Dies offenbart, dass das Schalten durch einen Ein-Elektronen-Prozess herbeigeführt wird. Die zwei übrigen Komplexe können nicht geschaltet werden. Wir ordnen einen der bistabilen Zustände den S=1/2- und den anderen den S=3/2-Spinzustand des Co-Zentralions zu. Bei positiver Probenspannung ist die Schaltausbeute des Übergangs HS zu LS drei Größenordnungen größer, im Vergleich zum Schaltübergang LS zu HS. Wir präsentieren ein Modell für den Mechanismus des „electron-induced excited spin-state trapping“ (ELIESST), welcher die große Abweichung der Schaltausbeuten qualitativ erklären kann.

Der SCO-Komplex Fe(neoim)$_2$ aufgedampft auf Ag(111) und Au(111) wurde mit Hilfe von Tieftemperatur-Rastertunnelmikroskopie untersucht. Auf der Ag-Oberfläche adsorbiert der Komplex intakt. Ohne Manipulation erscheint der Komplex zunächst im HS-Zustand. Einzelne Komplexe können ausgelöst durch Injektion von Elektronen zwischen HS- und LS-Zustand reversibel geschaltet werden. Im Gegensatz zu der Situation auf Ag fragmentieren die Komplexe auf der Au-Oberfläche. Berechnungen mit Dichtefunktionaltheorie zeigen, dass die adsorbierten Komplexe vor allem durch Van-der-Waals-Kräfte zwischen Substrat und Komplex stark deformiert werden. Desweiteren zeigen die Berechnungen, dass Wechselwirkungen aufgrund von Dispersion für die relativen Stabilitäten des HS- und LS-Zustands von adsorbierten Fe(neoim)$_2$ entscheidend sind. Weiterführende Berechnungen zeigen die Ausbildung kritischer kovalenter Bindungen zwischen Fragmenten von Komplexen und dem Au-Substrat. Diese deuten wir als Ursache für die Instabilität der Komplexe. Oft wird die Au-Oberfläche als weniger reaktiv als Ag betrachtet. In diesem vorliegenden Fall zeigen unsere Ergebnisse das Gegenteil.

Die letzte Untersuchung präsentiert die Forschungsergebnisse des auf Cu(111) adsorbierten SCO-Komplexes Fe(HB(1,2,4-triazol-1-yl)$_3$)$_2$. Die Komplexe ordnen sich auf der Oberfläche zu großen Inseln an. Einzelne Moleküle können durch Injektion von Elektronen zwischen zwei Zuständen geschaltet werden. Eine Vielzahl von Molekülen in einer Insel kann durch Strompulse in das Cu-Substrat neben der Insel reversibel geschaltet werden. Mit und ohne angelegtem Magnetfeld weisen Tunnelspektren an geschalteten Molekülen Merkmale um die Fermi-Energie auf, welche auf inelastische Prozesse hinweisen. Dies deutet auf ein magnetisches Moment des Moleküls hin. Gemessen an einem ungeschalteten Molekül zeigen Tunnelspektren keine Merkmale. Mit Hilfe von spin-flip-Spektroskopie ordnen wir dem ungeschalteten Grundzustand der Komplexe den LS-Zustand und dem geschalteten Zustand den HS-Zustand zu. Zusätzlich zeigen die Tunnelspektren der Komplexe im HS-Zustand eine magnetische Anisotropie.

Abstract

In this thesis metal-organic complexes, more specifically spin-crossover (SCO) complexes, in direct contact with metallic surfaces were investigated with low-temperature scanning tunneling microscopy (LT-STM) in ultra-high vacuum (UHV). Several complexes are deposited by sublimation on metallic single crystals. Structural, electronic and magnetic properties are explored on the single molecule scale. The different molecular systems investigated in this thesis are briefly summarized in the following paragraphs.

The first study focuses on Fe(H_2B(pyrazole)(pyridylpyrazole))$_2$ on Ag(111). At submonolayer coverage most of the complexes condense into gridlike tetramers on the surface. Two complexes per tetramer can be switched between two states by injecting current. Switching of the analogue Zn(H_2B(pyrazole)(pyridylpyrazole))$_2$ complex on Ag(111), where no spin transition is expected due to the fully occupied $3d$ shell, was unsuccessful. Therefore we assign the switching of individual Fe(H_2B(pyrazole)(pyridylpyrazole))$_2$ complexes to a spin transition between a low-spin (LS) and a high-spin (HS) state. Individual complexes were switched thousands of times without any signs of fatigue. Numerous switching events were monitored in the tunneling current time series, which exhibits a two level fluctuation at large voltages, where each level corresponds to a spin state. Rates and yields of the switching were analyzed from these measurements. The yields exceed by 2 orders of magnitude those of other SCO systems.
The remaining two non switchable complexes in a tetramer were used to trigger remote switching of the neighbor molecule by current injection. The state of the switchable neighbor affects slightly the apparent height of the non switchable complex. This allows sensing the remote switching and extracting rates and yields. The yield of the remote switching is only lower by one order of magnitude compared to the switching triggered by direct stimuli.
We present a model of the tetramers observed in the experiment, explaining why two molecules can be reversibly switched and two not, because of steric repulsion. Density functional theory (DFT) calculations support our suggestion.

A preliminary model of a mechanism based on electron transfer between neighboring complexes can approximately reproduce the efficiency of the remote switching.

The switching behavior of the $Fe(H_2B(pyrazole)(pyridylpyrazole))_2$ molecules at negative bias voltage is more complex and involves three states. A third state is observable in current-voltage (I-V) curves acquired at a switchable complex and can be imaged under mild tunneling conditions. It is stable in a specific sample voltage range, but decays at elevated positive sample voltage into the HS state. We elaborated a protocol to prepare a given switchable molecule in that third state, from which we could further analyze the decay dynamics at different voltages and currents. Experiments on the analogue $Co(H_2B(pyrazole)(pyridylpyrazole))_2$ complexes on Ag(111) revealed similar intramolecular image contrast. We interpret the new third state as a negatively charged HS state that has the same electronic $3d$ configuration than the Co complex.

Experiments on the spin switchable $Co(H_2B(pyrazole)(pyridylpyrazole))_2$ complexes on Ag(111) lead to deeper understanding of the switching mechanism triggered by electron injection. These $Co(H_2B(pyrazole)(pyridylpyrazole))_2$ complexes self assemble in tetramers on the surface, similar to the tetramers containing the Fe based complexes. Two Co complexes in a tetramer are switchable between two stable states at positive and negative sample voltages. The switching rate is linear with the current, revealing that the switching is induced by a single electron process. The remaining two complexes are stable and cannot be switched.
We associate the two bistable states to the S=1/2 state and the S=3/2 state of the Co central ion. At positive sample voltage the switching yield of the HS to LS transition is three orders of magnitude larger compared to the LS to HS switching yield. We present a model for the mechanism of electron-induced excited spin-state trapping (ELIESST), that can qualitatively explain the drastic difference in yield.

The SCO complex $Fe(neoim)_2$ deposited on Ag(111) and Au(111) is investigated with LT-STM. The complex remains intact adsorbed on the Ag surface. Without manipulation, the complexes are initially in the HS state. Individual complexes are reversibly switched between the HS and the LS state, triggered by electron injection. In contrast to this situation on Ag, the complexes fragment on the Au surface. Density functional theory calculations reveal that particularly due to van der Waals forces between the substrate and the complex, the adsorbed complex is strongly distorted. Furthermore, the calculations show that dispersion interactions are crucial for the relative stabilities of the HS and LS states of adsorbed $Fe(neoim)_2$. Extended calculations show a critical covalent bonding between the fragments of

the complex and the Au substrate. We attribute this as being the reason for the instability of the complex. Au has so far often been considered as a noble surface, less reactive than Ag. In this case, our results suggest the opposite.

The last study involves the SCO compound Fe(HB(1,2,4-triazol-1-yl)$_3$)$_2$ adsorbed on Cu(111). The complexes self assemble in large islands. Individual molecules can be switched between two states by injecting electrons. Several molecules within an island can be reversibly switched via current pulses on the Cu substrate, next to the molecular island. Inelastic features around the Fermi energy in the tunneling spectra acquired with and without magnetic field evidence a magnetic moment in the switched molecule. The tunneling spectra of the pristine state remain featureless around the Fermi energy. With this spin-flip spectroscopy we assign the initial state of the complex to the LS state and the switched state to the HS state. Additionally, the HS spectra reveal a magnetic anisotropy of the molecule, that implies a preferred orientation of the molecular magnetic moment.

Contents

1 Introduction

Since decades scientists aim for making electronic circuits more efficient. One main goal is to significantly increase the spatial density of such circuits. Miniaturization down to the molecular and atomic scale is desired [5]. The construction and investigation of such nanostructures are of high interest, especially to explore design criteria and functionality. The use of single molecules as electronic components triggered lots of research activity in recent years. Such microscopic systems rely on quantum effects, which makes it more difficult to predict their behavior and properties, but also gives room for a lot of new physical effects to be discovered. One of the key quantum property used in such systems is the spin. The field of spintronics deals with components, e.g. single molecules, that use spin to store, transport or compute information. In particular, spin-crossover (SCO) complexes are promising candidates for the use as building blocks for spintronic devices.

SCO molecules consist of a transition metal ion surrounded by organic ligands. Such molecules can be switched between two states with different conformations as well as different optical, electronic and magnetic properties. Switching can be triggered by external stimuli such as light, pressure, current and temperature. These characteristics make them promising for use in various applications such as actuators [6, 7], data storage [8–13] or sensors [14–17]. For technological application as devices, contacting the complexes with metal electrodes is required. This usually leads to a drastic deviation of the functionality of the complexes compared to the bulk material [18–26]. Contacting the complexes with metal electrodes can lead to fragmentation and the loss of the switching ability [21, 23, 27–30]. In particular, strong deformation of the complex, change of the molecules electronic structure, immobilization of important subunits and the weakness of the coordination bond are problems [21, 23, 27–31]. To overcome these obstacles, a better understanding of the molecule substrate interaction is required. To obtain design criteria for SCO complexes and their networks on surfaces, understanding cooperative effects and switching mechanisms is important.

By now, a few examples of successful deposition of functional complexes investigated with transport measurements [9–13, 32–37] and scanning tunneling microscopy (STM)

[20–22, 25, 38–43] were reported. Low-temperature STM is a powerful instrument to investigate individual molecules in direct contact with a metal surface and can give a deep insight into e.g. switching, assembly, electronic and magnetic properties. Improving the understanding of switching mechanisms of SCO complexes and their cooperative effects assembled in grids on a surface is desired.

Overview of this Thesis

In this thesis, various spin-crossover complexes adsorbed on metal surfaces were investigated using LT-STM, operated at $\approx 4.6\,\mathrm{K}$ or below in ultra-high vacuum. The complexes were successfully deposited on surfaces with submonolayer coverage. Switching, cooperative effects, magnetic moment and molecule substrate interactions were investigated in detail.

The following paragraphs summarize the chapters of this thesis and some aspects are highlighted. **Chapter 2** "Fundamentals" presents a brief introduction into the basic principles of STM and basic concepts needed for understanding this thesis. In **Chapter 3** "Experimental Setup" the used instruments and sample preparation are briefly explained.

Chapters 4 to 6 are the main parts of this thesis, presenting the investigations of the different SCO complexes. **Chapter 4.1** reports the investigation of a Fe based SCO molecule that self assembles into tetramers on a Ag(111) surface. Highly efficient electron induced SCO is presented. Two molecules per tetramer cannot be switched, but can be used to excite their neighbors. A structure model of the tetramer is suggested that can explain key observations in the experiment.

Chapter 4.2 deals with further investigations of the same SCO complex as in chapter 4.1. A third state has been identified by performing the switching at negative sample voltage. This state is associated to a negatively charged HS state. The decay dynamics of this third state, in particular at positive voltage, was analyzed in detail.

Chapter 4.3 focuses on a cobalt based SCO complex, that is isostructural to the complex investigated in chapter 4.1 and 4.2. Reversible switching between a LS and HS state can be triggered at positive and negative sample voltage. The switching yields at positive sample voltage are suprisingly different by three orders of magnitude. These were rationalized in a model describing electron-induced excited spin-state trapping (ELIESST).

Chapter 5 presents results of experiments on another Fe based SCO complex in direct contact with a Ag(111) and Au(111) surface. On the Ag(111) surface, the complex appears intact and functional. Switching between the HS and LS state is induced by injection of the tunnel electrons. In contrast the complex fragments on the Au(111) surface. With the help of DFT calculations, the fragmentation is suggested to be due to strong van der Waals interactions combined with a strong affinity of the Fe ion on the Au(111) surface. We suggest this as being the reason for the fragmentation on gold. Au(111) has often been considered as a less reactive surface than Ag(111), especially in the field of SCO. Our investigation shows that the trend is reversed.

In **Chapter 6**, an investigation of the SCO complex $Fe(HB(1,2,4\text{-triazol-1-yl})_3)_2$ on a Cu(111) surface is presented. The complexes self assemble into large islands and exhibit SCO. Tunneling spectra of the HS molecules reveal inelastic features around the Fermi energy, these can be associated with magnetic excitations. Spectra measured at the pristine LS state are featureless around the Fermi energy. Using spin-flip spectroscopy the magnetic state of the molecule can be identified. Furthermore, these spectra evidence a magnetic anisotropy of the molecule.

Chapter 7 summarizes the main findings and interpretations of this thesis. **Chapter 8 and 9** report a list of my publications and the acknowledgements.

The parts of this thesis written below are based on publications in peer-reviewed journals as indicated at the beginning of each chapter:

- **Chapter 4.1**:
  S. Johannsen et al., "Electron-Induced Spin-Crossover in Self-Assembled Tetramers", ACS Nano **15**, 11770–11778 (2021)

- **Chapter 4.2**:
  S. Johannsen et al., "Three-State Switching of an Fe Spin Crossover Complex", J. Phys. Chem. C **126**, 7238–7244 (2022)

- **Chapter 4.3**:
  S. Johannsen et al., "Spin Crossover in a Co Complex on Ag(111)", Angew. Chem. Int. Ed. **61**, e202115892 (2022)

- **Chapter 5**:
  S. Johannsen et al., "Spin-Crossover and Fragmentation of $Fe(neoim)_2$ on Silver and Gold", J. Phys. Chem. Lett. **14**, 7814–7823 (2023)

Chapter 6 of this thesis is based on a manuscript with supplemental information that is prepared for publication.

2 Fundamentals

This chapter provides a brief introduction into the fundamentals for understanding the present work. Within the scope of the thesis, spin-crossover (SCO) complexes in direct contact to metallic surfaces were investigated with low-temperature scanning tunneling microscopy (LT-STM). Consequently, the basic theory of STM and SCO will be explained in the following sections. The chapter "Experimental Setup" will point out details of the STM setup and the sample preparation.

2.1 Scanning Tunneling Microscopy

The scanning tunneling microscope was invented by Gerd Binnig and Heinrich Rohrer in the 1980s [44, 45]. In the same decade, both received the Nobel Prize in Physics for its invention. The STM is a powerful tool in surface science and allows a deep insight of surface systems by investigating conducting or semi-conducting solid samples. Since decades, the STM is a widely spread instrument in research with a large user community. Thus, STMs are continuously refined and nowadays allows performing a large variety of different experiments.
With STM, samples can be investigated in air, vacuum or liquid environment. It allows imaging of surfaces down to the atomic scale. Furthermore, STM enables the user to manipulate single individual atoms and molecules and gain information about the electronic, magnetic and chemical properties of the sample surface. In LT-STM, cryogenic cold samples can be investigated at temperatures down to a few mK.

Here, I will briefly explain the basic principle of STM. A very sharp metallic tip, e.g. made of tungsten, lead or platinum, is brought very close to a (semi-)conducting sample surface. The distance between tip and sample is usually on the order of a few nm or below. When a bias voltage between tip and sample is applied, a small tunneling current occurs, due to the quantum mechanical tunneling effect. The tunneling current is usually on the order of pA to nA.

The current decays exponentially with the tip-sample distance. Hence, the tunneling current is extremely sensitive to changes of the tip-sample distance. Regarding this sensitivity, STM can image surfaces with a high spatial resolution of the order of pm. Figure 2.1(a) shows a simplified model of an STM setup.

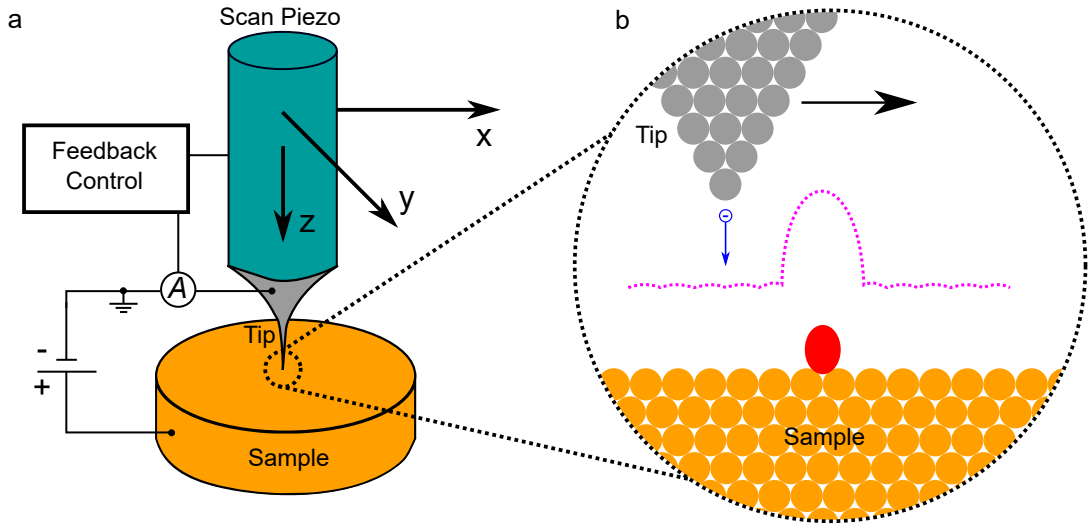

Figure 2.1: Simplified model of an scanning tunneling microscope. (a) Simplified shematic of an STM setup. A voltage source is connected to the tip and sample. The tip is mounted at the bottom of a piezoelectric scanner tube, that allows to move the tip controllably in xyz-directions. The tunneling current is measured and used as input signal of a feedback control. With this, the z tip height can be adjusted to keep the tunneling current constant. (b) Simplified picture of the tunnel junction. Grey and orange circles show the atoms of the tip and sample, respectively. An adsorbate on the sample surface is shown as a red object. If the tip is moved e.g. from left to right and the tunneling current is kept constant, the tip height z represents the profile of the surface as indicated with the magenta dotted line.

A voltage supply is connected between tip and sample, that provides the bias voltage. The tip is mounted at the end of a piezoelectric scanner. It can move the tip controllably in xyz-directions. The tunneling current is measured and guided as an input signal in a feedback control. This can control the z height of the tip, such that the tunneling current stays constant. Figure 2.1(b) shows a simplified picture of the tunnel junction, where the atoms of the tip and sample are presented as circles. At the top, the tip is shown where ideally only a single atom is at the apex. At the bottom the substrate is shown, represented by ordered atoms. On top of the substrate, an adsorbate is shown as a red object. Here, electrons can tunnel from the tip into the sample. If the tip is moved from e.g. left to right and the tunneling current is kept constant by the feedback loop due to control of the tip height, a profile $z(x, y)$ of the sample surface can be acquired, as indicated with magenta dotted line.

Basically, there are two ways to map the sample surface, briefly explained in the following paragraphs:

Constant-height topographs. In the constant-height mode the tip height z is kept constant and the tip is only moved laterally (x, y) over the sample surface. Due to the roughness of the surface, step edges or adsorbates, a change in the lateral position of the tip will lead to different tip-sample distances. As a consequence, the tunneling current I will change and reveal a profile $I(x, y)$ of the sample surface. Another important component that contributes to the tunneling current dependent on the lateral position of the tip, is the number of electronic states that are involved in the transport of electrons through the tunnel junction.

Constant-current topographs. In the constant-current mode a feedback loop controls the tip height and thereby the tip-sample distance so, that the tunneling current is kept constant at a chosen setpoint. The tip height depends on the geometric and electronic structure of the sample surface. In this operating mode, the z-channel as tip height is acquired in dependence of the lateral xy tip position. By processing these data, a topograph of the sample surface can be created. In this thesis, all topographs were acquired in the constant-current mode, unless indicated otherwise.

2.1.1 Tunneling Current

When the distance between tip and sample is sufficiently small, the wave functions of both electrodes overlap through the vacuum barrier. This allows electron transport from one electrode to the other. Figure 2.2 shows a simplified schematic energy scheme of the tunnel junction between two normal conducting electrodes, tip and sample. Between tip and sample a vacuum is assumed. When there is no bias voltage applied between the electrodes (Figure 2.2(a)), both Fermi energies of tip $\mathrm{E_{F,t}}$ and sample $\mathrm{E_{F,s}}$ are identical. When a bias voltage V is applied, the Fermi energies are shifted by eV with respect to each other. Depending on the polarity of the applied voltage, electrons can tunnel from the sample to the tip (Figure 2.2(b)) or vice versa (Figure 2.2(c)). Usually the experimentalist can choose the polarity of the bias voltage. Here a flat density of states is assumed for the tip.

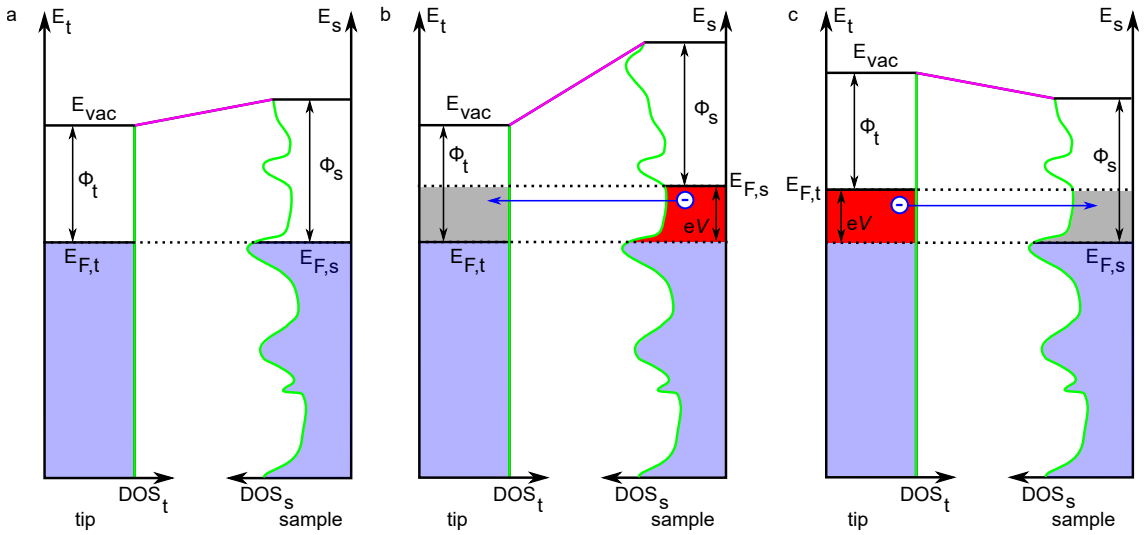

Figure 2.2: Schematic energy diagram of the tunnel junction between two normal conducting electrodes. (a) The density of states (DOS) for tip (DOS_t left) and sample (DOS_s right) are plotted as green solid curves over the energies E_t and E_s. Both DOS are filled with electrons up to their respective Fermi energy $\mathbf{E_{F,t}}$ and $\mathbf{E_{F,s}}$, visualized by blue colored regions. The work function Φ_t (Φ_s) of the tip (sample) is the energy difference between $\mathbf{E_{F,t}}$ ($\mathbf{E_{F,s}}$) and the vacuum level $\mathbf{E_{vac}}$. The tunnel barrier is approximated as trapezoidal shown as a solid magenta line between tip and sample. When no bias voltage is applied at the tunnel junction, both $\mathbf{E_{F,t}}$ and $\mathbf{E_{F,s}}$ are at the same energy marked by a dotted line. (b) A bias voltage V is applied at the tunnel junction with the sample being on a more negative electric potential than the tip electrode. The Fermi energy $\mathbf{E_{F,s}}$ is elevated by eV relative to $\mathbf{E_{F,t}}$. In this scheme electrons from occupied states of the sample (red region) can tunnel to unoccupied states of the tip. (c) The polarity of the applied bias voltage V is reversed compared to (b). Now the tip is on a more negative electric potential. Electrons from occupied tip states are tunneling to unoccupied sample states. In contrast to (b), a tunneling current flows from tip to sample.

WKB Approximation

The transmission probability τ of an electron to pass through the tunnel junction can be estimated with the Wentzel-Kramers-Brillouin (WKB) approximation. In this, a one dimensional approximation with the assumption of a trapezoidal barrier of width z, τ can be written as [46–48]:

$$\tau(z, V, E) \propto \exp\left(-2z\sqrt{\frac{2m}{\hbar^2}\left(\Phi + \frac{eV}{2} - E\right)}\right). \tag{2.1}$$

In expression (2.1) m is the electron mass, $\hbar$ the reduced Planck constant, Φ the average work function of tip and sample, e the elementary charge, V the applied bias voltage and E the energy of the electron.

Within the WKB approximation, the tunneling current density can be expressed using the transmission probability as follows [48]:

$$J(z,V,T) \propto \frac{2\pi e}{\hbar}\left(\frac{\hbar^2}{2m}\right)^2 \int_{-\infty}^{+\infty} \tau(z,V,E)[f(E-eV,T)-f(E,T)]\rho_S(E)\rho_t(E-eV)\,dE, \tag{2.2}$$

where $f(E,T)$ is the Fermi-Dirac distribution, T is the temperature, $\rho_S(E)$ and $\rho_t(E)$ are the surface and tip densities of electronic states, respectively. At the limit of low temperatures $k_BT \ll eV$ (k_B: Boltzmann constant), expression (2.2) can be simplified in the following form:

$$J(z,V) \propto \frac{2\pi e}{\hbar}\left(\frac{\hbar^2}{2m}\right)^2 \int_{0}^{eV} \tau(z,V,E)\rho_S(E)\rho_t(E-eV)\,dE. \tag{2.3}$$

Expressions (2.2) and (2.3) show that the density of the tunneling current is not only sensitive to the tip sample distance z, but also to the densities of electronic states of tip and sample, ρ_t and ρ_S, respectively.

Bardeen Approach

The Bardeen approach [49–51] estimates the tunneling current between two electrodes as follows [50]:

$$I = \frac{4\pi e}{\hbar}\int_{-\infty}^{+\infty}[f(E-eV,T)-f(E,T)]\rho_t(E-eV)\rho_S(E)|M|^2dE, \tag{2.4}$$

where e is the elementary charge, $f(E,T)$ is the Fermi-Dirac distribution, V the applied bias voltage, T the temperature, ρ_t and ρ_S are the densities of states of the tip and sample, respectively. The Bardeen tunneling matrix element M describes the overlap of the wave functions of tip and sample. Expressions (2.3) and (2.4) show that the tunneling current is sensitive to the densities of states of tip and sample. These densities of states can have a large influence on the acquired topographs and usually have to be taken into account for interpretation of the data.

Typically, the density of states of the tip is unknown. In the Tersoff-Hamann approximation [52] the electronic structure of the tip is approximated by a spherical s like orbital wave function located at the tip apex.

2.1.2 Tunneling Spectroscopy

STM provides the opportunity to gain information on the electronic structure of the investigated sample, besides imaging the sample surface. In this thesis, adsorbed spin-crossover (SCO) complexes on metal surfaces were investigated by STM. With scanning tunneling spectroscopy (STS), valuable information on the density of states of the adsorbed molecules can be extracted. Especially, information about the energetic position of the highest occupied molecular orbital (HOMO) and the lowest unoccupied molecular orbital (LUMO) are of great interest. Furthermore, for some SCO systems, spectral features around the Fermi Energy may reveal information on the magnetic state of the adsorbed complex.
By using the WKB approximation, the first derivative of the tunneling current with respect to the applied bias voltage reads [48]:

$$\begin{aligned}\frac{dI}{dV} \propto\, & e\,\tau(z,V,eV)\,\rho_S(eV)\,\rho_t(0) \\ & \underbrace{+\int_0^{eV} \tau(z,V,E)\,\rho_S(E)\,\frac{d\rho_t(E-eV)}{dV}dE}_{①} \\ & \underbrace{+\int_0^{eV} \frac{d\tau(z,V,E)}{dV}\,\rho_S(E)\,\rho_t(E-eV)dE}_{②}\,. \end{aligned} \tag{2.5}$$

The tunneling transmission probability $\tau(z,V,E)$ is a continuous exponential function. Hence, it will not contribute peaks or dips, but a background to the $\mathrm{d}I/\mathrm{d}V$. Usually the DOS of the tip ρ_t is assumed as constant. As a consequence, term ① is in general neglected. Term ② may become significant for elevated voltages, but is often neglected as well [53]. From this it follows that:

$$\frac{dI}{dV} \propto \rho_S(eV)\,\tau(z,V,eV). \tag{2.6}$$

Expression (2.6) implies that the differential conductance dI/dV is proportional to the density of states of the sample ρ_S at bias voltage V multiplied by the transmission probability τ.

2.1.3 Inelastic Electron Tunneling Spectroscopy

When an electron passes the tunnel junction, e.g. from tip to sample, part of the energy of the tunneling electron may be exchanged with the investigated system, causing an excitation. The inelastic electron tunneling process is sketched in Figure 2.3(a). For the corresponding process, the energy of the tunneling electron has to be larger than the excitation energy E_{ex}. Inelastic electron tunneling spectroscopy (IETS) is able to monitor this process. If the absolute value of the voltage applied at the tunnel junction overcomes $|E_{ex}/e|$, an inelastic conduction channel opens, that leads to a steeper slope in the $I(V)$ curve (Figure 2.3(b)). This causes step features at $|E_{ex}/e|$ in the dI/dV spectrum (Figure 2.3(c)). By acquiring such dI/dV spectrum for an appropriate sample system, inelastic processes can be explored.

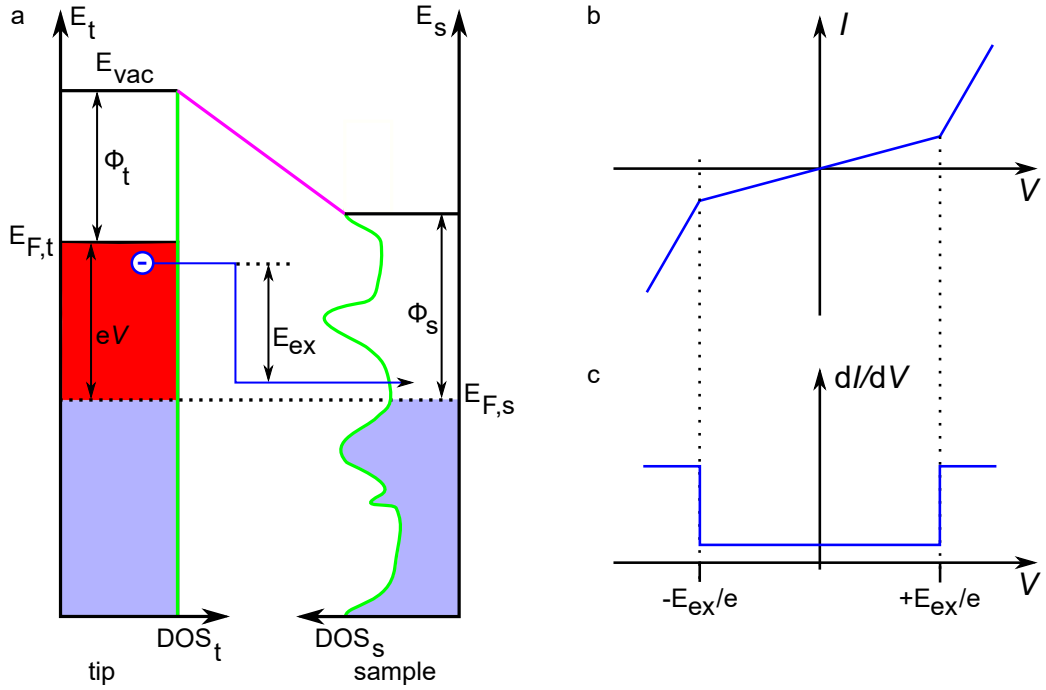

Figure 2.3: Schematic concept of inelastic electron tunneling spectroscopy. (a) Energy diagram of a tunnel junction with two normal conducting electrodes tip and sample. If the energy of an electron from an occupied state of the tip is larger than a certain excitation energy E_{ex}, it can transfer part of its energy and occupy an energetically lower unoccupied state of the sample. (b) Schematic $I(V)$ curve of the tunnel junction with inelastic electron tunneling process. If the absolute value of the applied voltage V is larger than $|E_{ex}/e|$, an inelastic conduction channel opens. As a consequence the slope in the $I(V)$ curve becomes steeper. (c) The corresponding dI/dV spectrum exhibits steps at $|E_{ex}/e|$.

2.2 Spin-Flip Spectroscopy

Depending on the spin state of a SCO complex (LS or HS), the central ion may have a non zero net magnetic moment. When the complex is adsorbed on a metal surface and imaged by a LT-STM, it is in general not straightforward to identify the magnetic state of the molecule. Usually, the central ion is a transition metal ion with partially filled d orbitals, depending on the actual electronic state. Electrons in these d orbitals can undergo spin-flip processes under certain conditions. Energy and angular momentum of the tunnel electrons are exchanged with the spin system, which induces transitions between magnetic states of the spin system. With the spectroscopic capability of the STM, it is possible to detect spin-flip processes using inelastic tunneling spectroscopy (IETS) [54]. Under certain conditions, this so called spin-flip spectroscopy provides the opportunity to identify the spin state of an adsorbed SCO complex on a metal surface. Hence, LS or HS states can be distinguished. This phenomenon was used in chapter 6 to characterize the magnetic properties of a molecule in the HS state. So far spin-flip spectroscopy has been used to investigate single atoms on surfaces [54–57], linear chains of atoms [58] and molecular magnets [59–61].
At certain values of the applied bias voltage, transitions of the z-component of the spin S_z may be excited. As a result, step features become observable in the $\mathrm{d}I/\mathrm{d}V$ spectrum.

A simple system to introduce spin-flip processes is the spin-1/2 system shown in Figure 2.4(a). Here two states $|S_z\rangle$ ($S_z = \pm 1/2$) are present, which are degenerate in the absence of magnetic field.

When a magnetic field is applied, both states are energetically split by the Zeeman energy. The energy is necessary to induce excitation from state $|-1/2\rangle$ to $|+1/2\rangle$. The energy is given by $\mathrm{E_{ex}} = g\mu_B B$, where g is the Landé g-factor, μ_B Bohr magneton and B is the applied magnetic field. When the applied voltage is sufficiently high ($|eV| > |\mathrm{E_{ex}}/e|$) tunneling electrons may induce the transition from $|-1/2\rangle$ to $|+1/2\rangle$. A tunneling conduction channel opens, that causes symmetric step features in the $\mathrm{d}I/\mathrm{d}V$ spectrum as illustrated in Figure 2.4(b).
Figure 2.4(c) shows the energy scheme for a spin-3/2 system without magnetic anisotropy. At zero magnetic field, all $2S + 1 = 4$ states are energetically degenerate. With applied magnetic field, all states split linearly in energy according to the Zeeman splitting. Here, only transitions between neighboring states are allowed, as indicated by red arrows. A tunneling electron can only flip its spin by $\Delta S_z = 1$. Higher excitation, e.g. to next-next-neighboring states, are not possible because of conservation of angular momentum.

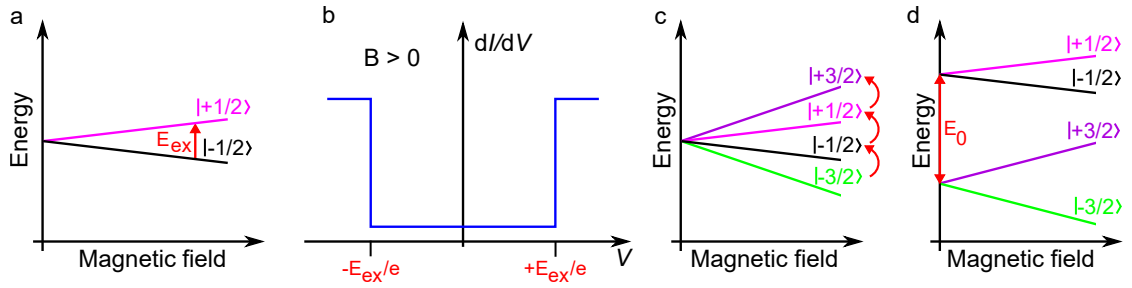

Figure 2.4: Schematic diagrams of spin excitation processes. (a) Energy of the two states $|S_z\rangle$ ($S_z = \pm 1/2$) of a spin-1/2 system as a function of the applied magnetic field. At zero magnetic field both states are energetically degenerate. When a magnetic field is applied, the energy difference $\mathrm{E_{ex}}$ between both states increases linearly with increasing magnetic field. $\mathrm{E_{ex}}$ corresponds to the Zeeman energy. (b) Schematic $\mathrm{d}I/\mathrm{d}V$ spectrum showing step features corresponding to the excitation energy $\mathrm{E_{ex}}$. (c) For a spin-3/2 system, only transitions between neighboring states are allowed, indicated by red arrows. The energy of the states $|S_z\rangle$ depends linearly on the magnetic field as in the spin-1/2 system. (d) If magnetic anisotropy is present, not all states are energetically degenerate at zero magnetic field. For this case, an energy splitting $\mathrm{E_0}$ between states $|\pm 3/2\rangle$ and $|\pm 1/2\rangle$ is indicated.

At zero magnetic field, not all states are energetically degenerate if there is a magnetic anisotropy, as shown in Figure 2.4(d). In this situation, even without applied magnetic field excitation steps can be found in the $\mathrm{d}I/\mathrm{d}V$ spectrum.

To quantitatively describe the energy of the magnetic states, the following phenomenological spin Hamiltonian can be used [55]:

$$\hat{H} = D\hat{S}_z^2 + E\left(\hat{S}_x^2 - \hat{S}_y^2\right) + g\mu_B \mathbf{B}\cdot\hat{\mathbf{S}}, \tag{2.7}$$

where D and E are the uniaxial and transverse anisotropy parameters, $\hat{\mathbf{S}} = \left(\hat{S}_x, \hat{S}_y, \hat{S}_z\right)$ the spin operator, g the Landé g-factor, μ_B the Bohr magneton and $\mathbf{B} = (B_x, B_y, B_z)$ the applied magnetic field. The first two terms of the Hamiltonian describe the zero field splitting. The third term describes the Zeeman energy.

2.3 Spin-Crossover

Spin-crossover (SCO) is the switching phenomenon between spin states of a molecule. It can occur under certain conditions in transition-metal coordination complexes with $3d^{4\text{-}7}$ electronic configuration [4]. By external perturbation such as light, temperature change, pressure change, electron transport or electric field, the spin state of the central metal ion may be switched. The state of the molecule can be characterized as a low-spin state (LS) or a high-spin state (HS). The presence of SCO depends on the relationship between the strength of the ligand field, that means the electrostatic field acting at the central ion, and the mean spin pairing energy. This corresponds to the energy cost for filling two electrons into the same orbital. If the strength of the ligand field is stronger or weaker than the spin pairing energy, the central ion may be in the LS or HS state, respectively. Depending on the spin state, structural, electronic, magnetic and optical properties of the compound can drastically change.

In this thesis, predominantly SCO molecules with a Fe^{II} central ion in an octahedral ligand field were investigated. An example of such a SCO complex is shown in Figure 2.5(a). Here, the central Fe^{II} ion is surrounded by 6 nitrogen atoms in an octahedral geometry. In a simplified model, the 5 d orbitals of the Fe^{II} split into 3 t_{2g} and 2 e_g orbitals, as shown in Figure 2.5(b).

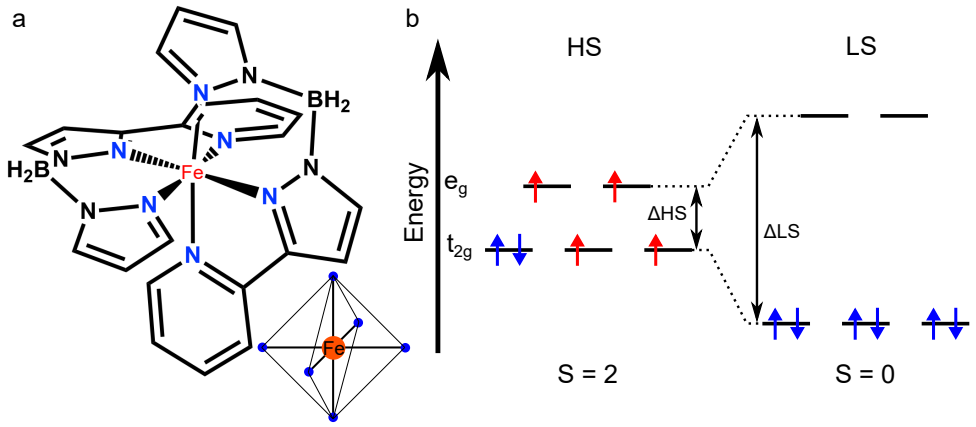

Figure 2.5: (a) Spin-crossover (SCO) complex $Fe(H_2B(pyrazole)(pyridylpyrazole))_2$ with a Fe^{II} central ion surrounded by two orthogonal ligands, adapted from ref. [1]. This complex has an octahedral ligand around the central metal ion. For clarity, in the lower right corner, the sketch shows the octahedral geometry of the nitrogen atoms (blue circles) surrounding the Fe^{II} ion (orange circle). (b) Simplified d-electron configuration of the central Fe^{II} ion in an octahedral ligand field.

The e_g orbitals are elevated in energy compared to the t_{2g} orbitals. If the energy difference ΔHS is smaller than the spin pairing energy, the d orbitals are filled according to Hund's rules. Consequently, one t_{2g} orbital is fully occupied with electrons.

2 t_{2g} and 2 e_g orbitals are only filled with a single electron each. This scenario corresponds to the HS state with S=2. In the other case, the energy splitting ΔLS is larger than the spin pairing energy, leading to fully occupied t_{2g} orbitals. This situation corresponds to the LS state with S=0. The perturbations, mentioned at the beginning of this chapter, may lead to transitions between LS and HS state.

Adsorption of SCO molecules on a metal electrode has often lead to dissociation or loss of the switching capability [21, 23, 27–30]. Therefore, investigating these molecules in direct contact with metal surfaces is not a trivial task. Ref. [18] is a useful publication that provides an overview of SCO complexes in direct contact with surfaces. In this thesis, successful deposition of submonolayers of SCO molecules and their investigation by LT-STM is presented. In one chapter, the role of the electrode material, gold and silver, is investigated in the view of fragmentation of the adsorbed SCO complexes.

2.4 Switching Rate and Yield

Analyzing switching rates and yields can reveal information about the effective trigger (tunneling electrons/electric field) and on the underlying microscopic switching mechanism of reversibly switchable molecules adsorbed on a metal surface.

If the STM tip is placed above the molecule and the bias voltage and setpoint current is changed, frequent reversible switching may be induced, e.g. by electron injection and/or a change of electric field within the tunnel junction. Figure 2.6(a) shows a sketch of this situation. The molecule can be switched between two states A and B, exhibiting different electrical conductance. Here, state A has a lower electrical conductance and B a higher one. If the tip height Z is frozen and the bias voltage is at a selected value, the tunneling current will exhibit two level fluctuations. The tunneling current in state B will be larger compared to state A, since the electrical conductance in B is larger. The two level fluctuations can be monitored in the time series of the tunneling current shown in Figure 2.6(b).
In the shown time series are $N_{\mathrm{A}\to\mathrm{B}} = 3$ switching events from state A to B and $N_{\mathrm{B}\to\mathrm{A}} = 3$ switching events from state B to A. A switching rate may be calculated for the switching from state A to B and vice versa as follows:

$$\mathrm{Rate}_{\mathrm{A}\to\mathrm{B}} = \frac{N_{\mathrm{A}\to\mathrm{B}}}{T_{\mathrm{A}}}, \qquad \mathrm{Rate}_{\mathrm{B}\to\mathrm{A}} = \frac{N_{\mathrm{B}\to\mathrm{A}}}{T_{\mathrm{B}}}, \tag{2.8}$$

where T_{A} and T_{B} are the residence times in the states A and B, respectively. This switching rate usually varies with the applied bias voltage and tunneling current.

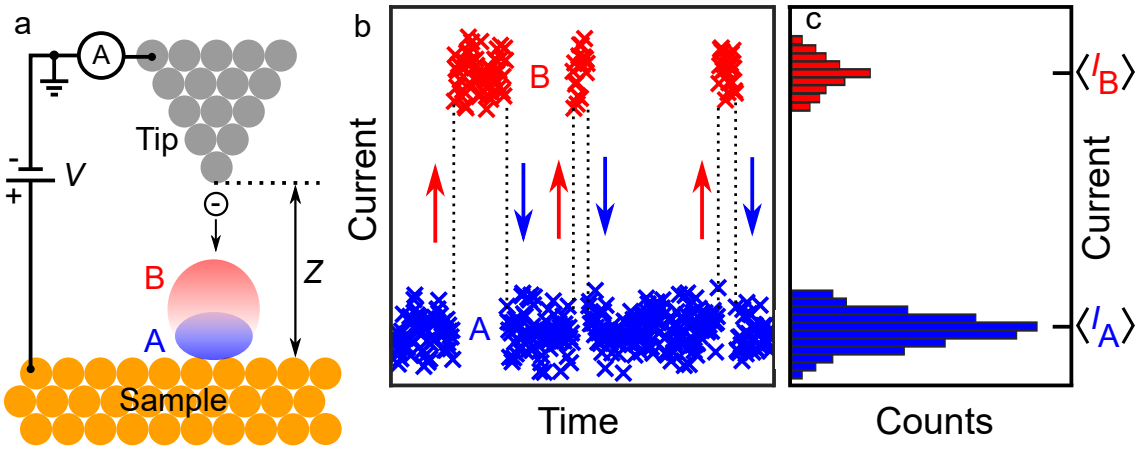

Figure 2.6: (a) Sketch of a tunnel junction with an adsorbate on the sample surface. Switching between states A and B, sketched as blue and red objects, is indicated. Transitions can be induced by electrons tunneling from the tip into the adsorbate. The tip height Z is kept constant. (b) Time series of the tunneling current. Two level fluctuations between states A and B are presented. Jumps from level A→B (B→A) are marked with red (blue) arrows. (c) Histogram of the tunneling current trace shown in (b). The average currents $\langle I_A \rangle$ and $\langle I_B \rangle$ are marked.

A rate proportional to the tunneling current I (rate $\propto I^1$) is indicative of switching due to a one-electron process. If this is the case, a switching yield can be defined as the probability of a single electron to induce switching:

$$\text{Yield}_{A\to B} = \frac{e\,\text{Rate}_{A\to B}}{\langle I_A \rangle}, \qquad \text{Yield}_{B\to A} = \frac{e\,\text{Rate}_{B\to A}}{\langle I_B \rangle}, \tag{2.9}$$

where e is the elementary charge, $\langle I_A \rangle$ and $\langle I_B \rangle$ are the corresponding average currents of the levels within the tunneling current time series. Figure 2.6(c) shows the histogram of the tunneling current. The average current of each level is indicated by $\langle I_A \rangle$ and $\langle I_B \rangle$. The switching yield may reveal valuable information about the efficiency of the switching and the switching mechanism. Further information about the analysis of current time series, switching rates and yields can be found in chapter 4.1.6 section "Analysis of current time series".

3 Experimental Setup

In this chapter, the experimental setup used to acquire the STM data is briefly introduced. Furthermore, the in vacuo preparation of the samples to achieve submonolayer coverage of SCO molecules on metal substrates is summarized.

3.1 Low-Temperature STM

The instrument used for STM measurements in chapter 4 and 5 is a cryogenic ($\approx 4.6\,\mathrm{K}$) STM from CreaTec operated in ultra-high vacuum (UHV). The apparatus consists of 3 UHV chambers separated by gate valves. One chamber contains the microscope and has a base pressure of $\approx 1.2 \cdot 10^{-10}\,\mathrm{mbar}$. The other chamber is the preparation chamber for in vacuo preparation. It has approximately the same base pressure as the STM chamber. After preparation of the sample, it can be directly transferred into the cooled STM. The third chamber is a load-lock chamber, where samples, STM tips and crucibles with powder of molecules are inserted from ambient conditions. After pumping the load-lock chamber, inserted items are directly transferred into the preparation chamber without breaking the vacuum of the other chambers. UHV is obtained using rotary vane, scroll, turbomolecular, ion getter and titanium sublimation pumps. A pneumatic damping system lifts the whole instrument during measurements, in order to damp the external vibrations. The microscope is based on a Besocke beetle type design and operated with Nanonis electronics.
The STM data presented in chapter 6 were in parts measured with a different instrument. In particular, the presented $\mathrm{d}I/\mathrm{d}V$ spectra were acquired at $\approx 1.7\,\mathrm{K}$ with an Unisoku USM1300 STM. Also for this instrument, a preparation chamber and a load-lock chamber were accessible. In vacuo preparation of the sample before inserting into the microscope was performed in the preparation chamber. The STM was also operated with Nanonis electronics.

3.2 Sample Preparation

In this thesis, individual molecules in direct contact to metallic surfaces were investigated with STM. Metallic single crystals, such as gold, silver and copper, exhibiting a defined (111) surface were used as substrates. In the preparation chamber, the single crystal surfaces were cleaned by repeated cycles of Ar^+ sputtering and annealing to $\approx 500\,°C$. For sputtering, a sputter source is mounted in the preparation chamber and connected to an argon gas cylinder. For the annealing process, single crystals are mounted on a button heater, that can be operated as a resistance heater. The temperature is monitored with, a thermocouple attached to the button heater. The single crystal, button heater and thermocouple are mounted on a metallic sample holder. This setup can be moved with a manipulator inside the UHV chambers.

To obtain molecular submonolayers on single crystal surfaces, molecules were thermally sublimated in the preparation chamber under UHV conditions. The molecules are stored inside a crucible that is mounted on a button heater. The evaporation setup is located under a quartz balance. The molecules sublimate into the gas phase if the crucible is heated and hit the detection area of the quartz balance. With a read-out device attached to the quartz balance, deposition rates depending on the temperature of the crucible can be measured. If a sufficient rate is detected, clean metallic single crystals are moved in front of the crucible and molecules cover the (111) surface. The amount of molecular coverage on the surface can be controlled by varying the time the sample is held in front of the evaporator. The distance between evaporator and sample is of the order of a few centimeters.

4 Spin Switching in Self-Assembled Tetramers

Chapter 4.1 is based on a publication in ACS Nano from 2021. Reprinted with permission from:
S. Johannsen et al., "Electron-Induced Spin-Crossover in Self-Assembled Tetramers", ACS Nano **15**, 11770–11778 (2021) DOI: 10.1021/acsnano.1c02698.

Author Contributions

Sven Johannsen performed the STM measurements. Sven Johannsen, Manuel Gruber and Richard Berndt analyzed and interpreted the data. Sascha Ossinger and Felix Tuczek synthesized the SCO complexes. Troels Markussen carried out the DFT calculations. Richard Berndt and Manuel Gruber wrote the manuscript with input from all authors. Sven Johannsen created all figures in the manuscript and supporting information, except figures 4.12–4.15. Richard Berndt supervised the project. All authors discussed the results.

4.1 Electron-Induced Spin-Crossover in Self-Assembled Tetramers

The spin crossover compound $Fe(H_2B(pyrazole)(pyridylpyrazole))_2$ was investigated in detail on Ag(111) with scanning tunneling microscopy (STM). A large fraction of the deposited molecules condenses into gridlike tetramers. Two molecules of each tetramer may be converted between two states by current injection. We attribute this effect to a spin transition. This interpretation is supported by control experiments on the analogous, magnetically passive Zn compound that forms virtually identical tetramers but exhibits no switching. The switching yields were studied for various electron energies, and the resulting values exceed those reported from other SCO systems by 2 orders of magnitude. The other two molecules of a tetramer were immutable. However, they may be used as contacts for current injection that leads to conversion of one of their neighbors. This "remote" switching is fairly efficient

with yields reduced by only one to two orders of magnitude compared to direct excitation of a switchable molecule. We present a model of the tetramer structure that reproduces key observations from the experiment. In particular, sterical blocking prevents spin crossover of two molecules of a tetramer. Density functional theory calculations show that the model indeed represents a minimum energy structure. They also reproduce STM images and corroborate a remote-switching mechanism that is based on electron transfer between molecules.

4.1.1 Introduction

Magnetic molecules may be used as building blocks for spintronic devices. While current devices rely on the material properties of molecular films, further miniaturization down to the molecular scale is desirable [5]. Spin-Crossover (SCO) molecules, whose magnetic states may be controlled by external stimuli, may manifestly be used to implement memory or processing functions. Their magnetic properties are also influenced by cooperative effects. In molecular crystals and films, intermolecular interactions mediate cooperativity and often affect the steepness of temperature-controlled transitions between different spin states [62–64]. In the limit of ultimate miniaturization as realized in grid complexes with a few magnetic centers, the interactions between the centers can stabilize certain magnetic patterns [65–68]. It has been suggested that such grid compounds may be used to implement quantum cellular automata [69].

In direct contact with metal electrodes, however, SCO molecules may dissociate or otherwise lose their switching capability [21, 23, 27–30]. Nevertheless, examples of successful deposition of functional ultrathin SCO films exist [18, 21, 24, 30, 70–81]. Using scanning tunneling microscopy (STM), a few studies of mononuclear complexes demonstrated that selective spin switching of single molecules may be achieved [20–22, 25, 38–43]. Indications of cooperativity were observed in two ultrathin layers in direct contact with substrates [72, 79]. While models reproduce some of the observations [73], obtaining a detailed picture of the microscopic effect is challenging. Conductance switching of SCO compounds has also been reported from transport measurements [9–13, 32, 33, 35–37].

As for SCO compounds with more than a single magnetic ion, fragmentation has been observed [29, 82]. A notable exception is ref [83], which reported a controllable geometrical isomerization of a binuclear complex. Interestingly, the isomerization of one subunit could be "remotely" triggered by injecting current into the other.

Here, we present results from the compounds $M(H_2B(pz)(pypz))_2$ (M = Fe or Zn, pz = pyrazole, pypz = pyridylpyrazole) (Figure 4.1a) deposited on Ag(111) single crystal surfaces.

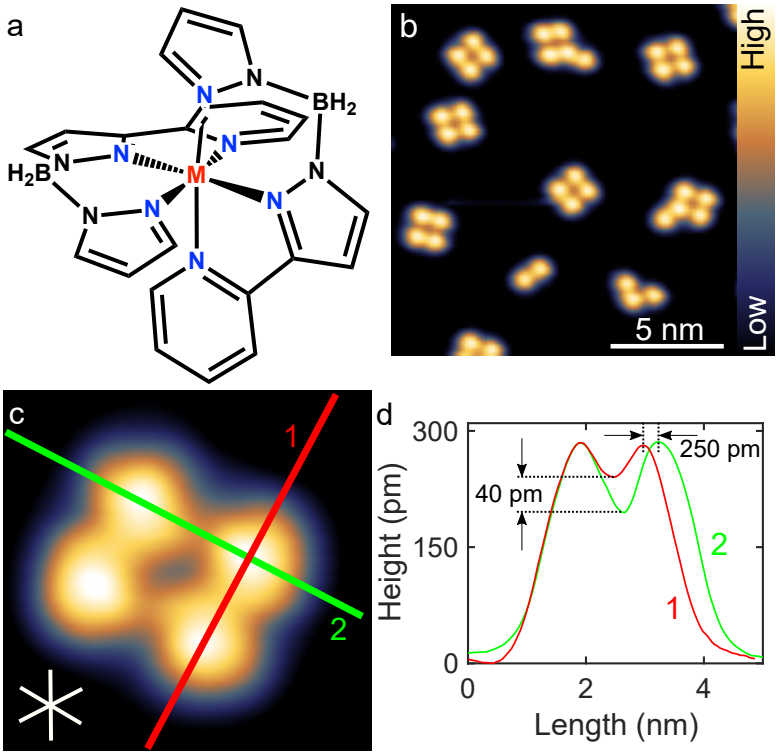

Figure 4.1: $M(H_2B(pz)(pypz))_2$ complexes and STM images from a submonolayer coverage of $Fe(H_2B(pz)(pypz))_2$ on Ag(111). (a) Structure of the synthesized complexes. The central metal ion (M = Fe or Zn) is surrounded by two orthogonal $H_2B(pz)(pypz)$ ligands. (b) Constant-current STM topograph of $Fe(H_2B(pz)(pypz))_2$ on Ag(111) (sample voltage 0.5 V, current 10 pA) showing primarily tetrameric islands. Each protrusion corresponds to an intact complex. The false colors represent a height range of 300 pm. (c) Constant-current topograph (0.5 V, 10 pA) of a tetramer. Close inspection reveals that the cluster is not 4-fold symmetric. Red and green lines indicate the positions of crosssectional profiles parallel to the edges of the tetramer. White lines (lower-left corner) indicate densely packed directions of the Ag(111) surface. (d) Separations of the topographic maxima in the profiles differ by approximately 250 pm.

The main results of our investigation with scanning tunneling microscopy were obtained with the Fe compound [84]. We find that these SCO molecules arrange themselves into gridlike tetramers that are composed of two identical subunits. One of the molecules in each subunit may be switched between two conformations that we attribute to the high-spin and low-spin states. The switching is induced by single electrons with a yield on the order of 10^{-7}, which is 100 times larger than previously reported from other SCO systems [39, 40]. While the other molecule of the subunit does not exhibit switching itself, it serves as a contact for current injection to induce switching of its neighbor. The efficiency of this "remote" switching

is smaller than observed for direct current injection into a switchable molecule by factors of 30 to 130. The variation in these factors is due to a configuration-dependent electronic coupling between molecules , which is quantitatively corroborated by DFT calculations. We extended the experiments to the analogous Zn compound. The complexes self-assemble into tetramers that are virtually identical to those of the Fe molecules. The magnetically passive Zn compound does not exhibit any switching, corroborating the interpretation of the Fe data in terms of SCO.

4.1.2 Results and Discussion

Self-Assembled Tetramers

$Fe(H_2B(pz)(pypz))_2$ is a neutral and vacuum-evaporable SCO complex based on linear tridentate organoborate ligands [84]. The M(II) cation is coordinated by two tridentate N-binding anionic $H_2B(pz)(pypz)$ ligands in a distorted octahedral arrangement. On Ag(111), the deposition of a submonolayer amount of $Fe(H_2B(pz)(pypz))_2$ leads to the formation of tetramers. Figure 4.1b shows a typical STM topograph with several tetramers. In addition a dimer, a trimer, and monomers attached to a corner of tetramers are observed. Along with the size of the tetramers, the presence of these smaller structures indicates that the tetramers are indeed clusters of four molecules rather than fragments of the deposited complex.

Closer inspection (Figure 4.1c) reveals that the topographic maxima are arranged in a rectangular array which leads to the visual impression of two dimers. According to cross-sectional profiles (Figure 4.1d), the separations of the maxima differ by $\sim 250\,\mathrm{pm}$.

Current-Induced Local Switching

Before developing a model of the tetramer structure, we present results on current-induced switching process. As demonstrated in Figure 4.2, two of the four molecules in a cluster may be switched between two states whose apparent heights differ by $\sim 50\,\mathrm{pm}$. These molecules are located along a diagonal of the tetramer. Switching of the molecule under the tip is induced by changing the bias voltage, and as a consequence, the tunneling current. Intriguingly, we did not succeed in inducing a comparable change of the two molecules on the other diagonal.

To further characterize the switching process, we recorded a time series of the tunneling current, initially with the tip placed above a molecule that is amenable to switching (Figure 4.3a). At suitable voltages, the current exhibits two-level fluctuations (Figure 4.3b) that correspond to the low and high states of the molecule in topographs as verified by subsequent imaging. The fluctuations occur on a time scale

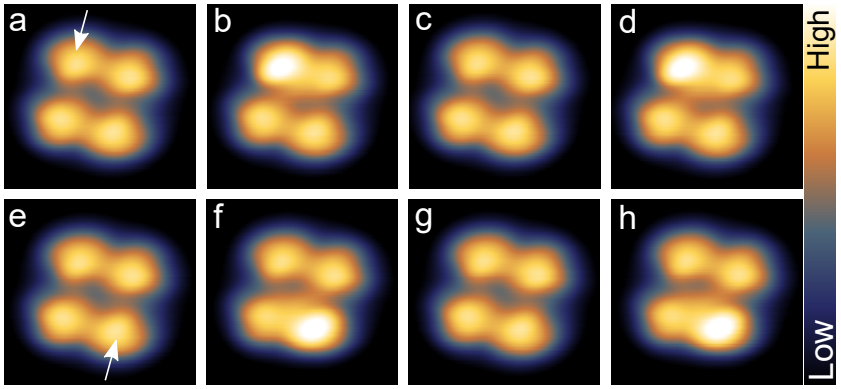

Figure 4.2: Reversible local switching of a complex under the tip. (a) Initial state of a tetramer. After imaging, the STM tip was placed above the complex indicated by a white arrow, the current feedback loop was disabled, and the sample voltage was changed from 0.5 to −1 V. We note in passing that switching may also be induced at positive polarity. This leads to a rapid rise of the current and triggers switching of the complex directly under the tip. (b) Image recorded after switching. The apparent height of the manipulated molecule has increased by ∼50 pm. (c, d) By repeating the manipulation procedure the same molecule is switched back and forth to its low and high state. The process may be repeated dozens of times without fatigue of the molecule. (e–h) The sequence described above is demonstrated again for the molecule at the lower right corner (arrow). Switching of the other two constituents (upper right and lower left corners) of the tetramer was never observed independent of the tip positions. All images were recorded at 0.5 V and 10 pA.

of ∼1 s and depend on the bias voltage and the current. Parts c and d of Figure 4.3 summarize data for the transitions from low to high and vice versa. The procedure to analyze the time series is described in chapter 4.1.6. The rates are proportional to the current (dashed lines show fits, see chapter 4.1.6 for the plot with linear scale), which implies that the switching is due to a one-electron process, and increase at slightly higher sample voltages. The tunneling currents used for conversion are on the order of a few picoamperes in contrast to currents on the order of nanoampere used in previous SCO studies [39, 40]. It may be worth mentioning that, in principle, the switching rate can be further increased by increasing the sample voltage. However, the tetramer become mobile on Ag(111) for voltages above ∼1.1 V.

The induced switching is attributed to SCO. We performed closely related experiments with the compound $Zn(H_2B(pz)(pypz))_2$. These molecules arrange themselves into tetramers on Ag(111) that are virtually identical to those found for the Fe complex (see chapter 4.1.6). The Zn ion is not expected to exhibit SCO because of its full d-shell ([Ar] $3d^{10}$ configuration). In the experiments, despite many attempts at various voltages and currents, we did not observe switching events that would be indicative of SCO. We note in passing that at excessive voltages or currents we observed destruction, lateral hopping or rotation of the tetramers.

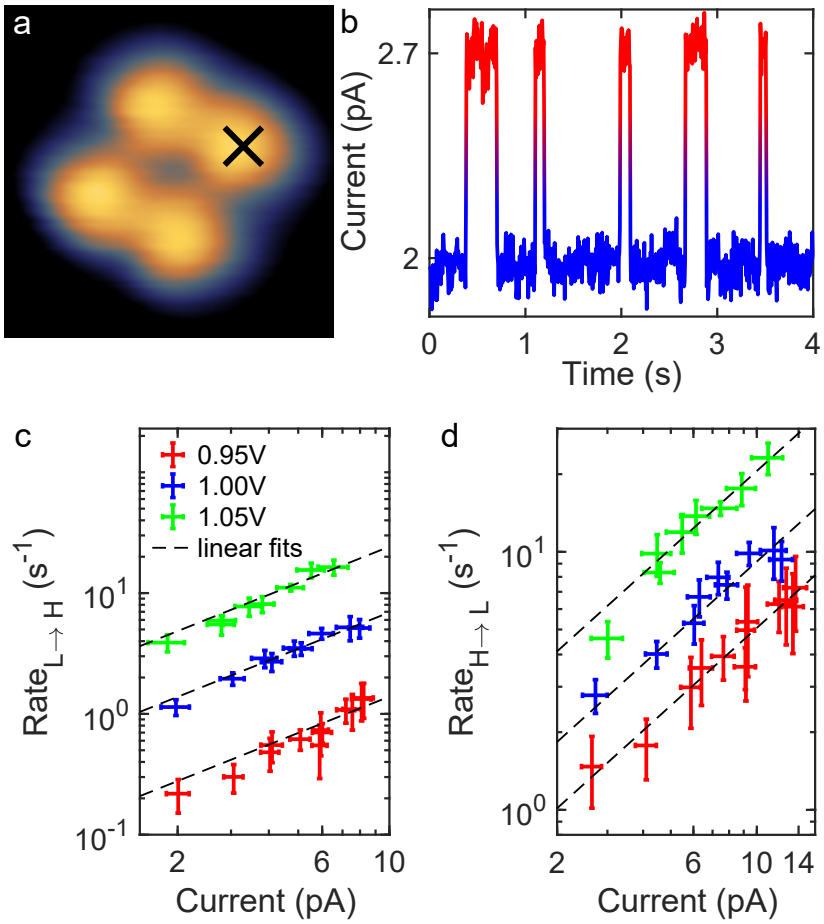

Figure 4.3: Local Switching: time series and rates. (a) Constant-current topograph (0.5 V, 3 pA) of a tetramer. For recording a time series of the current, the tip was positioned over a switchable complex (cross). (b) After disabling the feedback at 1 V and 2 pA, the current exhibits rapid jumps between levels that corresponds to the low (blue) and high (red) states in topographs. Switching rates (c) from low to high and (d) vice versa, inferred from time series such as shown in (b) (with open feedback loop). The values of the current and error margins were obtained from the mean and three time the standard deviation of the current over the entire time series when the molecule is in (c) in the low state and (d) in the high state. We used time series with durations between 30 s and 7 min with 40 to 2370 switching events. The error margins of the rates were obtained assuming a Poisson process for the switching (see chapter 4.1.6) and represent three standard deviations. Data were acquired for sample voltages 0.95 V, 1.00 V, and 1.05 V. Dashed lines are linear fits demonstrating that the rates are proportional to the current. The yields extracted from linear fits are approximately 2×10^{-8}, 1×10^{-7}, and 4×10^{-7} for low to high and 8×10^{-8}, 1×10^{-7}, and 3×10^{-7} at 0.95 V, 1.00 V, and 1.05 V, respectively.

We expect that the pristine complex is in a low-spin (LS) state and is converted to a high-spin (HS) state upon switching. This scenario is typical of Fe-based SCO complexes, which are in a S=0 state at low temperatures and converted to S=2 at elevated temperatures [85], as was observed for the title complex in the bulk [84]. In addition to an increased molecular volume, the HS state exhibits a drastically reduced gap between the highest occupied and lowest unoccupied molecular orbital (HOMO, LUMO). The low temperature (5 K) of our sample and the increased conductance of the switched (observed over the fairly wide bias range -0.6 to 1.1 V) suggest that the pristine (switched) state is a LS (HS) state. On the other hand, SCO complexes in the HS state adsorbed on a surface exist and the conductance depends on the spatial extent and the symmetry of the molecular orbitals [18]. The identification of the spin state consequently is ambiguous. In the following, we assume that the low and high states correspond to the LS and HS states, respectively. This assumption is motivated by the comparison to DFT simulated STM images (see chapter 4.1.6), suggesting that the switched state is a HS state. This is further supported by a smaller calculated HOMO-LUMO gap of HS monomers on Ag(111) compared to the corresponding LS state. This assignment leads to a consistent description of all data. We note that our spectroscopic data alone do not provide an unambiguous fingerprint of the molecular spin states (see chapter 4.1.6).

Figure 4.4 displays the switching yield, i.e., the probability of a single electron to induce SCO, as a function of sample voltage.

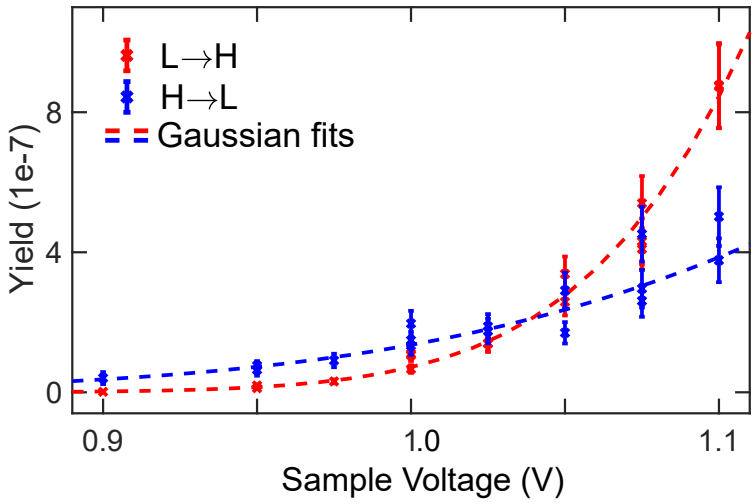

Figure 4.4: Voltage dependence of local switching yields. Yields as a function of voltage for switching from low to high (red) and high to low (blue) along with Gaussian fits. The uncertainty margins represent one standard deviation of the mean value ($\pm 1\sigma$, see chapter 4.1.6).

The yield evolves smoothly with the voltage and with Gaussian-like shape. In particular, we do not observe a threshold, which suggests that switching with a very low yield may be possible for voltages below 0.9 V. The smallest voltage at which we effectively observed switching is 0.9 V. We exclude a switching mechanism involving the direct excitation of vibrational modes decaying into a change of the spin state for two main reasons. First, the energies of vibrational modes involved in reactions are typically lower than 0.4 eV [86], while we observe substantial yields at significantly higher electron energies. Second, a (broadened) steplike increase of the yields is expected with increasing voltage for direct excitation of vibrational mode [87]. The Gaussian-like evolution of the yield observed in the present case suggests that molecular orbitals are involved in the switching process. In addition, SCO is associated with a change of molecular-orbital energies, which is in agreement with the observation of different yield evolution for low-to-high and high-to-low switching. We note that lateral hopping and the high switching yields prevented us from recording $\mathrm{d}I/\mathrm{d}V$ spectra revealing molecular-orbital energies (see chapter 4.1.6). Light-induced switching of SCO complexes often involves a metal-to-ligand charge transfer, i.e., an excited electronic state, which decays to the LS or HS state [88, 89]. A similar mechanism may be at play in the present study, yet involving another excited state (charged molecule). It may be worth mentioning that different excited states are involved in low-to-high and high-to-low switching in this scenario. Otherwise, the evolution of the yields would reflect the decay probabilities into the HS and LS states, which appears incompatible with the crossing of the yields observed in Figure 4.4.

The observed yields are unusually high. For SCO complexes on surfaces, the largest reported yields are on the order of 10^{-9} (refs [39] and [40]). In the present study, the switching from low to high at 1.1 V has a yield of $\sim 9 \times 10^{-7}$, which is almost 3 orders of magnitude higher. The observed yield is also larger than that of spin switching of Ni complexes assembled into chains on Au(111) ($\sim 6 \times 10^{-8}$, ref [90]), rotation of C_2H_2 on Cu(100) ($\sim 2 \times 10^{-9}$, ref [91]), and tautomerization of H_2 phthalocyanine on Ag(111) ($\sim 2 \times 10^{-8}$, ref [92]) but comparable to that of the rotation of a Cu phthalocyanine on Cu(111) (3.5×10^{-7}, ref [93]) and of the rotation of an ethoxy group on a molecular platform adsorbed on Au(111) (5×10^{-7}, ref [87]). Furthermore, Figure 4.4 suggests that we probe only the tails of the involved molecular orbitals. Significantly larger yields may be expected at voltages corresponding to the molecular-orbital energies. However, measuring those yields is challenging because of lateral mobility of the adsorbed tetramer that has so far prevented the recording of useful time series.

Next, a structure model of the tetramers will be presented. In this context it will be important to consider the geometrical changes between the LS and HS states. From our gas-phase DFT calculations we find that the most significant change is an increase of the angle between the terminal pyrazole subunit and the pypz plane of the $H_2B(pz)(pypz)$ ligand its belongs to.

Structure of the Tetramers

To arrive at a model of the tetramer structure, we start from the structure of crystalline $Fe(H_2B(pz)(pypz))_2$ as derived from X-ray diffraction data [84]. The crystal structure is stabilized by strong pyridine-pyridine and weaker pyridine-pyrazole interactions between neighbor complexes. Tetramer subunits of this structure, however, do not lend themselves to the self-terminating aggregation of four molecules per cluster that is observed on the Ag(111) surface. We therefore slightly modified the structure to the model of Figure 4.5.

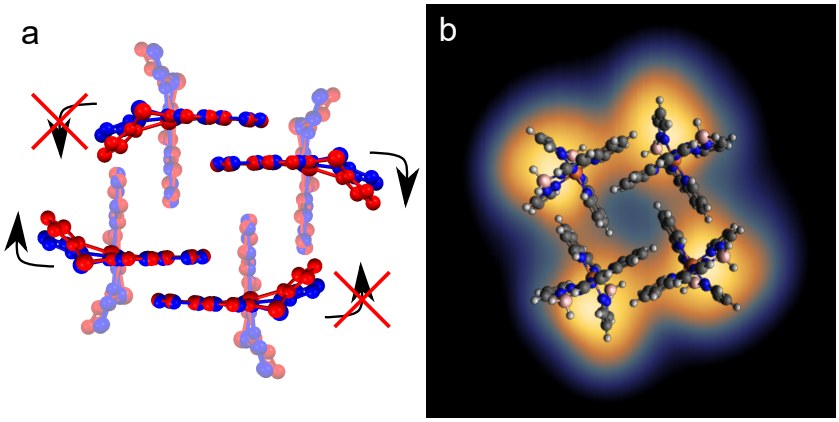

Figure 4.5: Model structure of a tetramer. (a) Schematic top view of a tetramer assembled from four $Fe(H_2B(pz)(pypz))_2$ molecules in their calculated gas-phase geometry. Blue and red complexes show the LS and HS structures, respectively. Lighter colors are used for the ligands at the bottom. While the same enantiomers are used per diagonal of the cluster, the chiralities on the two diagonals are different. Arrows and crosses indicate mobility and steric blocking of pyrazole moieties. (b) Relaxed model of a tetramer on Ag(111) superposed onto a measured topograph. Colors used in the model: gray = C, white = H, blue = N, rose = B, and orange = Fe.

This structure is stabilized by π-π interactions between neighbors, while the less strongly π-π interacting pyrazole subunits are at the exterior of the cluster. In addition, the dipole moments of the molecules point toward the center of the tetramer, which corresponds to a negative partial charge at the circumference of the cluster. It is important to realize that $M(H_2B(pz)(pypz))_2$ is chiral. The two enantiomers differ by a 180° rotation of one of the $H_2B(pz)(pypz)$ ligands. The proposed structure is composed of both enantiomers with identical enantiomers located on the diagonals of the tetramer. One ligand of each molecule touches the Ag substrate. The highest area

of each molecule is two hydrogen atoms in the central pyrazole of the $H_2B(pz)(pypz)$ ligand. In view of the exponential current-distance relation of the tunneling current, the highest area is a likely candidate for explaining the maxima in topographs. The rectangular shape of the STM images and the apparent division into two dimers is reflected by the C_2 symmetric model of the cluster, e.g., the positions of the interacting pyridine subunits are on the lower (upper) side of the tetramer along two opposite edges and the pyrazole subunits are bent toward (away from) each other. In this model, the bent pyrazoles, which display the largest structural change during SCO transition, are on the upper side of the cluster. In particular, two of these pyrazole subunits are close to the lower pyridine units of a neighbor and are therefore sterically blocked, whereas the other two pyrazoles are at the edges of the cluster and remain free to move. We experimentally observed two enantiomers of the tetramers (see chapter 4.1.6) in agreement with the chirality of the proposed structure in Figure 4.5.

In summary, this model is consistent with all main experimental observations. We used it as a starting point for further geometry optimizations of the tetramer on Ag(111) as detailed in chapter 4.1.6. We find that the formation of gas-phase tetramers is energetically favorable with a calculated formation energy of 3.9 eV. In addition, the adsorption of tetramers on Ag(111) is energetically stable with an adsorption energy of 5.7 eV. Generally, the monomers preserve their internal geometry in both the gas-phase tetramer and when adsorbed on Ag(111), although the pyrazole subunits bending toward a neighbor molecule are slightly straightened. Both LS and HS monomers preserve their spin configuration on Ag(111), and the HOMO-LUMO gaps are only slightly reduced compared to the gas-phase monomer. For the structurally relaxed tetramer, the calculated cluster is rectangular (e.g., distances between the highest points of 1.03 and 0.923 nm), in agreement with experimental topographs.
In addition to tetramers, isolated dimers were occasionally observed. All these dimers matched one of the short sides of the rectangular tetramers (e.g, top left and right molecules in Figure 4.5a), i.e., they were composed of complexes with their pyrazole groups oriented in opposite directions. The steric blocking we propose to occur in tetramers should be absent in these dimers. This is indeed the case (Figure 4.6). Pristine dimers are comprised of two molecules in their LS state, i.e., they appear low in topographs. By current-induced switching a HS state may be obtained on both constituents of the dimer. This observation lends further support to the proposed and calculated structure of the tetramers.

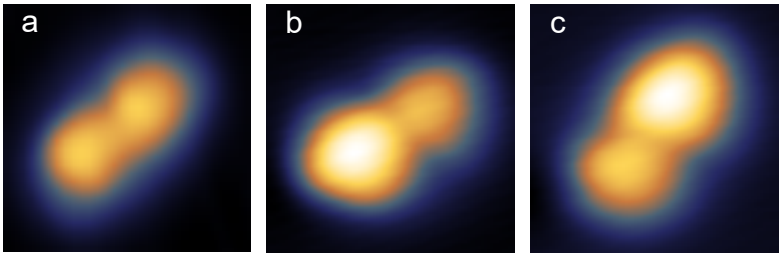

Figure 4.6: Topographs of $Fe(H_2B(pz)(pypz))_2$ dimers. (a) Dimer in its pristine conformation (0.5 V). Both molecules are in a LS state. (b, c) A dimer with its left or right molecule converted to the HS state demonstrating that both constituents may be switched. Toggling of a molecule between its LS and HS states was induced by placing the tip above it and applying a sample voltage of 1.2 V at 5 pA with feedback enabled. A rapid change of the tip height occurred after a few seconds signaling the transition from LS to HS or vice versa. In addition to the change of the spin-state, the manipulation often leads to a lateral motion of the dimer as verified by subsequent imaging.

Finally, we also attempted switching of single complexes. To obtain stable topographs, we used single molecules that were attached to a corner of a tetramer. These molecules also exhibited switching as expected (see chapter 4.1.6).

Current-Induced Remote Switching

In addition to the switching of a molecule under the tip, we also observed another surprising effect. When the tip is placed above a molecule that does not switch itself, its neighbor in a "dimer" subunit may switch with considerable probability (Figure 4.7a,b). The voltages required to induce this "remote" switching are similar to those used for "local" switching. We verified that the nonswitchable molecule is essential for the remote switching process. In fact, we did not observe any switching when applying various stimuli with the tip located above the substrate close to a switchable molecule. The excitation is apparently transmitted directly between the molecules rather than via the substrate.

Quantifying the remote switching effect seems tedious at first glance, because imaging of the tetramer is involved. As Figure 4.7 shows, however, the state of the switchable molecule of a subunit affects the apparent height of the inactive neighbor, where current is injected. Although the height change is fairly small, it corresponds to marked jumps in time series of the current. We used this opportunity to acquire data on the probabilities of local and remote switching. The height change of the nonswitchable molecule does not depend on the point of excitation, be it local or remote. We speculate that the height change may reflect structural and electronic relaxations of the entire dimer.

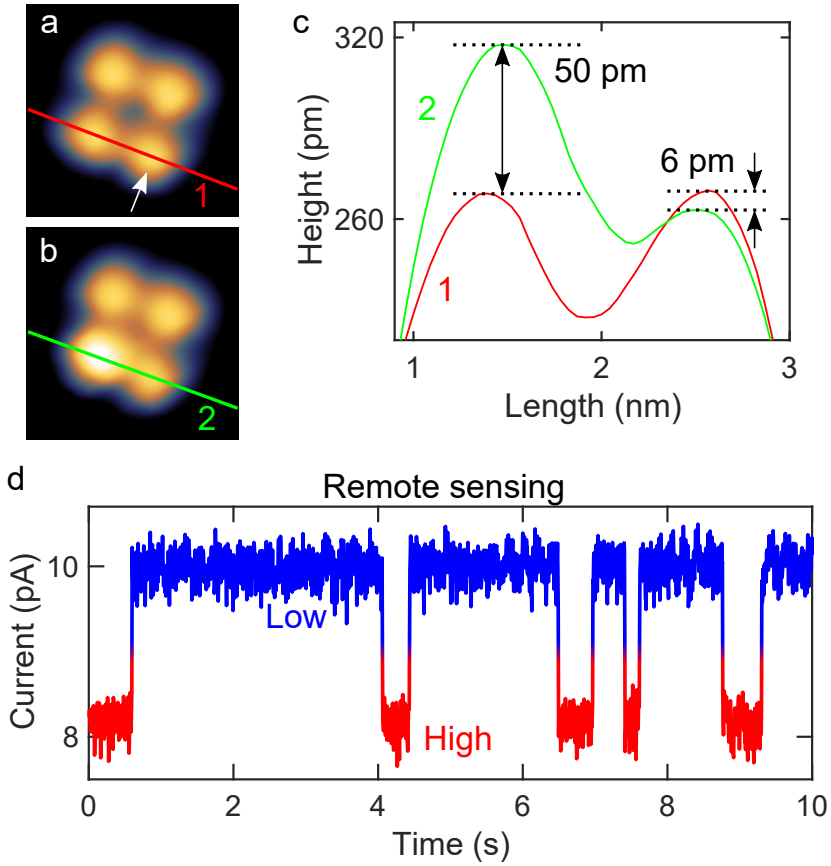

Figure 4.7: Remote switching and sensing. (a, b) Constant-current topographs (0.5 V, 10 pA) and (c) corresponding height profiles along a dimer subunit before (red, 1) and after (green, 2) the molecule in the lower left corner was switched from low to high by injecting electrons in the lower right molecule (see arrow). In addition to the 50 pm height difference observed on the switching complex itself, a small but clear height change of 6 pm is resolved on the molecule that does not switch. This effect may be used to remotely detect switching of the neighbor molecule in a "dimer" subunit. (d) After increasing the voltage from 0.5 to 1.1 V with fixed tip position (open feedback) over the inactive molecule (lower right molecule in (a) and (b)), two distinct current levels are observed in a time series. Topographs recorded subsequently confirmed that the red (blue) current level corresponds to the neighbor in its high (low) state.

The resulting yields are presented in Figure 4.8 along with that extracted for the local switching. Although statistical uncertainties are present, the observed evolutions of

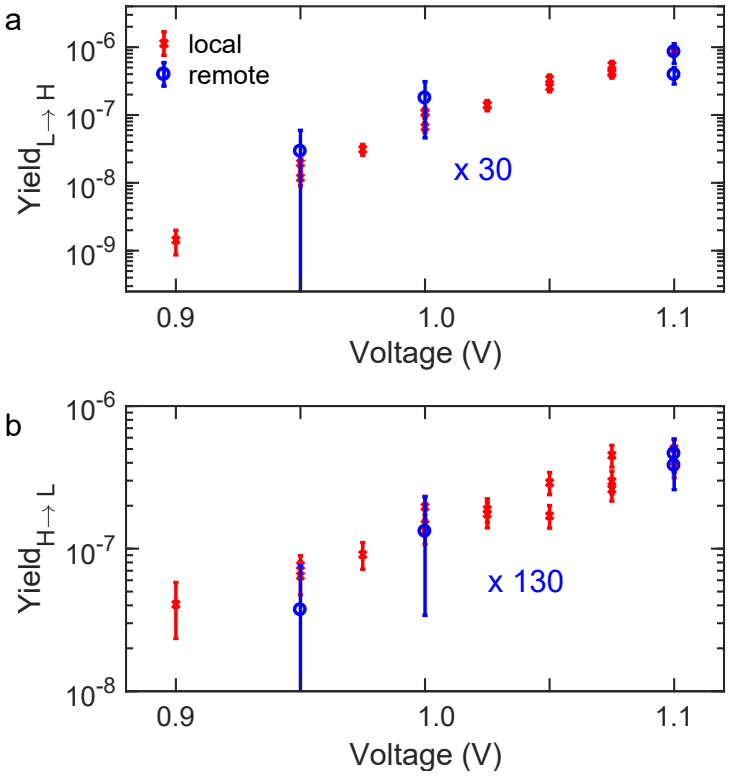

Figure 4.8: Yields of local and remote switching. Red (blue) symbols show the yield of local (remote) switching vs the sample voltage. Switching from (a) low to high and (b) high to low. The yields for remote switching have been multiplied by factors of 30 (L $\rightarrow$ H) and 130 (H $\rightarrow$ L), respectively. Uncertainty margins indicate one standard deviation of the mean value ($\pm 1\sigma$).

the yields appear identical. In a simple model, the total yields for local switching may be understood as the product of two factors, the yield of generating an excited state and the yield of this excitation to decay via SCO. Remote switching involves at least one further factor, the yield for transmitting the excitation from one molecule to its neighbor. The SCO transition happens on the same molecule in both cases, likely implying that the decay yields are the same. The similarity of the voltage dependencies therefore suggests that the excitation mechanism controls the evolution of the total yield while the transmission does not appear to add a further drastic energy dependence. The most likely scenario with these characteristics is an electron transfer from the nonswitching molecule to its switchable neighbor. In this model, the reduction of the remote switching yields reflect the probability for intermolecular electron transfer over that for electron transfer to the substrate. Using the measured reductions by factors $\sim$ 30 and $\sim$ 130 in the low-to-high and high-to-low cases, respectively, and assuming similar molecule-substrate couplings for the LS and HS

states, the yields suggest a $130/30 = 4.3$ more efficient intermolecular electron transfer for the LS-LS dimer than for the LS-HS one. In comparison, an electron transfer ratio of 9 is found from DFT calculations (PBE+U) using Fermi's golden rule (see chapter 4.1.6), which is on the same order of magnitude as the experimental ratio. The improved electron transfer in the LS-LS dimer is due to a combined effect of (i) more spatial overlap of the LUMOs and (ii) better match of the LUMO energies. We note that fine-tuning of the LUMO energy as shown in ref [94] could enable further tuning the intermolecular electron transfer.

4.1.3 Conclusions

$Fe(H_2B(pz)(pypz))_2$ complexes self-assemble into tetramers on Ag(111). Two molecules per tetramer exhibit highly efficient spin crossover upon injection of electrons at elevated voltages. The corresponding yields are almost 3 orders of magnitude larger than the values previously reported from SCO systems on surfaces. in addition, the switching occurs on a metal surface where electron-induced switching has so far proven to be challenging. While the remaining molecules in the clusters do not show SCO, they may be used as contacts to inject electrons and thereby switch one of their neighbors. These different roles of the molecules in the tetramer can be understood from geometric considerations. The yields of "remote" switching remain high and exhibit the same voltage dependence as those for local switching. The experimental data and DFT calculations suggest that intermolecular electron transfer mediates the "remote" switching. In particular, the transfer probability is found to depend on the spin-state configuration of the dimer (low-low or high-low), which is quantitatively rationalizes by a configuration-dependent coupling between the LUMOs. Cooperative effects in SCO systems, which have extensively been investigated, may be viewed as a cascade of remote switching events induced by intermolecular elastic interactions. The present findings suggest that intermolecular electron transfer may lead to similar effect. This may be particularly useful for spintronics devices utilizing SCO complexes.

4.1.4 Methods

Synthesis

The monoanionic ligand $H_2B(pz)(pypz)$ and the complexes based on it, $M(H_2B(pz)(pypz))_2$ were used from previous studies or synthesized according to the procedure reported by Ossinger et al. [84].

Experimental Details

All measurements were carried out with a STM operated at $\sim 4.6\,\mathrm{K}$ in ultra-high vacuum. Topographs were acquired at constant tunneling current. Ag(111) surfaces were prepared by repeated cycles of Ar^+ sputtering (1.5 keV) and subsequent annealing to 500 °C. $M(H_2B(pz)(pypz))_2$ were sublimated from a crucible heated to $\sim 150\,°\mathrm{C}$ onto clean Ag(111) held at $\sim 50\,°\mathrm{C}$ at a background pressure of $10^{-9}\,\mathrm{Pa}$. STM tips were prepared from a W wire by electrochemical etching and annealing in vacuo.

Theoretical Details

Calculations of the single molecules in the gas-phase were carried out with the ORCA package [95, 96]. Geometry optimizations, calculations of the dipole moments, and infrared and Raman modes were performed at the B3LYP [97–99] / def2-SVP [100, 101] level with the D3BJ dispersion correction [102, 103], the RIJCOSX approximation, fine numerical integration grids (grid4 and gridX4 in ORCA nomenclature), and the CG solver. The crystallographically determined structures of the two enantiomers of $Fe(H_2B(pz)(pypz))_2$ [84] were used as a starting point. The optimized coordinates are presented in chapter 4.1.6. Overlays of the calculated HS and LS structures (Figure 4.5) were created with the software Mercury [104, 105]. In addition to the gas-phase simulations of monomers, we have performed calculations of tetramers in the gas-phase and adsorbed on Ag(111). These simulations have been performed using QuantumATK [106, 107]. The gas-phase tetramer as well as tetramer on Ag(111) structural relaxations have been performed using the generalized gradient approximation (GGA) for the exchange-correlation functional. We use the PBE [108] functional with an additional Hubbard-U parameter of 4.0 eV on the Fe *d*-orbitals. Furthermore, we include D3BJ dispersion corrections to the total energy [102]. For the structural relaxation we use a DoubleZetaPolarized basis set. After structural relaxation, we have calculated the electronic structure, projected density of states, and partial electron densities for STM simulations using B3LYP with a SingleZetaPolarized basis set.

4.1.5 Acknowledgments

We thank Eugenio Coronado for a fruitful discussion and acknowledge financial support from the European Union's Horizon 2020 program, Grant No. 766726.

4.1.6 Supplementary Information

$Zn(H_2B(pz)(pypz))_2$ complexes on Ag(111)

As pointed out in the main manuscript, we verified the SCO nature of the switching by performing similar measurements on a complex with identical geometry but different metal ion (Zn instead of Fe). The $3d$ orbitals of the Zn^{2+} ion are fully occupied such that no SCO is expected. Upon deposition of the Zn compound on Ag(111), we observe the self-assembly of tetramers similar to those formed by the Fe compound (Figure 4.9).

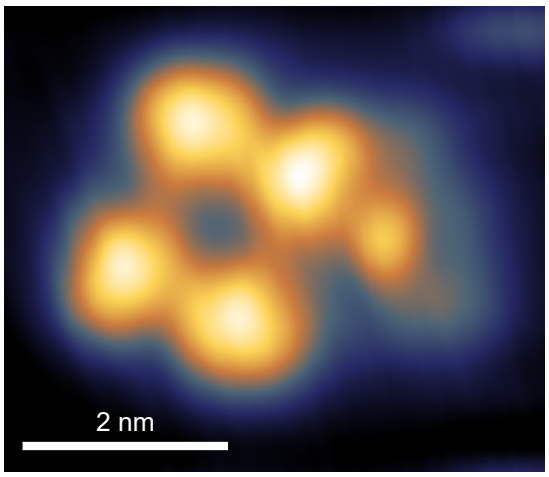

Figure 4.9: Topograph (0.5 V, 10 pA) of a $Zn(H_2B(pz)(pypz))_2$ tetramer on Ag(111). An additional protrusion on the right side is attributed to a fragment.

Nonetheless, as may be expected from a larger occupation of the antibonding e_g orbitals, the Zn complexes are more fragile and a significant number of fragments is observed on Ag(111). One such fragment appears as a protrusion next to the top right molecule of the cluster (Figure 4.9).

We performed more than 160 switching attempts per molecule with tunneling parameters that would have lead to switching of $Fe(H_2B(pz)(pypz))_2$ with high success rates. However, none of the attempts was successful. In particular, we did not observe any telegraph noise in time series, nor noticeable changes of the STM topographs. Incremental increase of the control voltage up to values above -3.5 V (-400 pA) did not induce switching of a complex but rather lead to the destruction of the investigated tetramer.

These observations show the importance of the central metal ion for the switching and suggest that the switching of $Fe(H_2B(pz)(pypz))_2$ is due to SCO.

Switching of single $Fe(H_2B(pz)(pypz))_2$ complexes

The impossibility to switch two of the molecules of a tetramer reflects steric hindrance in the tetramers. This geometric constraint is removed in dimers and switching is indeed observed as discussed in the manuscript. To further test the relevance of geometric constraints, we investigated single molecules at the border of tetramers (Figure 4.10). Such "pentamer" structures are observed on the pristine sample. The additional molecule next to the tetramer is not affected by the geometrical constraints, and switching between a low and high state is indeed possible (Figure 4.10).

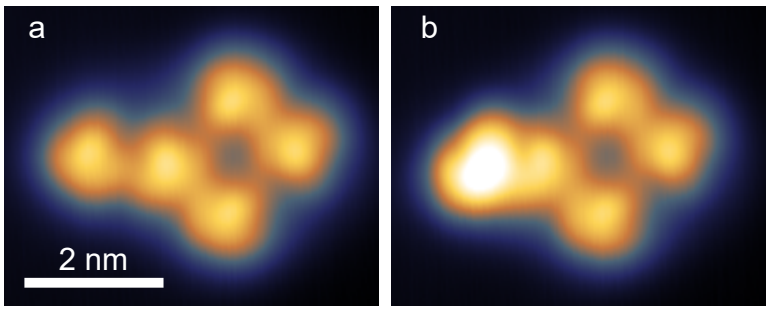

Figure 4.10: Topographs of a $Fe(H_2B(pz)(pypz))_2$ attached to a tetramer. An additional protrusion on the left side of the tetramer, identified as a individual Fe complex in his (a) pristine and (b) switched state. The conversion between these states was induced by placing the tip above the molecule at a sample voltage of 1.2 V at 5 pA. Imaging conditions: 0.5 V, 5 pA.

The bonding geometry of the fifth molecule to the tetramer is not known in detail. Nonetheless, in most of the cases, we observed that the fifth molecule appears to be attracted between the pyrazole end groups of a molecule in the tetramer (corner of a tetramer). Two kinds of intermolecular interactions may therefore be involved: a $\pi - \pi$ interaction and electric dipole-dipole interactions. Gas-phase DFT calculations reveal a dipole moment of the compound of approximately 7 Debye. From simple point dipole considerations, an intermolecular interaction energy on the order of tens of millielectronvolt is expected, which would be sufficient to stabilize such structures at low temperatures.

Structure of the gas-phase molecule

Figure 4.11 shows structures of $Fe(H_2B(pz)(pypz))_2$ in the LS and HS states resulting from gas-phase calculations. In the LS state, a pyrazole moiety of each ligand is tilted relative to the ligand plane (see for instance the angle of 10° marked in Figure

4.11a). Upon SCO, the tilt angle is significantly increased (35°, Figure 4.11b). As SCO involves a change of the pyrazole tilt angles, no SCO is expected when steric hindrance blocks the tilting of the pyrazole.

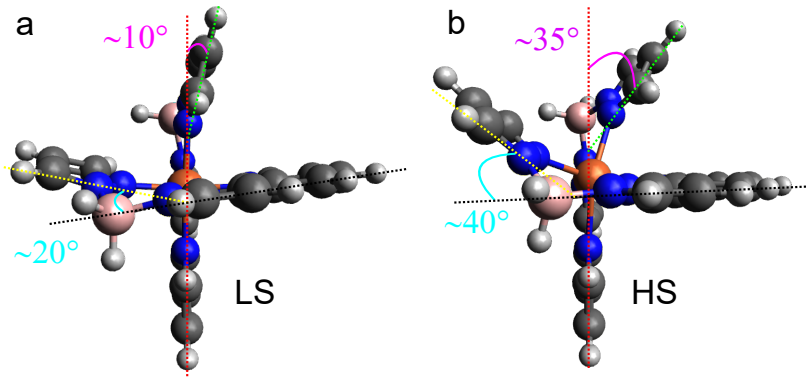

Figure 4.11: Calculated gas-phase structure of $Fe(H_2B(pz)(pypz))_2$ in (a) the LS and (b) the HS state. The angle between the pyrazole moieties and the ligand plane indicated in magenta (cyan) is $\sim 10°$ ($\sim 20°$) and $\sim 35°$ ($\sim 40°$) in the LS and HS states, respectively. Note that only one of the two enantiomers is shown.

Tetramer simulations

In addition to the gas-phase simulations of monomers, we have performed calculations of tetramers in the gas-phase and adsorbed on Ag(111) using QuantumATK [106, 107]. The atomic structure with a tetramer on four layers of Ag(111) contains 548 atoms, which is computationally very demanding with the B3LYP hybrid functional. For this reason, we performed the structural relaxations of tetramers in the gas-phase and on Ag(111) with the generalized gradient approximation (GGA) for the exchange-correlation functional. We used the PBE [108] functional with an additional Hubbard-U parameter of 4.0 eV on the Fe *d*-orbitals. Furthermore, we included van-der-Waals interactions via the Grimme DFT-D3 correction to the total energy [102]. For the structural relaxation we employed a DoubleZetaPolarized basis set.

Gas-phase Tetramer

We verified that the relaxed structures of the monomers in the LS and HS configurations calculated with PBE+U closely agreed with the structures obtained with B3LYP as described in the previous section.

Next, we proceeded to finding the structure of the tetramers. The relaxation of the tetramers was done in two steps. We started from the relaxed monomer structures and fixed all internal coordinates of each monomer and relaxed the structure by rigidly moving the monomers to the minimum energy position. In the second step, a

full relaxation of all atomic coordinates was carried out until the maximum force was below 0.05 eV/Å. The relaxed structure is shown in Figure 4.12.

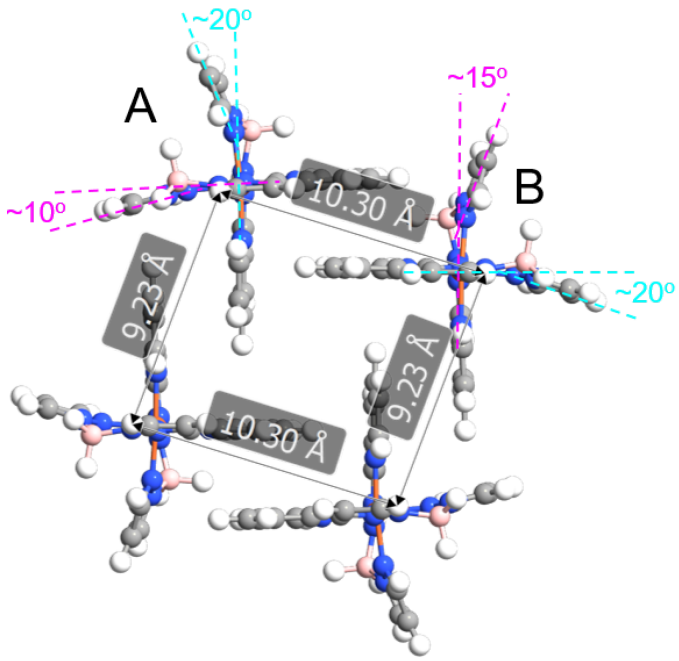

Figure 4.12: Calculated gas-phase structure of a tetramer with four LS monomers. The indicated distances are measured between the topmost hydrogen atoms of each monomer. The formation of a rectangular shape is in agreement with the STM topographs.

The calculated binding energy of the tetramer with four LS monomers is 3.91 eV. The distances shown in the figure are measured between the topmost hydrogen atoms in each monomer. The rectangular shape of the optimized tetramer matches the STM topographs shown in the main manuscript chapters 4.1.1, 4.1.2 and 4.1.3. Within one "dimer" of the tetramer consisting of a "A" and "B" enantiomers indicated in Figure 4.12 we observe a slight difference in one of the angles between the pyrazole moieties and the ligand plane. In enantiomer B in Figure 4.12 the angle of $\sim 15°$ is slightly larger than the corresponding angle of $\sim 10°$ in enantiomer A.

The different angles in enantiomer A and B (Figure 4.12) already suggests that enantiomer B may be easier to switch to a HS state, where the angles are larger. To further address the switching capability of the monomers we calculated the gas-phase structure of tetramers in which we replaced one of the LS monomers A or B with a HS monomer and subsequently relaxed the atomic coordinates. The calculated total energy of the structure with the HS monomer in enantiomer B turned out 0.27 eV lower that the tetramer with enantiomer A in a HS state.

This energy difference supports the model presented in Figure 4.5 in chapter 4.1.2 and indicates that one of the enantiomers (A) is unable to switch due to steric hindrance.

Tetramer on Ag(111)

Figure 4.13 shows the relaxed geometry of a tetramer with four LS monomers adsorbed on four layers of Ag(111). For the structural relaxation, we fixed the three bottom Ag layers while doing a full geometry optimization of the remaining atoms. The k-point sampling was (2, 2, 1), the real-space grid was determined by a density mesh cutoff of 80 Hartree, and we used a DoubleZetaPolarized basis set.

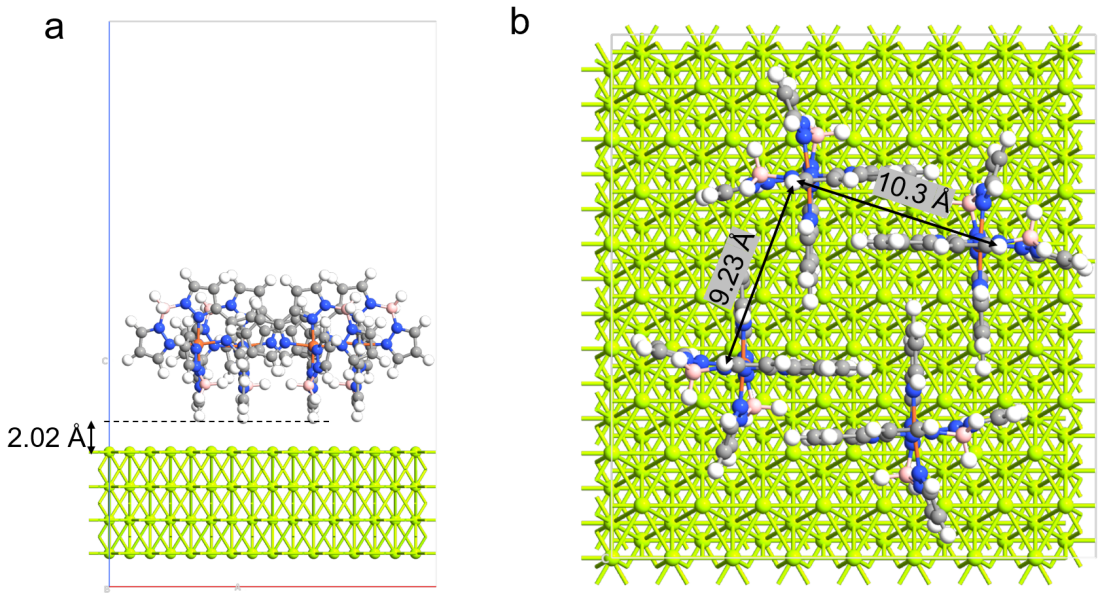

Figure 4.13: Calculated adsorption geometry of four LS monomers on four layers of Ag(111). The binding distance is 2.02 Å as indicated in (a). The distance between the topmost hydrogen atoms on each monomer is indicated in (b).

The calculated binding distance is 2.02 Å as indicated in Figure 4.13a. In qualitative agreement with the STM topographs we find that the monomers are arranged in a rectangular array with distances between the topmost hydrogen atoms of 9.23 Å and 10.03 Å as indicated in Figure 4.13b.

We next substituted one of the LS monomer with the HS configuration and repeated the structural relaxation using the PBE+U functional. Subsequently, we performed a calculation with the B3LYP exchange-correlation functional using a SingleZetaPolarized basis set.

Figure 4.14 shows the projected density of states (PDOS) on the HS monomer and neighboring LS monomer. The PDOS of monomer A is defined as

$$D_A(E) = \sum_i \sum_{\mu \in A} w_i |\langle \phi_\mu | \psi_i \rangle| \delta(E - \epsilon_i) \tag{4.1}$$

where the sum over i runs over all eigenstates $|\psi_i\rangle$ in the system with eigenvalues ϵ_i including k-point summation and corresponding weight factors w_i. The μ-sum runs over basis orbitals centered on atoms belonging to monomer A. In the calculations, the δ-function is replaced by a Gaussian with a width of 0.025 eV.

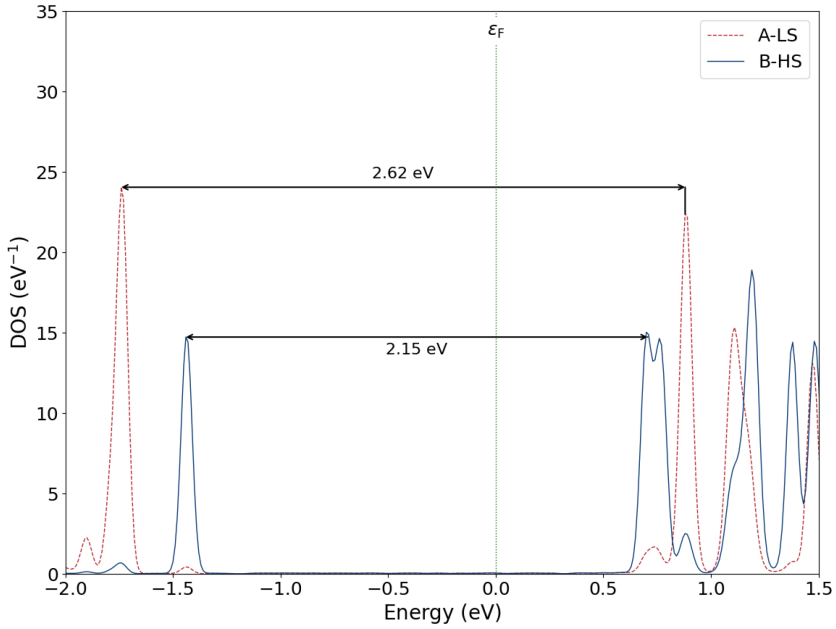

Figure 4.14: Projected density of states (PDOS) of the tetramer with three LS and one HS monomer on Ag(111) also shown in Figure 4.15. The density of states is projected onto the basis orbitals located on the HS monomer and on the neighboring LS monomer. The LUMO orbital on the HS is 0.18 eV lower in energy than the LUMO peak of the LS monomer.

The PDOS of monomer B is easily obtained by replacing A by B. It is evident from Figure 4.14 that the HS monomer has a smaller HOMO-LUMO gap of 2.15 eV than the LS monomer with 2.62 eV. The smaller gap of the HS monomer is in accordance with the gas-phase results, where we find HOMO-LUMO gaps of 2.26 eV and 2.73 eV for the HS and LS monomers, respectively, using the same computational settings. The smaller HOMO-LUMO gap and, in particular, the reduced LUMO energy of the HS monomer is consistent with the larger apparent height in STM topographs presented in the main manuscript chapters 4.1.1, 4.1.2 and 4.1.3.

To further address the apparent height difference observed in the experiments we also calculated and analyzed the partial electron density. The partial electron density is obtained from eigenstates within specified energy interval $[E_0; E_1]$ and is defined as

$$n_{E_0,E_1}(\mathbf{r}) = \sum_i w_i |\langle \mathbf{r}|\psi_i\rangle|\Theta(\epsilon_i - E_0)\Theta(E_1 - \epsilon_i) \tag{4.2}$$

where the i-sum again runs over both k-points and eigenstates. $\Theta(x)$ is the Heaviside step function. Within the Tersoff-Hamann approximation, the current measured by the STM at a sample voltage of V is proportional to the partial electron density $n_{0,e\cdot V}(\mathbf{r})$. Figure 4.15 shows the partial electron density at a constant height of 2.12Å above the topmost hydrogen atoms.

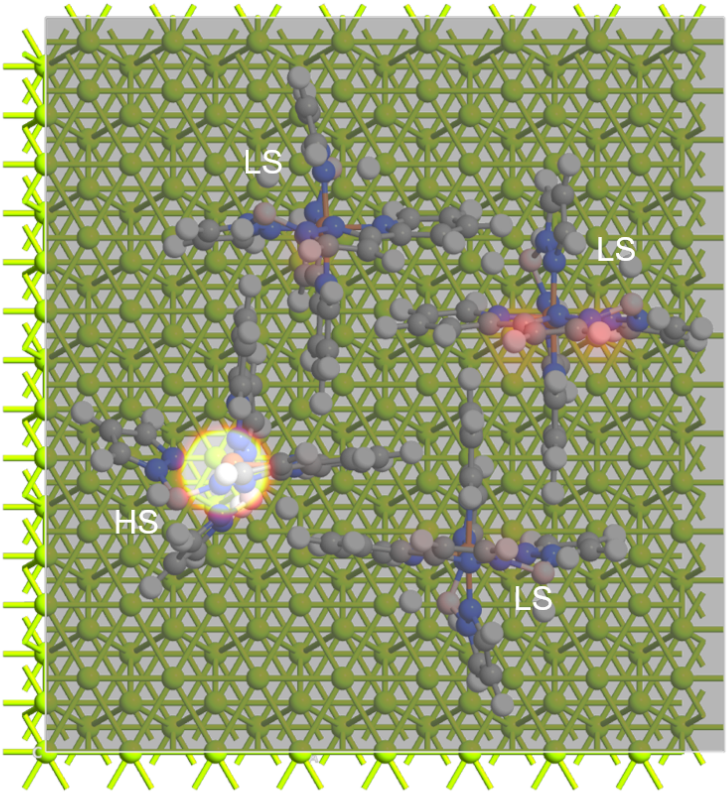

Figure 4.15: Simulated constant-height STM image of a tetramer with three LS and one HS monomer on Ag(111). The figure shows the partial density summed in the energy interval $[0, 0.65]$ eV for a constant height 2.12 Å above the topmost hydrogen atoms. Yellowish area at the HS monomer indicate a significant higher density than on the rest of the supercell. A Sticks and balls representation of the supercell is overlaid.

The calculated image shows a bright spot above the HS monomer as compared to the LS monomers. Although this is not a direct comparison to the STM measurements, which show the height variations at a constant current, the simulated STM image

together with the PDOS plot in Figure 4.14 indicates that the taller molecules observed in the measured STM topographs correspond to the HS state.

Simple model of electronic coupling between LUMO orbitals

We now describe a simple model to address the remote switching and, in particular, the different switching efficiency from LS to HS and vice versa.

We consider a transition of an electron initially in the LUMO orbital located on a non-switchable monomer (A) to the LUMO of the neighboring, switchable monomer (B). The initial LUMO state is always in a LS configuration with the energy E^{LS}_{LUMO}, while the final state is a LS LUMO for LS→HS switching and a HS LUMO state for HS→LS switching. We estimate the transition probabilities using Fermi's golden rule

$$\Gamma_{A\to B} = \frac{2\pi}{\hbar}|\langle\psi^{(A)}_{LS}|H'|\psi^{(B)}_{LS/HS}\rangle|^2\rho^{(B)}_{LS/HS}(E^A_{LS}) \tag{4.3}$$

where $|\psi^{(A)}_{LS}\rangle$ is the LUMO orbital located on the LS monomer A, $|\psi^{(B)}_{LS/HS}\rangle$ is the LUMO orbital on monomer B, which can either be in a LS or HS configuration. The perturbation to the Hamiltonian H' is detailed below. Finally $\rho^{(B)}_{LS/HS}(E^A_{LS})$ is the density of states on the B monomer (either LS or HS) but always evaluated at the LUMO energy for the LS monomer A. From the projected density of states shown in Figure 4.14 we estimate the LUMO peak separation to be $\Delta E \sim 0.2\,\text{eV}$ and the broadening of the peaks to be $\gamma \sim 0.1\,\text{eV}$. Next, a Lorentzian shape is assumed for the LUMO density of states such that

$$\rho^{(B)}_{LS}(E^A_{LS}) \propto \frac{\gamma}{(E^B_{LS} - E^A_{LS})^2 + \gamma^2} = \frac{1}{\gamma} \tag{4.4}$$

since $E^B_{LS} = E^A_{LS}$ and

$$\rho^{(B)}_{HS}(E^A_{LS}) \propto \frac{\gamma}{(E^B_{HS} - E^A_{LS})^2 + \gamma^2} = \frac{\gamma}{(\Delta E)^2 + \gamma^2} \tag{4.5}$$

The coupling matrix elements entering Equation 4.3 are estimated as follows. To simplify the notation, we consider a dimer although the final results are obtained for tetramers. We obtain the full Hamiltonian matrix from the DFT calculation with elements $\mathbf{H}_{ij} = \langle\phi^\mu_i|\hat{H}|\phi^\nu_j\rangle$, where $|\phi^\mu_i\rangle$ is an atomic basis orbital located on atom μ and $\hat{H}$ is the Hamiltonian operator from the converged DFT calculation.

We divide the total Hamiltonian matrix for a given spin (either up or down) into a two-by-two form:

$$\mathbf{H} = \begin{pmatrix} \mathbf{H}_1 & 0 \\ 0 & \mathbf{H}_2 \end{pmatrix} + \begin{pmatrix} 0 & \mathbf{H}_{12} \\ \mathbf{H}_{21} & 0 \end{pmatrix} \tag{4.6}$$

and similarly for the overlap matrix. The sub-matrix $\mathbf{H}_1$ contains matrix elements between atomic basis orbitals located on monomer 1 and likewise for the sub-matrix $\mathbf{H}_2$. The second term in Equation 4.6 contains matrix elements where one basis orbital is located on monomer 1 and the other basis orbital on monomer 2. This matrix thus describes the coupling between the monomers and we will treat this as the perturbation H'.

We now find the eigenvalues and eigenvectors for the monomer subsystems 1 and 2, i.e. we solve the equation

$$\mathbf{H}_1 \psi_1^{(n)} = \epsilon^{(n)} \mathbf{S}_1 \psi_1^{(n)} \tag{4.7}$$

for the n'th eigenstate of monomer 1 and similarly for monomer 2. $\mathbf{S}_1$ is the basis set overlap matrix for monomer 1, where the matrix element ij reads $(S_1)_{ij} = \langle \phi_i | \phi_j \rangle$. The coupling between the LUMO orbitals of monomer 1 and monomer 2 is then calculated as

$$\Gamma_{12} = \begin{pmatrix} \psi_1^{LUMO} \\ 0 \end{pmatrix}^{\dagger} \mathbf{H}' \begin{pmatrix} 0 \\ \psi_2^{LUMO} \end{pmatrix} \tag{4.8}$$

Using a gas-phase tetramer with four LS monomers we calculate the coupling $|\langle \psi_{LS}^A | H' | \psi_{LS}^B \rangle|$. Similarly, from a tetramer with a single HS monomer and three LS monomers we obtain $|\langle \psi_{LS}^A | H' | \psi_{HS}^B \rangle|$.

We can now estimate the ratio of the transition rates $\Gamma_{(A,LS)\to(B,LS)}$ for the remote LS $\to$ HS switching event and $\Gamma_{(A,LS)\to(B,HS)}$ for the remote HS $\to$ LS switching event as

$$\frac{LS \to HS}{HS \to LS} = \frac{|\langle \psi_{LS}^A | H' | \psi_{LS}^B \rangle|^2}{|\langle \psi_{LS}^A | H' | \psi_{HS}^B \rangle|^2} \frac{(\Delta E)^2 + \gamma^2}{\gamma^2} \tag{4.9}$$

The results from both PBE+U and B3LYP calculations are summarized in Table 4.1. The estimated experimental ratio is obtained from the multiplying factors of 30

and 130 for remote LS → HS and HS → LS switching, respectively from Figure 4.8 in chapter 4.1.2.

	PBE+U	B3LYP	Exp.
$\lvert\langle\psi^A_{LS}\lvert H'\rvert\psi^B_{LS}\rangle\rvert$	32 meV	20 meV	-
$\lvert\langle\psi^A_{LS}\lvert H'\rvert\psi^B_{HS}\rangle\rvert$	22 meV	6 meV	-
$\frac{LS\rightarrow HS}{HS\rightarrow LS}$	9.0	47.1	4.3

Table 4.1: Coupling elements between LUMO orbitals and estimated ratios of the transition rates involved in remote LS→HS and HS→ LS switching. The experimental ratio is obtained from the multiplying factors of 30 and 130 from Figure 4.8 in chapter 4.1.2.

From this we estimate the ratio as (LS→HS)/(HS→LS) = 130/30 = 4.3. The ratios determined from the DFT calculations strongly depend on the used functional (9.0 with PBE+U and 47.1 with B3LYP), which implies a large uncertainty. Nonetheless, the ratios inferred from theory have a similar order of magnitude as the experimental one and support an intermolecular electronic transfer mechanism for the remote switching.

Proportionality of rate and current

Figure 4.16 shows the same data as in Figure 4.3 of chapter 4.1.2 but with a linear scale to highlight the proportionality of the rates to the current. This proportionality indicates that the switching is a single electron process.

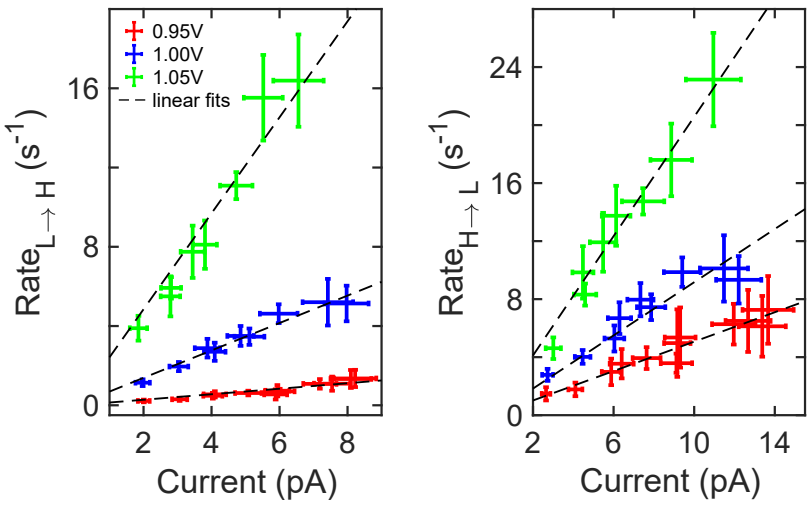

Figure 4.16: Current dependence of the switching rates. (a) Low-to-high and (b) high-to-low switching rates as a function of the tunneling current for different voltages (crosses). The dashed lines are a linear fit to the data. See caption to Figure 4.3 for further experimental details.

Switching at negative voltages

In chapters 4.1.1, 4.1.2 and 4.1.3, we consider switching at positive voltages, i.e. electron current from the tip to the molecule. Switching between the LS and HS state may also be realized at negative voltages as illustrated in Figure 4.17.

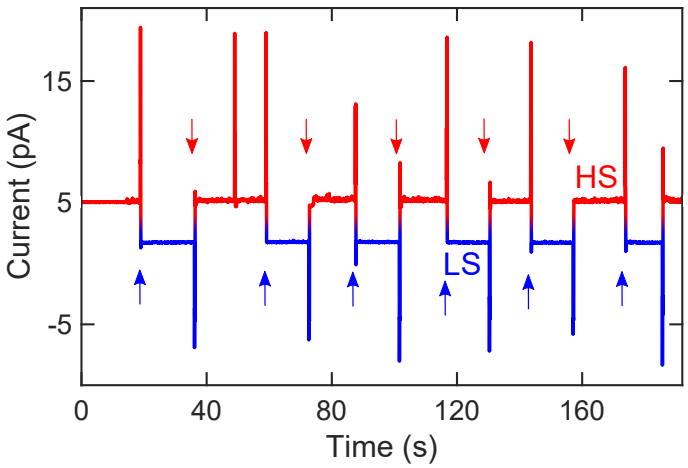

Figure 4.17: Switching with positive and negative voltage pulses. Evolution of the tunneling current across a switchable molecule for a constant tip-substrate distance (current feedback disabled). At the position indicated by the blue (red) arrows, a voltage pulse of 1 V (-1 V) was applied over 280 ms. The current level in the absence of the pulses, measured with a DC voltage of 0.5 V, is a readout of the molecular state.

However, switching at negative voltages appears to be more complex than at positive voltage. In particular, a detailed monitoring of the switching at negative voltages (not shown) suggests that an intermediate state is involved in the switching at this polarity. A detailed description of this intermediate state, and hence of the switching at negative sample voltages, is out of the scope of the present chapter.

Analysis of current time series

The probability of a molecule to switch (under appropriate tunneling parameters) is expected to be independent of the history of the molecule. Consequently, the number of switching events within a time interval may be described by a Poisson distribution. We define the discrete random variable $\mathcal{X}$ as the number of switching events per time interval τ. $\mathcal{X}$ follows a Poisson distribution:

$$\mathcal{P}(\mathcal{X} = k) = \frac{\mu_\tau^k e^{-\mu_\tau}}{k!}, \tag{4.10}$$

where k is a given realization of $\mathcal{X}$ and $\mu_\tau = \langle \mathcal{X} \rangle$ is the average number of switching events during τ. The standard deviation of the distribution is given by $\sigma_\mathcal{X} = \sqrt{\langle \mathcal{X} \rangle} = \sqrt{\mu_\tau}$. The last property is useful for estimating the uncertainty of a measurement from the mean value. Below, we show that the switching events in $Fe(H_2B(pz)(pypz))_2$ on Ag(111) can indeed be described by a Poisson distribution. We then describe how the rates and related uncertainties were determined.

To test the distribution of the switching events we recorded long time series of the tunneling current, divided them into shorter intervals, counted the number of switching events, and compared the resulting histogram of the number of switching events per interval with the expectation from a Poisson distribution. We distinguished between low-to-high and high-to-low events because they are associated with different yields. This effectively leads to two separate time series, one with the molecule in its low state (referred to as time series low) and one with the molecule in its high state (referred to as time series high). This artificial separation is necessary because the molecule cannot exhibit a low-to-high switching when it already is in the high state. The time series low and high are divided into smaller intervals. The normalized histograms of the number of low-to-high and high-to-low switching in those intervals are shown in Figure 4.18 for a time series recorded at 1 V and a current of 5 pA in the low state. In time intervals of 0.5 s, we observe between 0 and 7 low-to-high switching events between 0 and 8 high-to-low processes. Poisson distribution (red) do indeed reproduce the histograms. We note that small deviations are visible [e.g. 4 high-to-low switching events (Figure 4.18b) appear more often than predicted by the Poisson distribution] presumably owing to the limited size of the data set (total of 279 high-to-low switching in the present case).

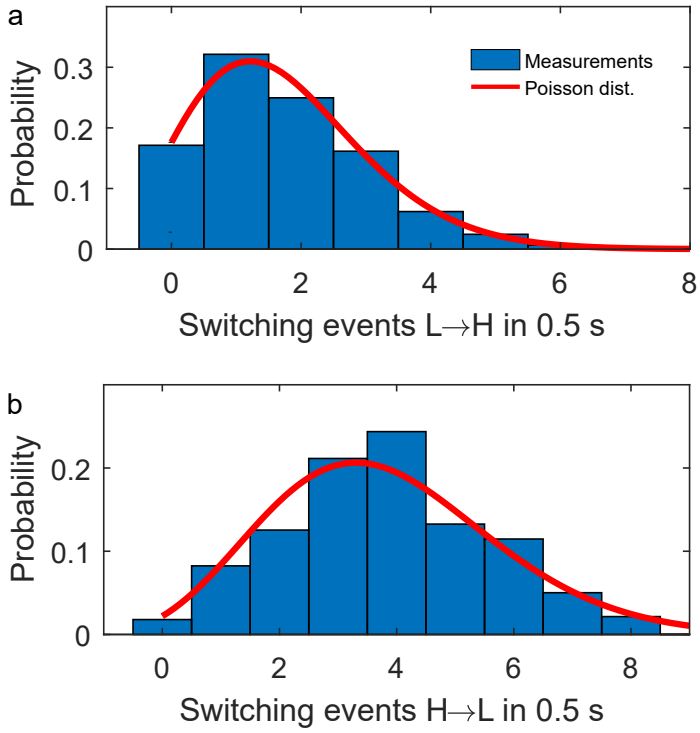

Figure 4.18: Number of switching events described by Poisson distribution. Histograms of the number of switching events in a time interval of 0.5 s (blue) (a) from the low to high state and (b) high to low state, along with Poisson distributions (red) with (a) $\mu_{0.5\,\mathrm{s}} = 1.74$ and (b) $\mu_{0.5\mathrm{s}} = 3.82$. The factorial in Equation 4.10 has been replaced by $\int_0^\infty e^{-t}t^k dt$ for non-integer values of k.

For sufficiently long time series (low and high) the number of switching events provides an estimate of $\bar{\mu}_\tau$ with an associated uncertainty $\sqrt{\bar{\mu}_\tau}$. The switching rate R, defined as the average number of switching per second, is estimated from $R = \bar{\mu}_\tau/\tau$. The uncertainty of the rate estimate is

$$\sigma_R = \frac{\sqrt{\bar{\mu}_\tau}}{\tau} = \sqrt{\frac{R}{\tau}}. \tag{4.11}$$

As expected a decrease of the uncertainty by a factor 2 requires a time interval that is four times longer.
The yield, describing the probability of an electron to induce switching, is inferred from

$$Y = \frac{eR}{\langle I \rangle}, \tag{4.12}$$

where e is the elementary charge and $\langle I \rangle$ the mean value of the current.
We recall that we distinguish between low-to-high and high-to-low switching, which

are linked to the mean current values in the low and high states, respectively. The uncertainty of the yield is related to those of the rate σ_R and the current σ_I as follows:

$$\sigma_Y = \left(\frac{\sigma_R}{R} + \frac{\sigma_I}{\langle I \rangle} \right) |Y|. \tag{4.13}$$

Spectroscopic data

The spectroscopic data do unfortunately not exhibit any feature that would enable a direct and unambiguous identification of the spin states. Figure 4.19 shows $\mathrm{d}I/\mathrm{d}V$ spectra recorded over a large voltage range.

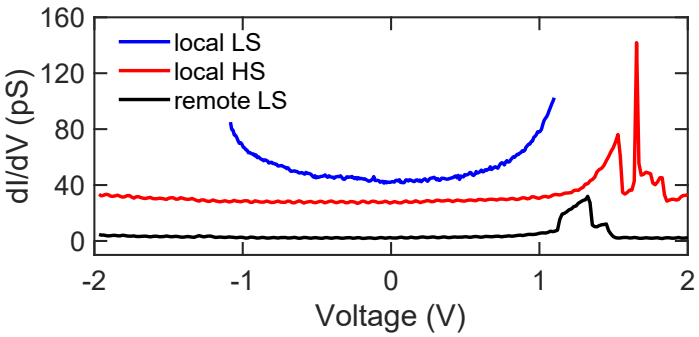

Figure 4.19: Differential-conductance spectra over a large voltage range. $\mathrm{d}I/\mathrm{d}V$ spectra acquired over a switchable molecule in the LS (blue) and in the HS (red) states and over a non-switchable neighboring molecule in the LS state (black). Besides strong variations of $\mathrm{d}I/\mathrm{d}V$ for voltages above 1 V, which result from the lateral displacement of the investigated tetramer, the spectra are essentially free of features. The spectra were acquired using a lock-in amplifier with root-mean-square voltage modulations of 15 mV (10 mV) for the red and black (blue) curves. Before disabling the current feedback, the tunneling conditions were 15 pA and -2 V (10 pA and -1 V) for the red and black (blue) spectra. The red and blue spectra are shifted by 25 pS and 40 pS, respectively.

Based on the yield versus voltage data, we may expect an unoccupied molecular orbital at an energy of ~ 1.5 eV. Such an orbital, however, is not resolved because the tetramers are not stable at voltages above ~ 1 V and hop laterally. This motion induces abrupt changes in the differential conductance as shown in Figure 4.19.

Figure 4.20 shows $\mathrm{d}I/\mathrm{d}V$ spectra of a molecule in the HS (red) and LS (blue) states over a narrow range around the Fermi energy. No spin-related features such as a Kondo resonance or spin-flip excitation are apparent, which prevents a direct spin-state identification from the spectra.
It should be noted that the absence of such features is not surprising. Spin-flip excitations have so far never been reported for SCO complexes and require magnetic

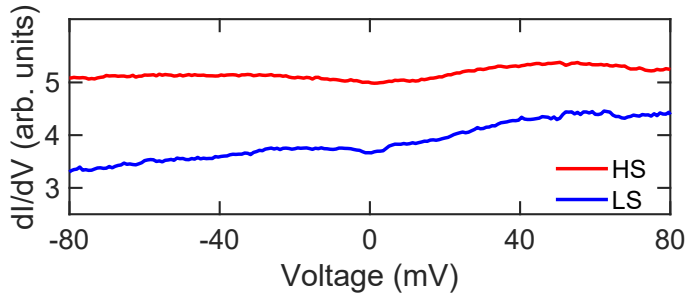

Figure 4.20: Differential-conductance spectra close to the Fermi energy. The $\mathrm{d}I/\mathrm{d}V$ spectra acquired on a switchable molecule in the HS (red) and LS (blue) states essentially appear featureless. The $\mathrm{d}I/\mathrm{d}V$ signal was recorded using a lock-in amplifier (root-mean-square voltage modulation of 2.5 mV) with the current feedback off (initial tunneling conditions of 80 pA and -100 mV). The red spectrum is vertically shifted for clarity.

anisotropy. Alternatively, a necessary condition for an observation of a Kondo resonance is a sufficiently strong electronic coupling between the spin of the molecule and the conduction electrons of the substrate. The induced lateral hopping of the tetramer, however, suggest that the molecule-substrate coupling is not particularly strong.

Orientation of the tetramers

The tetramers adopt six different orientations on the Ag(111) surface (Figure 4.21), which suggests a specific interaction between the molecules and the substrate. Considering the three equivalent close-packed directions of the Ag(111) surface, there are presumably two preferred adsorption geometries of the molecules on the surface.

Chirality of the tetramers

The structure of the tetramers proposed in Figure 4.5a of the chapter 4.1.2 is chiral and one may expect the presence of a second enantiomer. Such an enantiomer is indeed observed (Figure 4.22). The topograph in Figure 4.22a cannot be reproduced by a mere rotation of that in Figure 4.22b, but requires a mirror symmetry operation.

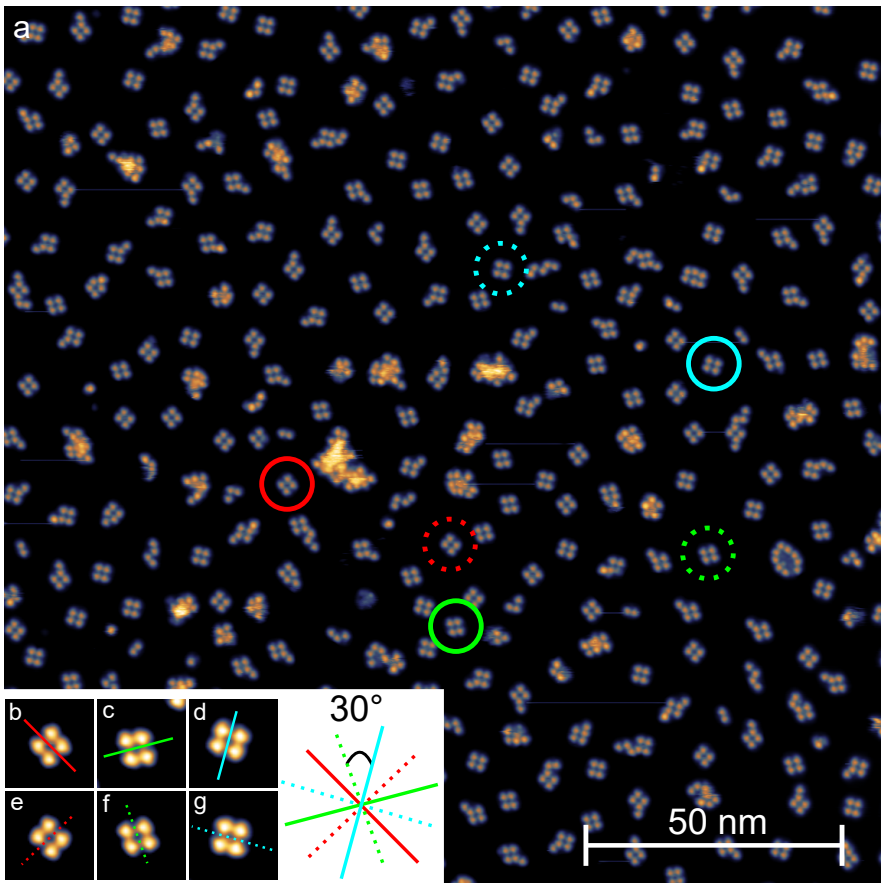

Figure 4.21: Orientations of the tetramers. (a) STM topograph of the Fe complex on Ag(111) showing a large number of tetramers along with few unidentified aggregates. (b–g) Examples of the six different orientations of the tetramers observed on the surface. Tetramers may be seen as composed of two dimers. Lines are drawn between such dimers to highlight the different possible orientations. In this particular image, we counted 33, 25, 38, 38, 36 and 36 tetramers with orientations such as shown in (b–g), respectively. Overall, the abundances of the six orientations appear to be equal.

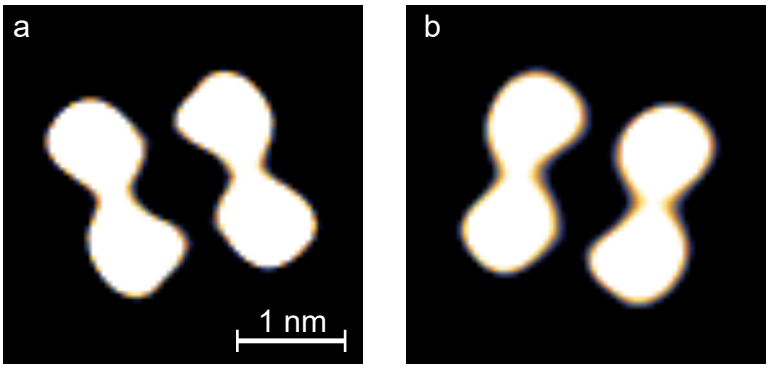

Figure 4.22: Chirality of the tetramers. Constant-current STM topographs of the two enantiomers found on the surface. The topograph (b) has been rotated by 30° to simplify comparison. Note that the color scale has been saturated over a large fraction of the molecules to be better visualize the chirality of the structure.

Atomic coordinates

	Enantiomer A HS			Enantiomer A LS			Enantiomer B HS			Enantiomer B LS		
Fe	–0.481	4.685	4.116	–0.118	4.610	3.949	4.969	0.398	10.671	4.605	0.473	10.838
N	1.651	4.071	3.205	1.675	3.993	3.212	2.836	1.012	11.582	2.812	1.090	11.575
C	2.039	4.871	2.189	2.145	4.754	2.185	2.448	0.212	12.599	2.342	0.329	12.602
C	3.151	4.554	1.394	3.319	4.417	1.500	1.336	0.529	13.393	1.168	0.666	13.287
H	3.444	5.217	0.578	3.664	5.050	0.681	1.043	–0.133	14.209	0.823	0.033	14.106
C	3.859	3.384	1.660	4.018	3.273	1.876	0.628	1.699	13.127	0.469	1.810	12.911
H	4.726	3.115	1.051	4.934	2.989	1.353	–0.238	1.968	13.735	–0.447	2.094	13.434
C	3.440	2.557	2.706	3.525	2.493	2.926	1.047	2.526	12.081	0.962	2.590	11.861
H	3.960	1.627	2.942	4.035	1.584	3.250	0.526	3.455	11.845	0.452	3.499	11.537
C	2.325	2.947	3.451	2.350	2.891	3.562	2.162	2.136	11.336	2.137	2.192	11.225
H	1.956	2.329	4.274	1.928	2.302	4.377	2.530	2.753	10.513	2.559	2.781	10.410
C	1.213	6.059	1.976	1.312	5.908	1.889	3.274	–0.975	12.811	3.175	–0.824	12.898
N	0.145	6.220	2.778	0.224	6.020	2.674	4.342	–1.136	12.010	4.263	–0.936	12.113
N	–0.472	7.352	2.432	–0.461	7.099	2.309	4.960	–2.268	12.355	4.949	–2.015	12.478
C	0.180	7.931	1.398	0.170	7.701	1.270	4.307	–2.847	13.390	4.317	–2.617	13.517
H	–0.175	8.867	0.975	–0.235	8.609	0.832	4.663	–3.783	13.812	4.723	–3.525	13.955
C	1.278	7.137	1.067	1.319	6.973	0.962	3.209	–2.053	13.720	3.168	–1.889	13.825
H	2.009	7.318	0.284	2.043	7.183	0.179	2.478	–2.234	14.504	2.444	–2.099	14.608
B	–1.644	7.914	3.305	–1.623	7.635	3.208	6.132	–2.830	11.482	6.111	–2.551	11.579
H	–1.174	8.285	4.375	–1.113	8.268	4.128	5.662	–3.201	10.413	5.601	–3.184	10.659
H	–2.179	8.818	2.689	–2.354	8.331	2.527	6.667	–3.734	12.098	6.842	–3.247	12.260
N	–2.691	6.793	3.557	–2.443	6.445	3.778	7.179	–1.709	11.230	6.931	–1.361	11.009
N	–2.393	5.601	4.129	–1.923	5.333	4.355	6.881	–0.517	10.658	6.411	–0.249	10.432
C	–3.544	4.929	4.285	–2.934	4.672	4.935	8.032	0.154	10.502	7.422	0.411	9.852
H	–3.534	3.919	4.693	–2.756	3.718	5.422	8.022	1.164	10.093	7.244	1.365	9.365
C	–4.619	5.703	3.824	–4.139	5.366	4.745	9.107	–0.619	10.963	8.627	–0.282	10.042
H	–5.675	5.445	3.814	–5.132	5.086	5.087	10.163	–0.361	10.973	9.620	–0.002	9.700
C	–4.023	6.878	3.367	–3.776	6.484	4.000	8.511	–1.794	11.420	8.264	–1.400	10.787
H	–4.457	7.772	2.926	–4.368	7.315	3.624	8.945	–2.688	11.861	8.856	–2.231	11.163
N	0.761	5.578	5.799	0.770	5.572	5.484	3.726	–0.493	8.988	3.717	–0.488	9.303
C	1.175	4.679	6.720	0.969	4.802	6.591	3.312	0.405	8.067	3.518	0.281	8.197
C	2.032	5.049	7.766	1.606	5.306	7.731	2.455	0.034	7.021	2.881	–0.222	7.056
H	2.353	4.304	8.497	1.747	4.658	8.598	2.134	0.779	6.291	2.740	0.425	6.189
C	2.452	6.375	7.854	2.041	6.629	7.735	2.034	–1.291	6.933	2.446	–1.545	7.052
H	3.120	6.687	8.662	2.538	7.045	8.615	1.367	–1.603	6.125	1.949	–1.961	6.172
C	2.008	7.297	6.903	1.827	7.415	6.599	2.479	–2.213	7.884	2.660	–2.331	8.188
H	2.310	8.345	6.939	2.142	8.459	6.560	2.177	–3.261	7.848	2.345	–3.375	8.227
C	1.160	6.848	5.889	1.189	6.845	5.498	3.327	–1.764	8.898	3.298	–1.761	9.289
H	0.778	7.526	5.121	0.992	7.426	4.598	3.709	–2.442	9.666	3.495	–2.342	10.189
C	0.671	3.319	6.524	0.464	3.447	6.448	3.816	1.764	8.263	4.023	1.636	8.340
N	–0.225	3.138	5.538	–0.172	3.211	5.284	4.713	1.945	9.249	4.660	1.872	9.503
N	–0.513	1.838	5.464	–0.533	1.932	5.246	5.001	3.245	9.323	5.021	3.151	9.541
C	0.178	1.163	6.410	–0.140	1.319	6.392	4.309	3.920	8.377	4.628	3.764	8.395
H	0.066	0.087	6.513	–0.357	0.265	6.553	4.422	4.996	8.273	4.845	4.817	8.235
C	0.960	2.074	7.123	0.504	2.253	7.200	3.527	3.009	7.664	3.983	2.830	7.587
H	1.640	1.860	7.943	0.944	2.087	8.179	2.847	3.223	6.844	3.543	2.996	6.608
B	–1.599	1.326	4.460	–1.461	1.382	4.120	6.087	3.757	10.327	5.949	3.701	10.667
H	–2.683	1.769	4.817	–2.621	1.607	4.442	7.171	3.314	9.970	7.109	3.476	10.345
H	–1.562	0.108	4.453	–1.250	0.186	3.997	6.050	4.975	10.334	5.738	4.897	10.790
N	–1.265	1.841	3.028	–1.154	2.084	2.759	5.753	3.242	11.759	5.642	2.999	12.028
N	–1.109	3.150	2.721	–0.933	3.408	2.570	5.596	1.933	12.066	5.421	1.675	12.217
C	–1.000	3.237	1.389	–1.069	3.653	1.259	5.488	1.847	13.398	5.557	1.430	13.528
H	–0.852	4.207	0.918	–0.922	4.656	0.868	5.340	0.876	13.869	5.410	0.427	13.919
C	–1.090	1.962	0.809	–1.383	2.468	0.574	5.578	3.122	13.978	5.871	2.615	14.213
H	–1.043	1.698	–0.244	–1.553	2.338	–0.491	5.531	3.385	15.032	6.041	2.745	15.279
C	–1.257	1.105	1.896	–1.423	1.499	1.570	5.745	3.978	12.891	5.911	3.584	13.217
H	–1.384	0.026	1.942	–1.648	0.436	1.524	5.872	5.057	12.846	6.136	4.647	13.263

Table 4.2: Atomic coordinates of relaxed structures inferred from gas-phase calculations of monomers.

Chapter 4.2 is based on a publication in The Journal of Physical Chemistry C from 2022. Reprinted with permission from:
S. Johannsen et al., "Three-State Switching of an Fe Spin Crossover Complex", J. Phys. Chem. C **126**, 7238–7244 (2022) DOI: 10.1021/acs.jpcc.2c00473.
The layout of the text, figures and tables has been adapted to this thesis without changing their contents.

Author Contributions

Sven Johannsen carried out the STM measurements. Sascha Schüddekopf did supporting STM measurements for figures 4.26–4.28 within the framework of his bachelor thesis. Sascha Ossinger, Jan Grunwald and Felix Tuczek provided the SCO complex. Sven Johannsen, Manuel Gruber and Richard Berndt analyzed and interpreted the data. Sven Johannsen created all figures in the manuscript and supporting information, except 4.31, 4.33–4.36. Richard Berndt and Manuel Gruber wrote the manuscript with input from all authors. Richard Berndt was the supervisor of the project. All authors discussed the results.

4.2 Three-State Switching of an Fe Spin Crossover Complex

4.2.1 Abstract

Isolated tetramers of the spin crossover compound $Fe(H_2B(pyrazole)(pyridylpyrazole))_2$ were investigated on Ag(111) at cryogenic temperature (5 K) with a scanning tunneling microscope (STM) in ultra-high vacuum. In addition to spin states obtained by electron-induced spin crossover, a third state of the complexes is discovered with different current-voltage characteristics and intramolecular image contrast. It is stable over a limited range of voltages beyond which it decays into the low- and high-spin states of the Fe complex. The state may be prepared in a deterministic manner that enables measurements of its decay dynamics at various currents and voltages. We interpret this state as being due to a negatively charged Fe complex in its high-spin state, which is isoelectronic to the analogous Co compound.

4.2.2 Introduction

Spin crossover (SCO) molecules are transition metal complexes that exhibit bistable spin states. The spin states are intimately coupled to the binding and geometry of the ligand shell, and consequently various external parameters may be used to impact on the spin states of a SCO compound. For applications in electronic devices, the interface between the complexes and electrode surface is relevant, in particular when miniaturization is desired. Consequently, various functional ultrathin SCO

films have been prepared [18, 21, 24, 30, 70–81] although the adsorption to metal electrodes may cause SCO molecules to dissociate or become dysfunctional [21, 23, 27–30].

Single molecules or nanometer-sized assemblies of SCO complexes have been investigated with transport measurements [9–13, 32–37] and scanning tunneling microscopy (STM) [20–22, 25, 38–43]. It is hoped that microscopic characterization of small structures will help to develop a detailed microscopic picture of the switching process and cooperative effects among neighbor molecules.

Here we extend the microscopic approach to the complex $Fe(H_2B(pz)(pypz))_2$ (pz = pyrazole, pypz = pyridylpyrazole, Figure 4.23) deposited on Ag(111) single crystal surfaces. We previously showed that this complex and also $Co(H_2B(pz)(pypz))_2$ (chapters 4.1 and 4.3) assemble into regular tetramers with unique switching characteristics [1, 3]. Only two molecules of a tetramer exhibit electron-induced spin transitions while the other two do not switch because of steric hindrance. In an attempt to more comprehensively characterize the dynamics of the electron-induced processes, we discovered that $Fe(H_2B(pz)(pypz))_2$ molecules on Ag(111) exhibit a new, third state.

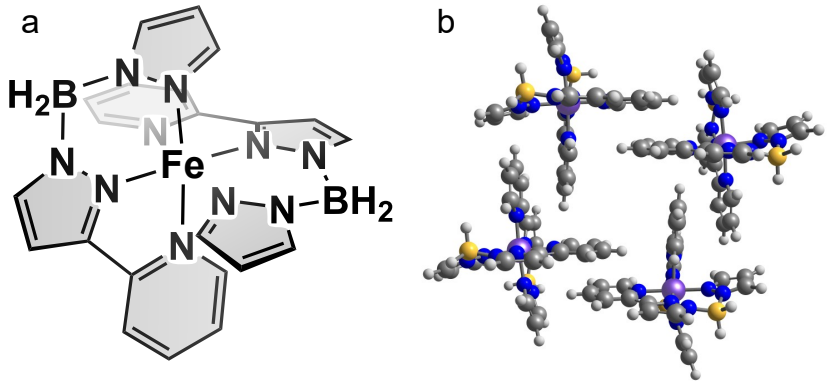

Figure 4.23: Schemes of (a) the $Fe(H_2B(pz)(pypz))_2$ compound and (b) a tetramer. Violet: Fe, yellow: B, blue: N, gray: C, light gray: H. All complexes are shown in their low-spin state. The molecules in the upper right and lower left corners can undergo electron-induced switching.

4.2.3 Methods

Synthesis

The Fe(II) complex $Fe(H_2B(pz)(pypz))_2$ was synthesized as reported by Ossinger et al [84].

Experimental Details

The Ag(111) substrate was prepared by cycles of Ar^+ sputtering (1.5 keV) and annealing to 500 °C. $Fe(H_2B(pz)(pypz))_2$ molecules were sublimated from a heated crucible ($\sim$ 150 °C) onto the substrate at $\sim$ 50 °C. STM tips were electrochemically etched from W wire and annealed in vacuo. The measurements were performed in ultra-high vacuum with a STM operated at $\sim$ 5 K.

Theoretical Details

Gas phase calculations were performed with the ORCA software package [95, 96]. The crystallographic structure of $Fe(H_2B(pz)(pypz))_2$ (polymorph II) was used as a starting point [1]. Geometry optimizations were performed with ORCA at the B3LYP [97–99] / def2SVP [100, 101] level with the D3BJ dispersion correction [102, 103], the RIJCOSX approximation, fine numerical integration grids (grid4 and gridX4 in ORCA nomenclature), and the CG solver. The orbitals and their energy were calculated with ORCA at the B3LYP/def2-QZVP [100, 101] level with the RIJCOSX approximation.

4.2.4 Experimental Results

Observation of intermediate State i

Data were recorded by freezing the position of the STM tip above a switchable molecule within a tetramer and varying the sample voltage while recording the current. As discussed previously [1], the bistability due to spin crossover between the low-spin (LS) and high-spin (HS) states of $Fe(H_2B(pz)(pypz))_2$ leads to two major branches of the current-voltage (I-V) curves (Figure 4.24) labeled **L** (blue) and **H** (green).
In addition, an unexpected third state denoted **i** is resolved (red line). It is stable over a limited range of voltage $|V| < 0.3$ V and exhibits rapid transitions to the **H** (-0.3 V $< V < -0.8$ V) and **L** ($V < -0.8$ V) states. This third state has been systematically observed on all switchable molecules, i.e., two molecules per tetramers. Besides its distinct I-V curve, this state also presents a particular image contrast to be discussed below. From a large number of measurements we determined voltage ranges that correspond to characteristic stability or dynamics of the switchable complexes.

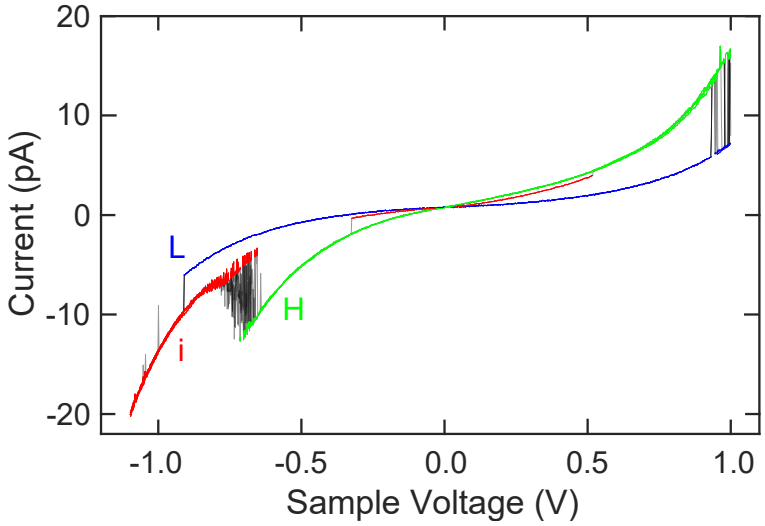

Figure 4.24: Current-voltage characteristics of a switchable $Fe(H_2B(pz)(pypz))_2$ complex in a tetramer on Ag(111). The data were recorded by sweeping V from -1.1 to 1 V and back four times. At low voltages, $|V| < 0.3$ V, three distinct branches are observed, which correspond to the high-spin (**H**, green), low-spin (**L**, blue), and an intermediate (**i**, red) state. At more positive voltage, **i** is not observed. Rather, rapid transitions between **H** and **L** occur. At more negative sample bias, first transitions between **i** and **H** are found. Beyond $V = -0.8$ V, **H** is no longer detected and **i** predominates with occasional excursions to **L**.

Figure 4.25 schematically summarizes our observations. At low bias, $|V| < 0.3$ V (white area, α), all states are stable over many minutes at currents up to 50 pA. For $V > 0.3$ V (green area, δ), the intermediate state **i** becomes unstable and decays toward **H** on a time scale of seconds. We occasionally observed the reverse process, albeit at much lower rate. At $V > 0.9$ V (gray area, ϵ), **i** is no longer observed. However, switching between **H** and **L** occurs.

At negative sample voltages, a different evolution is found. Between -0.8 and -0.3 V (red area, β), we observed transitions between **H** and **i**. The **L** state, however, remained stable. When the bias is even more negative, $V < -0.8$ V (blue area, γ), we do no longer observe state **H** but rather find transitions between **L** and **i**.

Before attempting an interpretation of this diverse behavior, we first present additional data on the dynamics.

Instability of State i at V < -0.3 V

We first focus on the transitions involving the **i** state at negative sample voltages. Time series of the current show that the transition rates between **i** and **L** and **H** are proportional to the current used. We therefore defined yields as the number of

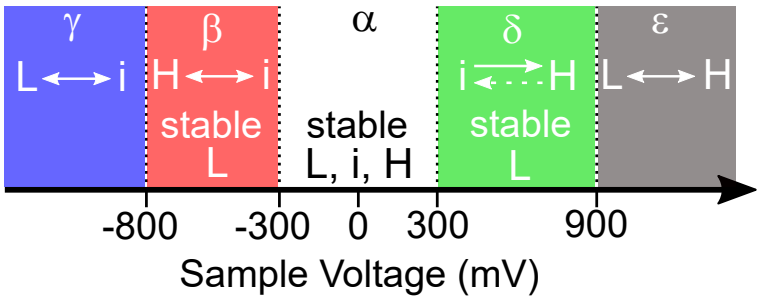

Figure 4.25: Schematic diagram of the stability and switching of a molecule in a tetramer. Between -300 and 300 mV, states **L**, **H**, and **i** are stable over hours. At increasingly negative voltages, conversions (double-sided arrow) between **i** and **H** commence at ~ -300 mV. Beyond ~ -800 mV, **H** is not observed and **i** and **L** interconvent. At positive $V > 300$ mV, **i** becomes unstable and decays to **H**. Switching from **H** to **i** is occasionally observed. Beyond $V \sim 900$ mV, switching between **L** and **H** sets in, and state **i** was not observed. Sample voltages $|V| > 1.1$ V led to lateral hopping or destruction of the tetramer under investigation.

transitions per tunneling electron (Figure 4.26). The data reveal that the yields vary rapidly with the sample voltage. Over the accessible voltage range the variations are approximately exponential. While the **L**→**i** (violet) and **i**→**L** (black) transitions have similar yields near -0.85 V, the **i**→**L** yield grows less rapidly at more negative bias. A related evolution is initially observed for the **i**↔**H** transitions. Near the threshold at -0.3 V, the yields of **i**→**H** (red) and **H**→**i** (blue) match. Toward negative voltages down to -0.6 V, the **H** state is less prone to switching. Beyond this voltage, its switching yield rises rapidly and exceeds the **i**→**H** yield at ≈ -0.75 V. At even more negative voltages, the complex is more likely to be found in the **i** state. Histograms of the current illustrating the crossing of the yield curves are shown in the Supporting Information.

Instability of State i at V > 0.3 V

At sufficiently positive V (Figure 4.25), the **i** state becomes unstable and usually decays to **H**. Quantifying decay times from time series is unpractical because state **i** is hardly observed at these voltages. We therefore used the following preparation scheme (Figure 4.27a).

The positively biased tip was first placed above a switchable complex in its **H** state. Then, the tip height was frozen, and V was quickly (1 ms) changed to -750 mV for 350 ms, which led to an increased current. After the pulse, with a 85 % probability, the **i** state was observed as signaled by a characteristic current level. The **i** state then survived over a short time interval until the complex ended up in the **H** state.

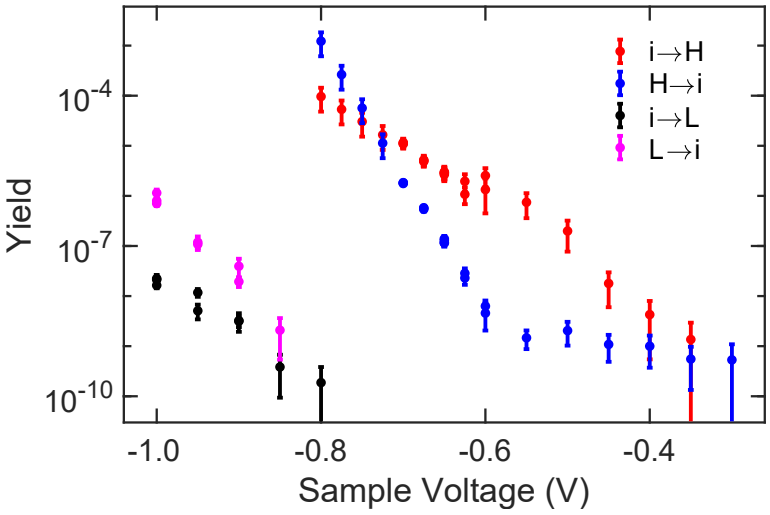

Figure 4.26: Yields of the transitions **i**→**H**, **H**→**i**, **i**→**L**, and **L**→**i** at negative voltages. The data were determined by evaluating time series of the tunneling current. For most data points, uncertainty margins indicate the range $\pm\sigma$. The data at the highest yields (**i**↔**H** in the range -0.8 to -0.7 V) were affected by the low-pass characteristics of the current measurement. This effect has been approximately corrected for and the corresponding uncertainty margins are estimates.

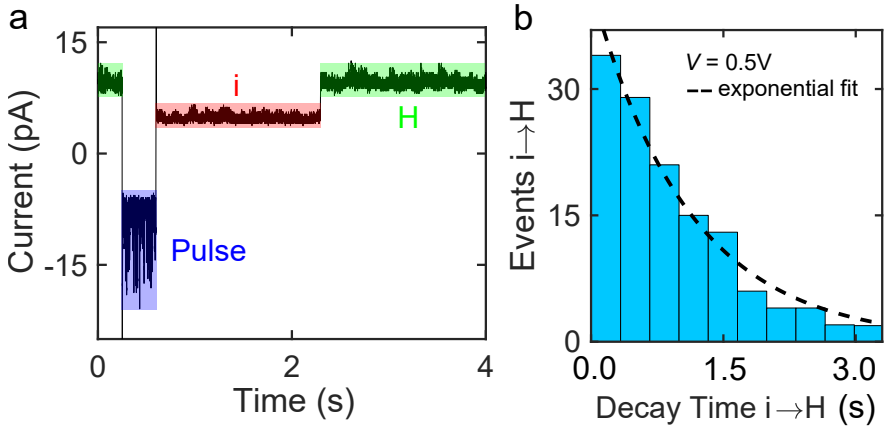

Figure 4.27: (a) Time series of the current recorded above a switchable complex. The tip was positioned above the molecule in its **H** state at $I = 10\,\mathrm{pA}$ and $V_0 = 460\,\mathrm{mV}$. Next, a rectangular voltage pulse (-750 mV, 350 ms, tip position frozen) was used to prepare the **i** state. After the pulse, V was reset to V_0, and the current was measured until a relaxation to the **H** state was detected via an abrupt return to the corresponding current level. In the present example, the **i** state lived for $\sim 2\,\mathrm{s}$. (b) Histogram of decay times evaluated from 130 **i**→**H** transitions at $V = 0.5\,\mathrm{V}$ along with an exponential fit.

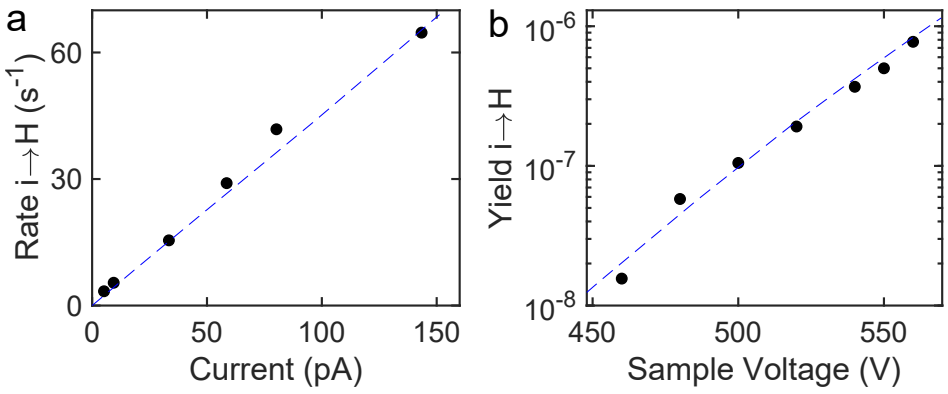

Figure 4.28: (a) Rate of transitions **i**→**H** vs tunneling current measured at $V = 0.5\,\mathrm{V}$. The experimental rates (dots) evolve proportional to the current as indicated by a linear fit (line). (b) Yield defined as number of **i**→**H** transitions per tunneling electron. The experimental data (dots) may be modeled with a Gaussian (line). Currents were ~ 5 and 10 pA for **i** and **H**.

The preparation procedure of the **i** state turned out sufficiently reproducible for obtaining histograms of the decay at various currents and voltages. An example is shown in Figure 4.27b. We again found that the switching rate is proportional to the current. Single electrons apparently induce the transition (Figure 4.28a). Moreover, the decay time is exponentially reduced at larger voltages (Figure 4.28b), which may indicate that the electrons inducing the transition are injected into the low-energy tail of an unoccupied resonance.

Image Contrast of State i

Many aspects of the experimental data may be understood by assigning the **i** state to a negatively charged high-spin (S=3/2) Fe complex. The additional electron renders the Fe complex isoelectronic to its Co analogue.

A fairly direct indication in favor of this interpretation is the image contrast observed from **i**. Figure 4.29 shows constant current topographs of tetramers comprising the Fe complex and its Co analogue. Initially (Figures 4.29a,d), all complexes are in their low-spin state. Next (Figures 4.29b,e), the molecules in the upper right corner of each tetramer are manipulated to obtain the **i** and high-spin states of the Fe and Co complexes, respectively. Finally, Figure 4.29c displays the high-spin state in the Fe case. The similarity between panels b and e is striking. The Fe **i** state and the Co high-spin state display clear intramolecular contrast with an apparent nodal line that is oriented approximately parallel to a diagonal of the tetramer.
Figure 4.30 displays results of calculations for the anionic Fe complex and its neutral Co analogue. Additional information may be found in the Supporting Information. The calculated structures (panels a and c) closely resemble each other.

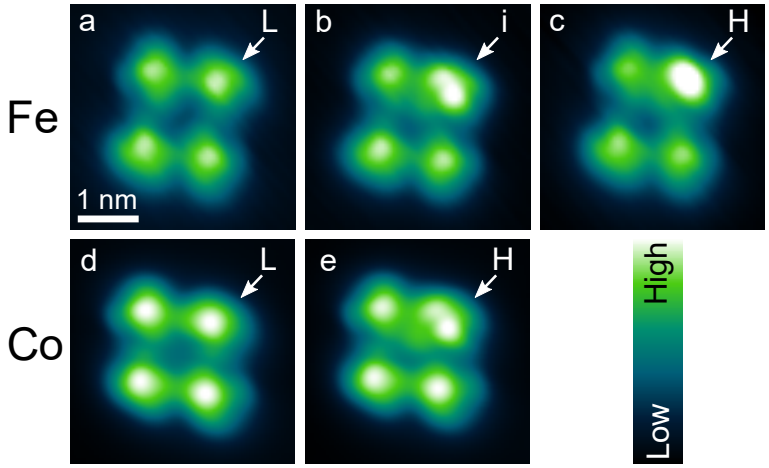

Figure 4.29: STM topographs of (a–c) $Fe(H_2B(pz)(pypz))_2$ and (d, e) $Co(H_2B(pz)(pypz))_2$ tetramers on Ag(111). The upper right molecules (arrows) have been switched via voltage and current pulses to their low (**L**), intermediate (**i**), and high (**H**) states, as indicated in each panel. The color scale covers ranges of 290 and 300 pm for Fe and Co, respectively.

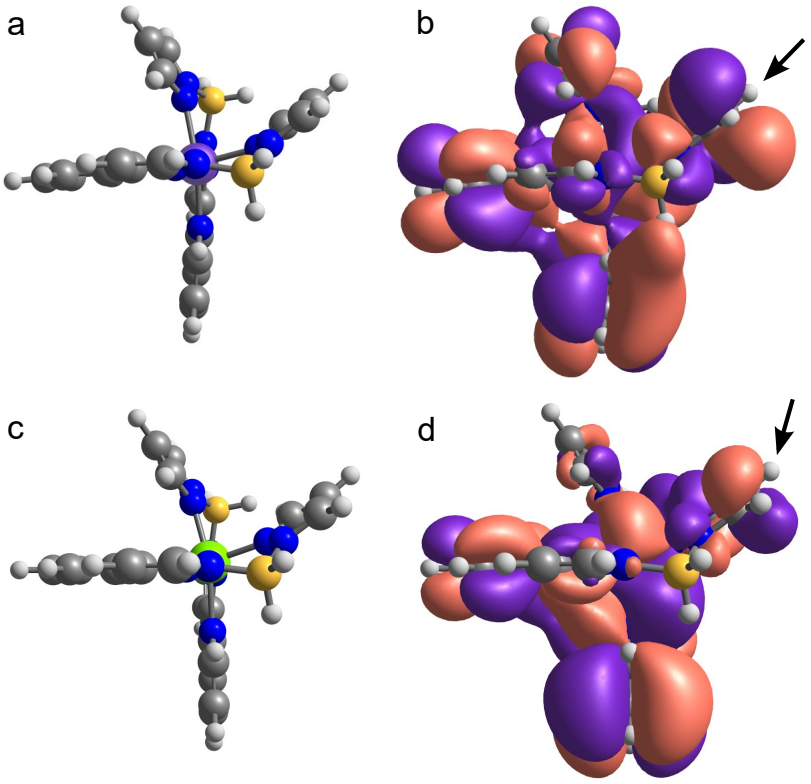

Figure 4.30: Calculated molecular structures and orbitals producing image contrast. (a, c) Models of charged $Fe(H_2B(pz)(pypz))_2$ and neutral $Co(H_2B(pz)(pypz))_2$. (b) HS β LUMO+3 of the Fe complex. (d) HS β LUMO of the Co complex. Violet: Fe, green: Co, yellow: B, blue: N, gray: C, light gray: H.

In both cases, a particular frontier orbital in the β spin system exhibits a nodal plane through the pyrazole subunit. According to the structural model of the tetramers, this orbital (arrows in Figure 4.30b,d) extends particularly far into the direction of the tip making it a likely candidate for explaining the unusual image contrast.

The experimental data provide another important hint toward the nature of state **i**. At fairly low bias voltages, independent of the bias polarity, **i** decays toward the high-spin state of the Fe compound and the transition rate is proportional to the tunneling current. A corresponding single electron event may more easily convert from S=3/2 (charged HS) to S=2 (neutral HS) rather than to S=0 (neutral LS). In a similar vein, significantly larger $|V|$ are required to access the LS state. The additional energy available at larger $|V|$ then makes possible more complex transitions that involve several electron spins.

4.2.5 Model

Gas-phase DFT calculations of neutral and charged $Fe(H_2B(pz)(pypz))_2$ were performed to further substantiate the model. To simplify the notation, we refer LS^- and HS^- for the LS and HS states of the anionic complex, while LS and HS denote the spin states of the neutral molecule. While LS (S=0) is typically the most stable spin state of neutral Fe^{2+} SCO compounds, the HS^- state (S=3/2) of the charged complex is calculated to be $\approx 0.2\,\text{eV}$ more favorable than the LS^- state (S=1/2). On the substrate, the interaction with an image charge is expected to fairly rigidly shift these energies by more than 1 eV [94]. The average Fe-N bond lengths of the LS, LS^-, HS^-, and HS states are 1.98, 1.99, 2.18, and 2.20 Å, respectively. Corresponding energy landscapes of the neutral (blue/black) and anionic (red) molecules are proposed in Figure 4.31a. Transitions between neutral and charged states involve a modification of the molecular structure visible through the change of the average Fe-N bond lengths. Therefore, both energy and charge have to be transferred to the molecule to induce a transition. According to the energy landscapes, the LS, HS, and HS^- states are stable in voltage range α, in agreement with the experimental data (Figure 4.25).

To enable charging of the molecule, we assume that the molecular levels are not pinned to those of the substrate, i.e., a fraction of the voltage between the sample and the tip drops between the molecule and the substrate. The energy of the anion is reduced when the chemical potential of the substrate rises. It thus directly depends on the applied voltage. This scenario is familiar from molecules between electrodes [109–111] and, in a STM context, has often been observed from atoms or molecules on spacer layers [112–115] as well as from three-dimensional molecules [116, 117]. The three-dimensional structure of the present tetramers is likely to promote charging

effects. While macroscopic lifetimes of a charge on a molecule close to a metal surface may be unexpected at first glance, tunneling of the charge to the metal may be efficiently prevented if a reorganization energy is involved. Upon charging, this energy is dissipated to the substrate and tunneling out of the molecule is consequently suppressed at low temperatures.

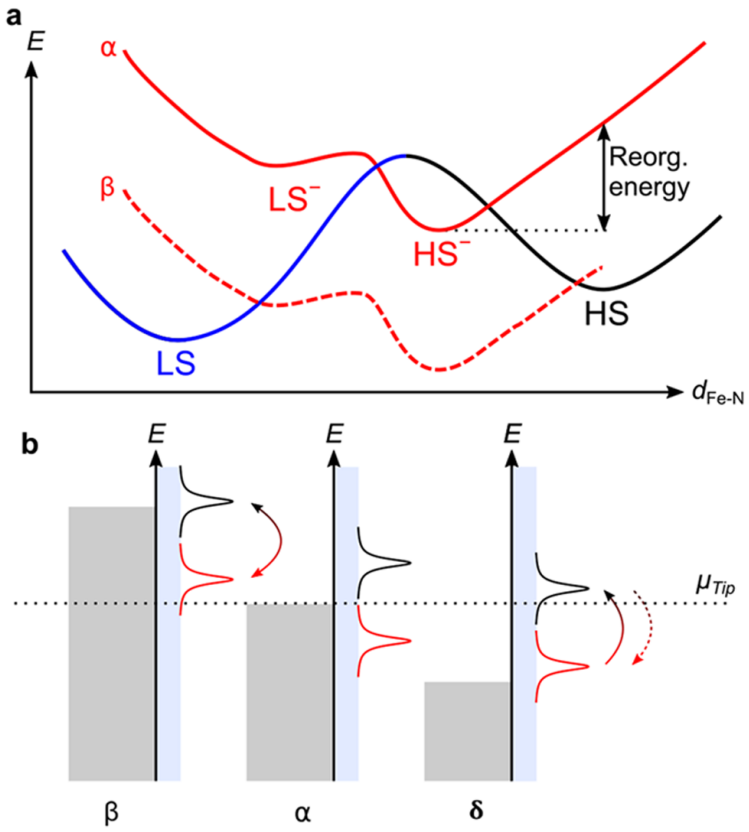

Figure 4.31: (a) Proposed energy landscape of neutral (blue/black) and negatively charged (red) [Fe(H_2B(pz)(pypz))$_2$] along the reaction coordinate, the Fe-N distance $d_{\text{Fe-N}}$. The energy difference between the neutral and charged molecules depends on the chemical potential of the sample and hence on the sample voltage. Greek letters refer to voltage ranges in Figure 4.25. (b) Level diagrams depicting the chemical potential of the sample (gray rectangles indicate occupied states), the LUMO of the high-spin complex (black), and the SOMO of the singly charged complex (red) for three voltage ranges (β, α, and δ). The chemical potential of the tip is indicated by a dotted line. The light blue bar is to indicate that the molecular levels are partially decoupled from the substrate. Curved arrows indicate transitions between charged and neutral complexes. Consequently, a fraction of the tip-sample voltage drops between the molecule and the substrate thus shifting the orbital energies.

Transitions between neutral and charged states require (i) energy or a shift of chemical potential and (ii) the transfer of an electron between the molecule and an electrode. To visualize the voltage ranges for which electron transfer is possible, we consider the energy of the lowest unoccupied molecular orbital (LUMO) of the HS state

(black) and the singly occupied molecular orbital (SOMO, red) of HS^- relative to the chemical potential of the electrodes (Figure 4.31b). For simplicity, we refer to the black and red orbitals below. For an electron to enter into (leave from) the black (red) orbital, the chemical potential of the sample or tip has to cross or be larger (lower) than the orbital energy.

In voltage range α, the black orbital is above the chemical potentials of the sample (top of the gray rectangle) and the tip (dashed line); that is, there is no electron transfer and hence no switching from HS to HS^-. Should the molecule already be charged, the extra electron remains trapped in the red orbital because the reorganization energy is not available. Application of a negative sample voltage increases the chemical potential of the sample. The energy of the orbitals increases as well but to a lesser extent because of the partial decoupling of the molecule from the substrate.

In range β, the HS LUMO is pulled below the chemical potential of the sample. A substrate electron may be injected into the black orbital (Figure 4.31b, β) leading to a HS to HS^- ($= \mathbf{i}$) transition, which releases reorganization energy to the substrate. For the reverse transition, an electron in the red orbital may transfer energy to the molecule and escape to the tip if it makes the reorganization energy available. In other words, HS$\leftrightarrow$$HS^-$ transitions are possible in voltage range β, as experimentally observed.

Upon further increase of $|V|$ (range γ), more energy can be transferred to the molecule as the electron escapes the red orbital, such that $H^- \rightarrow$LS transitions are feasible. Injection of an electron to the LS LUMO (thereby charging the molecule) would create LS^-, which is unstable and decays to the HS^- (red curve in Figure 4.31a).

At reverse bias, in range δ, the HS^- SOMO is shifted above the chemical potential of the sample. HS^- to HS transitions then occur via electrons that transfer energy to the molecule and escape from the red orbital to the sample. The reverse process, which is occasionally observed, may be induced by tunneling from the tip that leads to HS^-.

Finally, at very positive sample (range ϵ), the negatively charged state is no longer detected, presumably because it rapidly decays to a neutral state. However, the energy available in tunneling processes is now large enough to enable HS$\leftrightarrow$LS transitions.

4.2.6 Summary

The complex $Fe(H_2B(pz)(pypz))_2$ exhibits unexpected switching between three states that may be reproducibly prepared with a scanning tunneling microscope. The stability of the states and the transitions between them depend in a fairly complex manner on the bias voltage of the tunneling junction. The experimental data are consistent with a model that takes into account a negatively charged high-spin state of the Fe complex, which is isoelectronic to the analogous Co compound. We hint that the stability of the anionic state is greatly enhanced by the presence of a metal substrate that provides screening. In a broader context, the present Fe complexes combine memristive switching between redox [118, 119] and spin [5] states on the scale of single molecules in clusters.

4.2.7 Acknowledgments

Richard Berndt thanks Alexander Weismann for discussions. We acknowledge financial support from the European Union's Horizon 2020 program, Grant 766726.

4.2.8 Supplementary Information

Histograms of the tunneling current

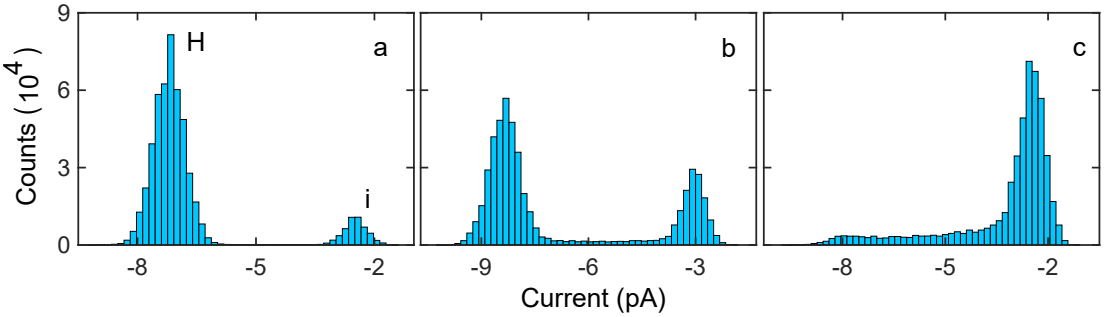

Figure 4.32: Histograms generated from time series of the tunneling current recorded at a switchable complex at sample voltages (a) -650, (b) -700, and (c) -750 mV. While the complex is mainly in its **H** state in (a), the **i** state becomes increasingly probable at more negative voltages.

Electronic structure of the Fe(I) complex

The electronic structure of the (anionic) Fe(I) complex can be understood on the basis of the MO scheme of the parent, neutral Fe(II) complex (Figure 4.33 and 4.34). In the LS state of the latter, the three t_{2g} orbitals d_{xy}, d_{xz} and d_{yz} (130, 129, 128) are doubly occupied. LUMO and LUMO+1 (131, 132) are represented by combinations of π^* orbitals on pyridine and the central pyrazole with small contributions of metal

d-orbitals. The e_g orbitals $d_{x^2-y^2}$ and d_{z^2} (136 and 137) are unoccupied. Orbitals 133 and 134 are π^* orbitals on the pyridine residues.

In the HS state of the Fe(II) complex, all *d*-orbitals are occupied with α spins and lowered in energy due to spin polarization, whereas one orbital is occupied with a β spin and raised in energy. Correspondingly, the α-spin orbitals at highest energy correspond to $d_{x^2-y^2}$ (132α) and d_{z^2} (131α); the other *d*-orbitals follow at lower energy. The lowest unoccupied α-spin orbitals are combinations of π^* orbitals on pyridine and the central pyrazole (133α, 134α) and π^* orbitals on the pyridine residues (135α, 136α), respectively. The highest occupied β-spin orbital containing the 6$^{\text{th}}$ electron corresponds to d_{xy} (128β), which also represents the HOMO (SOMO) of the molecule. The β-spin LUMO (129β) is composed of π^* orbitals on pyridine and the central pyrazole with a large contribution of a metal *d*-orbital. Likewise, the unoccupied β-spin orbitals at higher energy correspond to hybrids of metal *d*-orbitals and π^*-orbitals on the central pyrazole and/or pyridine residues.

In the Fe(I) complex generated by one-electron reduction of the Fe(II) complex, all metal *d*-orbitals are shifted to higher energy because the effective nuclear charge is reduced (Figure 4.35 and 4.36). In the LS state, e.g., this corresponds to a shift of the three doubly-occupied t_{2g} orbitals from approximately -5 to $\approx$ -2 eV. In this state (S=1/2), the additional electron is accommodated in an α-spin orbital with ligand character (131α), being composed of π^* orbitals on the pyridine residues and the central pyrazole (see above). There is a second orbital of very similar character (132α), which represents the lowest unoccupied α-spin orbital (133α); notably, the splitting of 131α and 132α is small (0.7 eV). The (unoccupied) e_g orbitals $d_{x^2-y^2}$ and d_{z^2} (or hybrids of these with ligand π^* orbitals) follow at higher energy. The three β-spin electrons are accommodated in the corresponding d_{xz}-, d_{yz} and d_{xy}-orbitals (128β, 129β, and 130β) which appear approximately at the energies as their α-spin counterparts, reflecting a very small degree of spin-polarization in the *d*-shell of the Fe(I) center. This is due to the fact that the spin is small and the additional, unpaired electron is located in a ligand orbital rather than a metal orbital (see above).

The HS state of the Fe(I) complex involves five electrons in α-spin orbitals (as in the Fe(II) HS case), but two electrons in β spin-orbitals (in contrast to one for Fe(II)). Correspondingly, the highest occupied α-spin orbitals correspond to d_{z^2} (132α and 131α) and the other *d*-orbitals follow at lower energies. The lowest unoccupied α-spin orbitals are combinations of π^* orbitals on pyridine and the central pyrazole (133α and 134α) and π^* orbitals on the pyridine residues (135α and 136α), similar to Fe(II) (see above). Larger changes occurs in the β-spin space. Apart from orbital 128β

(d_{yz}), which is already occupied in Fe(II), there is now a second β-spin electron that occupies 129β. This orbital is a combination of d_{xy} and π^*-orbitals at the central pyrazole and the pyridine residue. The lowest unoccupied β-spin orbital, 130β, is of similar type, and the splitting between 129β and 130β is small (1.17 eV). Interestingly, there is a close similarity between the HOMOs and LUMOs of the LS (α spin) and HS (β spin) as well as their energy differences, which are small. At higher energy, in the β-spin space, we find unoccupied π^* orbitals on the pyridine residues (131β and 132β) and comparatively pure metal d-orbitals (d_{xy} and d_{xz}).

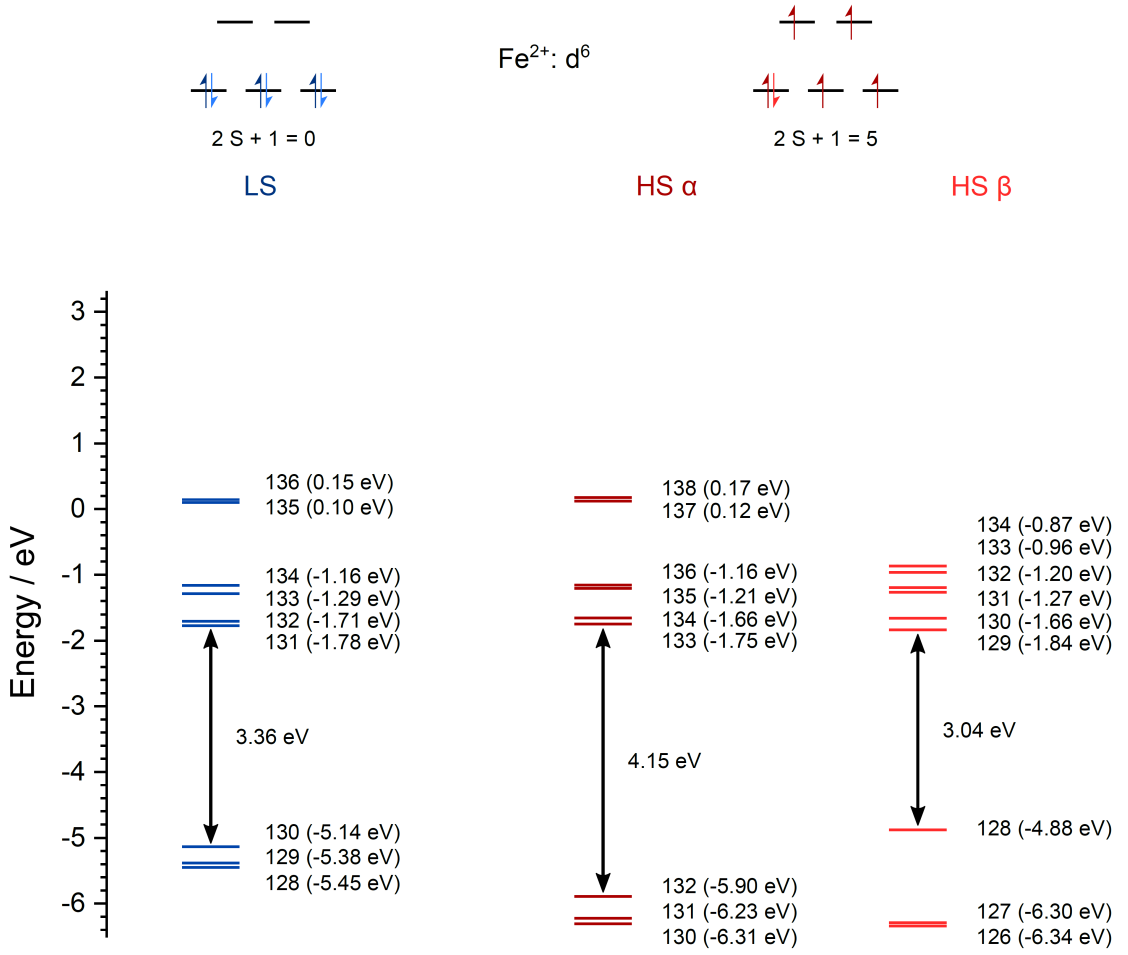

Figure 4.33: Calculated orbital energies of the frontier orbitals of neutral [Fe(H_2B(pz)(pypz))$_2$].

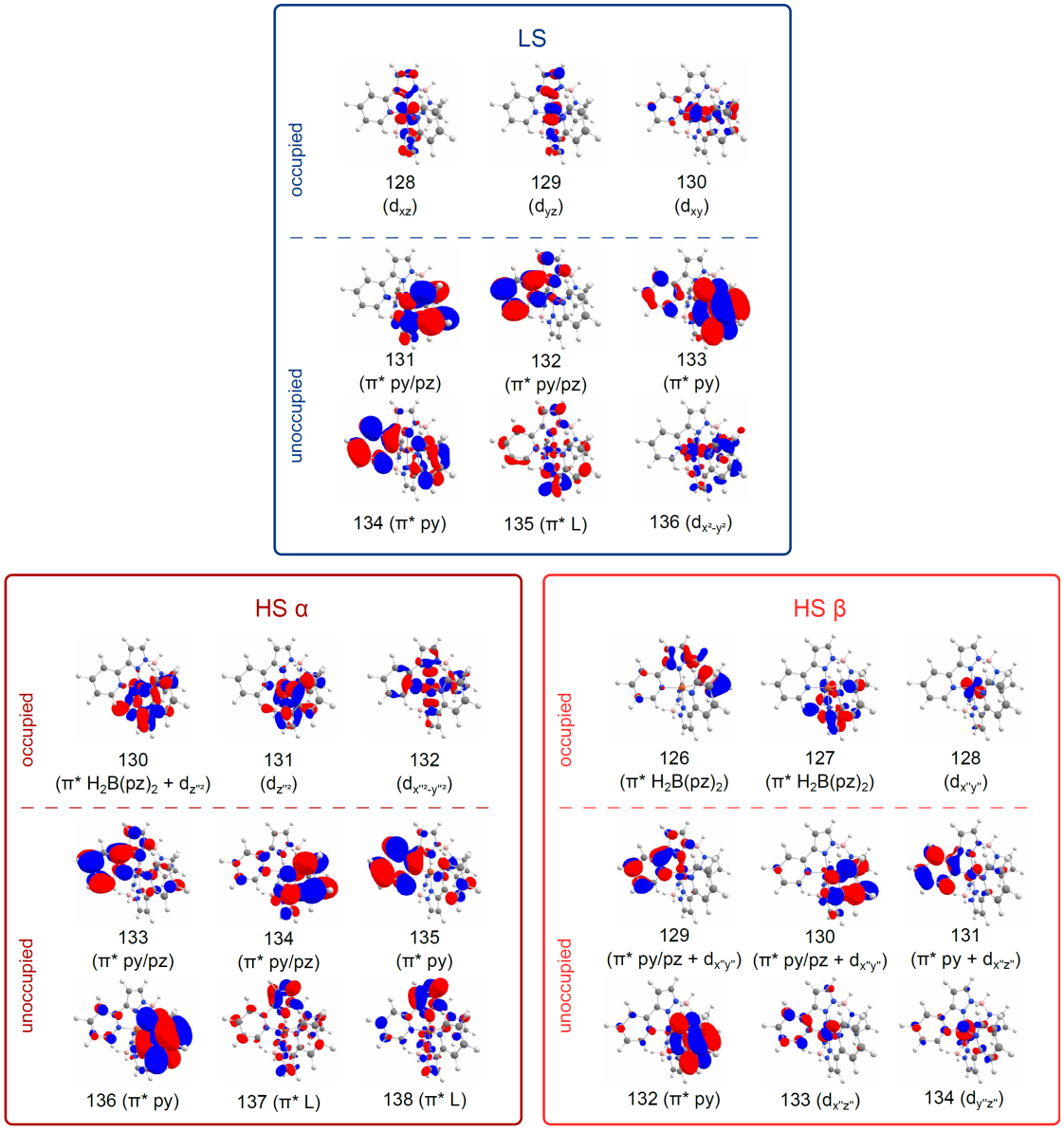

Figure 4.34: Calculated isodensity contours of the frontier orbitals of neutral $[Fe(H_2B(pz)(pypz))_2]$.

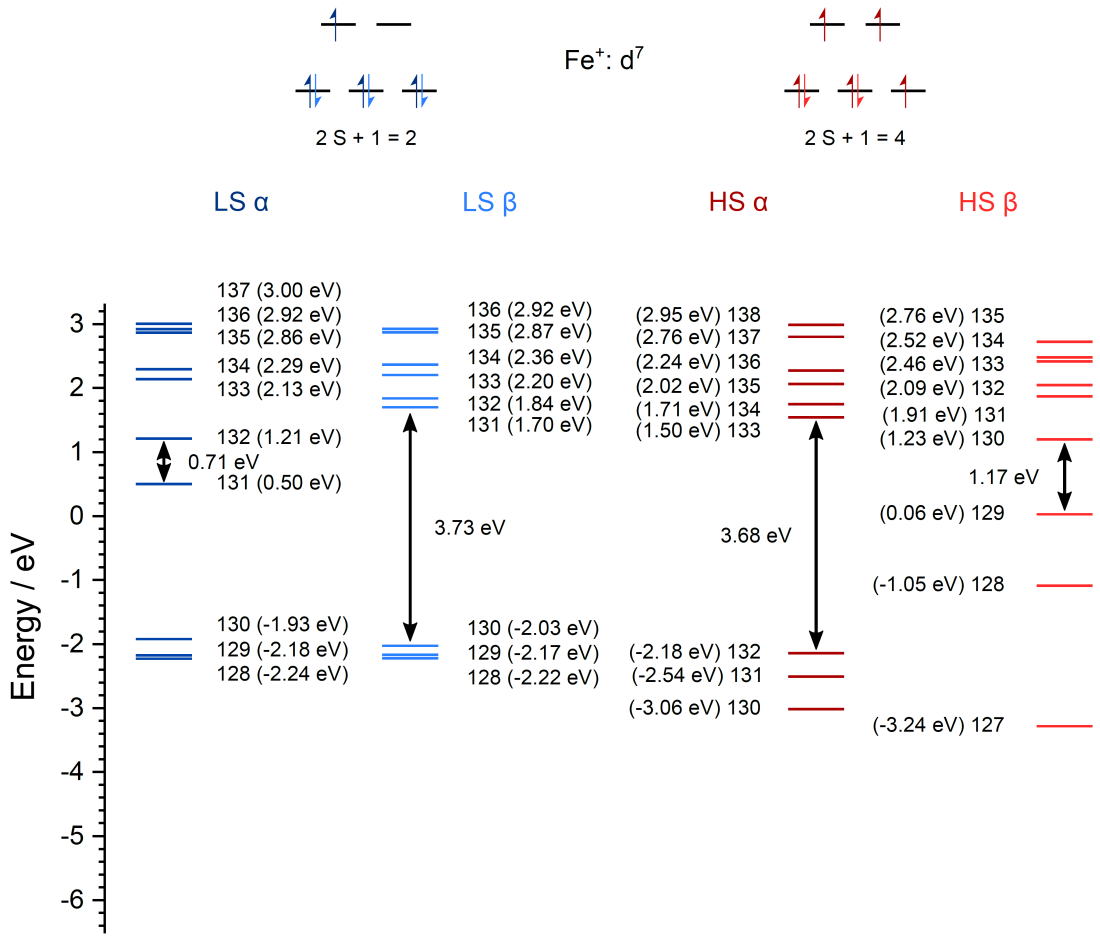

Figure 4.35: Calculated orbital energies of the frontier orbitals of negatively charged $[Fe(H_2B(pz)(pypz))_2]$.

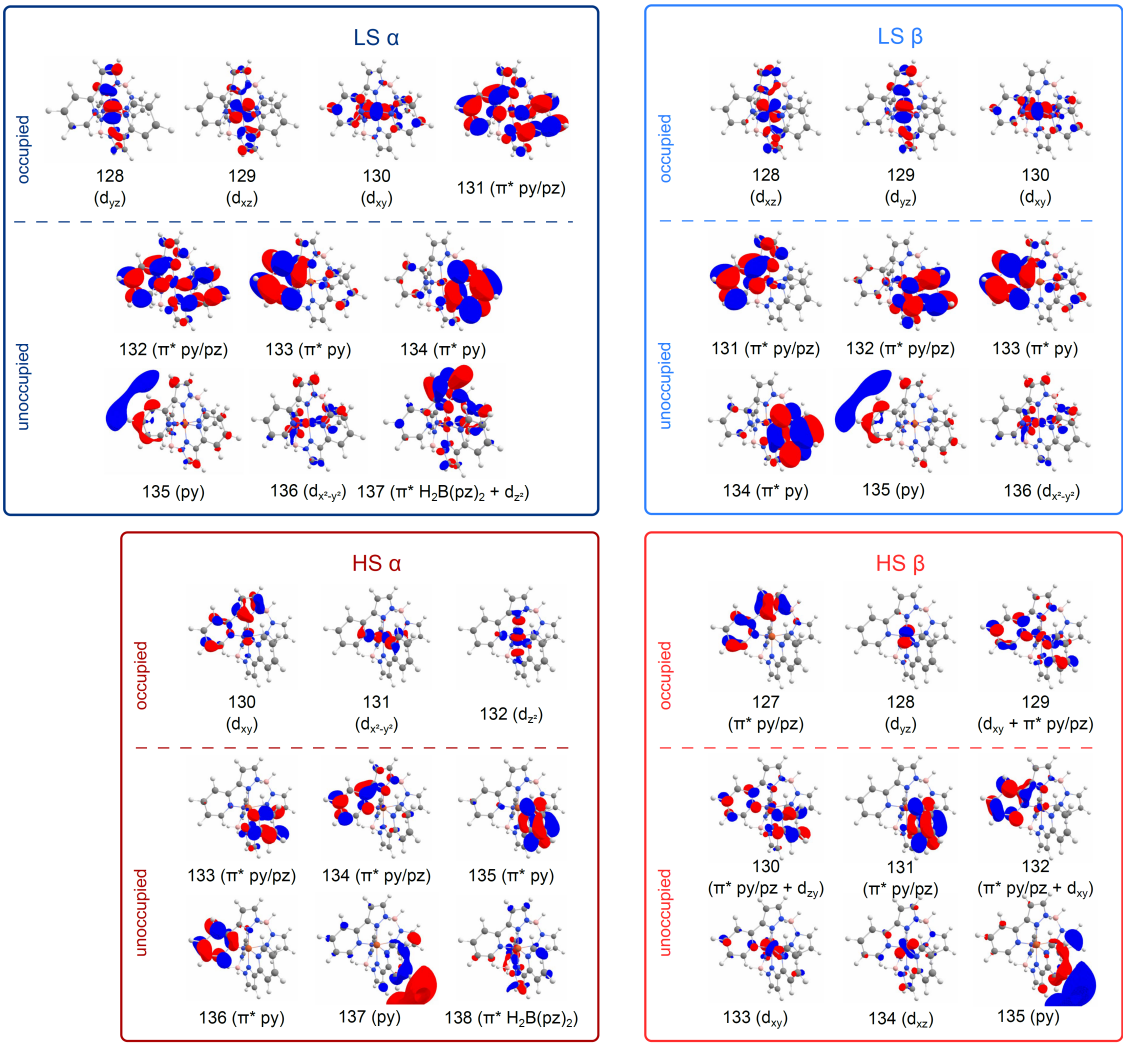

Figure 4.36: Calculated isodensity contours of the frontier orbitals of negatively charged $[Fe(H_2B(pz)(pypz))_2]$.

Chapter 4.3 is based on a publication in Angewandte Chemie International Edition from 2022. The article is freely available and distributed under the terms of the Creative Commons CC BY-ND-NC license:
S. Johannsen et al., "Spin Crossover in a Co Complex on Ag(111)", Angew. Chem. Int. Ed. **61**, e202115892 (2022) DOI: 10.1002/anie.202115892.

Author Contributions

Sven Johannsen acquired the STM data. Sascha Ossinger, Jan Grunwald and Felix Tuczek provided the SCO complex. Sven Johannsen, Manuel Gruber and Richard Berndt analyzed and interpreted the data. Alexander Herman and Heiko Wende performed XPS measurements and provided the XPS spectra in figure 4.44. Sven Johannsen created all figures in the manuscript and supporting information, except 4.41, 4.43–4.47. Richard Berndt and Manuel Gruber wrote the manuscript with input from all authors. Richard Berndt supervised the project. All authors discussed the results.

4.3 Spin Crossover in a Cobalt Complex on Ag(111)

4.3.1 Abstract

The Co-based complex $[Co(H_2B(pz)(pypz))_2]$ (py=pyridine, pz=pyrazole) deposited on Ag(111) was investigated with scanning tunneling microscopy at $\approx 5\,K$. Due to a bis(tridentate) coordination sphere the molecules aggregate mainly into tetramers. Individual complexes in these tetramers undergo reversible transitions between two states with characteristic image contrasts when current is passed through them or one of their neighbors. Two molecules exhibit this bistability while the other two molecules are stable. The transition rates vary linearly with the tunneling current and exhibit an intriguing dependence on the bias voltage and its polarity. We interpret the states as being due to S=1/2 and 3/2 spin states of the Co^{2+} complex. The image contrast and the orders-of-magnitude variations of the switching yields can be tentatively understood from the calculated orbital structures of the two spin states, thus providing first insights into the mechanism of electron-induced excited spin-state trapping (ELIESST).

4.3.2 Introduction

Spin-crossover complexes may change their spin between a low-spin (LS) and a high-spin (HS) state depending on parameters such as temperature, light and current [18, 19, 85, 120, 121]. Employing different transition-metal ions (Fe, Co, Mn, Cr and Ni)

and oxidation states [122–126] different spin states are accessible. Nonetheless, most investigations have so far dealt with Fe-based complexes. The LS to HS transition in Co complexes involves the transfer of a single electron from a t_{2g} to an e_g orbital, whereas two electrons are involved for Fe^{II} compounds. The corresponding change in the coordination bond lengths and molecular volume as well as the change in entropy upon spin crossover (SCO) are consequently smaller than for Fe complexes [125]. As a result, the thermal spin transition of Co SCO compounds is often more gradual because a smaller volume change leads to less cooperativity and it is more sensitive to the environment as small perturbations may easily overcome the entropy-driven SCO.

Investigations of SCO molecules in direct contact with metal surfaces, so far solely involving Fe-based compounds, have shown that the SCO properties usually deviate from those of the bulk material [18–26]. One may therefore speculate that Co complexes on metal surfaces may show similar SCO behavior as Fe molecules.

Although several examples of functional Fe-based SCO complexes in direct contact with surfaces have been reported [1, 21, 26, 30, 39, 40, 43, 75–80, 127–130], the weakness of the coordination bonds has often been an issue [23, 27, 29–31]. Coordination bonding in Co complexes is expected to be even weaker owing to the larger population of the antibonding e_g orbitals. To increase the chance of success, we designed and synthesized a Co complex (Figure 4.37) inspired by one of the most robust Fe^{2+} SCO compounds [84], which is functional on Ag(111) [1]. Here we show that the Co^{2+} compound, where spin states S=1/2 and S=3/2 are expected, aggregates into tetramers on Ag(111). The complexes are reversibly switched by the injection or extraction of electrons. Memristive characteristics are found although the molecules are directly adsorbed on a metal substrate without the intervening decoupling layer previously used for other compounds [27, 38–40]. The data can be consistently understood in terms of SCO.

So far, little has been known about the mechanism leading to electron-induced excited spin-state trapping (ELIESST). The present case of $[Co(H_2B(pz)(pypz))_2]$ provides an opportunity to improve on this state of affairs. A distinct dependence of this switching yield on the current direction and spin state is observed and sets margins that a model of ELIESST has to respect. Below we outline a model that fulfills this requirement.

4.3.3 Results and Discussion

$[Co(H_2B(pz)(pypz))_2]$ is a complex with linear tridentate ligands (Figure 4.37a–c) [1, 84]. The integrity of the molecules upon sublimation has been verified with complementary X-ray photoelectron spectroscopy and infrared spectroscopy measurements (Supporting Information). Figure 4.37d displays an overview of Ag(111) with sub-monolayer coverage. The complexes aggregate into rectangular tetramers although a degree of disorder is present. A detailed image of a tetramer (Figure 4.37e) reveals separations between topographic maxima of ≈ 1 and $\approx 1.15\,\mathrm{nm}$, which are virtually identical to those observed of $[Fe(H_2B(pz)(pypz))_2]$ tetramers [1]. Even the apparent heights, which are fairly bias-independent in the range $|V| < 1\,\mathrm{V}$, are similar to the Fe case. The proposed structure of the tetramers is consequently the same as previously determined for the Fe compound (Figure 4.37f). The tetramers involve both enantiomers of $[Co(H_2B(pz)(pypz))_2]$ (Figures 4.37b and c) and are stabilized by π-π interactions.
Stable imaging of the tetramers is possible as long as $|V| \lesssim 1\,\mathrm{V}$. Beyond this range, the current jumps between two levels when the tip is placed above either of two of the molecules of each cluster. The curren-voltage characteristic (Figure 4.38a) displays two distinct evolutions marked L and H that may repeatedly be measured. Transitions between the levels occur at $|V| \gtrsim 1\,\mathrm{V}$ and appear as vertical line segments in the graph. When the voltage is reduced below the range where switching occurs, the state of the molecule is frozen and can be imaged. Figure 4.38b and c display a typical pair of images. In the pristine cluster (Figure 4.38b), all molecules are in the L state.
Decreasing the negative voltage (and the current, owing to open-feedback conditions) to -1 V on the molecule indicated by L causes a change to H. The apparent height slightly increases and the topograph displays clear intramolecular structure.

Transitions can also be induced in the molecule on the other end of the diagonal when the tip is moved above that molecule. The other two molecules, however, remain stable, even at more harsh conditions. This striking effect was previously observed from $[Fe(H_2B(pz)(pypz))_2]$ tetramers and attributed to their geometrical structure [1]. The terminal-pyrazole moieties, which display the largest geometrical change during the Fe spin transition from S=0 to S=2, are sterically blocked for two molecules while the other two pz are free to move. Similar to the case of $[Fe(H_2B(pz)(pypz))_2]$ tetramers, injecting current into the stable molecules induces switching of their closest neighbors [1].

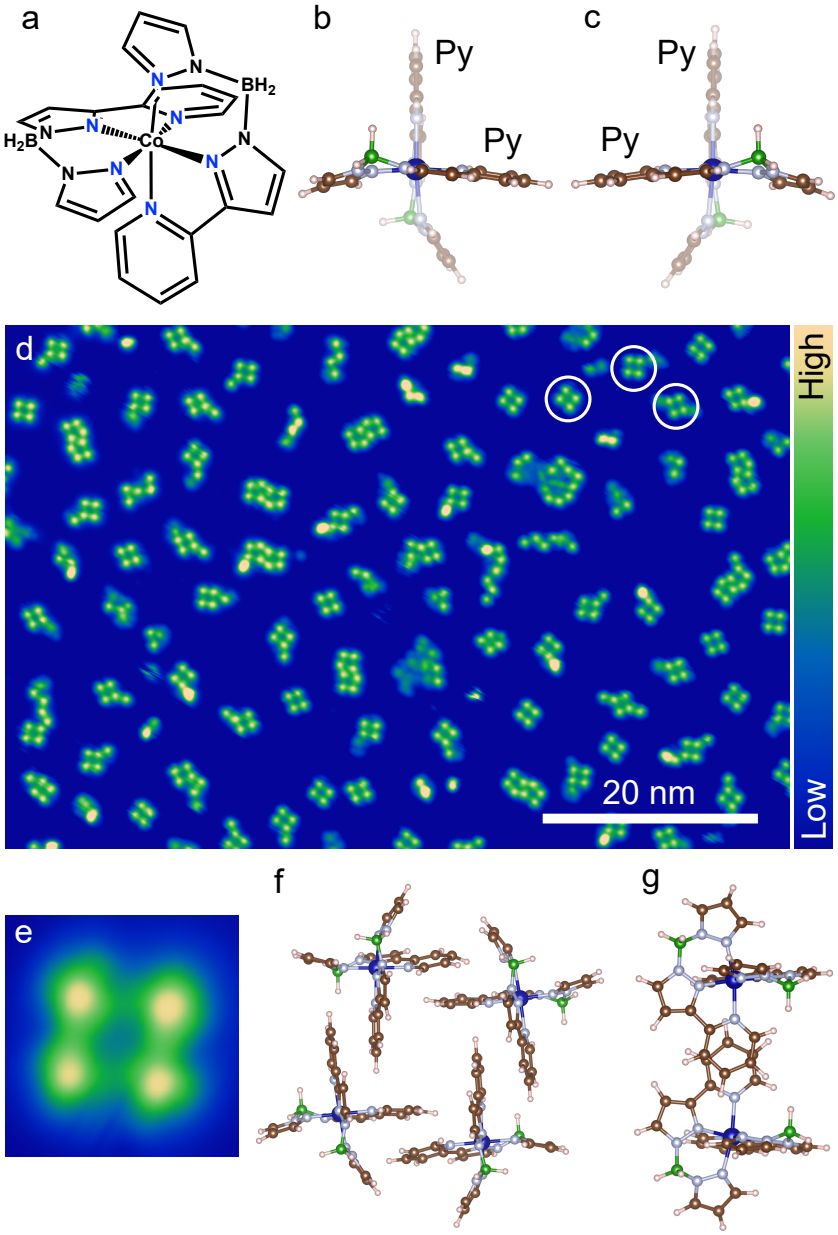

Figure 4.37: a) Structure of $[Co(H_2B(pz)(pypz))_2]$. b) and c) Suggested geometries of the two enantiomers of adsorbed complexes viewed from the vacuum side. The atoms of the lower ligand are semitransparent. Blue: Co, gray: N, brown: C, rose: H, green: B. d) Constant-current topograph (sample voltage -0.5 V, current 10 pA, $72\times48\,nm^2$). The main structural motifs are tetramers although some smaller structures and touching tetramers are observed, too. Examples of the three observed cluster orientations are indicated by circles. The false colors cover a height range of 300 pm. e) Detailed topograph of a rectangular tetramer (3.15 nm wide). Each complex gives rise to a featureless protrusion. f) Model of the tetramer shown in (e). Two identical enantiomers are arranged on each of the diagonals of the rectangle. g) View from the right side of the model in (f). The substrate (not shown) would be on the right. Only two complexes are included for clarity.

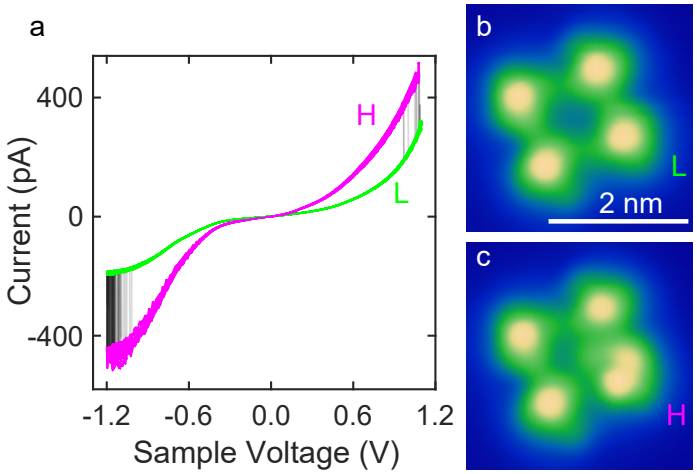

Figure 4.38: a) Current-voltage data recorded from a molecule in a tetramer. 16 sweeps of the sample voltage between -1.2 to 1.1 V and back are shown. Abrupt transitions between two states denoted L and H are observed at $|V| > 1\,\mathrm{V}$, and lead to hysteresis. b) Image of a tetramer in its pristine state. c) Image recorded after current injection ($V = -1\,\mathrm{V}$, $I = -18\,\mathrm{pA}$, duration 1 s) to the molecule marked with an L in (b). In its new state H, the molecule displays intramolecular contrast. Images recorded at -0.5 V and 10 pA.

Figure 4.39a and d present time series of the current for negative and positive sample voltages. The data were recorded after placing the tip above a switchable molecule. Clear two-level fluctuations are observed. At both polarities, the magnitude of the current predominantly is low and short excursions to high values occur over sub-second intervals.
From these and similar data, we determined transition rates as functions of the sample voltage. The rates are proportional to the current (Supporting Information, Figure 4.42) suggesting that the transitions are caused by one-electron processes and motivating the definition of a switching yield as the probability of an electron to induce a transition.

Figures 4.39b and c display yield data. At both bias polarities, we observe non-zero yields when $|V|$ exceeds 0.9 V. The corresponding electron energies are much larger than vibrational energies of the metal-organic compounds. In particular, the N-Co-N stretch modes relevant for the spin crossover transition are calculated to lie below 150 meV. It does therefore not appear likely that the transitions are caused by vibrational excitation alone.

We suggest that the observed current-induced transitions are spin transitions between the S=1/2 and S=3/2 state of the Co ion. Several indications render this interpretation most likely. First, we prepared the closed-shell complex $[Zn(H_2B(pz)(pypz))_2]$ on the same Ag(111) substrate and found tetramers which are almost indistinguishable

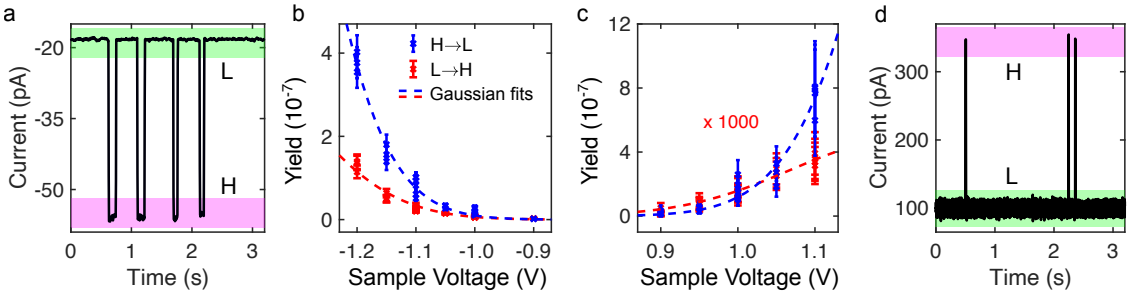

Figure 4.39: a) Time series of the tunneling current through a switchable molecule in a tetramer at negative sample bias $V = -1\,\mathrm{V}$ with open feedback loop. From its initial level denoted L the current approximately doubles to level H. Changes occur abruptly with a rate of $\approx 1/\mathrm{s}$. b) Switching yield, i.e. the number of switching events per tunneling electron, at negative voltages for transitions from H to L (blue) and vice versa (red). Dashed lines indicate Gaussian fits to the data. The yields were determined from measurements with durations between 20 and 180 s and 42 to 177 switching events (procedure outlined in the Supporting Information to ref. [1]). The error margins indicate one standard deviation assuming Poisson statistics. c) Yields at positive sample voltage. d) Time series at $V = 1\,\mathrm{V}$. The molecule is predominantly in its L state with short intermissions of H. The time series have been acquired for different tip-sample distances to obtain rates that can be conveniently measured.

from the Co compound [1]. Despite this similarity, however, the Zn complex does not exhibit the transitions observed in the Co case. This directly indicates the relevance of the partly filled *d*-shell of Co. Second, the similarities with the SCO compound $[Fe(H_2B(pz)(pypz))_2]$ are striking. Tetramers of both compounds exhibit transitions only in two molecules that are located opposite to each other on a diagonal. This effect can be understood from the structure of the tetramers in combination with the geometrical change that accompanies the spin transition [1]. The angle between the terminal pyrazole subunit and the pypz plane of the $H_2B(pz)(pypz)$ ligand it belongs to is significantly larger in the high spin state of both Fe and Co. The required free space is not available for two of the constituents of the tetramers, which prevents them from switching.

Finally, the difference of the topographic images of the two states is remarkable. While the pristine L state is imaged as a fairly featureless protrusion, images of the H state exhibit a nodal line that approximately points to the center of the tetramer. As discussed below, this feature is consistent with differences between the electronic structures of the LS and HS states. Unfortunately, a detailed and reliable image calculation of the clusters is not within reach. We therefore considered the orbitals obtained from our gasphase DFT calculations. In contrast to the Fe-based compounds [1, 38], where the spin transition is accompanied by a substantial change of the gap between the highest occupied and the lowest unoccupied molecular orbitals

(HOMO, LUMO), the orbital energies of $[Co(H_2B(pz)(pypz))_2]$ change less and do not directly lead to an image interpretation. However, an inspection of the spin-state dependence of the frontier orbitals suggest the following scenario.

Several of the orbitals exhibit significant density above the upper half of the molecule, in particular above the central pyrazole moiety, and thus presumably contribute to the tunneling current. However, upon the spin transition, one particular orbital, the LUMO, shows a drastic change that matches the image change. For illustration, we use a molecule from the lower left corner of a tetramer in its low- and high-spin states (Figure 4.40a and b). Our calculations predict essentially identical lowest unoccupied orbitals for α and β spins in the low-spin state (Figure 4.40c and e). The HS, α channel (Figure 4.40d) is also very similar, except for some geometrical distortion. However, the lowest unoccupied orbital of β spin in the HS state -the LUMO- looks strikingly different and exhibits a high density at the terminaly pyrazole moiety, where the other unoccupied orbitals have little weight (Figure 4.40f). This orbital has a nodal plane along the pyrazole that approximately matches the orientation of the nodal line in the experimental image. A side view of the orbital (not shown) reveals that this part of the LUMO is located particularly high above the substrate. Moreover, it is much closer to the Fermi level than any other unoccupied orbital and it extends throughout the molecule. Both factors make it a likely candidate for high conductance. Finally, the composite image comprising a scaled model of the tetramer and its STM image (Figure 4.40g) reveals that the lateral position of this key orbital and the image contrast are fairly consistent.

Unfortunately, the spectroscopic data do not exhibit the fingerprints of spin excitations or a Kondo effect, which could help to more directly identify the spin states involved. Acquisition of spectroscopy data to identify orbitals was unsuccessful as well because of the high switching rates and diffusion occurring at larger voltages, even with small currents in the pA range. We therefore rely on the image contrast and consequently favor S=1/2 as being the pristine states of the complex on Ag(111). While $[Co(H_2B(pz)(pypz))_2]$ has a S=3/2 ground state in bulk material [84], several studies have shown that the interaction with a metal substrate and possibly with neighbors can -even in the case of Fe compounds- lead to, e.g., the coexistence of both states [21, 23, 39, 73, 77, 79, 131]. Moreover, cobalt complexes with similar structural and electronic properties have been found to exhibit or lack thermal SCO in the bulk, indicating the importance of intermolecular interactions [132–134].

The SCO properties are not expected to significantly vary with the temperature. First, no thermal spin transition is observed in a 3 ML-thick film of the Co complex on Ag(111) as revealed by x-ray photoemission data acquired at 100 and 300 K

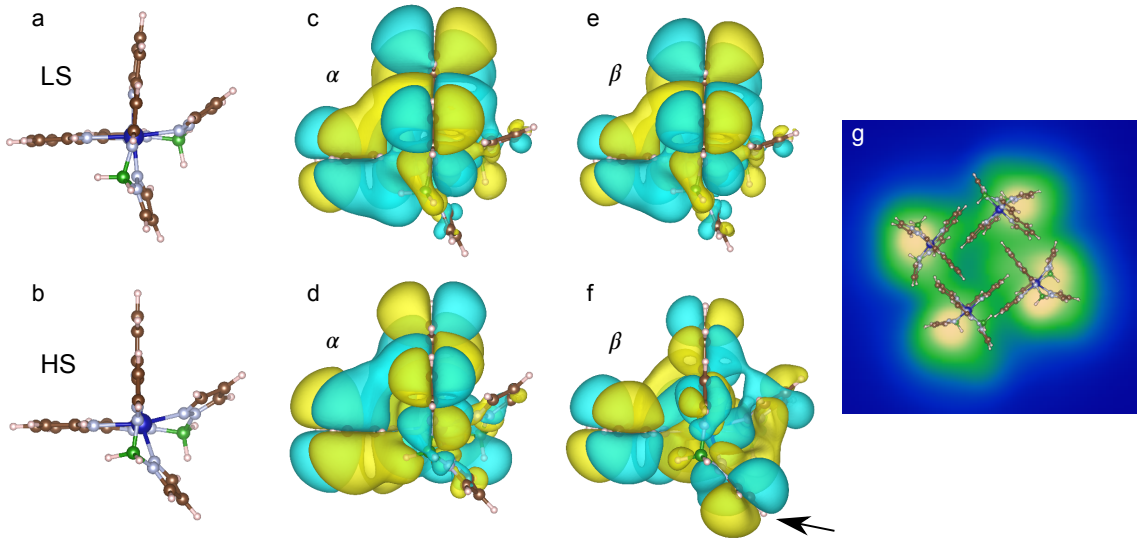

Figure 4.40: a),b) Optimized models of the LS and HS states of a gas-phase $[Co(H_2B(pz)(pypz))_2]$ molecule. Calculated spin α and spin β lowest unoccupied molecular orbitals for c),e) the LS, S=1/2 state, and d),f) HS, S=3/2 state. An arrow indicates the high density of states at the terminal pz subunit in the β channel. g) Superposition of a model cluster on the STM image of a tetramer. Only the molecule in the lower righthand corner is in the S=3/2 state.

(Supporting Information). Second, thermal energy is negligible relative to that of the tunneling electrons inducing switching (on the order of an electronvolt). Higher temperatures would most probably increase the mobility of the molecules on the surfaces and significantly complicate STM measurements.

Next, we discuss the yield data of Figure 4.39. Intriguingly, the yield of the L to H transition at positive sample bias is three orders of magnitude lower than the other measured yields, which in turn are fairly similar to each other. Below, we discuss a tentative model to describe ELIESST by considering electron/hole injection into the d-orbitals of the Co^{II} complex and a ligand-type, L^*. This model predicts a negligible yield of the L to H transition at positive sample voltage, in agreement with the experimental results.

The symmetry of the ligand field around the Co atom is not perfectly octahedral but rather exhibits a tetragonal distortion, which lifts the degeneracy of the t_{2g} and e_g orbitals. In the HS state, both d_{z^2} and $d_{x^2-y^2}$ orbitals along with the three t_{2g} orbitals at lower energy are occupied with α-spin electrons whereas two of the t_{2g} orbitals are occupied with β-spin electrons (Supporting Information, Figure 4.43). In the LS state, the three t_{2g} orbitals d_{xy}, d_{xz} and d_{yz} are doubly occupied and one additional α-spin electron occupies $d_{x^2-y^2}$ while the other e_g-orbital, d_{z^2}, is empty

(Figure 4.43). In fact, the situation is slightly more involved in the title complex because the molecular z-axis re-orientates in the LS state. However, as shown in the Supporting Information, this leaves the essence of the proposed model of electron-induced spin-state switching unaffected. For simplicity, we therefore neglect this change of coordinate system. The calculations indicate that the lowest unoccupied orbitals of the complex have ligand character. We refer to them as L^*.

For a positive sample voltage $V > 0$, an electron is first transferred from the tip into L^*, and the additional negative charge on the molecule is removed by transfer of an electron from one of the highest-energy occupied orbitals (i.e., a d-orbital) to the substrate. The individual molecules in the tetramer are oriented with their axes connecting the two central pyrazole moieties perpendicular to the surface, in the direction of the tip. Denoting these axes as z, electron transfer from the molecule to the substrate will predominantly be mediated by d_{z^2} and, to a lesser extent, by d_{xz} and d_{yz} orbitals whereas no or little electron transfer will proceed via orbitals in the corresponding xy-plane; i.e., $d_{x^2-y^2}$ and d_{xy}. At negative sample voltage, an electron is first transferred from an occupied d-orbital to the tip, following the same rules, and the hole on the molecule is filled by transfer of an electron from the substrate to the L^* orbital of the cationic complex (Supporting Information, Figure 4.43).

If the incoming and the outgoing electrons in the described electron-in/electron-out processes carry different spins, spin-state switching ensues. Taking the high spin (S=3/2) state of Co^{II} at $V > 0$ as an example (Figure 4.41, top), a β-spin electron is first transferred to L^*. This generates an anionic (Co^{I}) S=1 state which subsequently releases an electron to the substrate. Among the occupied d-orbitals of Co^{I}, the best coupling is provided by d_{z^2} (see above) whence the electron is removed from it with the highest probability. If it carries a β spin, an excited S=1/2 state of Co^{II} results which rapidly relaxes to the LS ground state, completing the spin state switching process.

As detailed in the Supporting Information, Figure 4.43, similar scenarios can be conceived to account for HS→LS and LS→HS switching at negative sample voltages. However, an analogous mechanism is much less probable for LS→HS transitions at $V > 0$ (Figure 4.41, lower panel). In order to induce switching to S=3/2, the spin has first to increase to S=1. This occurs through transfer of an α electron from the tip to L^* which is at lower energy than d_{z^2}. However, electronic relaxation of the resulting Co^{I} state leads to a configuration in which the additional electron occupies d_{z^2}. As this orbital efficiently couples to the substrate the electron is rapidly removed from the molecule, restoring the original spin state. In the unlikely event

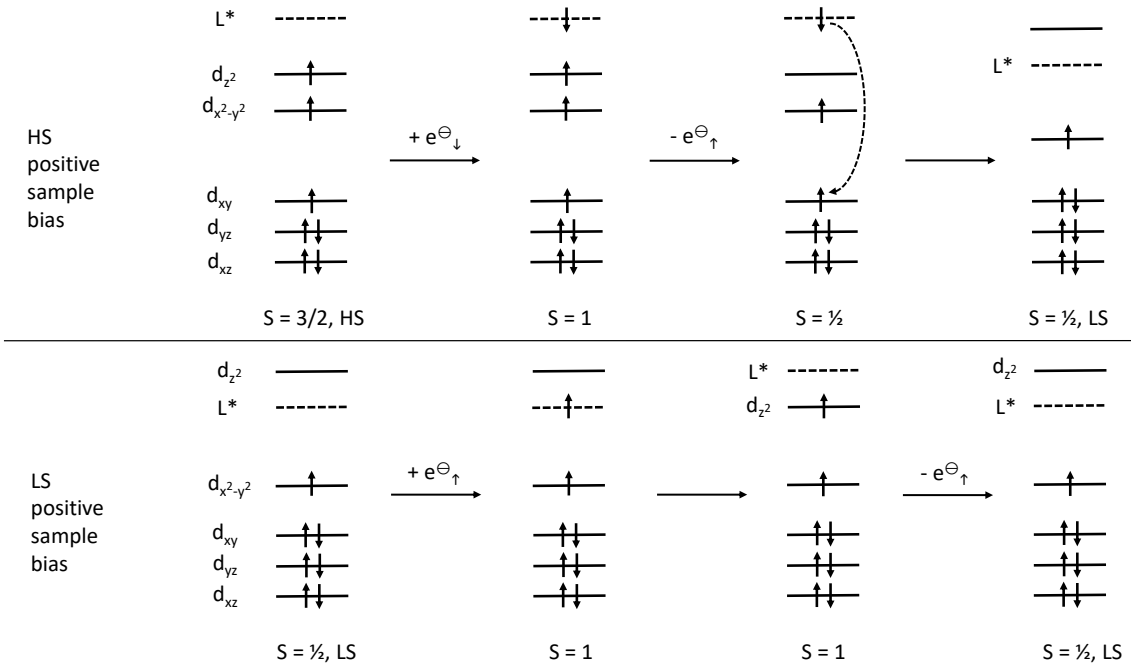

Figure 4.41: Schematic diagrams of the transitions from HS to LS (upper panel) and vice versa (lower panel) at positive sample voltage. Up and down arrows represent α- and β-spin electrons, respectively.

that an electron is removed from the d_{xz} and d_{yz} orbitals despite the d_{z^2} state being occupied, S=3/2 may be obtained. In summary, this scenario is consistent with the experimental observation of a low LS→HS switching rate at $V > 0$.

4.3.4 Conclusions

The present results illustrate that molecules assembled into nanoscale structures can exhibit unusual spin crossover phenomena. In the present case, electron induced spin state trapping (ELIESST) is observed from a tridentate Co compound that is robust enough to enable detailed measurements of switching yields and image contrast. We propose a first tentative model of ELIESST that takes into account the orbital structure of the compound and qualitatively explains yield data. The results further indicate that molecular interactions drastically affect the switching capability of individual molecules. However, no decoupling layer is required to preserve the memristive functionality of the molecules directly on a metal substrate.

4.3.5 Acknowledgements

We thank Troels Markussen for preliminary calculations and discussions. Financial support from the European Union's Horizon 2020 program, Grant No. 766726 is acknowledged. H.W. and A.H. acknowledge financially support by the Deutsche

Forschungsgemeinschaft (DFG, German Research Foundation) through the Collaborative Research Centre (CRC) 1242 (Project No. 278162697) and project WE 2623/17-1 No. 389895192. Open Access funding enabled and organized by Projekt DEAL.

4.3.6 Supporting Information

Experimental details

Synthesis The ligand ($H_2B(pz)(pypz)$) and the Co(II) complex $[Co((H_2B(pz)(pypz)))_2]$ were synthesized according to the procedure reported by Ossinger et al. [84].

Experimental Details The Ag(111) substrate was prepared by cycles of Ar^+ sputtering (1.5 keV) and annealing to 500 °C. $[Co((H_2B(pz)(pypz)))_2]$ molecules were sublimated from a heated crucible ($\approx$ 150 °C) onto the substrate at $\approx$ 30 °C. STM tips were electrochemically etched from W wire and annealing in vacuo. All measurements were carried out in ultra-high vacuum with a STM cooled to $\approx$ 4.6 K. The XPS setup consist of a regular X-ray source with Al anode source with an x-ray power of 200 W (15 kV) and a hemispherical electron analyzer (SPECS PHOIBOS 150). The x-ray source and the analyzer have a fixed angle of 90 °. Infrared (IR) spectra were recorded with a Bruker ALPHA-P ATR IR Spectrometer.

Theoretical Details Gas phase calculations were carried out with the ORCA software package [95, 96]. The crystallographic structure of $[Fe((H_2B(pz)(pypz)))_2]$ (polymorph II) was used as a starting point [1]. Geometry optimizations were performed with ORCA at the B3LYP [97–99] / def2SVP [100, 101] level with the D3BJ dispersion correction [102, 103], the RIJCOSX approximation, fine numerical integration grids (grid4 and gridX4 in ORCA nomenclature), and the CG solver. The orbitals and their energy were calculated with ORCA at the B3LYP/def2-QZVP [100, 101] level with the RIJCOSX approximation.

One-electron process

Figure 4.42 shows that the switching rate evolves linearly with the magnitude of the tunneling current. This evolution suggests that the switching mechanism involves a single tunneling electron and motivates the definition of a switching yield as the probability of an electron to induce a transition.

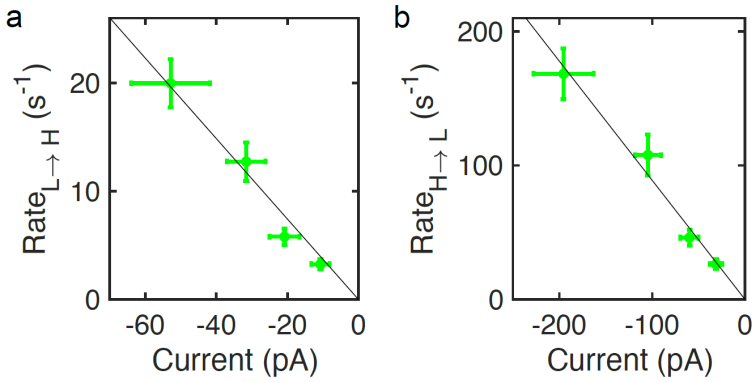

Figure 4.42: Switching rates **a** from L to H and **b** H to L as a function of the tunneling current at a sample voltage of -1.1 V (green crosses). The solid lines are linear fits of the data with slopes of **a** -0.37 and **b** -0.89 $\mathrm{pA^{-1}s^{-1}}$. The error margins indicate three standard deviations assuming Poisson statistics.

Switching at $V < 0$

Figure 4.43 displays proposed mechanisms for the transitions between LS and HS at negative sample voltages. Starting from the high-spin, S=3/2 state (upper panel), an α-spin electron is first removed from the occupied orbital providing the best coupling to the tip; i.e., d_{z^2}. Subsequently a β-spin electron is added to L*. As a result, the spin of the complex is changed to S=1/2. Spin-allowed relaxation to the LS state completes the spin switching process. In the low-spin, S=1/2 state at negative sample bias, the d_{z^2} orbital is not occupied and the occupied $d_{x^2-y^2}$ state is ineffective because it is oriented parallel to the surface. Therefore, the electron is most likely withdrawn from the d_{xz} or d_{yz} orbitals, generating a S=1 state. Next, an α-spin electron is transferred to L*. This generates an excited S=3/2 configuration, which relaxes to the HS ground state by a (spin-allowed) transition.

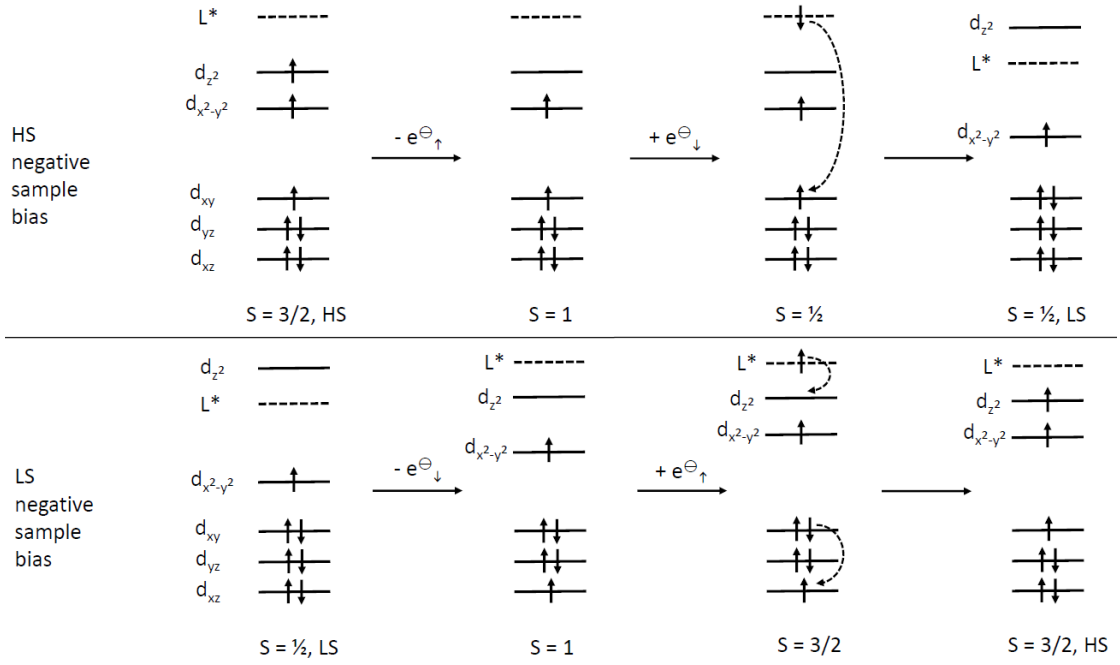

Figure 4.43: Schematic diagrams of switching processes at negative sample voltage from (upper panel) HS to LS and (lower panel) vice versa. Up and down arrows represent α- and β-spin electrons, respectively.

Chemical analysis of sublimated Co complexes

To further ascertain the intactness of the molecules after sublimation, we performed complementary x-ray photoelectron spectroscopy of ≈ 1...3 monolayers (MLs) of $[Co((H_2B(pz)(pypz)))_2]$ sublimated onto Ag(111) prepared in situ. Overview spectra acquired at room temperature are shown in Figure 4.44 for three different thicknesses. The peaks are assigned to their respective core-levels. The relative intensities of the Co $2p_{1/2,3/2}$, N 1s and C 1s peaks are comparable for the three spectra, indicating similar chemical compositions for 1, 2 and 3 MLs.

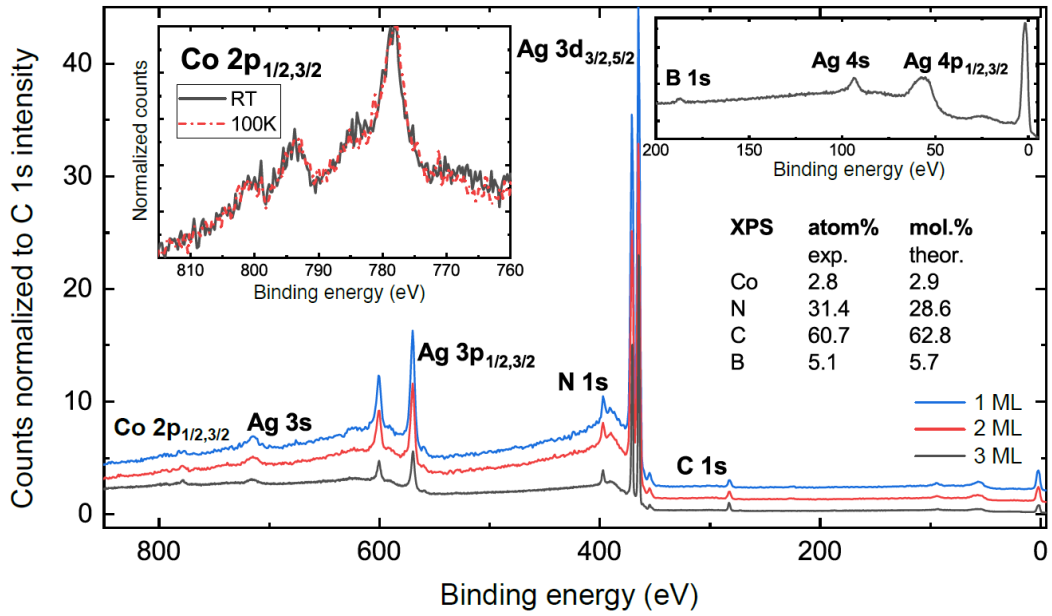

Figure 4.44: XPS spectra of ≈ 1 (blue), 2 (red) and 3 MLs (gray) $[Co((H_2B(pz)(pypz)))_2]$ on Ag(111) measured using an Al K_α x-ray source. Two spectra at Co $2p_{1/2,3/2}$ edges of ≈ 3 ML $[Co((H_2B(pz)(pypz)))_2]$ on Ag(111) taken at room temperature (gray) and 100 K (red) are shown in the upper-left inset. The upper-right inset is a zoom over binding energies ranging from 200 to -5 eV (3 MLs coverage). All spectra are normalized to the intensity of the C 1s peak. Spectra of 1 and 2 MLs were acquired with 1 eV energy steps and a pass energy of 80 eV, while the spectrum of 3 ML was measured with energy steps of 0.25 eV and a pass energy of 44 eV. The thicknesses have been estimated with a quartz microbalance.

The atomic fractions of the 3 MLs sample are evaluated with CasaXPS [135] by comparing the weighted spectral areas after a Tougaard-type background subtraction and are compared to the expected atomic fractions of the molecule. The experimentally determined fractions (Figure 4.44), with associated uncertainties of a few percents, are very close to the ones expected for the Co complex suggesting that the molecules withstand adsorption on the Ag(111) surface.

XPS measurements performed at 100 K (3 ML thick sample) shows no evolution of the Co $2p_{1/2,3/2}$ edges (upper-left inset to Figure 4.44), suggesting the absence of thermal spin transition. Temperature is therefore expected to have no significant direct influence on the spin-crossover properties of the Co tetramers in direct contact with Ag(111).

Infrared spectroscopy

Figure 4.45 shows IR spectra recorded on $[Co((H_2B(pz)(pypz)))_2]$ powder and on a film upon sublimation. Both systems exhibit the same vibration modes. The stability of the Co complex during sublimation is confirmed by the combination of XPS and IR data. The former indicate that the elements are present in the correct stoichiometry after sublimation while the latter show that the bonds between the constituents are preserved.

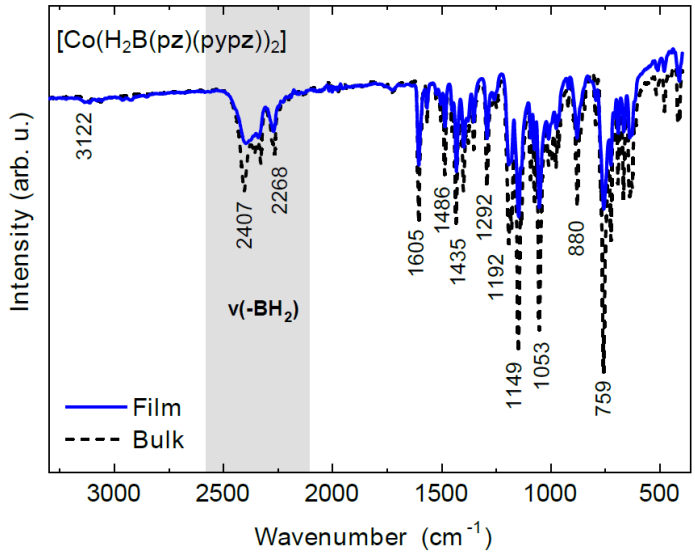

Figure 4.45: IR spectra of $[Co((H_2B(pz)(pypz)))_2]$ powder (black) and thick film (blue). For the thick film measurements, the Co complex was sublimated under a pressure of 1×10^{-2} mbar at a temperature of 180 °C. The film was then scratched off the substrate and measured similarly to the powder.

LS-HS Transitions: Calculated orbital scheme

In the main text and in the previous paragraph, the current induced transitions between the LS and HS states discussed using a generic model of the *d*-orbitals. Figures 4.46 and 4.47 present more realistic, calculated orbitals of $[Co((H_2B(pz)(pypz)))_2]$. The molecular z-axes in the LS and HS states turn out to be different.

In the HS state, the molecular z-axis connects the central pyrazole moieties. This axis is also perpendicular to the substrate surface according to the model geometry of the tetramers. Here, both d_{z^2} and $d_{x^2-y^2}$ orbitals along with the three t_{2g} orbitals at lower energy are occupied with α-spin electrons while two of the t_{2g} orbitals are occupied with β-spin electrons.

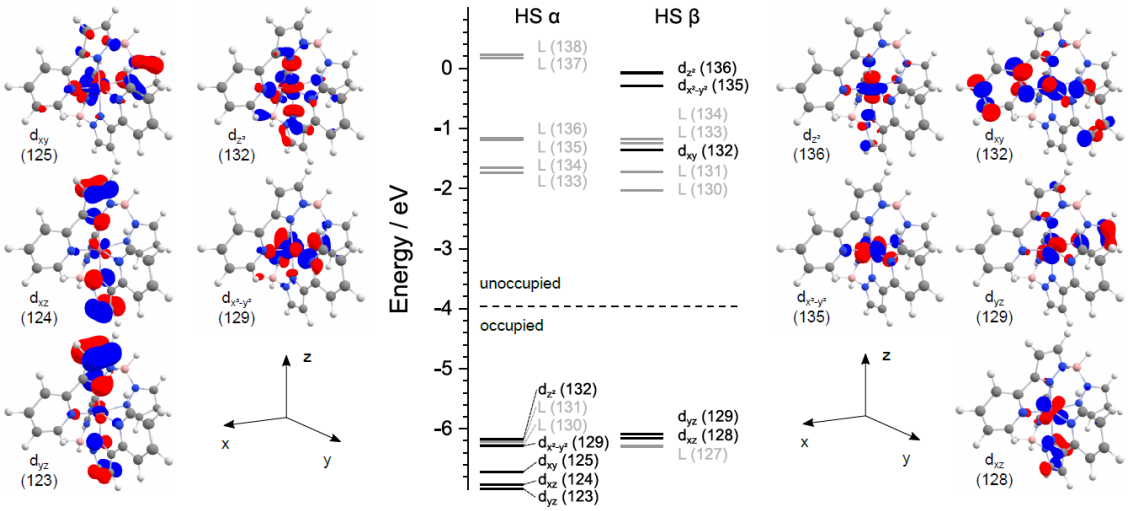

Figure 4.46: Calculated spin-resolved orbitals of $[Co((H_2B(pz)(pypz)))_2]$ in the HS state. L denotes ligand orbitals displayed in gray. Co d-orbitals are shown in black.

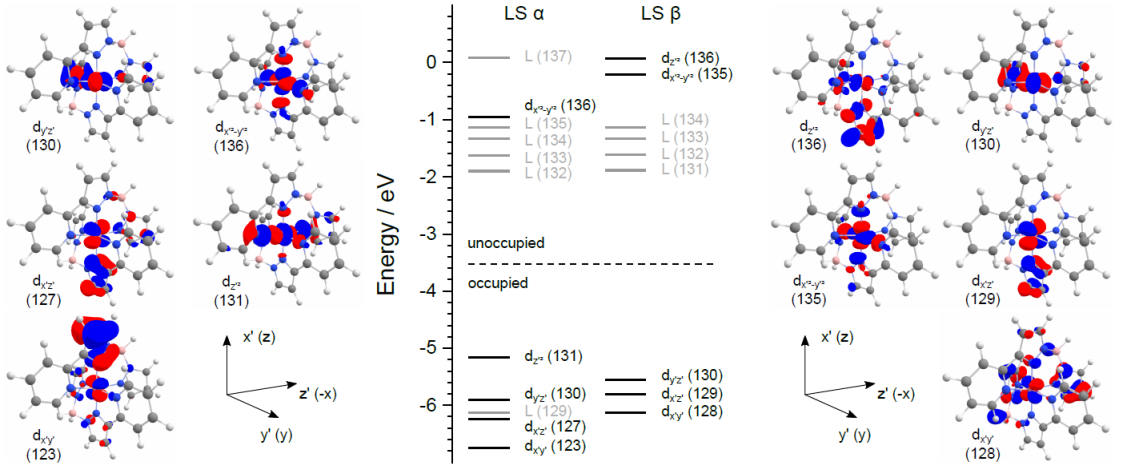

Figure 4.47: Calculated spin-resolved orbitals of $[Co((H_2B(pz)(pypz)))_2]$ in the LS state. L denotes ligand orbitals displayed in gray. Co d-orbitals are shown in black.

In the LS state, the molecular z-axis is directed along one of the pyridine-terminal pyrazole axes (Figure 4.47). The three t_{2g} orbitals $d_{x'y'}$, $d_{x'z'}$ and $d_{y'z'}$ are occupied by α- and β-spin electrons while the seventh electron occupies $d_{z'^2}$.

Irrespective of the re-orientation of the z-axis, the basic features of the model proposed in the main text and in Figure 4.43 remain valid. Specifically, the highest-energy, unoccupied $d_{x'^2-y'^2}$ orbital of the LS has a lobe perpendicular to the surface and thus effectively mediates electron transfer between the tip, the complex molecule and the surface, similar to the role of the d_{z^2} orbital of the HS state. Likewise, the $d_{z'^2}$ orbital of the LS state has lobes essentially parallel to the surface and thus poorly mediates electron transfer, in analogy to the $d_{x^2-y^2}$ orbital of the HS state. Regarding the t_{2g} orbitals of the LS state, the correspondence to the orbitals of the HS state is obtained using the relations $d_{xy} \rightarrow d_{y'z'}$, $d_{xz} \rightarrow d_{x'z'}$ and $d_{yz} \rightarrow d_{x'y'}$. While the first of these orbitals is parallel to the surface and thus ineffective for the electron transport, the latter two can mediate electron transfer albeit less effectively than d_{z^2} and $d_{x'^2-y'^2}$ in the HS and LS states, respectively.

5 Spin-Crossover and Fragmentation of Fe(neoim)$_2$ on Silver and Gold

Chapter 5 is based on a publication in The Journal of Physical Chemistry Letters from 2023. Reprinted with permission from:
S. Johannsen et al., "Spin-Crossover and Fragmentation of Fe(neoim)$_2$ on Silver and Gold", J. Phys. Chem. Lett. **14**, 7814–7823 (2023)
DOI: 10.1021/acs.jpclett.3c01551.

Author Contributions

Sven Johannsen performed the STM measurements. Sven Johannsen, Manuel Gruber and Richard Berndt analyzed and interpreted the data. Maksym Seredyuk and José Antonio Real provided the SCO complexes. Troels Markussen and Cyrille Barreteau carried out the DFT calculations. Sven Johannsen created all figures in the manuscript and supplementary information, except 5.1, 5.6–5.15, 5.18 and 5.19. Richard Berndt and Manuel Gruber wrote the manuscript with input from all authors. Richard Berndt supervised the project. All authors discussed the results.

5.1 Abstract

The neutral spin crossover complex Fe(neoim)$_2$, neoim being the deprotonated form of the ionogenic ligand 2-(1H-imidazol-2-yl)-9-methyl-1,10-phenanthroline (neoimH), is investigated on the (111) surfaces of Au and Ag using scanning tunneling microscopy and density functional theory calculations. The complex sublimates and adsorbs intact on Ag(111), where it exhibits an electron-induced spin crossover. However, it fragments on Au. According to density functional theory calculations, the adsorbed complex is drastically distorted by the interactions with the substrates, in particular by van der Waals forces. Dispersion interaction is also decisive for the relative stabilities of the low- and high-spin states of the adsorbed complex.

The unexpected instability of the complex on the gold substrate is attributed to enhanced covalent bonding of the fragments to the substrate.

5.2 Results and Discussion

Spin crossover (SCO) molecules are transition metal complexes with $3d^{4-7}$ electronic configurations that exhibit labile spin states, which are controlled by the geometry and binding of the ligand shell. These complexes may find various applications because switching between two spin states is induced by various external stimuli including light, temperature, pressure, and current. Deposition on a substrate can modify the SCO properties. To explore the substrate influence several compounds have been deposited as ultrathin films [18, 21, 24, 30, 70–81, 121, 128, 136, 137]. Although fragmentation often is an issue [21, 23, 27–31, 82, 138], electron-induced excited spin state trapping (ELIESST) and light-induced excited spin state trapping (LIESST) have been reported from transport measurements [9–11, 13, 25, 32–37, 139–142] and scanning tunneling microscopy (STM) [2, 20–22, 25, 38–43, 136].

The importance of dispersion interaction in the chemistry of various compounds is well established [143–147]. It is further enhanced when molecules are adsorbed to metal substrates, where, in simple models assuming pairwise forces, the interaction energy decays only with the first power of the distance [148]. It can lead to significant conformational changes [149] and also affect the stability of adsorbed complexes [150]. The ligand shell makes SCO complexes fairly bulky three-dimensional structures. As a result, dispersion interaction is expected to play a significant role in understanding the structure of complexes adsorbed to metal substrates.

Here we investigate the new pseudo-octahedral complex Fe(neoim)$_2$ (Figure 5.1). It comprises a new tridentate chelating anionic ligand (neoim)$^-$, which affords electroneutrality. The triple coordination bond per ligand makes the molecule more robust for sublimation.
We find that the complex remains intact and functional on the Ag(111) surface. In contrast to SCO complexes that involve (H_2B(pyrazole)(pyridylpyrazole))$_2$ as tridentate ligands [1–3], the present compound does not aggregate into oligomers and experiments can be carried out on isolated molecules. Spin-crossover may be induced via current injection from the tip of a scanning tunneling microscope (STM). Control experiments with the homologous Ni(neoim)$_2$ compound, which has a very similar pseudo-octahedral geometry but $3d^8$ electron configuration, showed no SCO. Astonishingly, however, the Fe(neoim)$_2$ fragments on Au(111), a substrate that is frequently used for its inertness. The experimental results are analyzed on the

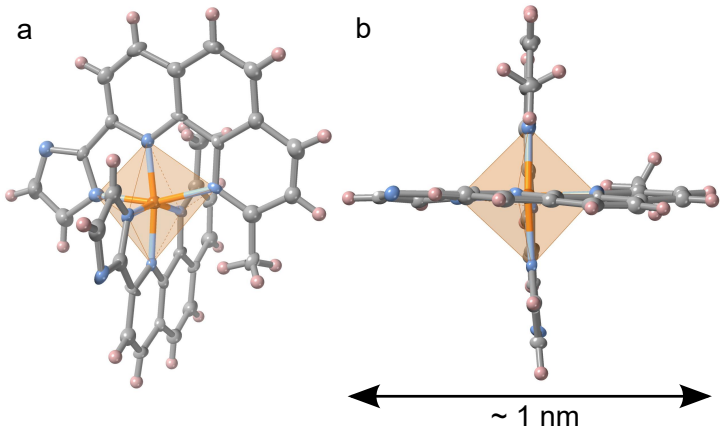

Figure 5.1: Schemes of the $Fe(neoim)_2$ compound in its low-spin state. Key: orange, Fe; blue, N; gray, C; pink, H. Parts a and b show different perspectives. Yet another perspective of the molecules, albeit somewhat deformed, because of binding to a Ag substrate, is shown in Figure 5.6.

basis of extensive density functional theory (DFT) calculations. The calculations reveal significant distortion of the adsorbed complexes compared with their gas phase structures and also shed light on the unexpected catalytic activity of the gold substrate.

Upon deposition of submonolayer amounts of $Fe(neoim)_2$ on Ag(111) (≈ 0.17 molecules per $100\,nm^2$), we predominantly observed isolated molecules along with a few dimers. Figure 5.2a displays a constant-current topograph of an $Fe(neoim)_2$ complex along with a profile of the apparent height in Figure 5.2c. We find two identical main protrusions (height $\approx 250\,pm$), each with a shallow extension in the direction perpendicular to the axis connecting the protrusions. The pattern suggests that the complex adsorbs in a symmetric fashion that corresponds to the scheme shown in Figure 5.1b with identical subunits of the neoim ligands pointing toward vacuum. Since the imidazole subunits of the ligands likely bind most strongly with the substrate atoms, we tentatively attribute the topographic maxima to the 2-methylpyridine subunits. Their lateral distance nicely matches the distance between the two molecular maxima in topographs. From images of large surface areas, we found that the axis connecting the molecular maxima deviates by $\approx +10$ or -10° from the closely packed directions of the (111) surface.

The image contrast of the pristine molecules hardly varies in a range of sample voltages ($1.4\,V > V > -1.2\,V$) so long as small currents ($I \approx 10\,pA$) are used. At more elevated voltages, instabilities occur. At $V > 1.4\,V$, the molecules exhibit random switching between their pristine and a new state as revealed by subsequent imaging at nonperturbing voltages. Lateral hopping or rotation may also occur.

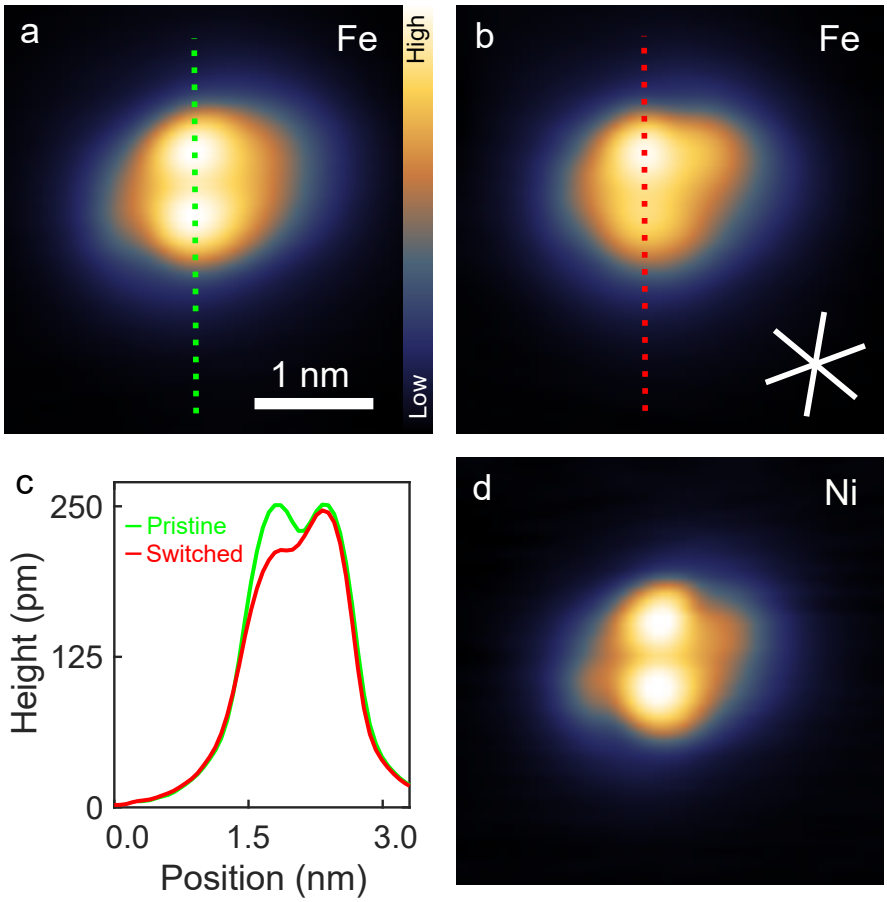

Figure 5.2: Constant-current STM data from Fe(neoim)$_2$ and Ni(neoim)$_2$ on Ag(111). (a) Topograph of Fe(neoim)$_2$ in its pristine, as-deposited state. (b) Topograph of the same molecule after a switching process. Bars indicate densely packed substrate directions. The transition was induced by placing the STM tip above the center of the molecule at 300 mV and 10 pA, opening the feedback loop, and increasing V to 2 V for 200 ms. The topographs of Fe(neoim)$_2$ were obtained with $V = 0.3$ V and $I = 10$ pA. (c) Profiles of the above topographs along the dashed lines. (d) Topograph of Ni(neoim)$_2$. Image size: $(3.5\,\mathrm{nm})^2$. $V = -0.2$ V, and $I = 10$ pA.

At $V <$ -1.2 V, the molecules may similarly switch to the new state or laterally move away from the tip over distances exceeding 1 nm.

The new state (Figure 5.2b and height profile in part c) exhibits a lower symmetry. In particular, one of the protrusions is ≈ 40 pm higher and exhibits a fairly prominent lateral extension. It may be stably imaged at low voltages. Some lateral motion is induced beyond voltage thresholds of ≈ -0.6 and ≈ 0.3 V. Switching back to the original, more symmetric state is observed for slightly higher voltages (thresholds ≈ -0.9 and ≈ 0.8 V). Telegraph noise of the tunneling current may be observed because the molecule under the tip may switch between the pristine symmetric and the induced asymmetric state. It may also carry out reversible lateral hops. On a single occasion, we were able to record a conductance spectrum ($\mathrm{d}I/\mathrm{d}V$) of a molecule in the pristine state over a fairly wide voltage range without inducing instability. It indicates the presence of an unoccupied state around 0.8 V which may be involved in the switching process.

$Fe(neoim)_2$ is a spin-crossover complex, and one may speculate that the different STM images reflect different spin states. To experimentally test this hypothesis, we synthesized and deposited $Ni(neoim)_2$ on Ag(111). The low-spin to high-spin transition of Fe corresponds to the transfer of two electrons from the t_{2g} states to e_g states (Figure 5.3). In Ni the t_{2g} orbitals are fully occupied, and this transition is no longer possible. Calculations for the Ni compound confirm this scenario. STM images of $Ni(neoim)_2$ (Figure 5.2d) are almost identical with those of pristine $Fe(neoim)_2$. However, attempts to induce the switching observed from $Fe(neoim)_2$ were not successful, although an extended range of voltages and currents was explored. These observations strongly indicate that the observed switching of the Fe complex is related to spin crossover.

The free complex is chiral, with the enantiomers differing by a 180° rotation of one of the ligands. Close inspection of Figures 5.4a and 5.4b shows that this chirality is visible on the surface.

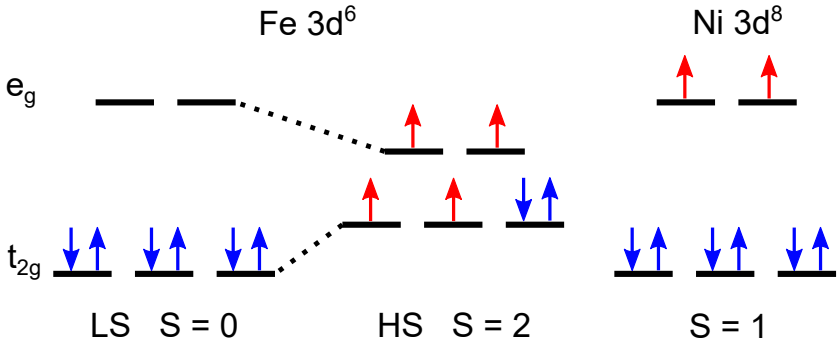

Figure 5.3: *d*-Electron configurations of the Fe and Ni.

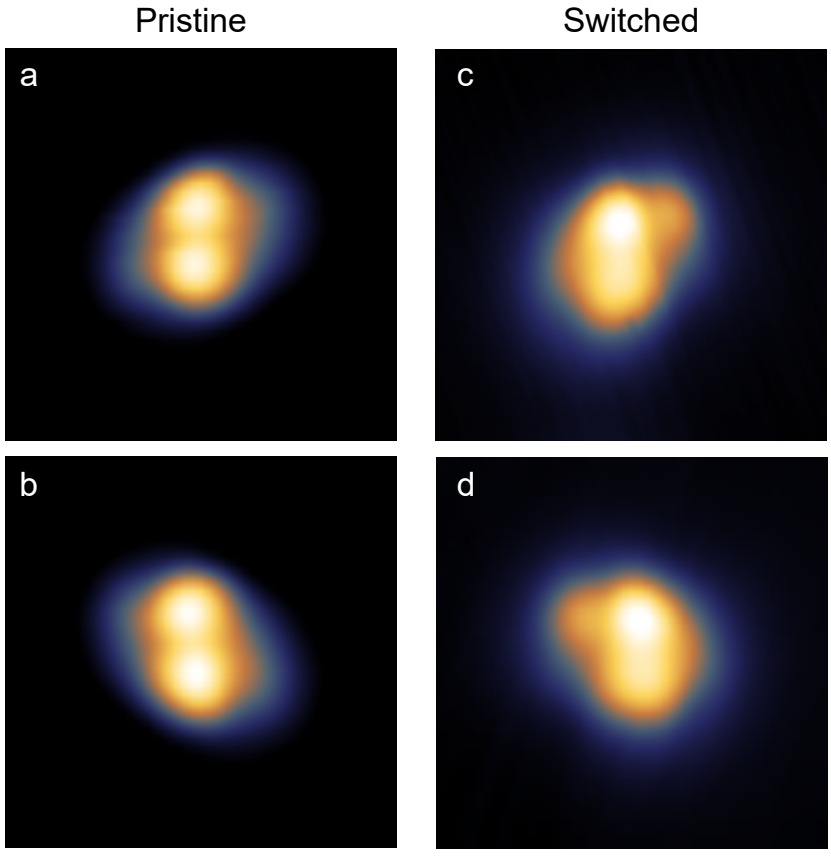

Figure 5.4: Constant-current topographs of Fe(neoim)$_2$ enantiomers on Ag(111). (a, b) Enantiomers in their pristine states. (c, d) Corresponding switched states. Image size: $(3.6\,\mathrm{nm})^2$, $I = 10\,\mathrm{pA}$. $V = -0.4\,\mathrm{V}$ (a), and $-0.5\,\mathrm{V}$ (b–d).

The shallow extensions oriented perpendicular to the main molecular axis are arranged in two mirror-symmetric fashions. Models of the enantiomers are shown in the Supporting Information. The chirality of the molecules is also observed in images of the switched state (Figures 5.4c and 5.4d).

Several studies pointed out that SCO compounds, intact in the gas phase or adsorbed on semiconducting or semimetallic surfaces, fragment upon adsorption on Au(111) [19, 23, 27, 29, 30]. This trend was rationalized by higher van der Waals forces on metallic surfaces compared to that on semiconducting and semimetallic surfaces [23]. How adapted is Au(111) as a metal substrate for SCO complexes? Is it the most inert surface of the coinage metals? Surprisingly, deposition on the Au surface leads to fragmentation of the $Fe(neoim)_2$ complex. The overview image in Figure 5.5a shows that a range of different features are observed in contrast to the case of Ag(111), where almost exclusively monomers and a few dimers were found. More details of the fragments are listed in Figure 5.5b. Overlaid scaled models of neoim ligands show some similarity with the fragments although additional features, possibly due to Fe or Au atoms, are resolved.

The fact that the noble metal Au is a more efficient catalyst for cracking $Fe(neoim)_2$ than Ag(111) appears astonishing. However, it is known that relativistic effects significantly affect the chemistry of Au atoms. For example, covalent bond lengths are reduced compared to Ag, and an oxidation state III may be formed [151, 152]. Further discussion in light of DFT calculations may be found below.

We performed DFT calculations to model the interaction of $Fe(neoim)_2$ with Ag(111) and Au(111) substrates. For comparison, additional calculations were carried out for $Ni(neoim)_2$. Computational details are presented in the method section. In view of the complexity of the system, we nevertheless present some technical aspects related to the choice of functional here. The electronic and geometric structures of the molecule in contact with the silver substrate will be detailed next. Finally, the fragmentation of the molecule on the gold substrate is analyzed in some detail.

Although quantum chemistry wave function-based methods have been used for the study of transition metal complexes, in the case of spin crossover molecules in particular when deposited on a surface, DFT is the only possible choice due to its superior computational efficiency. However, standard DFT functionals (LDA, GGA) fail to describe the energetics of SCO molecules and one faces the "functional dilemma" [153].

In particular, the delicate energy balance between LS and HS states $\Delta E = E_{\mathrm{LS}} - E_{\mathrm{HS}}$ is poorly reproduced, with the stability of the LS state being greatly overestimated.

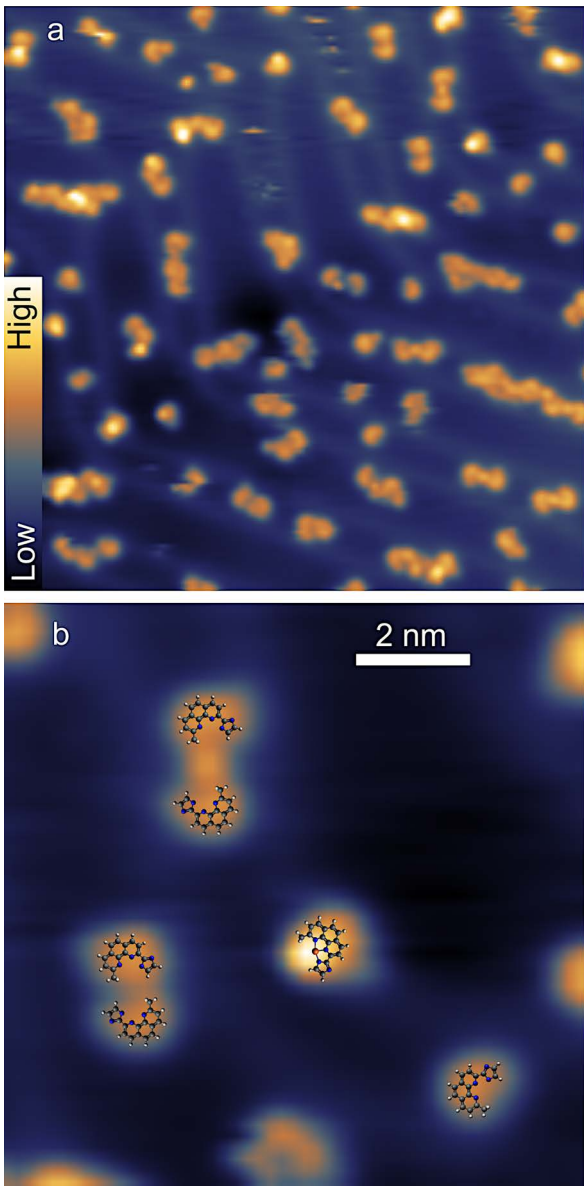

Figure 5.5: (a) Overview topograph of a 1200 nm^2 area of Au(111) after the deposition of Fe(neoim)$_2$. The color scale (inset) covers a range of 350 pm. (b) Topograph of fragments along with models of neoim ligands that approximately match some image features. Additional protrusions may be due to Fe atoms from the original molecules or Au atoms from the substrate that are binding to the ligands. $V = -0.5$ V, $I = 10$ pA.

Two approaches are often used to alleviate this problem, namely (i) the DFT+U scheme, where an Hubbard-like Hamiltonian treated in mean field is added, or (ii) the hybrid functional approach, where a portion of exact exchange is included to the exchange correlation functional. In DFT+U, the Coulomb interaction potential U is often treated as a parameter that is adjusted to match a quantity that is poorly

reproduced by standard DFT. In the case of SCO molecules, U is adjusted to obtain a reasonable value of ΔE [73, 154]. Attempts to determine U ab initio from a linear response approach were not very conclusive. Hybrid functionals usually include a fixed fraction of exact exchange $\alpha = 0.25$, however this ratio has proven to be too large (favoring HS states) to describe the energetics of SCO correctly [153, 155]. Typical values of $\alpha = 0.15$ have been proposed in the literature [155, 156]. In the case of Fe(neoim)$_2$, we verified that $\alpha = 0.15$ is a reasonable value, but α needs to be adjusted upon inclusion of van der Waals (vdW) forces. van der Waals forces are crucial to describe the interaction between the molecule and the surface, therefore it is mandatory to include them in the calculation. We used the HSE06 functional [157, 158] with $\alpha = 0.17$ and Grimme DFT-D3 dispersion correction [102] of the energy and forces including only pairwise 2-body terms. With these parameters, the energy difference ΔE between S=0 and S=2 is $\Delta E = -0.075\,\text{eV}$.

Fe(neoim)$_2$ follows the general rule of filling of the d states, with in its LS state the t_{2g} orbitals being filled while the e_g are empty (t_{2g}^6, e_g^0). However, even in the LS state, the octahedral environment of the iron center is significantly distorted, which implies that there are deviations from the perfect $t_{2g} - e_g$ picture illustrated in Figure 5.14, where the density of states projected on the Fe-d orbitals is presented. The 3-fold (2-fold) degeneracy of the t_{2g} (e_g) orbitals is strongly lifted, and there are delocalized (LUMO) ligand states 2 eV above the t_{2g} states (HOMO). In the high spin state (S=2), both t_{2g} and e_g orbitals are partially filled (t_{2g}^4, e_g^2). Consequently, the energy levels of the iron ion are rearranged, but the positions of the LUMO (ligand) states remain almost unchanged and are hardly affected by the spin polarization of the iron.

Motivated by the experimental STM observations, we have defined three plausible adsorption geometries of Fe(neoim)$_2$ on Ag(111). In the "pyri$_2$" configuration (Figure 5.6) both imidazole groups are in contact with the substrate, and the pyridine subunits point toward a vacuum. In configuration "imi-pyri" ("imi$_2$") one imidazole and one pyridine (both imidazole) subunits are oriented toward a vacuum; i.e., they may be obtained by rotations along the axis pointing out toward the reader. Structural optimization of these starting geometries was performed for the LS and HS states.

We observed that slight modifications of the starting geometry lead to different final geometries with energies that generally differ by less than ±0.03 eV.

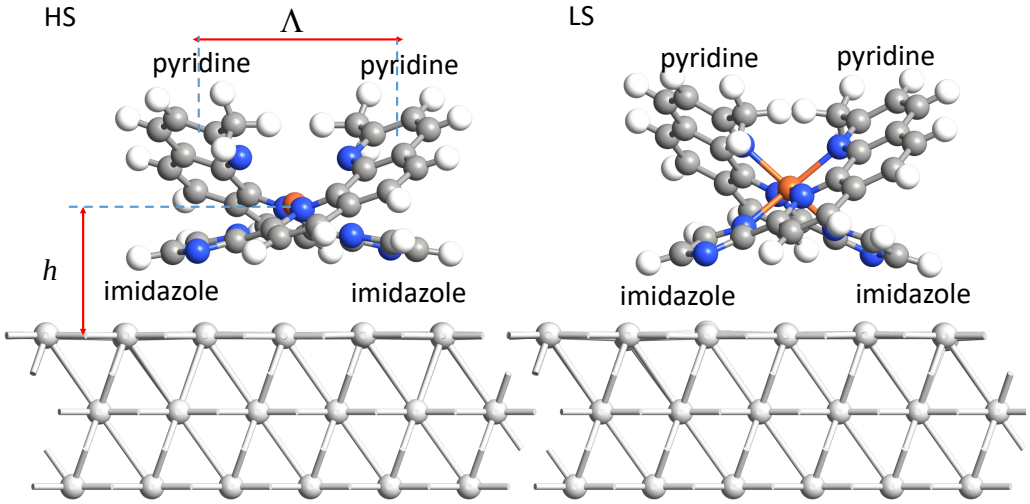

Figure 5.6: Side view of an Fe(neoim)$_2$ molecule on Ag(111) in its pyri$_2$ configuration for both HS (left) and LS (right) states as obtained from DFT optimization. A width parameter, Λ, and the height, h of the Fe center above the surface are indicated.

These various final geometries are most likely a consequence of a flat and complex energy landscape of the adsorbed molecule. Variations of energies lower than ±0.03 eV between closely related structures are not trusted. In the following, we will essentially focus on the most symmetric geometries of configuration pyri$_2$.

Table5.1 summarizes the total energies for the different configurations in the LS and HS states. Configuration pyri$_2$ is the most favorable geometry with an energy significantly lower than that of other configurations (by 400 meV or more).

spin state	pyri$_2$	imi-pyri	imi$_2$
LS	0.200	0.611	0.734
HS	0.000	0.395	1.109

Table 5.1: Total energies (eV) of the three adsorption configurations of Fe(neoim)$_2$ on Ag(111) relative to the total energy of pyri$_2$ in its HS state.

A comparison of the adsorbed structure to the geometry of the isolated molecules reveals a drastic flattening of the molecule. This distortion is enabled by two factors. First, the imidazole groups are more flexible than the methyl-pyridine subunits. Second, the distortion allows for a substantial gain in the vdW energy. Indeed, further analysis of the energetics shows that the vdW interaction is the main source of differences between the three configurations, in the LS or HS state.

In addition, the vdW interaction is also essential for stabilizing the HS state with respect to the LS state. This effect is due to the greater flexibility of the former state in configuration $pyri_2$, which leads to stronger flattening and consequently a larger gain in vdW energy (Figure 5.6). The flattening may be quantified by defining a ligand distance Λ between the center of two hexagonal pyridine rings of the opposite ligands. We also define a height h between the outermost surface plane and the Fe atom. h is not directly related to the experimental data but is an indication of the strengths of the molecule-surface interaction in different structures. We find $\Lambda = 0.63$ (0.56) nm and $h = 0.42$ (0.46) nm for the HS (LS) states in the $pyri_2$ configuration.

The switching of $Fe(neoim)_2$ on Ag(111) observed in the STM experiments is most likely related to spin crossover, as no conformation change was observed for the analogue Ni compound, which has no spin transition (see Section on $Ni(neoim)_2$). We propose that the pristine, as-deposited state corresponds to the HS state, given that the calculated energy of the HS molecule is 200 meV lower than that of the LS molecule (configuration $pyri_2$ in Table 5.1). This assignment is also qualitatively consistent with the observed increased mobility of the switched state.

We investigated the electronic structure of the adsorbed molecule by calculating the density of states projected on the atomic orbitals of $Fe(neoim)_2$ on silver in the HS and LS states (Figure 5.7). As expected from the electronic structure of the isolated molecule, a broad peak is observed above the Fermi level, which originates from the LUMO ligand state and its hybridization with the substrate. This ligand state is almost insensitive to the Fe spin, and consequently, the LS and HS states are very similar. Below the Fermi level, the HS state exhibits a narrow Fe-d resonance that is absent from the LS complex.

Due to the large distance between the Fe ion and the STM tip and the rapid decay of d-orbitals, the Fe d states are not expected to contribute much to the STM images. The tunneling current is more likely to involve the ligand orbitals, which exhibit minor variations upon spin crossover. The calculated electronic structures therefore suggest little contrast change between STM images of HS and LS molecules, in agreement with the experimental observations. The molecule exhibits an apparent height of ≈ 250 pm in both the pristine and switched state over a fairly large voltage range (-1.2 V $< V <$ 1.4 V, Figure 5.2c).

Calculations of $Ni(neoim)_2$ were performed with the same hybrid functional and Grimme DFT-D3 correction as those used for $Fe(neoim)_2$.

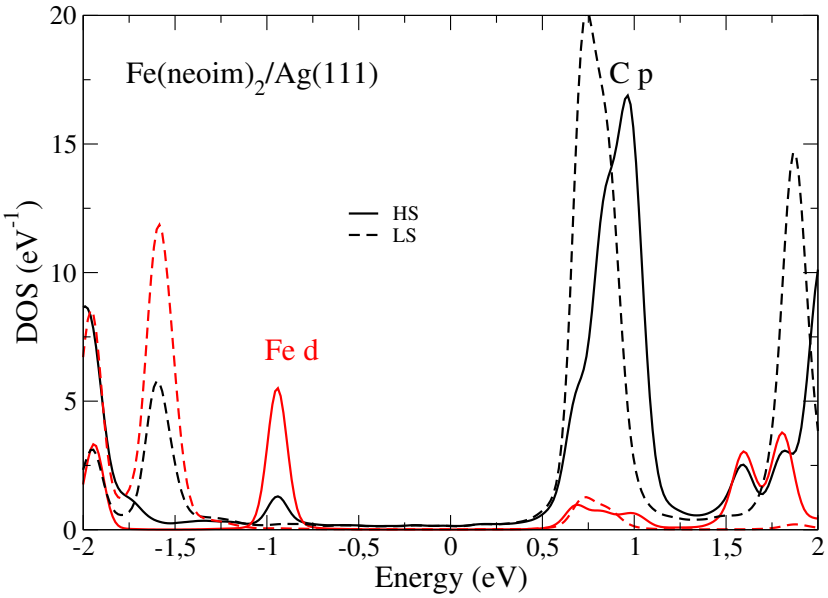

Figure 5.7: Projected density of states on Fe-d (red) and C-p (black) orbitals of Fe(neoim)$_2$ adsorbed on Ag(111) in the HS (full line) and LS (dashed-line) states. A broad C-p peak is present ≈ 0.7 eV above the Fermi level in both cases. Near -1 eV, a narrow peak originating from the Fe-d orbitals is found in the HS state.

As expected, Ni(neoim)$_2$ does not exhibit spin crossover, the S=1 state being more than 1 eV more favorable than the S=0 solution. The electronic spectrum of Ni(neoim)$_2$ exhibits a LUMO that is delocalized over the ligand, just like Fe(neoim)$_2$. However, the HOMO states are also of ligand character, in clear contrast to that of HS Fe(neoim)$_2$. The filled Ni-d states are slightly below the HOMO state, while the empty Ni-d states are above the LUMO ligand states. When deposited on Ag(111) from the starting configuration pyri$_2$, the optimized geometry is almost identical with that of Fe(neoim)$_2$. In particular, its width of $\Lambda = 0.62$ nm is very close to the value calculated for HS Fe(neoim)$_2$. The projected density of states (Figure 5.8) is also very similar to that of Fe(neoim)$_2$, characterized by a dominant contribution of the LUMO ligand states in the same energy range. Hence, the STM image at positive sample voltage is mainly due to these states and an image very similar to the case of Fe(neoim)$_2$ is expected and experimentally observed.

This section addresses the interaction of intact Fe(neoim)$_2$ and fragments thereof with gold and silver substrates.

We first performed a structural relaxation of Fe(neoim)$_2$ on Au(111) starting from the optimized configuration pyri$_2$ obtained on Ag(111). The resulting relaxed geometry is very similar to that obtained on the silver substrate.

The distance h between the gold surface and the iron atom is smaller by 4 pm reflecting a stronger interaction with the gold substrate. The calculated adsorption energy is 0.7 eV larger on gold (3.7 eV) than on silver (3 eV).

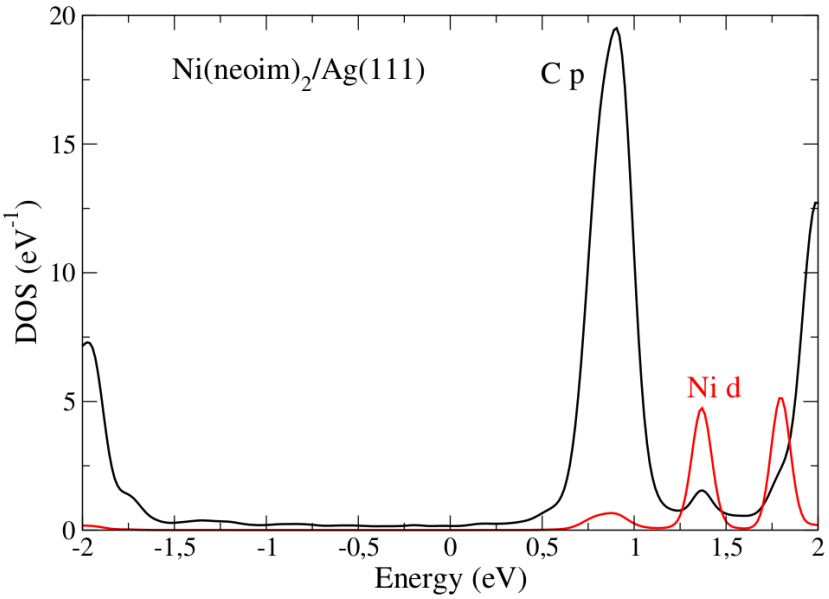

Figure 5.8: Projected density of states on Ni-d (red) and C-p (black) orbitals of $Ni(neoim)_2$ adsorbed on Ag(111). A broad C-p peak is present around 0.7 eV above the Fermi level, as previously found for $Fe(neoim)_2$.

We then considered a $Fe(neoim)_2$ molecule that was split into two separate fragments, namely, a bare ligand and a ligand that was still connected to the iron atom (Figure 5.9). The final relaxed configurations on Au and Ag are similar, but the average distance between the fragments and the surface distance is slightly smaller on Au. The iron is moved away from the average plane of the ligand approaching the substrate and hence hybridizes with a substrate atom as well as with two N atoms. the most salient result is the difference between the total energies of the intact molecule and its fragments. On Ag, the intact molecule is more stable than its fragments by 0.25 eV while on Au, the balance is reversed to -0.32 eV. In other words, assuming a sufficiently low kinetic barrier, fragmentation is predicted on Au(111) in agreement with the experimental finding. The calculated stability of the complex on Ag(111) is also in line with the data.

To trace back the origin of the fragmentation, we consider the case of a single ligand, connected (Fe-ligand) or not (ligand) with an iron atom, deposited on a gold or silver substrate.

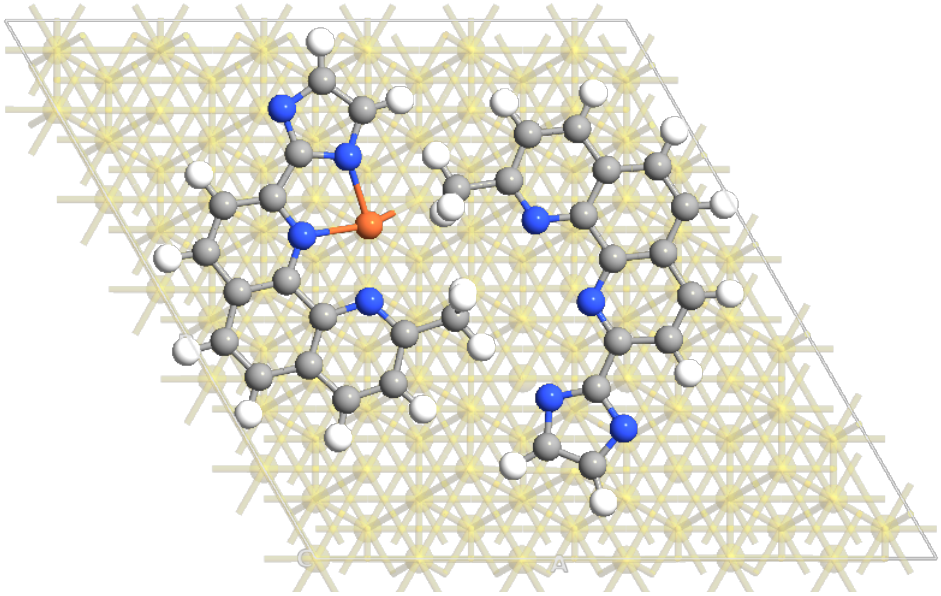

Figure 5.9: Top-view of the adsorbed geometry of fragmented Fe(neoim)$_2$ on silver. The structure on gold is virtually identical.

We relaxed the individual ligand and the Fe-ligand on Au and Ag surface and subsequently shifted the fragment in the z direction perpendicular to the surface (all other atomic positions being fixed) and calculated the adsorption energy for a series of z values around the equilibrium position ($z = 0$):

$$E_{\mathrm{ad}}(z) = E_{\mathrm{ligand/M}} - E_{\mathrm{ligand}} - E_{\mathrm{M}} \tag{5.1}$$

Here E_{ligand} and E_{M} are the total energies of the ligand (or Fe-ligand) and the metal surface separated and $E_{\mathrm{ligand/M}}$ is the total energy of the combined system of the ligand and the substrate. Since the Grimme DFT-D3 method used is a pairwise additive correction, a vdW contribution to the adsorption energy may also be defined. Figure 5.10 displays the adsorption energy as a function of z for the ligand and Fe-ligand adsorbed on Ag(111) and Au(111). The interaction is clearly stronger with the gold substrate, and this difference is much more pronounced for the Fe-ligand, the adsorption energy being 1.1 eV larger for the Fe-ligand on Au and 0.32 eV larger for the isolated ligand. Fe(neoim)$_2$ would not fragment without the vdW interaction because a strong vdW-energy gain occurs for ligands lying flat on the substrate. While the vdW contribution represents approximately half of the total adsorption energy of the intact complex, the different fragmentation behavior also stems from the distinct electronic structures of Ag and Au. To further analyze these results, we first present the ligand-substrate charge transfer and then quantify the Fe-ligand-substrate bond strength.

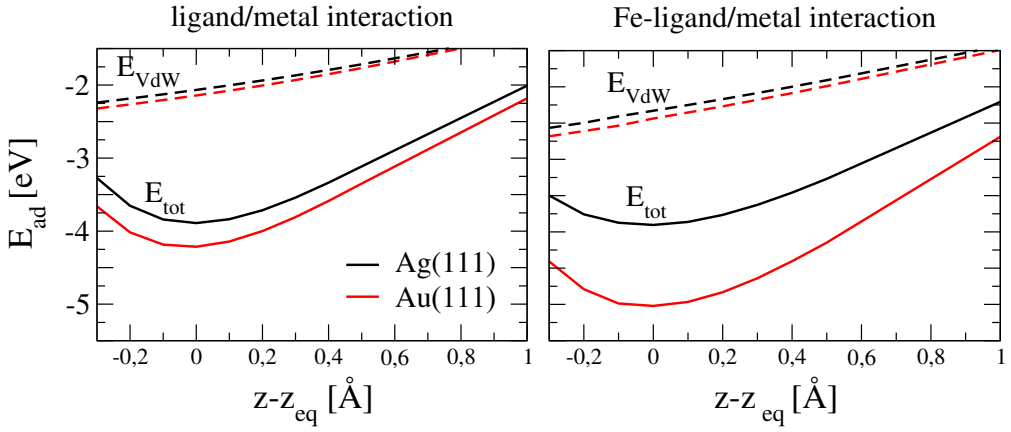

Figure 5.10: Calculated adsorption energy of the ligand (left) and the Fe ligand (right) on Ag and Au (111) surfaces as a function of the ligand-surface distance. The vdW contribution (Grimme DFT-D3) to the adsorption energy is also shown.

Some insight into the origin of the fragmentation may be obtained from the charge transfer between the metal surfaces and the adsorbed ligands, which are slightly closer to the Au substrate, as mentioned above. A similar analysis of adsorbates on coinage metals was previously presented in ref [159].

To characterize the charge rearrangement at the interface we use the charge density difference

$$\delta\rho(x,y,z) = \rho_{\text{ligand/M}} - \rho_{\text{ligand}} - \rho_{\text{M}} \tag{5.2}$$

where ρ_{ligand} and ρ_{M} are the charge densities of the ligand and the metal separated but with the geometries of the adsorbed state, and $\rho_{\text{ligand/M}}$ is the density in the combined system of the ligand and the substrate. Figure 5.11 shows isosurfaces of $\delta\rho(x,y,z)$ and reveals some charge accumulation between the ligand and the Au surface. For a more quantitative analysis, we integrated $\delta\rho$ along the direction perpendicular to the surface, $\Delta\rho(z) = \int_{(x,y)} \delta\rho(x,y,z)\mathrm{d}x\mathrm{d}y$ (Figure 5.12). The charge rearrangement on Au (red curve) is significantly larger than that on Ag (black curve). The largest effect is electron accumulation in the gap between the ligand and the surface. It reflects a singly occupied molecular orbital (SOMO) of the ligand delocalized over the carbon atoms (see Figure 5.15). A Mulliken charge analysis further confirms this result and reveals a larger electron donation from the metal to the ligand on gold ($0.73\,e$) than that on silver ($0.24\,e$).

This large charge transfer is at the origin of the slightly larger interaction with gold; the amplitude of this effect, however, is not sufficient to explain the fragmentation.

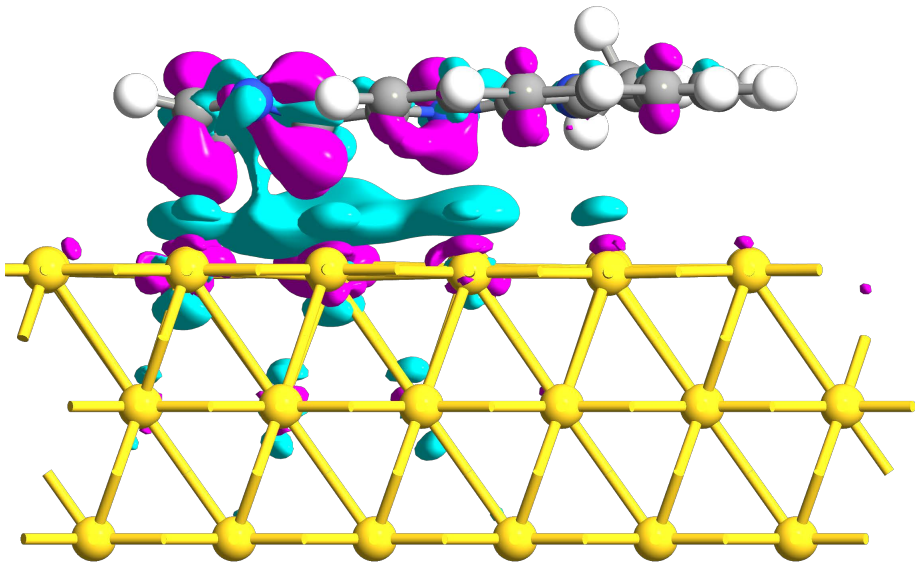

Figure 5.11: Side view of an isosurface of the charge density difference ($0.01\,e/\text{Å}^3$) for the ligand adsorbed on Au(111). Cyan areas show increased electron density; violet areas indicate depletions.

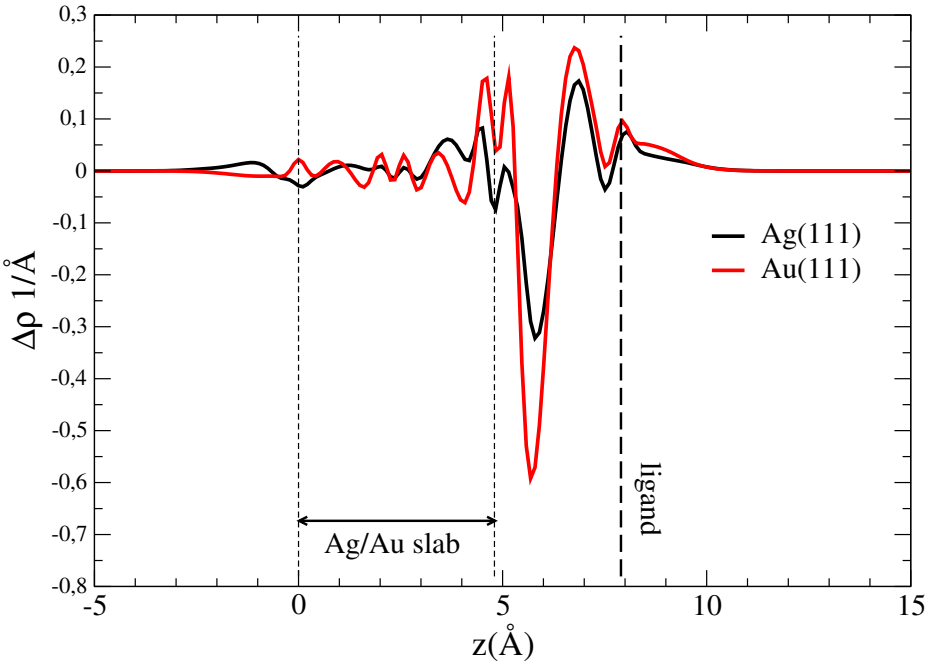

Figure 5.12: Integrated electron density $\rho(z)$ along the direction perpendicular to the surface of the ligand.

Finally, we consider the interaction between the Fe-ligand and the metallic substrate. When isolated, the Fe-ligand exhibits several magnetic states (S=3/2, S=2 and S=5/2), the most stable being S=3/2. When deposited on the metallic surface the iron atom tends to move away from the plane of the ligand toward the surface. In this configuration, the Fe-ligand adopts a different state close to S=2. The total magnetization is slightly larger on Ag ($3.91\,\mu_B$) than on Au ($3.74\,\mu_B$) as a consequence of a stronger interaction with the gold surface and a shorter iron-surface distance ($\approx 5\,$pm reduction). The stronger Fe-Au interaction compared to Fe-Ag is a direct consequence of the much wider d-band of Au and the larger density of occupied electronic states between -3.5 and -1 eV. This very different electronic structure for two elements with the same band filling and lattice parameter can be traced back to the relativistic nature of gold [160, 161], which has consequences for various chemical [161] and physical [162] properties of this element. More specifically, it was shown in ref [163] how the different interface properties between Fe-Ag and Fe-Au can affect the shape of core-shell nanoparticles. To quantify the strength of Fe-Au and Fe-Ag interactions, we performed calculations of the adsorption energy of an Fe atom on Ag(111) and Au(111). Figure 5.13 shows that the interaction with the gold surface is stronger over the whole range of distances. In particular, the interaction energy is 0.6 eV larger at the equilibrium distance. This confirms the essential role of the Fe-Au interaction in the fragmentation mechanism. This strong Fe-metal interaction is also made possible by the shape of the ligand that adsorbs flat on the surface, optimizing the vdW interaction with the substrate.

Using the tridentate chelating ligand neoim, we synthesized the neutral and sublimable complexes Fe(neoim)$_2$ and Ni(neoim)$_2$. Scanning tunneling microscopy shows that the molecules remain intact on Ag(111) but fragments on Au(111), presumably by splitting off one of the neoim ligands. Electron-induced spin crossover (ELIESST) is achieved from the Fe complex while the Ni analogue is passive as expected. DFT calculations reproduce important aspects of the experimental data. They highlight the importance of van der Waals interactions for the molecular geometry and the relative stabilities of the spin states. In particular, the S=2 state of Fe(neoim)$_2$ is stabilized by the combined effects of greater flexibility of the ligand shell and vdW forces. The experimentally observed fragmentation on Au and the stability on Ag are also found in the calculations, which show that the bonding of the fragments to Au is stronger and involves electron accumulation at the ligand-substrate interface.

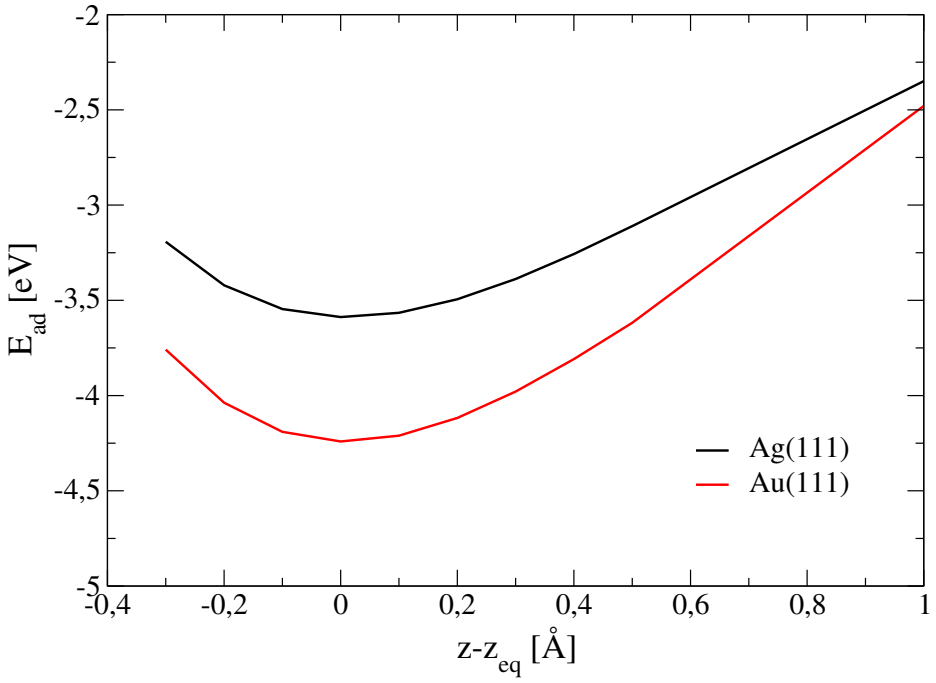

Figure 5.13: Calculated adsorption energy of an Fe atom in an fcc position on Ag and Au (111) surfaces as a function of the Fe-surface distance.

The present work shows that 3D complexes on surfaces require a fresh look at the significance of van der Waals interactions and the reactivity of coinage metals.

5.3 Methods

The ligand Hneoim and the complex Fe(neoim)$_2$ were synthesized as described elsewhere [164]. The homologous Ni(neoim)$_2$ derivative was synthesized by following the same procedure. To a solution of neoimH (1000 mg, 3.8 mmol) in MeOH (20 ml), was added Ni(BF$_4$)$_2$·6H$_2$O (650 mg, 1.9 mmol). The resulting yellowish solution was refrigerated (4 °C) overnight, and the plate-like yellowish crystals that formed were filtered off, air-dried, and suspended in a mixture of aqueous NH$_3$, 25 % (30 ml), and CHCl$_3$ (100 mL). The yellow-colored organic layer was separated, and the aqueous phase was extracted three more times with chloroform (in portions of 50 mL each). The organic solutions were combined, dried over MgSO$_4$, and evaporated to dryness, producing a yellow powder of the complex. Yield is 850 mg, 74 %. Anal. Calcd for C$_{34}$H$_{28}$N$_8$Ni: C, 67.24; H, 4.65; N, 18.45. Found: C, 67.12; H, 4.33; N, 18.12.

Aiming at characterizing the molecular structure of this complex through X-ray diffraction studies, yellow plate-like single crystals of [Ni^{II}(neoim)$_2$]·1.3H$_2$O·2.3CHCl$_3$ were obtained by slow diffusion of hexane vapors into solutions of Ni^{II}(neoim)$_2$ in chloroform previously prepared from microcrystalline powders of Ni^{II}(neoim)$_2$,

ca. 100 mg, dissolved in 7 mL of boiling $CHCl_3$ and filtered. Anal. Calcd for $C_{34.30}H_{26.97}C_{16.90}N_8NiO_{1.33}$: C, 46.99; H, 3.03; N, 12.79. Found C, 46.52; H, 3.03; N, 12.65.

Single crystals of $[Ni^{II}(neoim)_2]\cdot 1.3H_2O\cdot 2.3CHCl_3$ were mounted on a glas fiber by using a viscous hydrocarbon oil to coat the crystal and then transferred directly to the cold nitrogen stream for data collection. X-ray data were collected on a Supernova diffractometer equipped with a graphite-monochromated Enhance (Mo) X-ray Source ($\lambda = 0.71073$ Å). The program CrysAlisPro, Oxford Diffraction Ltd., was used for unit cell determinations and data reduction. Empirical absorption correction was performed using spherical harmonics, implemented in the SCALE3 ABSPACK scaling algorithm. The structures were solved by direct methods using SHELXS-2014 and refined by full matrix least-squares on F2 using SHELXL-2014 [165]. Non-hydrogen atoms were refined anisotropically, and hydrogen atoms were placed in calculated positions refined using idealized geometries (riding model) and assigned fixed isotropic displacement parameters. CCDC 2260044 contains the supplementary crystallographic data for this paper. These data can be obtained free of charge from the Cambridge Crystallographic Data Centre via www.ccdc.cam.ac.uk/data_request/cif.

DFT functional modeling has been performed with QuantumATK-T-2022.03 [106, 107] using the norm conserving pseudopotentials [166] and a medium basis set. For all calculations we used the HSE06 hybrid functional [157, 158] with a fraction of exact exchange α adapted to the $Fe(neoim)_2$ molecule such that the energy difference $\Delta E = E_{LS} - E_{HS}$ is of the order of -0.1 eV. van der Waals interaction has been included via the Grimme DFT-D3 dispersion correction adapted to the HSE06 functional. For the modeling of the molecule on a metallic substrate we considered a three-layer (6×6)M(111) surface cell (M = Ag or Au). Geometry optimization was performed at the Γ point until forces were below 0.01 eV/Å, while total energies and electron densities were calculated with 5×5 grid of k-points.

Ag(111) and Au(111) surfaces were prepared by cycles of Ar^+ sputtering (1.5 keV) and annealing to ≈ 500 °C. $Fe(neoim)_2$ and $Ni(neoim)_2$ molecules were sublimated from a heated crucible (≈ 130 °C) onto the substrates at ≈ 20 °C. STM tips were electrochemically etched from a W wire and annealed in vacuo. Usually, the tips were indented into the substrate until a stable tip was achieved. The measurements were carried out with a cryogenic (≈ 4.6 K) STM (Createc) in ultra-high vacuum (base pressure lower than 1.2×10^{-10} mbar).

5.4 Acknowledgments

We acknowledge financial support from the European Union's Horizon 2020 program, grant number 766726. J.A.R. thanks the Spanish Ministerio de Ciencia e Innovación (Grant PID2019-106147GB-I00 funded by MCIN/AUI/10.13039/501100011033). M.S. thanks the Ministry of Education and Science of Ukraine (Grants 22BF037-03 and 22BF037-04). M.G. acknowledges funding from the Deutsche Forschungsgemeinschaft (Project-ID 278162697, CRC 1242, Project A08). R.B. thanks Felix Tuczek and Alexandre Tkatchenko for discussions.

5.5 Supplementary Information

5.5.1 DOS of Isolated LS Complex Projected on Fe-d states

Figure 5.14 presents the density of states of an isolated LS $Fe(neoim)_2$ complex projected onto Fe-d orbitals. $t_{2g} - e_g$ splitting is evident. In addition, weak features are visible around 1 eV and -3 eV. They are due to ligand states that couple weakly to the iron ion as indicated by the spatial distributions of the states. In particular, the states at -3 eV are localized to nitrogen and the imidazole group while the 1 eV states are delocalized over all carbon atoms of the ligand except the imidazole group. These states play an important role since they provide the main current contribution at positive voltages in the experiments.

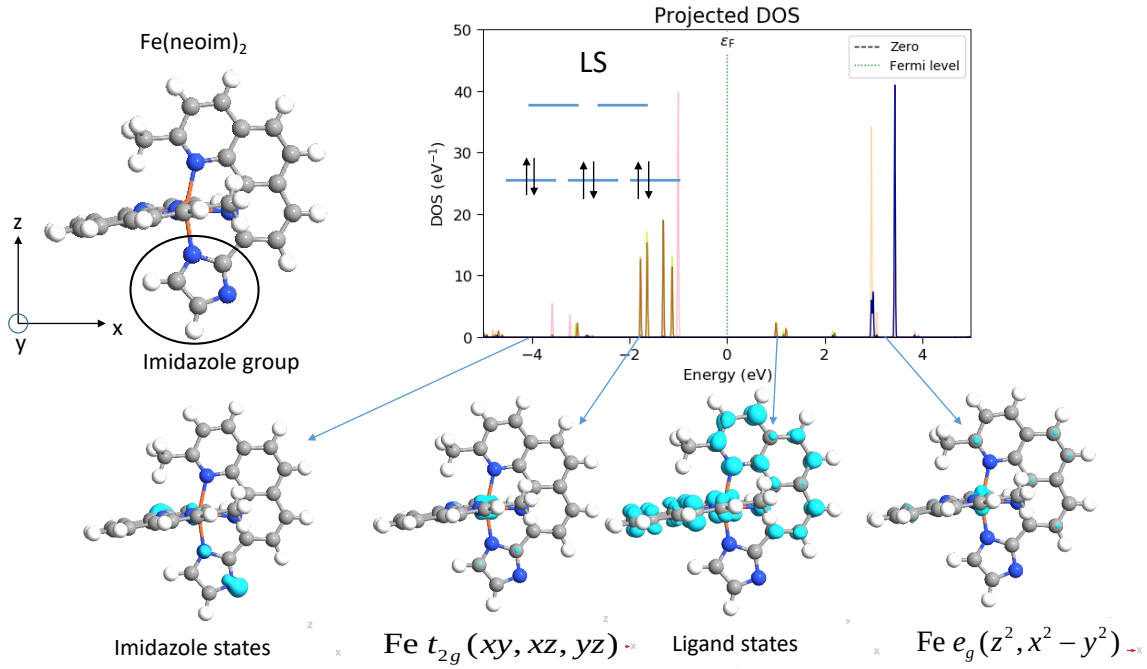

Figure 5.14: Projected Fe-d density of states of gas phase LS $Fe(neoim)_2$ molecule and spatial distributions of the electron density of some molecular orbitals. t_{2g} states are shown in red and e_g states in blue. The ligand and imidazole states have major C and N components (not shown) and a small Fe-d component.

5.5.2 DOS of an Isolated LS Complex Projected on C-p$_z$ states

Figure 5.15 shows the density of states of the isolated ligand ($C_{16}H_{11}N_4$) projected onto C-p_z orbitals. The ligand contains an odd number of valence electrons (95) and hence the HOMO state is a singly occupied molecular orbital (SOMO). When deposited on silver or gold the SOMO molecular state gets partially filled.

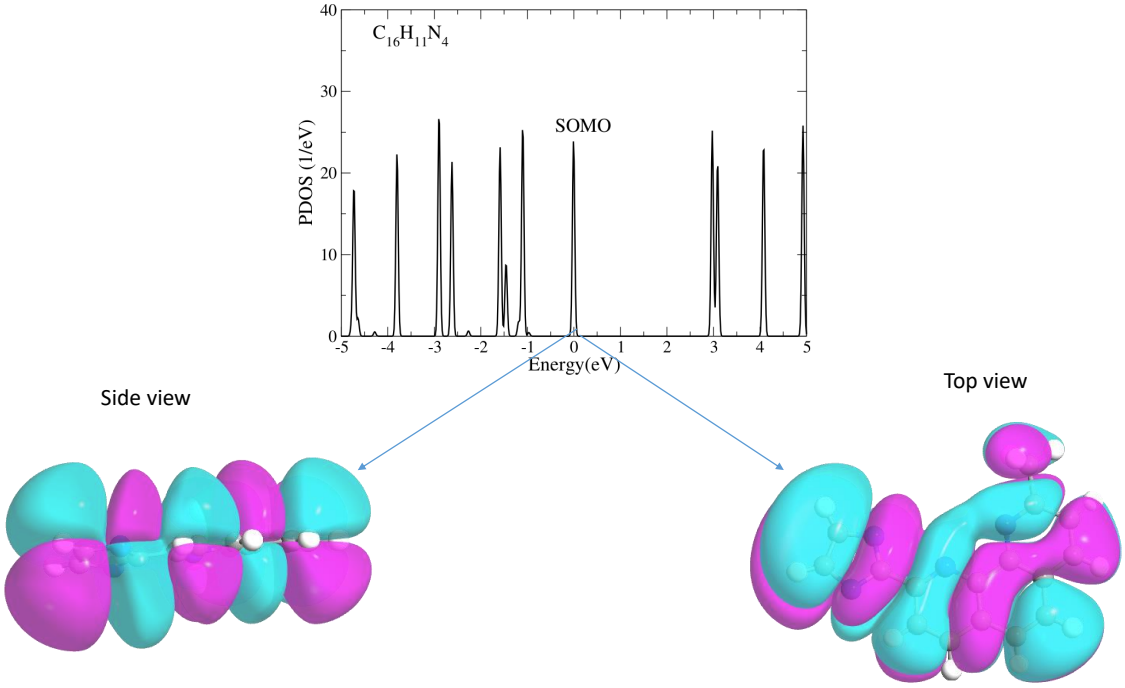

Figure 5.15: Projected C-p_z density of states of gas phase ligand and the spatial distribution of the SOMO wavefunction. Blue and violet indicate positive and negative signs of the wavefunction.

5.5.3 Stability of Fe(neoim)$_2$ Toward Charging

To evaluate the stability of Fe(neoim)$_2$ with respect to negative charging we performed a series of molecular dynamics simulations of an isolated Fe(neoim)$_2$ molecule with various charges. Interestingly, we found that the molecule explodes above a threshold charge of 0.80 e. While this scenario is not a faithful representation of the adsorbed molecule, it may be viewed as a hint toward a possible fragmentation mechanism. Indeed, the fragmentation occurs on gold, i.e. the substrate that donates more electrons to the molecule, but not on silver.

5.5.4 Mobility and Telegraph Noise of Fe(neoim)$_2$

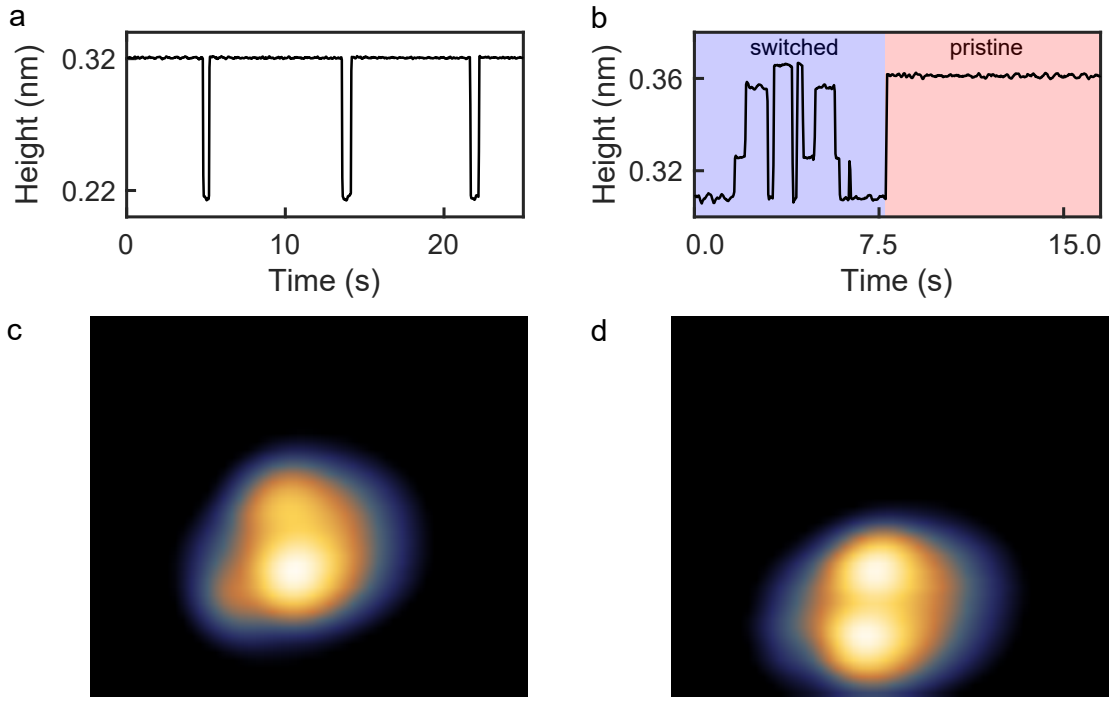

Figure 5.16: (a) Time-series of the constant-current height measured above a Fe(neoim)$_2$ complex in the spin-switched state. Data recorded at 600 mV and 10 pA. These parameters lie below the threshold for spin switching. The observed two-level fluctuations are due to rotation or small lateral shifts of the molecule. (b) Similar time-series from another complex recorded at 800 mV and 10 pA. Initially, switching is due to geometrical changes. After ≈ 7.5 s, spin-switching to the pristine state occurs. The pristine state being more stable, no further height changes occur over an interval of 8 s. (c) Constant-current topograph ($V = 300$ mV, $I = 10$ pA) of a molecule probed in (b), recorded before the time series. The molecule is in the spin-switched state. Image size: 3.5×3 nm^2. (d) Topograph of the same complex recorded after the time series. The complex is in the pristine state and has laterally moved compared to its original position in (c).

5.5.5 dI/dV Spectrum of Fe(neoim)$_2$

Figure 5.17 shows a dI/dV spectrum of a Fe(neoim)$_2$ complex that was in its pristine state before recording the data. These data have only been observed once whereas usually the elevated voltages used caused instabilities. Apparently, an unoccupied state around 0.8 V is present. The small feature near 0.08 V is larger than the experimental noise but we cannot exclude that it is due to the electronic structure of the tip.

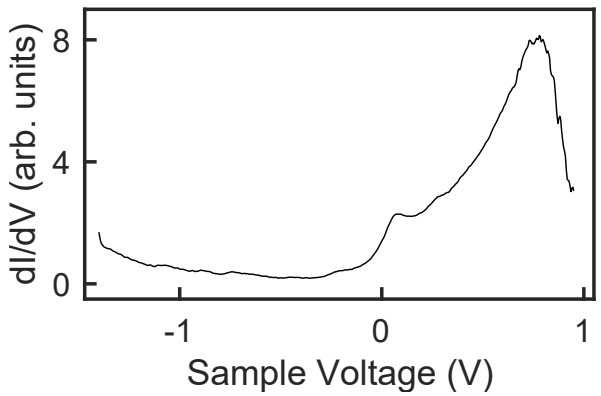

Figure 5.17: dI/dV spectrum of a Fe(neoim)$_2$ complex recorded at a constant height determined by $V = -1.4\,\mathrm{V}$ and $I = 25\,\mathrm{pA}$ prior to disabling current feedback.

5.5.6 Crystal Data for [Ni^{II}(neoim)$_2$]

Empirical formula	$C_{34.30}H_{26.97}N_8O_{1.33}Cl_{6.90}Ni$
Mr	875.88
Crystal system	triclinic
Space group	P-1
a (Å)	11.9235(12)
b (Å)	12.1727(12)
c (Å)	13.8799(13)
α (°)	76.846(3)
β (°)	88.317(4)
γ (°)	79.523(4)
V (Å^3)	1928.8(3)
Z	2
T (K)	124
D_c (mg cm^{-3})	1.508
F(000)	889
μ(Mo-K$_\alpha$) (mm^{-1})	1.022
Crystal size (mm)	0.02×0.02×0.04
No. of total reflections [$l > 2\sigma(l)$]	6875
R [$l > 2\sigma(l)$]	0.1067
wR [$l > 2\sigma(l)$]	0.2782
S	1.152

Table 5.2: Crystal data for $[Ni^{II}(neoim)_2] \cdot 1.3H_2O \cdot 2.3CHCl_3$ at 124 K.

$$R = \frac{\sum ||Fo| - |Fc||}{\sum |Fo|}$$

$$wR = \left[\frac{\sum w(Fo^2 - Fc^2)^2}{\sum w(Fo^2)^2}\right]^{1/2}$$

$$w = \frac{1}{\sigma^2(Fo^2) + (mP)^2 + nP},$$

$$P = \frac{Fo^2 + 2Fc^2}{3}$$

where $m = 0.0660$ and $n = 33.7252$.

5.5.7 Selected Bond Parameters of Ni(neoim)$_2$

	Experiment	Calculation
Ni-N(1)	2.276(6)	2.28
Ni-N(2)	2.004(6)	2.00
Ni-N(3)	2.094(6)	2.06
Ni-N(5)	2.276(6)	2.29
Ni-N(6)	2.010(6)	2.00
Ni-N(7)	2.095(6)	2.06
N(1)-Ni-N(2)	76.2(2)	76.02
N(1)-Ni-N(3)	154.1(2)	154.67
N(1)-Ni-N(5)	89.7(2)	93.17
N(1)-Ni-N(6)	105.5(2)	108.30
N(1)-Ni-N(7)	93.7(2)	89.20
N(2)-Ni-N(3)	78.4(2)	79.16
N(2)-Ni-N(5)	105.3(2)	107.05
N(2)-Ni-N(6)	177.6(2)	175.59
N(2)-Ni-N(7)	99.8(2)	98.09
N(3)-Ni-N(5)	92.4(2)	89.27
N(3)-Ni-N(6)	100.1(2)	97.76
N(3)-Ni-N(7)	95.3(2)	99.26
N(5)-Ni-N(6)	76.5(2)	75.91
N(5)-Ni-N(7)	154.7(2)	154.58
N(6)-Ni-N(7)	78.5(2)	79.22

Table 5.3: Experimental bond lengths [Å] and angles [°] for $[Ni^{II}(neoim)_2] \cdot 1.3H_2O \cdot 2.3CHCl_3$ at 124 K along with calculated (DFT) values for free $[Ni^{II}(neoim)_2]$.

5.5.8 Selected Bond Lengths of Fe(neoim)$_2$ (DFT)

	HS	LS
Fe-N(1)	2.34	2.05
Fe-N(2)	2.09	1.89
Fe-N(3)	2.11	1.94
Fe-N(5)	2.35	2.05
Fe-N(6)	2.09	1.89
Fe-N(7)	2.11	1.94
N(1)-Fe-N(2)	73.24	80.90
N(1)-Fe-N(3)	148.56	160.98
N(1)-Fe-N(5)	94.53	94.32
N(1)-Fe-N(6)	110.04	106.04
N(1)-Fe-N(7)	86.52	89.77
N(2)-Fe-N(3)	76.79	80.14
N(2)-Fe-N(5)	109.19	106.32
N(2)-Fe-N(6)	176.03	169.85
N(2)-Fe-N(7)	101.42	92.67
N(3)-Fe-N(5)	86.42	89.59
N(3)-Fe-N(6)	100.32	92.96
N(3)-Fe-N(7)	108.74	92.57
N(5)-Fe-N(6)	73.11	80.89
N(5)-Fe-N(7)	148.34	160.97
N(6)-Fe-N(7)	76.83	80.12

Table 5.4: Calculated (DFT) bond lengths [Å] and angles [°] for free [Fe^{II}(neoim)$_2$]

5.5.9 ORTEP Representation of [Ni^{II}(neoim)$_2$]

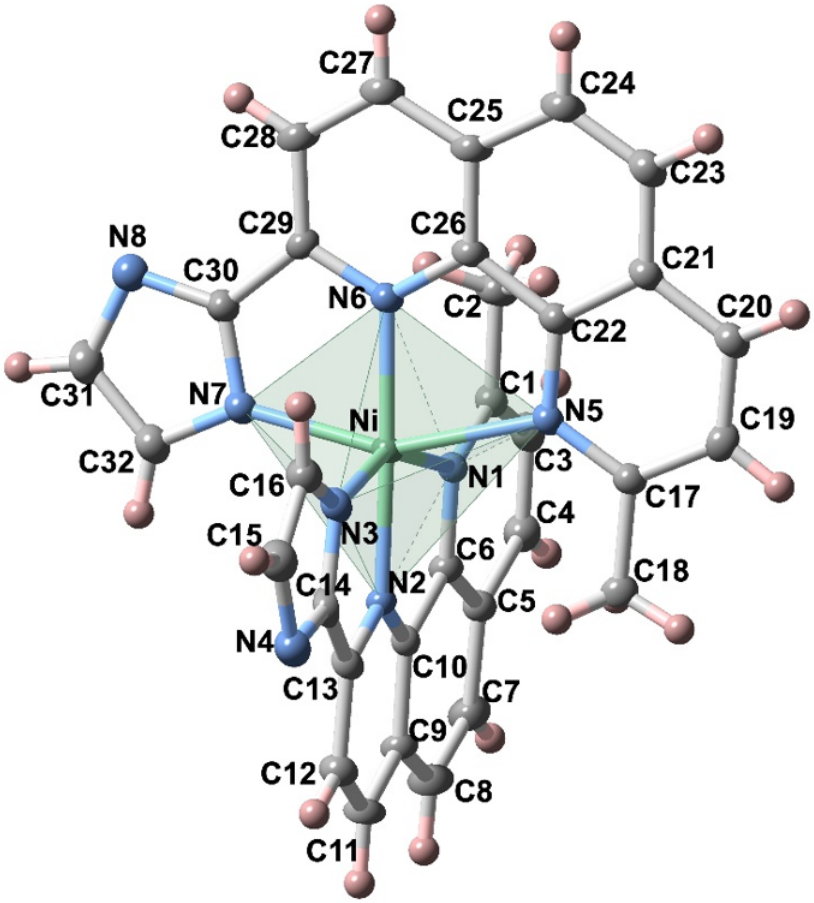

Figure 5.18: ORTEP representation of [Ni^{II}(neoim)$_2$]·1.3H_2O·2.3$CHCl_3$ at 124 K. Thermal ellipsoids are represented at 50% probability. Water and chloroform molecules have been omitted.

5.5.10 Models of Ni(neoim)$_2$ enantiomers

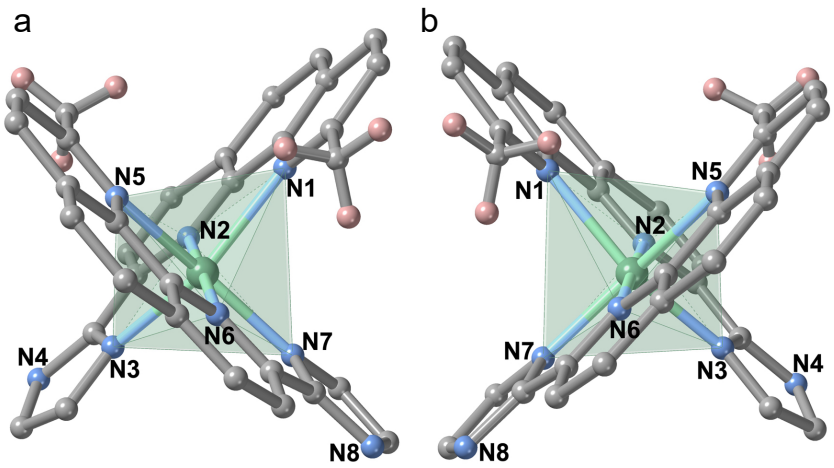

Figure 5.19: (a,b) Models of the enantiomers of [Ni(neoim)$_2$]. The structures from bulk crystals are shown. The orientation chosen corresponds to a side view of the adsorbed molecules. Any distortions caused by the adsorption are not included.

6 Spin-crossover of complexes on Cu(111) evidenced by spin-flip spectroscopy

Chapter 6 is based on a manuscript and supporting information prepared for publication.

Author Contributions

Sven Johannsen performed the STM measurements. Sven Johannsen, Alexander Weismann, Manuel Gruber and Richard Berndt analyzed and interpreted the data. Karl Ridier provided the SCO molecules. Sven Johannsen created all figures in the manuscript and supporting information, except 6.1a and b and 6.7. Manuel Gruber wrote the manuscript with input from all authors. All authors discussed the results. Richard Berndt supervised the project.

6.1 Abstract

Spin-crossover compounds can be switched between two stable states with different magnetic moments, conformations, electronic, and optical properties, which opens appealing perspectives for technological applications including miniaturization down to the scale of single molecules. Although control of the spin states is crucial their direct identification is challenging in single-molecule experiments. Here we investigate the spin-crossover complex [Fe(HB(1,2,4-triazol-1-yl)$_3$)$_2$] on a Cu(111) surface with scanning tunneling microscopy. Spin crossover of single molecules in dense islands is achieved via electron injection. Spin-flip excitations are resolved in scanning tunneling spectra in a magnetic field enabling the direct identification of the spin state (S=2) and the transitions ($m_s = -1 \rightarrow -2$ and $0 \rightarrow 1$) involved.

6.2 Introduction

Spin-crossover (SCO) compounds are transition-metal complexes that can be switched between a low-spin (LS) and a high-spin (HS) state using various external stimuli such as temperature, light, and electrical current [167]. The spin-state transition is associated with a change of the molecular conformation and of the electronic and optical properties making such systems attractive for applications such in data storage, displays, and sensors [168], possibly on the scale of single molecules [18, 169]. Along this line, ultrathin films of SCO compounds have been fabricated by thermal evaporation under vacuum [121] and investigated [18, 21, 24, 30, 70–81, 121, 128, 136, 137]. Examples of successful electron and light induced excited spin state trapping (ELIESST, LIESST) have been reported from transport measurements [9–13, 32–37] and scanning tunneling microscopy (STM) [1–4, 20–22, 25, 38–43, 136].

SCO complexes in direct contact with surfaces have attracted much interest but direct proof of single molecule SCO is difficult to obtain. The absence of switching of analogue Ni or Zn complexes [1, 4], where no SCO is expected, has provided indirect evidence in the case of Fe compounds. Comparisons with the results of density functional theory calculations, which predict different geometries and frontier orbital energies for the high and low spin states have also been used. Finally, the observation of a Kondo resonance, which signals the presence of a localized spin, has been employed.[21, 38, 39] In the case of Fe(II) complexes only the HS state carries a magnetic moment and can lead to this effect. However, the Kondo effect is only observed when the coupling of the molecular spin and the conduction electrons happens to be suitably strong. A spin-state readout that is directly related to the magnetic moment of the metal-ion remains desirable.

Here we investigate the SCO complex [Fe(HB(1,2,4-triazol-1-yl)$_3$)$_2$] on a Cu(111) surface with STM. Individual molecules in large monolayer islands are switched by injecting electrons. Tunneling spectra of the molecule in the HS state exhibit steps that shift in a magnetic field. These inelastic features reflect spin-flip excitations that represent direct information on the molecular spin state.

6.3 Results and Discussion

6.3.1 Self-assembly on Cu(111)

The investigated [Fe(HB(1,2,4-triazol-1-yl)$_3$)$_2$] complex (Figure 6.1a) composed of two identical tridentate ligands, exhibits a transition temperature of $\approx 334\,\mathrm{K}$ in the bulk material [170]. As common for Fe(II) complexes in an octahedral ligand-field

geometry, the electronic configuration in the LS and HS state leads to a total spin of S=0 and S=2, respectively (Figure 6.1b). Thin films (20 – 200 nm) of this compound prepared via sublimation in vacuum are of high quality, crystallize upon exposure to water vapor, and essentially exhibit the same transition temperature as bulk samples [171].

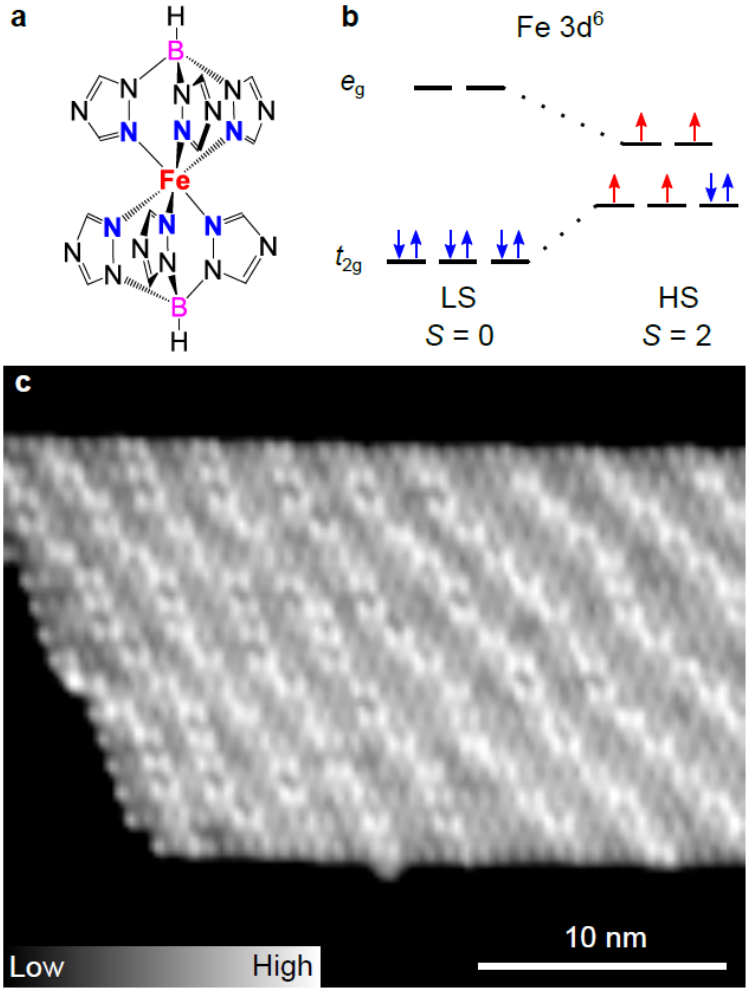

Figure 6.1: **a** Molecular structure of the complex [Fe(HB(1,2,4-triazol-1-yl)$_3$)$_2$]. **b** Schematic representation of the 3d orbitals for an Fe(II) ($3d^6$) complex in an octahedral ligand field. Blue (red) arrows indicate the orbital occupations with paired (unpaired) spins for low-spin (LS) and high-spin (HS) states. **c** Overview STM topograph (0.2 V, 5 pA, 30 × 25 nm^2) of a [Fe(HB(1,2,4-triazol-1-yl)$_3$)$_2$] island on Cu(111). The apparent height of the layer with respect to the Cu substrate is 220 pm. In addition to the molecular contrast, bright stripes with an apparent height of ≈ 30 pm are observed.

Upon sublimation of submonolayer amounts of [Fe(HB(1,2,4-triazol-1-yl)$_3$)$_2$] on Cu(111), the molecules self-assemble into large islands, typically ≈ 20 nm wide and ≈ 40 − 80 nm long with an apparent height of ≈ 220 pm at 0.2 V (Figure 6.1c). The islands exhibit bright stripes with a periodicity of ≈ 3 nm. It seems that the

molecules have an epitaxial relation with the substrate, as observed for the complex [Fe((3,5-$(CH_3)_2$Pz)$_3$BH)$_2$] on Au(111) [73]. The stripes are likely due to misfit dislocations to release the strain within the layer caused by lattice mismatch.

Figure 6.2a shows a smaller area of the molecular layer on Cu(111). A regular arrangement of circular protrusions is observed along with fuzzy areas parallel to the top-left to bottom-right diagonal of the image. The protrusions and fuzzy areas correspond to individual molecules and the stripes, respectively (discussed above). To gain more information about the orientation of the molecules, we picked up a molecule from the layer by approaching the tip toward a protrusion and increasing the setpoint current from 5 to 20 pA at $V = 50$ mV. After depositing the molecule elsewhere, the remaining hole is observed as an horizontal depression (Figure 6.2b). Assuming that the image contrast is mainly caused by the upper part of a flat-lying molecule, we suggest that the orientation of the molecules is as shown in Figure 6.2c, where the lateral dimensions of the depression match with the upper two triazole groups of a molecule. Picking up further molecules from the same island leads to depressions with the same orientation (SI, Section 1), indicating that all molecules within an island have the same orientation. We therefore propose the molecular structure shown in Figure 6.2d and in the overlay of Figure 6.2a.

According to the proposed structure, the molecules form lines along the long direction of the islands with a periodicity of 1.1 nm (Figure 6.2d). Within each line, two neighboring molecules are connected via C-H...N bonds between the underlying triazole groups (dotted lines in Figure 6.2d) leading to a center-to-center distance of ≈ 0.8 nm. Adjacent lines are vertically shifted and most probably stabilized by two C-H...N interactions between the upper triazole groups (dashed lines in Figure 6.2d). We note that the adsorbed molecule is chiral and the two enantiomers form different stackings leading to two types of islands (SI, Section 2 and 3).

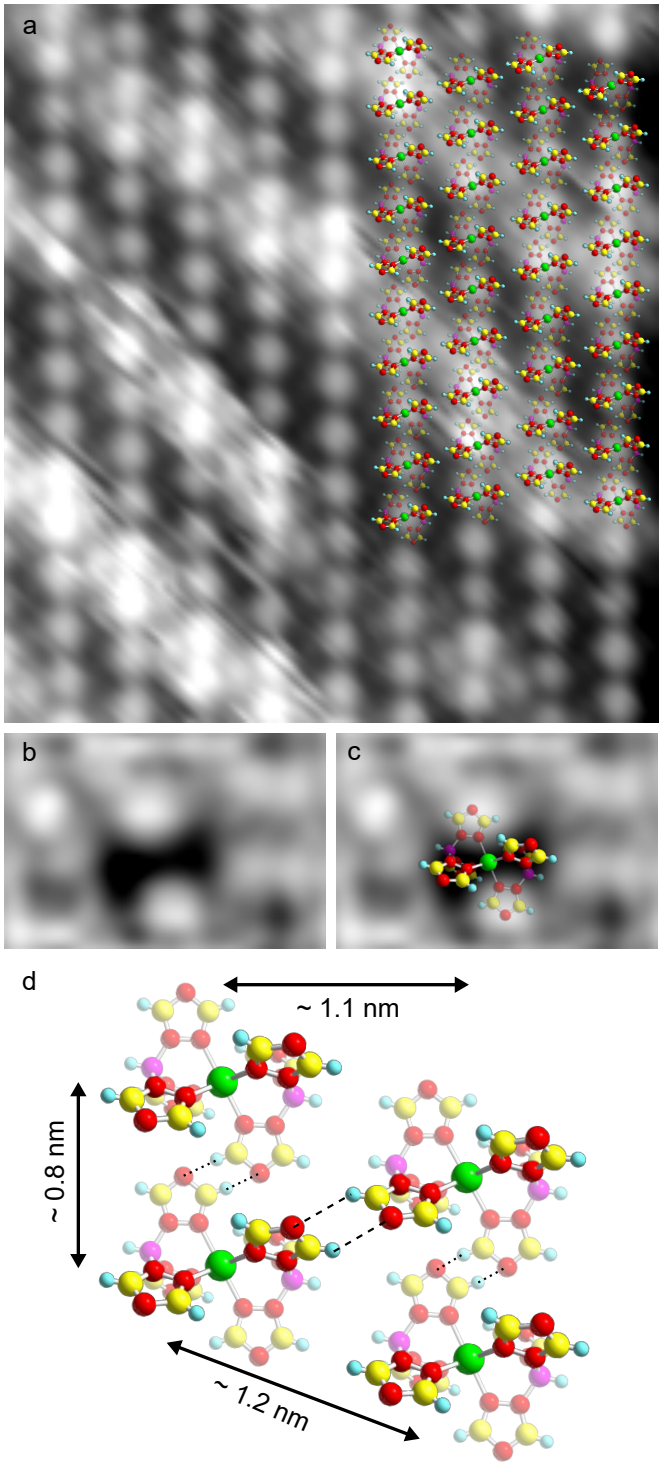

Figure 6.2: **a** STM topograph of [Fe(HB(1,2,4-triazol-1-yl)$_3$)$_2$] on Cu(111) with overlaid molecular models (1.6 V, 5 pA, 10×11 nm^2). **b** and **c** Zoomed STM topographs of an area from which a molecule has been picked up (200 mV, 5 pA, 3×2 nm^2). The remaining depression is horizontally elongated with a lateral extent matching that of the upper two triazole groups of a flat lying molecule. **d** Proposed arrangement of the molecules on the Cu(111) surface. For **a**–**d**, the transparency of the atoms indicates the height relative to the Cu(111) surface with transparent atoms being closer to the substrate. Green, yellow, red, purple, and cyan spheres respectively represent Fe, C, N, B, and H atoms.

6.3.2 Voltage dependent image contrast

The appearance of the molecules as circular protrusions at 1.6 V (Figures 6.3a,c) presented above, drastically changes when the sample voltage is reduced to 0.2 V (Figures 6.3b,d). At this voltage, the molecules essentially appear as depressions (see Figure 6.3b, where green dots indicate the positions of the Fe atoms). The change of the sample voltage leads to a reduction of the apparent height by almost a factor 2, from ≈ 430 pm at 1.6 V to ≈ 220 pm at 0.2 V (Figure 6.3e). This drastic modification of the molecular contrast indicates a large non-geometric contribution to the STM image. The importance of electronic contributions is further evidenced in images of island edges, where the border molecules appear smaller (SI, Section 4). One or more unoccupied molecular orbitals are expected to have energies between 0.2 and 1.6 eV. Unfortunately, the acquisition of $\mathrm{d}I/\mathrm{d}V$ spectra to confirm the presence of the orbitals failed because of large current fluctuations at voltages exceeding ≈ 0.5 V, as further discussed below. It is worth mentioning that, at a given voltage, all the molecules have the same appearance suggesting that they are all in the same pristine state.

6.3.3 Electron-induced switching

Switching of the molecules may be induced by injecting electrons at a sample voltage of ≈ 0.5 V or higher. Figure 6.4 shows an example. The pristine molecule appears as a depression at 0.2 V as previously described (white arrow in Figure 6.4a). After having placed the tip above the center of the depression, raising the voltage to 0.5 V for a few seconds, and decreasing it back to 0.2 V, while maintaining the current feedback loop active, the same molecule appears as a small protrusion (Figure 6.4b). The molecule may then be switched back to its pristine state using the same procedure (Figure 6.4c). Alternatively, for voltages above 0.5 V, telegraph noise is observed in time series of the tunneling current (feedback loop inactive). The low and high current levels correspond to a molecule appearing as a depression and protrusion, respectively.

Telegraph noise of the tunneling current was acquired for different tip-molecule distances and voltages, from which we can extract the switching rates (see Ref. [1] for details). The switching rates from a low (L) to a high (H) current value and vice versa evolve linearly with the tunneling current (Figure 6.5a) indicating that each switching event is caused by a single electron (the rate of a multi-electron process would evolve with I^N with $N > 1$). The probability of a tunneling electron to induce the switching is on the order of 10^{-7}, comparable to the highest reported yields for SCO molecules on surfaces (up to $\approx 8 \times 10^{-7}$ in Ref. [1]). The yield evolves rapidly with the applied voltage (Figure 6.5b).

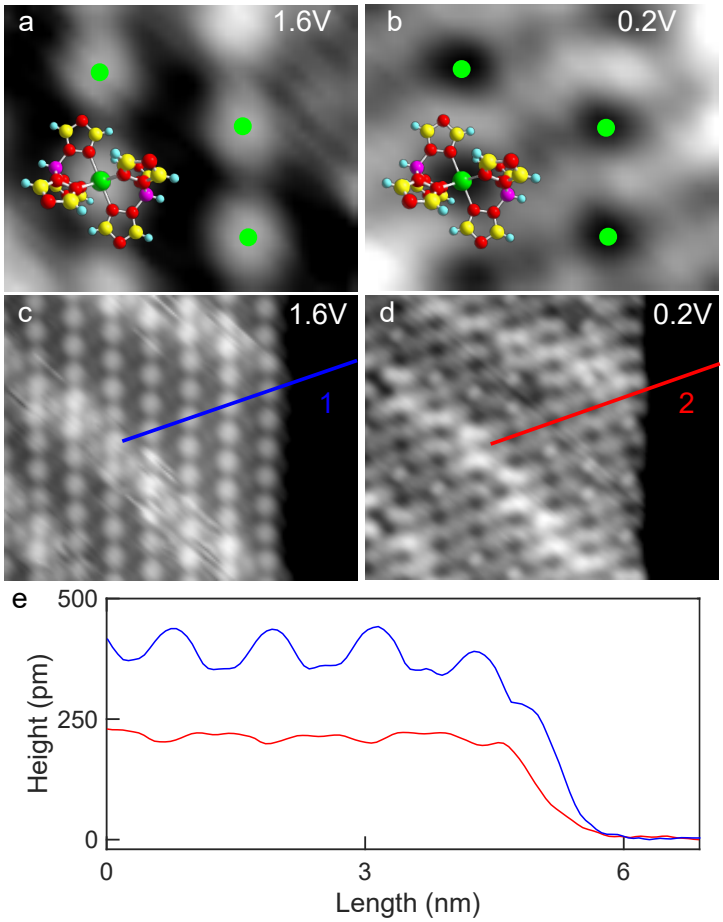

Figure 6.3: **a, b** Topographs of a $2.6 \times 2.1\,\mathrm{nm}^2$ area from a molecular island recorded at 1.6 and 0.2 V, respectively with $I = 5\,\mathrm{pA}$. While each $[\mathrm{Fe(HB(1,2,4\text{-}triazol\text{-}1\text{-}yl)_3)_2}]$ complex is imaged as a single protrusion at 1.6 V, the image contrast is reversed at 0.2 V. The suggested adsorption geometry is indicated by a superposed model and by green dots at the positions of the Fe ion centers. **c, d** Larger topographs ($10 \times 8\,\mathrm{nm}^2$) of an island measured with the parameters used in panels **a** and **b**. At 1.6 V parallel columns of virtually identical protrusions are observed along with diagonal stripes. At 0.2 V the former protrusions, which correspond to single molecules, appear mostly as depressions (or as small protrusions upon switching as detailed below). **e** Cross-sectional profiles along the paths indicated by blue and red lines in **c** and **d**. At 1.6 V, the molecules appear approximately twice as high compared to 0.2 V (≈ 430 vs. $\approx 220\,\mathrm{pm}$). The plateau at the right side of the height profiles shows the bare Cu(111) substrate.

At 0.45 V, two transitions were observed in a time window of 50 s (for $I = 5$ pA), while at 0.5 V switching is monitored every few seconds for currents as low as 5 pA. This implies that only electrons with an energy $\gtrsim 0.5$ eV can switch the molecules. Interestingly, a similar threshold has been determined for the compound [Fe((3,5-$(CH_3)_2$Pz)$_3$BH)$_2$] on Cu(111) [136], suggesting that the two compounds might share a common microscopic switching mechanism.

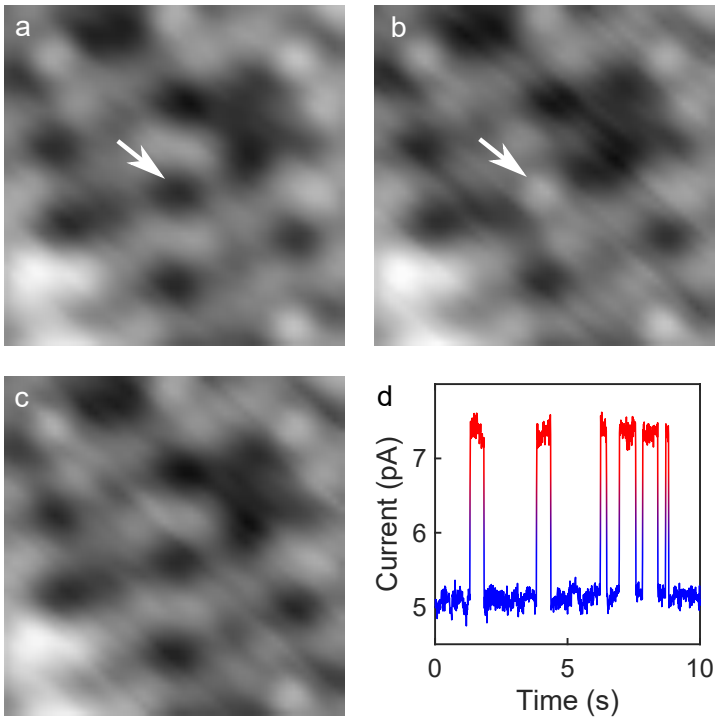

Figure 6.4: Reversible switching of an individual molecule under the tip. **a** Topograph (0.2 V, 5 pA, 3×3 nm^2) of an island with the molecule at the center (white arrow) in its pristine state appearing as a depression. **b** Same area imaged at 0.2 V after the voltage had been raised to 0.5 V for a few seconds with the tip placed above the central molecule (current feedback enabled). The former depression converted to a small protrusion. **c** After repeating the manipulation procedure, the center molecule reverted to its original state. **d** Time series of the tunneling current measured at $V = 0.5$ V with feedback disabled. Frequent switching is detected between current levels of ≈ 5.1 and 7.4 pA. Imaging at low bias revealed that the current levels reflect a depression and a protrusion, respectively.

Besides the local, controlled conversion of individual molecules, switching may be remotely triggered at distances up to ≈ 20 nm (Figure 6.6). Pulses of 2 V were applied on the Cu(111) surface (red dot in Figure 6.6a), which lead to the switching of many molecules, some of them encircled in red in Figure 6.6b. Interestingly, molecules up to ≈ 20 nm away from the location of the pulses were switched as well. This fairly efficient and long range remote switching is most probably due to hot electrons that propagate along the Cu(111) surface [172].

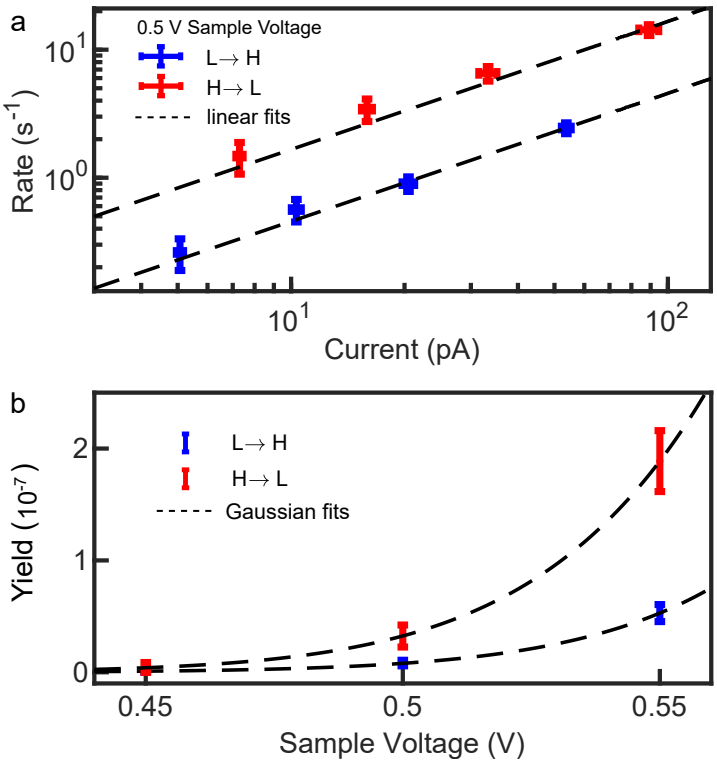

Figure 6.5: Switching rates and yields. **a** Rate of switching from the pristine L state to the H state and back as a function of the tunneling current. **b** Switching yields, defined as the switching rate normalized to the tunneling current, measured at three sample voltages. The uncertainty bars represent one standard deviation.

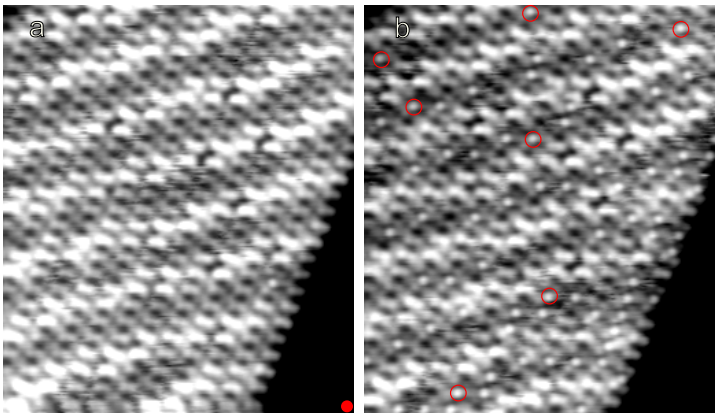

Figure 6.6: Long-range switching. **a** STM image of an island with molecules in the pristine (L) state. 10 pulses of 2 V for 200 ms each (I reaching $\approx$ 55 pA during the pulses) were applied on the Cu(111) substrate at the position indicated by a red dot. **b** STM image after the series of pulses. Several molecules switched to the H state, some of which are highlighted with red circles. Switched molecules are observed at distances as far as 21 nm away from the excitation point. This distance represents a lower bound as molecules outside the scanned area may have switched as well. Both images were acquired at 0.2 V, 5 pA ($15.6 \times 18.2\,\mathrm{nm}^2$).

6.3.4 Identification of the spin states

High-resolution dI/dV spectra of the molecules have been recorded with and without magnetic field. Molecules in the pristine (L) state essentially exhibit no features in the energy range ±8 meV (blue curve in Figure 6.7a). In contrast, the spectrum of the switched (H) state shows a pronounced dip centered at the Fermi level (red curve in Figure 6.7a). The dip is consistent with broadened inelastic excitation steps. The energy shift and amplitude decrease of these inelastic steps in a magnetic field of 8 T evidence that these excitations are related to the molecular spin. They are associated to spin flips involving an exchange of angular momentum between the molecule and the tunneling electrons. Based on these observations, we ascribe the pristine and switched states to the LS and HS states, respectively.

The presence of magnetic excitation steps at 0 T indicate that the molecular magnetic moment has a preferred orientation in the absence of magnetic field, *i.e.* magnetic anisotropy is present. We use the following phenomenological spin Hamiltonian to describe the energy of the magnetic states [55]:

$$\hat{H} = D\hat{S}_z^2 + E\left(\hat{S}_x^2 - \hat{S}_y^2\right) + g_z\mu_B B\hat{S}_z, \tag{6.1}$$

where D and E are the uniaxial and transverse anisotropy parameters, $\hat{S} = \left(\hat{S}_x, \hat{S}_y, \hat{S}_z\right)$ the spin operator, g_z the Landé g-factor, μ_B the Bohr magneton, and B the applied magnetic field perpendicular to the surface. For simplicity, the quantization axis z is chosen perpendicular to the substrate. We consider a total spin S=2, *i.e.* the formal spin of the HS state, which leads to an effective magnetic moment of $2 \cdot \sqrt{S\,(S+1)} \approx 4.9\,\mu_B$ per molecule comparable with that inferred from magnetometry measurements[170]. The diagonalization of the Hamiltonian of Eq. 6.1 leads to eigenstates $|\psi_i\rangle$ ($i = 1 \ldots 5$ for S=2) and eigenenergies E_i, from which differential-conductance spectra are simulated [173]. The parameter set $D = 0.8$ meV, $E \approx 0$, and $g_z = 1.8$ leads to the best agreement with the experimental data (dashed curves in Figure 6.7). (Fits considering S=1 or 3 lead to much poorer agreements.) The uniaxial anisotropy parameter is very close to $D = 0.9$ meV as inferred from X-ray magnetic circular dichroism measurements of the complex [Fe((3,5-$(CH_3)_2$Pz)$_3$BH)$_2$] on Cu(111), which lends further support to the model.

The fit of the dI/dV spectra with the Hamiltonian of Equation 6.1 shows the consistency of the data with a spin S=2. The exact values of the anisotropy parameters should be confirmed using more detailed measurements in magnetic

vector fields or using complementary techniques. With $D = 0.8\,\text{meV}$, $E = 0$, $g = 1.8$ and in the absence of a magnetic field, the ground state of the system is $|\psi_1\rangle = |0\rangle$ (expressed in the basis $|S_z\rangle$), *i.e.* with a spin orientation in the plane of the molecular layer.

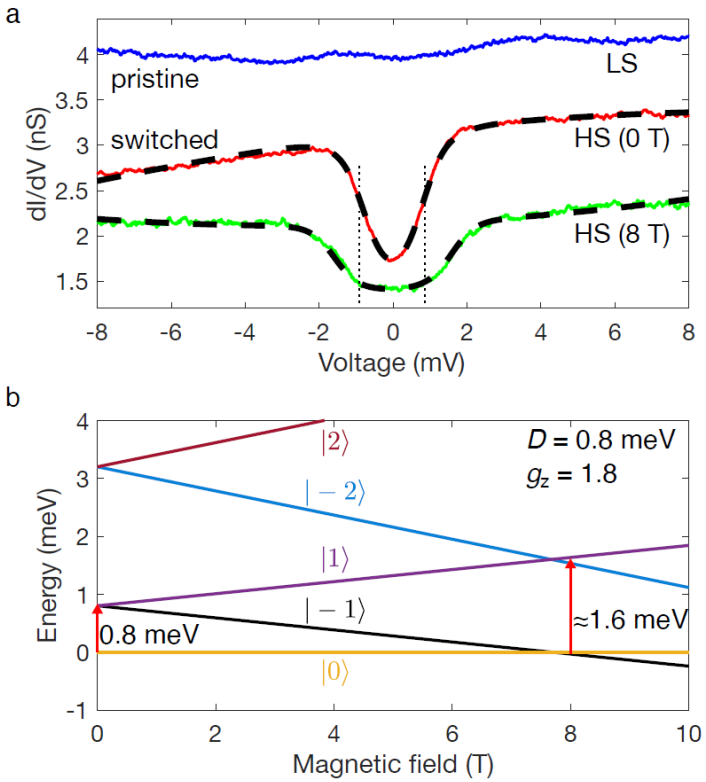

Figure 6.7: Identification of the spin states via spin-flip spectroscopy. **a** $\mathrm{d}I/\mathrm{d}V$ spectra acquired atop the center of a molecule in the pristine (blue, LS) and switched (red, HS) states at 1.7 K (with no external magnetic field). The spectrum of the switched molecule exhibits a dip consistent with broadened inelastic excitation steps (spin flips). In a magnetic field of 8 T, the steps are shifted to higher energies and have a lower amplitude (green), confirming the magnetic origin of the excitation steps. The spectra of the switched molecule can be conjointly fitted (dashed lines) using the spin Hamiltonian of Equation 6.1 with S=2, $g = 1.8$, $D = 0.8\,\text{meV}$ and $E \approx 0$ (adjustable parameters) including temperature broadening ($T = 2.5\,\text{K}$) as well as a cubic background. Spectra acquired over a pristine molecule under 8 T remain featureless (not shown). The vertical dotted lines are guide to the eye to better visualize the increase of the step energies with magnetic field. The LS and HS (8 T) spectra have been vertically shifted by +1 and −1 nS for clarity. Prior to the voltage sweep, the current feedback was opened at 10 mV and 30 pA. **b** Energies of the eigenstates $|S_z\rangle$ as a function of the external magnetic field for $D = 0.8\,\text{meV}$, $E = 0$, and $g_z = 1.8$. The vertical red arrows indicate possible transitions at 0 and 8 T via spin-flip processes with tunnel electrons.

The excitation steps then correspond to transitions to $|\psi_{2,3}\rangle = |\pm 1\rangle$ at $E_{2,3} = 0.8\,\mathrm{meV}$, which are experimentally observed as a single transition (Figure 6.7b). In a magnetic field, the Zeeman term tends to favor large $|S_z|$ in contrast to the uniaxial anisotropy term ($D > 0$) that stabilizes small $|S_z|$. At 8 T, both terms are comparable in magnitude. As a consequence,$|0\rangle$ and $|-1\rangle$ are almost degenerate and so are $|+1\rangle$ and $|-2\rangle$ (Figure 6.7b). The separation of these two pairs is $\approx 1.6\,\mathrm{meV}$. In other words, at 8 T, we essentially observe transitions from $|-1\rangle$ to $|-2\rangle$ and from $|0\rangle$ to $|1\rangle$.

It should be emphasized that the identification of the spin states via the observation of magnetic excitations in the $\mathrm{d}I/\mathrm{d}V$ spectra is not limited to SCO systems exhibiting magnetic anisotropy. In the case of an isotropic spin system, the Hamiltonian of Eq. 6.1 would be reduced to the Zeeman term, which splits the $|S_z\rangle$ states under a magnetic field. Transitions from $|-2\rangle$ to $|-1\rangle$ would then be observed at an energy $g\mu_B B$ ($\approx 0.9\,\mathrm{meV}$ at 8 T for $g = 2$) in $\mathrm{d}I/\mathrm{d}V$ spectra.

6.4 Conclusion

We investigated the molecular SCO complex [Fe(HB(1,2,4-triazol-1-yl)$_3$)$_2$] adsorbed on a Cu(111) surface with scanning tunneling microscopy. The complexes self-assemble into an ordered structure and form large islands. The molecules are efficiently switched between the LS and HS states by injecting electrons. This may be realized locally by placing the tip above a targeted molecule with a mild voltage ($\gtrsim 0.5\,\mathrm{V}$) or by injecting more energetic electrons ($V \approx 2\,\mathrm{V}$) into the substrate. The latter procedure allows the remote switching of molecules in a radius of at least 20 nm from the excitation point. Spectra acquired atop the center of HS molecules reveal excitation steps that change in an applied magnetic field, while no features are found for LS molecules. The inelastic steps correspond to magnetic excitations of the HS molecule and show that the magnetic moment of the molecule has a preferred orientation. Besides enabling an unambiguous identification of the spin states, these results suggest that manipulation of the quantum spins of the SCO complexes may be feasible.

6.5 Acknowledgement

We acknowledge financial support from the European Union's Horizon 2020 program, grant number 766726. M.G. acknowledges funding from the Deutsche Forschungsgemeinschaft (DFG; Project-ID 278162697 - CRC 1242, Project A08). We are indebted to D. Moreno, D. Ecija and F. Calleja (IMDEA Nanoscience, Madrid, Spain) for their involvement in initial evaporation and room-temperature STM tests on this compound. We thank G. Molnar and A. Bousseksou (LCC-CNRS, Toulouse, France) for fruitful discussions.

6.6 Methods

6.6.1 Synthesis

The [Fe(HB(1,2,4-triazol-1-yl)$_3$)$_2$] powder was synthesized following the description of Ref. [170].

6.6.2 STM

The Cu(111) surface was prepared by cycles of Ar ion bombardment (1.5 keV) and annealing to 500 °C. [Fe(HB(1,2,4-triazol-1-yl)$_3$)$_2$] was sublimated from a heated crucible ($\approx$ 210 °C). STM tips were electrochemically etched from W wire and annealed *in vacuo*. Experiments were carried out in ultra-high vacuum mostly with a STM operated at $\approx$ 4.6 K (Createc). dI/dV spectra were acquired at 1.7 K with a Unisoku USM1300 STM. The shown dI/dV spectra are obtained from numerical derivation of the current, followed by a convolution with a Gaussian for low-pass filtering.

6.6.3 Author contributions

MG, RB, and KR designed the experiment. SJ, AW performed the STM experiments. SJ, MG, and RB analyzed the STM data. MG wrote the manuscript with contributions from all authors. All authors discussed the results and commented on the manuscript.

6.7 Supporting Information

6.7.1 Molecule removal from an island

Figure 6.8 shows a series of images illustrating the sequential removal of single molecules from an island. For picking up a molecule, the tip is positioned above the targeted molecule and the tunneling parameters are adjusted to 50 mV and 5 pA. The current feedback remains active during the entire procedure. The tip is then approached toward the molecule by progressively increasing the setpoint current to 20 pA. After typically 50 ms, the current increases to ≈ 65 pA and the feedback responds by retracting the tip by ≈ 180 pm. The tip was then indented in the Cu(111) substrate to remove the attached molecule form the tip. As discussed in the main text, the orientation of the depressions left behind indicates the orientation of the molecules within the layers. We removed up to 6 molecules from a single island. All resulting depressions exhibited the same orientation. In particular, we verified that molecules belonging to adjacent rows and columns have the same orientation.

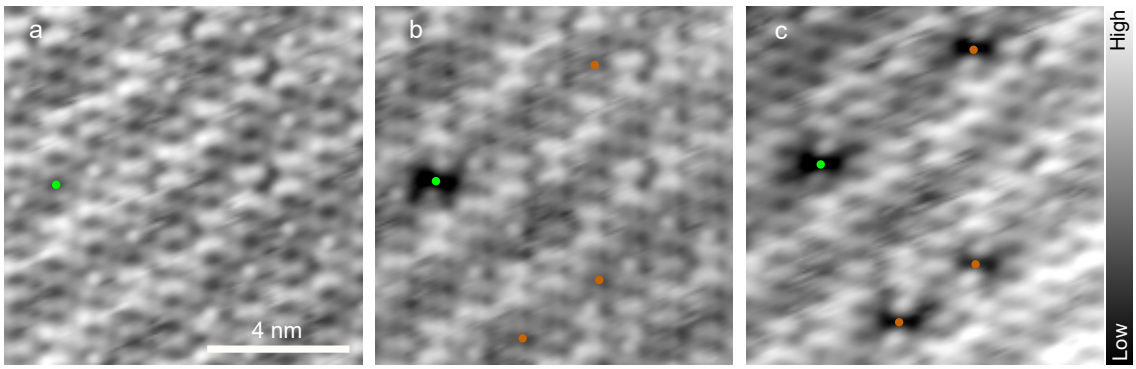

Figure 6.8: **a**–**c** Series of constant-current topographs of [Fe(HB(1,2,4-triazol-1-yl)$_3$)$_2$] on Cu(111) (200 mV, 5 pA, 10×10 nm^2) illustrating the evolution of a layer as single molecules are removed. The procedure described in the text was applied to the molecule marked in green in **a**, which leads to a depression in the molecular layer after the manipulation (shown in **b**). The molecule removal procedure was then repeated on the molecules marked in orange, leading to the image shown in **c**. The color scales cover **a** 105 pm and **b**–**c** 100 pm.

6.7.2 Adsorption-induced chirality

We assume that the molecules lie flat on the surface with the B-Fe-B axis parallel to the surface. A triazole group from each of the two scorpionate ligands is making the contact to the surface (see for instance Figure 6.9a). Viewed along the B-Fe-B axis, the angle between the triazole groups in contact with the substrate is approximately 60°. The configuration shown in Figure 6.9b is obtained by rotating the molecule by −60° around the B-Fe-B axis. An azimuthal rotation of the molecule displayed

in Figure 6.9a around the axis perpendicular to the surface cannot lead to that in Figure 6.9b (see also top views in Figures 6.9c–d). In other words, the adsorption of the molecule on the surface induces a chirality.

The depression left upon the removal of a molecule provides information on the orientation of the molecule defined by the upper triazole groups (opaque atoms in Figures 6.9c–d), which is the same for all molecules within an island. The periodicity of the molecular structure is directly inferred from the STM images. Attempts to reproduce the regular structure observed in Figure 6.2 of the manuscript by using the enantiomer shown in Figure 6.9b, and with a combinations of both enantiomers failed due to unphysical partial overlap of the molecules. Only the structure composed of solely the enantiomer shown in Figure 6.9a led to a reasonable result, the one displayed in Figure 6.2 of the manuscript.

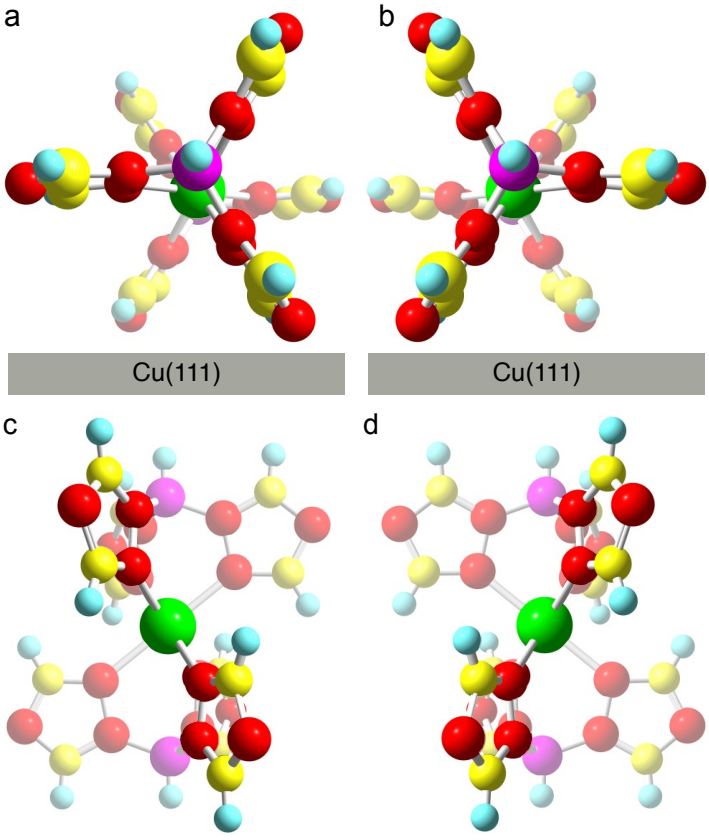

Figure 6.9: **a**–**b** View of the [Fe(HB(1,2,4-triazol-1-yl)$_3$)$_2$] molecule along the B-Fe-B axis adsorbed on a Cu(111) surface. From **a** to **b** the molecule is effectively rotated by −60°. The two configurations correspond to two adsorption-induced enantiomers. **c**–**d** Corresponding top views of the configurations. The transparency of the atoms indicates the distance from the observer. Opaque atoms are closer than semi-transparent atoms.

6.7.3 Chirality of islands

As the chirality is induced by adsorption, both enantiomers are expected to be present on the surface. If an island is indeed composed of a single enantiomer, different islands should be present on the surface. This is indeed the case. As detailed in the main text, the islands exhibit stripes, which make them chiral. For instance, the island of Figure 6.10a has stripes going from the top left to the bottom right. Azimuthal rotation of that island cannot reproduce the island shown in Figure 6.10b. The removal of molecules from these islands reveals different orientations of the depressions (Figures 6.10c–d), and hence different orientations of the molecules.
The island shown in Figure 6.10a is equivalent to that shown in Figure 2 of the manuscript, with the molecular structure shown in Figure 6.10g. Attempts to reproduce the island shown in Figure 6.10b using the same enantiomer failed due to unphysical overlaps. Instead, the structure shown in Figure 6.10h made with the other enantiomer leads to a good match. The two structures are equivalent in terms of the molecule-molecule interactions but are chiral.

6.7.4 Reduced height of edge molecules

Molecules at the edge of an island appear $\approx 55\,\mathrm{pm}$ lower than molecules within islands at 1.6 V (see for instance the left column in the inset to Figure 6.11). Red circles in Figure 6.11 shows a cross-sectional profile of an island edge. The height difference may be understood from a simple model that takes into account the lateral extension of the tip. The limited lateral resolution implies that the current above the center of a molecule is increased by the contributions of the neighbors, which are fewer for a molecule at an edge. Adding these current contributions with exponentially decaying weight the experimental data may be qualitatively reproduced (black curve in Figure 6.11).

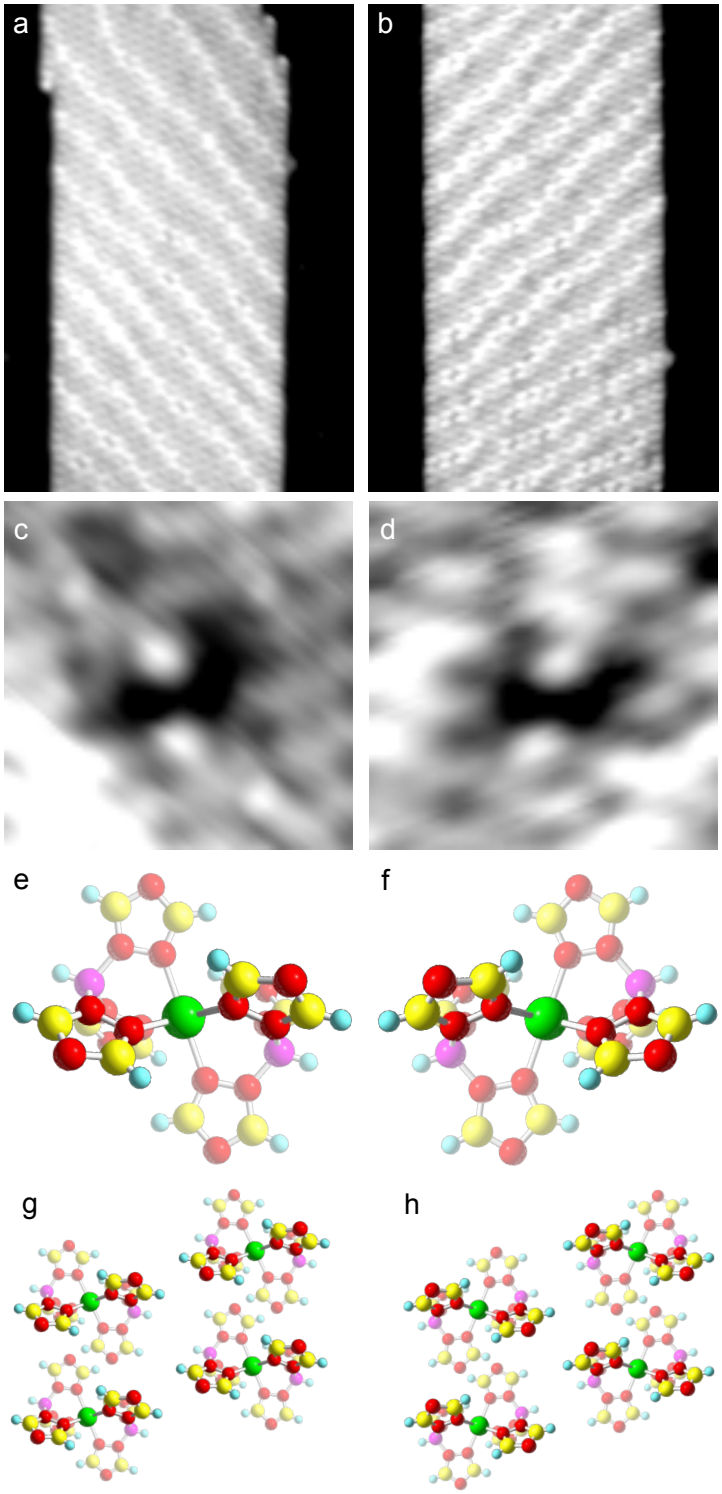

Figure 6.10: **a**–**b** STM images displaying the chirality of the islands. The island in **a** exhibits stripes from the top left to the bottom right. An azimuthal rotation **a** cannot reproduce the pattern in **b**, which was observed on the same sample. **c** and **d** Depressions after removal of a molecule from the islands in **a** and **b**, respectively. The molecular structures of island **a** and **b** may be reproduced by using the enantiomers **e** and **f**, respectively. The corresponding molecular structures are shown in **g** and **h**.

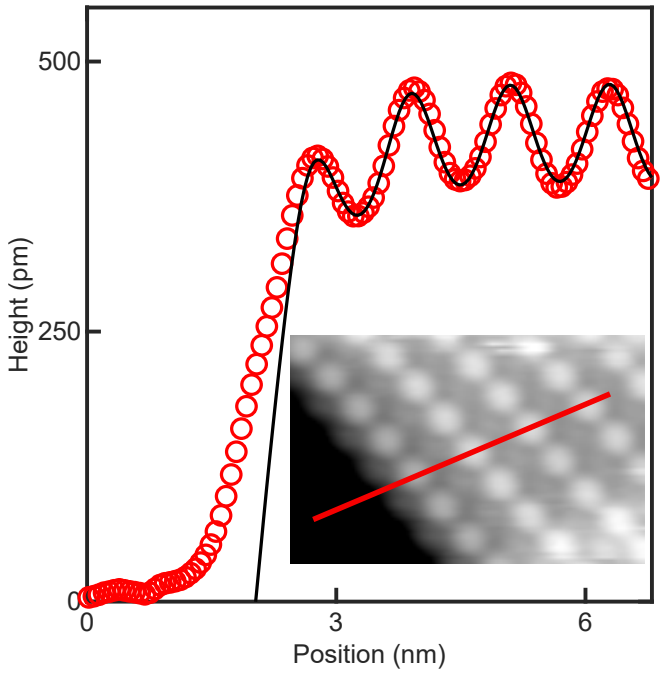

Figure 6.11: Cross-sectional profile of a [Fe(HB(1,2,4-triazol-1-yl)$_3$)$_2$] island edges along the line shown in the topograph in the inset ($V = 1.6\,\mathrm{V}$, $I = 5\,\mathrm{pA}$). Red circles show experimental data. The black line results from a simple model of a tip with limited lateral resolution. No attempt was made to fit the data at low apparent heights because the large vertical excursion of the tip of the STM implies that the unknown three-dimensional tip structure must be taken into account.

7 Conclusion

In this thesis, different spin-crossover (SCO) complexes in direct contact with metal substrates were investigated using low-temperature scanning tunneling microscopy (LT-STM). These investigations allow a better understanding of cooperative effects in SCO complexes, of the mechanism in the electron-induced switching, and of the importance of the molecule-substrate interactions. Results of this thesis may help to understand and design further SCO systems.

In chapter 4.1, the SCO complex $Fe(H_2B(pyrazole)(pyridylpyrazole))_2$ is investigated in detail. Adsorbed on a Ag(111) surface it self assembles in grid like tetramers. Highly efficient reversible switching can be performed at only two complexes in a tetramer by electron injection. Investigations on the magnetically passive $Zn(H_2B(pyrazole)(pyridylpyrazole))_2$ complex reveal no switching in STM experiments. With this the reversible switching is interpreted as a spin transition. A model for the structure of a tetramer is presented, that fits to the observed topographic features in the experiment. It explains why the remaining two molecules in a tetramer are immutable against injection of electrons. Steric repulsion hinders the movement of molecular subunits, which is required for switching. With current injection into the immutable molecules, remote switching of the remaining molecules in a tetramer is induced. A simplified model of hybridization between LUMO orbitals is presented, that can reproduce the efficiency of the remote switching. Cooperative effects in SCO systems has so far been interpreted in terms of intermolecular elastic interactions. Our study shows, intermolecular electron transfer may lead to similar effects. The presented system may be a model system, that can be used to design larger grids of SCO complexes. By using steric repulsion and tuning the electronic coupling between neighboring complexes, specific switching properties may be achieved in future SCO systems.
At negative sample voltages, reversible switching between LS, HS and a new state is observed, presented in chapter 4.2. The new state can be consistently explained as a negatively charged HS state.

In chapter 4.3, experiments on isostructural Co(H_2B(pyrazole)(pyridylpyrazole))$_2$ are reported. Self assembly into tetramers and reversible switching between two spin states at both polarities of the sample voltage is observed. Strong deviations of the switching yields for different sample voltages are evidenced. With this a tentative model of the switching mechanism is derived, named electron-induced excited spin-state trapping (ELIESST). This model might be the basis for more advanced pictures of the switching mechanism in the future. It shows, that the electronic structure of the complexes, e.g. the spatial orientation and the energy of orbitals play a key role in the switching mechanism. Hence, e.g. the switching mechanism may be sensitive to the orientation of adsorbed complexes. This might be an important design criterion.

In chapter 5, investigations on the SCO complex Fe(neoim)$_2$ are presented, where the role of the metal substrate is explored. Fe(neoim)$_2$ remains intact on Ag(111) after deposition and reversible electron induced switching is performed. In contrast to this and against the common expectation, the complex fragments on a Au(111) surface. Extensive DFT calculations reveal a strong geometric distortion of the complex on Ag(111) due to van der Waals forces. Enhanced covalent bonding of the fragments to the Au(111) substrate are likely the reason for fragmentation.

In chapter 6, experiments on the SCO complex Fe(HB(1,2,4-triazol-1-yl)$_3$)$_2$ on a Cu(111) surface are shown. The complexes self assemble into large ordered islands. Efficient switching between two states can be triggered by direct electron injection. Additionally, by injecting electrons at high energies, e.g. at $\approx 2\,\mathrm{V}$, into the Cu substrate next to an island, many molecules over larger distances from the excitation point ($> 20\,\mathrm{nm}$) can be reversibly switched. Scanning tunneling spectroscopy reveals inelastic steps, whose energies change in an applied magnetic field. The steps correspond to magnetic excitations of the HS molecule. The spectra of the LS state remain featureless around the Fermi energy. With this spin-flip spectroscopy, the molecules magnetic state can be identified. Moreover, magnetic anisotropy is observed. This indicates, the magnetic moment of the molecule has a preferred orientation. Identifying the magnetic state might be a challenging task with STM. This study presents successfully performed spin-flip spectroscopy on a SCO complex.

8 List of Publications

First Author

S. Johannsen et al., "Electron-Induced Spin-Crossover in Self-Assembled Tetramers", ACS Nano **15**, 11770–11778 (2021)

S. Johannsen et al., "Spin Crossover in a Co Complex on Ag(111)", Angew. Chem. Int. Ed. **61**, e202115892 (2022)

S. Johannsen et al., "Three-State Switching of an Fe Spin Crossover Complex", J. Phys. Chem. C **126**, 7238–7244 (2022)

S. Johannsen et al., "Spin-Crossover and Fragmentation of Fe(neoim)$_2$ on Silver and Gold", J. Phys. Chem. Lett. **14**, 7814–7823 (2023)

Co-Author

S. Rohlf et al., "Influence of Substrate Electronic Properties on the Integrity and Functionality of an Adsorbed Fe(II) Spin-Crossover Compound", J. Phys. Chem. C **123**, 17774–17780 (2019)

T. Brandl et al., "Iron in a Cage: Fixation of a Fe(II)tpy$_2$ Complex by Fourfold Interlinking", Angew. Chem. Int. Ed. **59**, 15947–15952 (2020)

A. Köbke et al., "Reversible Coordination-Induced Spin-State Switching in Complexes on Metal Surfaces", Nat. Nanotechnol. **15**, 18–21 (2020)

T. Jasper-Toennies et al., "Rotation of Ethoxy and Ethyl Moieties on a Molecular Platform on Au(111)", ACS Nano **14**, 3907–3916 (2020)

9 Acknowledgements

Here I would like to thank the following people:

- Prof. Dr. Richard Berndt for offering me the opportunity to create this thesis. Furthermore he gave me the chance to work at state of the art STM equipment. He was always available for fruitful discussions and for tackling any problems. He was an excellent supervisor in all of my scientific projects and work.
- Jun. Prof. Dr. Manuel Gruber for additional supervision in the first years of my time as a PhD student. I gained a lot of experience from his expertise in STM and SCO systems. He was a great mentor in teaching how to solve problems in an efficient way. With his suggestions and supervision, all of my scientific projects obtained more impact. He did proofreading of parts of this thesis.
- Prof. Dr. Felix Tuczek, Dr. Sascha Ossinger and Jan Grunwald for synthesizing and providing the SCO complexes investigated in chapter 4 and their work at the manuscript and SI. Discussions with Prof. Dr. F. Tuczek led to valuable ideas.
- Prof. Dr. Heiko Wende and Alexander Herman for performing the XPS measurements and providing the shown XPS spectra in chapter 4.3.
- Prof. Dr. Cyrille Barreteau for performing the DFT calculations in chapter 5 and his inputs to the publication.
- Prof. Dr. José Antonio Real for providing the SCO complexes investigated in chapter 5 and his support of text and figures in the manuscript and SI in chapter 5.
- Prof. Dr. Eugenio Coronado for fruitful discussion about the project of self-assembled tetramers.
- Dr. Karl Ridier for providing the molecules investigated in chapter 6 and for his input.

- Dr. Troels Markussen for his DFT calculations, figures and input to the project in chapter 4.
- Dr. Alexander Weismann and Niklas Ide for introducing me in working at the Unisoku STM. Additionally Dr. A. Weismann did proofreading of parts of this thesis.
- Sascha Schüddekopf for measuring parts of the STM data in chapter 4.2 under my supervision during his bachelor thesis.
- all other collaborators for their help, support and input to the corresponding scientific projects.
- Dr. Thomas Jürgens for technical and IT support and proofreading of parts of this thesis.
- ESI lab team Alexander Köbke, Dr. Torben Jasper-Toennies, Dr. Xiangzhi Meng, Dr. Chao Li and all others for a comfortable working atmosphere and support.
- Prof. Dr. Markus Gruyters for offering me good options in choosing my teaching duties at the physics department and proofreading of parts of this thesis.
- technicians René Woltmann, Jörg Neubauer, Hans-Joachim Neumann for technical support and fruitful discussions.
- Claudia Läufer for support in all bureaucratic matters.
- Marten Treichel, Behzad Mortezapour and all the remaining group members for a nice atmosphere and support within the work group.
- staff from CAU that are not listed above who provided services that lead to progress of my work.
- financial support from the European Union's Horizon 2020 program, Grant No. 766726 and the state Schleswig-Holstein.
- my friends and family, especially my parents Jürgen and Meike and my fiancée Ariane Aquino for unconditional support.

List of Abbreviations

DFT	density functional theory
ELIESST	electron-induced excited spin-state trapping
HOMO	highest occupied molecular orbital
HS	high-spin
I-V	current-voltage
IETS	inelastic electron tunneling spectroscopy
IR	infrared
LIESST	light-induced excited spin state trapping
LS	low-spin
LT-STM	low-temperature scanning tunneling microscopy
LUMO	lowest unoccupied molecular orbital
ML	monolayer
MO	molecular orbital
PDOS	projected density of states
SCO	spin-crossover
SOMO	singly occupied molecular orbital
STM	scanning tunneling microscopy
STS	scanning tunneling spectroscopy
UHV	ultra-high vacuum
vdW	van der Waals
WKB	Wentzel-Kramers-Brillouin

Bibliography

[1] S. Johannsen, S. Ossinger, T. Markussen, F. Tuczek, M. Gruber, and R. Berndt, "Electron-Induced Spin-Crossover in Self-Assembled Tetramers", ACS Nano **15**, 11770–11778 (2021).

[2] S. Johannsen, S. Schüddekopf, S. Ossinger, J. Grunwald, F. Tuczek, M. Gruber, and R. Berndt, "Three-State Switching of an Fe Spin Crossover Complex", J. Phys. Chem. C **126**, 7238–7244 (2022).

[3] S. Johannsen, S. Ossinger, J. Grunwald, A. Herman, H. Wende, F. Tuczek, M. Gruber, and R. Berndt, "Spin Crossover in a Co Complex on Ag(111)", Angew. Chem. Int. Ed. **61**, e202115892 (2022).

[4] S. Johannsen, M. Gruber, C. Barreteau, M. Seredyuk, J. Antonio Real, T. Markussen, and R. Berndt, "Spin-Crossover and Fragmentation of $Fe(neoim)_2$ on Silver and Gold", J. Phys. Chem. Lett. **14**, 7814–7823 (2023).

[5] E. Coronado, "Molecular magnetism: from chemical design to spin control in molecules, materials and devices", Nat. Rev. Mater. **5**, 87–104 (2020).

[6] H. J. Shepherd, I. A. Gural'skiy, C. M. Quintero, S. Tricard, L. Salmon, G. Molnár, and A. Bousseksou, "Molecular actuators driven by cooperative spin-state switching", Nat. Commun. **4**, 2607 (2013).

[7] A. Diaconu, S.-L. Lupu, I. Rusu, I.-M. Risca, L. Salmon, G. Molnár, A. Bousseksou, P. Demont, and A. Rotaru, "Piezoresistive Effect in the $[Fe(Htrz)_2(trz)](BF_4)$ Spin Crossover Complex", J. Phys. Chem. Lett. **8**, 3147–3151 (2017).

[8] O. Kahn and C. J. Martinez, "Spin-transition polymers: from molecular materials toward memory devices", Science **279**, 44–48 (1998).

[9] V. Shalabaeva, K. Ridier, S. Rat, M. D. Manrique-Juarez, L. Salmon, I. Séguy, A. Rotaru, G. Molnár, and A. Bousseksou, "Room temperature current modulation in large area electronic junctions of spin crossover thin films", Appl. Phys. Lett. **112**, 013301 (2018).

[10] G. Hao, A. Mosey, X. Jiang, A. J. Yost, K. R. Sapkota, G. T. Wang, X. Zhang, J. Zhang, A. T. N'Diaye, R. Cheng, X. Xu, and P. A. Dowben, "Nonvolatile voltage controlled molecular spin state switching", Appl. Phys. Lett. **114**, 032901 (2019).

[11] A. Gee, A. H. Jaafar, B. Brachňaková, J. Massey, C. H. Marrows, I. Šalitroš, and N. T. Kemp, "Multilevel Resistance Switching and Enhanced Spin Transition Temperature in Single- and Double-Molecule Spin Crossover Nanogap Devices", J. Phys. Chem. C **124**, 13393–13399 (2020).

[12] Y. Zhang, I. Séguy, K. Ridier, V. Shalabaeva, M. Piedrahita-Bello, A. Rotaru, L. Salmon, G. Molnár, and A. Bousseksou, "Resistance Switching in Large-Area Vertical Junctions of the Molecular Spin Crossover Complex $[Fe(HB(tz)_3)_2]$: ON/OFF Ratios and Device Stability", J. Phys. Condens. Matter **32**, 214010 (2020).

[13] E. P. Geest, K. Shakouri, W. Fu, V. Robert, V. Tudor, S. Bonnet, and G. F. Schneider, "Contactless Spin Switch Sensing by Chemo-Electric Gating of Graphene", Adv. Mater. **32**, 1903575 (2020).

[14] C. Bartual-Murgui, A. Akou, C. Thibault, G. Molnár, C. Vieu, L. Salmon, and A. Bousseksou, "Spin-crossover metal–organic frameworks: promising materials for designing gas sensors", J. Mater. Chem. C **3**, 1277–1285 (2015).

[15] C. M. Jureschi, J. Linares, A. Rotaru, M. H. Ritti, M. Parlier, M. M. Dîrtu, M. Wolff, and Y. Garcia, "Pressure sensor via optical detection based on a 1d spin transition coordination polymer", Sensors **15**, 2388–2398 (2015).

[16] K. Boukheddaden, M. H. Ritti, G. Bouchez, M. Sy, M. M. Dîrtu, M. Parlier, J. Linares, and Y. Garcia, "Quantitative contact pressure sensor based on spin crossover mechanism for civil security applications", J. Phys. Chem. C **122**, 7597–7604 (2018).

[17] B. Benaicha, K. Van Do, A. Yangui, N. Pittala, A. Lusson, M. Sy, G. Bouchez, H. Fourati, C. J. Gómez-García, S. Triki, and K. Boukheddaden, "Interplay between spin-crossover and luminescence in a multifunctional single crystal iron(II) complex: towards a new generation of molecular sensors", Chem. Sci. **10**, 6791–6798 (2019).

[18] M. Gruber and R. Berndt, "Spin-Crossover Complexes in Direct Contact with Surfaces", Magnetochemistry **6**, 35 (2020).

[19] L. Kipgen, M. Bernien, F. Tuczek, and W. Kuch, "Spin-Crossover Molecules on Surfaces: From Isolated Molecules to Ultrathin Films", Adv. Mater. **33**, 2008141 (2021).

[20] M. Gruber, V. Davesne, M. Bowen, S. Boukari, E. Beaurepaire, W. Wulfhekel, and T. Miyamachi, "Spin state of spin-crossover complexes: From single molecules to ultrathin films", Phys. Rev. B **89**, 195415 (2014).

[21] M. Gruber, T. Miyamachi, V. Davesne, M. Bowen, S. Boukari, W. Wulfhekel, M. Alouani, and E. Beaurepaire, "Spin crossover in Fe(phen) $_2$ (NCS) $_2$ complexes on metallic surfaces", J. Chem. Phys. **146**, 092312 (2017).

[22] T. Jasper-Tönnies, M. Gruber, S. Karan, H. Jacob, F. Tuczek, and R. Berndt, "Deposition of a Cationic Fe ^{III} Spin-Crossover Complex on Au(111): Impact of the Counter Ion", J. Phys. Chem. Lett. **8**, 1569–1573 (2017).

[23] S. Ossinger, H. Naggert, L. Kipgen, T. Jasper-Toennies, A. Rai, J. Rudnik, F. Nickel, L. M. Arruda, M. Bernien, W. Kuch, R. Berndt, and F. Tuczek, "Vacuum-Evaporable Spin-Crossover Complexes in Direct Contact With a Solid Surface: Bismuth Versus Gold", J. Phys. Chem. C **121**, 1210–1219 (2017).

[24] K. S. Kumar, M. Studniarek, B. Heinrich, J. Arabski, G. Schmerber, M. Bowen, S. Boukari, E. Beaurepaire, J. Dreiser, and M. Ruben, "Engineering On-Surface Spin Crossover: Spin-State Switching in a Self-Assembled Film of Vacuum-Sublimable Functional Molecule", Adv. Mater. **30**, 1705416 (2018).

[25] L. Zhang, Y. Tong, M. Kelai, A. Bellec, J. Lagoute, C. Chacon, Y. Girard, S. Rousset, M.-L. Boillot, E. Rivière, T. Mallah, E. Otero, M.-A. Arrio, P. Sainctavit, and V. Repain, "Anomalous Light-Induced Spin-State Switching for Iron(II) Spin-Crossover Molecules in Direct Contact with Metal Surfaces", Angew. Chem. Inter. Ed. **59**, 13341–13346 (2020).

[26] S. Ossinger, L. Kipgen, H. Naggert, M. Bernien, A. J. Britton, F. Nickel, L. M. Arruda, I. Kumberg, T. A. Engesser, E. Golias, C. Näther, F. Tuczek, and W. Kuch, "Effect of ligand methylation on the spin-switching properties of surface-supported spin-crossover molecules", J. Phys. Condens. Matter **32**, 114003 (2020).

[27] T. G. Gopakumar, M. Bernien, H. Naggert, F. Matino, C. F. Hermanns, A. Bannwarth, S. Mühlenberend, A. Krüger, D. Krüger, F. Nickel, W. Walter, R. Berndt, W. Kuch, and F. Tuczek, "Spin-Crossover Complex on Au(111): Structural and Electronic Differences Between Mono- and Multilayers", Chem. Eur. J. **19**, 15702–15709 (2013).

[28] S. Gueddida and M. Alouani, "Spin crossover in a single $Fe(phen)_2$ $(NCS)_2$ molecule adsorbed onto metallic substrates: An *ab initio* calculation", Phys. Rev. B **87**, 144413 (2013).

[29] T. Knaak, C. González, Y. J. Dappe, G. D. Harzmann, T. Brandl, M. Mayor, R. Berndt, and M. Gruber, "Fragmentation and Distortion of Terpyridine-Based Spin-Crossover Complexes on Au(111)", J. Phys. Chem. C **123**, 4178–4185 (2019).

[30] S. Rohlf, J. Grunwald, T. Jasper-Toennies, S. Johannsen, F. Diekmann, M. Studniarek, R. Berndt, F. Tuczek, K. Rossnagel, and M. Gruber, "Influence of Substrate Electronic Properties on the Integrity and Functionality of an Adsorbed Fe(II) Spin-Crossover Compound", J. Phys. Chem. C **123**, 17774–17780 (2019).

[31] S. Gueddida, M. Gruber, T. Miyamachi, E. Beaurepaire, W. Wulfhekel, and M. Alouani, "Exchange Coupling of Spin-Crossover Molecules to Ferromagnetic Co Islands", J. Phys. Chem. Lett. **7**, 900–904 (2016).

[32] F. Prins, M. Monrabal-Capilla, E. A. Osorio, E. Coronado, and H. S. J. van der Zant, "Room-Temperature Electrical Addressing of a Bistable Spin-Crossover Molecular System", Adv. Mater. **23**, 1545–1549 (2011).

[33] N. Konstantinov, A. Tauzin, U. N. Noumbé, D. Dragoe, B. Kundys, H. Majjad, A. Brosseau, M. Lenertz, A. Singh, S. Berciaud, M.-L. Boillot, B. Doudin, T. Mallah, and J.-F. Dayen, "Electrical read-out of light-induced spin transition in thin film spin crossover/graphene heterostructures", J. Mater. Chem. C **9**, 2712–2720 (2021).

[34] P. Stegmann, A. Gee, N. T. Kemp, and J. König, "Statistical analysis of spin switching in coupled spin-crossover molecules", Phys. Rev. B **104**, 125431 (2021).

[35] E. A. Osorio, M. Ruben, J. S. Seldenthuis, J. M. Lehn, and H. S. J. van der Zant, "Conductance Switching and Vibrational Fine Structure of a [2×2] $Co(II)_4$ Gridlike Single Molecule Measured in a Three-Terminal Device", Small **6**, 174–178 (2010).

[36] G. D. Harzmann, R. Frisenda, H. S. J. v. d. Zant, and M. Mayor, "Single-Molecule Spin Switch Based on Voltage-Triggered Distortion of the Coordination Sphere", Angew. Chem. Int. Ed. **54**, 13425–13430 (2015).

[37] R. Frisenda, G. D. Harzmann, J. A. Celis Gil, J. M. Thijssen, M. Mayor, and H. S. J. van der Zant, "Stretching-Induced Conductance Increase in a Spin-Crossover Molecule", Nano Lett. **16**, 4733–4737 (2016).

[38] T. G. Gopakumar, F. Matino, H. Naggert, A. Bannwarth, F. Tuczek, and R. Berndt, "Electron-Induced Spin Crossover of Single Molecules in a Bilayer on Gold", Angew. Chem. Int. Ed. **51**, 6262–6266 (2012).

[39] T. Miyamachi, M. Gruber, V. Davesne, M. Bowen, S. Boukari, L. Joly, F. Scheurer, G. Rogez, T. K. Yamada, P. Ohresser, E. Beaurepaire, and W. Wulfhekel, "Robust spin crossover and memristance across a single molecule", Nat. Commun. **3**, 938 (2012).

[40] T. Jasper-Toennies, M. Gruber, S. Karan, H. Jacob, F. Tuczek, and R. Berndt, "Robust and Selective Switching of an Fe ^{III} Spin-Crossover Compound on Cu_2N/Cu(100) with Memristance Behavior", Nano Lett. **17**, 6613–6619 (2017).

[41] M. Atzori, L. Poggini, L. Squillantini, B. Cortigiani, M. Gonidec, P. Bencok, R. Sessoli, and M. Mannini, "Thermal and light-induced spin transition in a nanometric film of a new high-vacuum processable spin crossover complex", J. Mater. Chem. C **6**, 8885–8889 (2018).

[42] A. Köbke, F. Gutzeit, F. Röhricht, A. Schlimm, J. Grunwald, F. Tuczek, M. Studniarek, D. Longo, F. Choueikani, E. Otero, P. Ohresser, S. Rohlf, S. Johannsen, F. Diekmann, K. Rossnagel, A. Weismann, T. Jasper-Toennies, C. Näther, R. Herges, R. Berndt, and M. Gruber, "Reversible Coordination-Induced Spin-State Switching in Complexes on Metal Surfaces", Nat. Nanotechnol. **15**, 18–21 (2020).

[43] T. Brandl, S. Johannsen, D. Häussinger, N. Suryadevara, A. Prescimone, S. Bernhard, M. Gruber, M. Ruben, R. Berndt, and M. Mayor, "Iron in a Cage: Fixation of a Fe(II)tpy_2 Complex by Fourfold Interlinking", Angew. Chem. Int. Ed. **59**, 15947–15952 (2020).

[44] G. Binnig, H. Rohrer, C. Gerber, and E. Weibel, "Tunneling through a controllable vacuum gap", Appl. Phys. Lett. **40**, 178–180 (1982).

[45] G. Binnig, H. Rohrer, C. Gerber, and E. Weibel, "Surface Studies by Scanning Tunneling Microscopy", Phys. Rev. Lett. **49**, 57–61 (1982).

[46] A. Selloni, P. Carnevali, E. Tosatti, and C. D. Chen, "Voltage-dependent scanning-tunneling microscopy of a crystal surface: graphite", Phys. Rev. B **31**, 2602–2605 (1985).

[47] J. G. Simmons, "Generalized Formula for the Electric Tunnel Effect between Similar Electrodes Separated by a Thin Insulating Film", J. Appl. Phys. **34**, 1793–1803 (2004).

[48] V. A. Ukraintsev, "Data evaluation technique for electron-tunneling spectroscopy", Phys. Rev. B **53**, 11176–11185 (1996).

[49] J. Bardeen, "Tunnelling from a many-particle point of view", Phys. Rev. Lett. **6**, 57–59 (1961).

[50] C. Chen, "Introduction to Scanning Tunneling Microscopy Third Edition", OUP (2021).

[51] C. J. Chen, "Perturbation approach for quantum transmission", Modern Physics Letters B **05**, 107–115 (1991).

[52] J. Tersoff and D. R. Hamann, "Theory and Application for the Scanning Tunneling Microscope", Phys. Rev. Lett. **50**, 1998–2001 (1983).

[53] M. Ziegler, N. Néel, A. Sperl, J. Kröger, and R. Berndt, "Local density of states from constant-current tunneling spectra", Phys. Rev. B **80**, 125402 (2009).

[54] A. J. Heinrich, J. A. Gupta, C. P. Lutz, and D. M. Eigler, "Single-Atom Spin-Flip Spectroscopy", Science **306**, 466–469 (2004).

[55] C. F. Hirjibehedin, C.-Y. Lin, A. F. Otte, M. Ternes, C. P. Lutz, B. A. Jones, and A. J. Heinrich, "Large Magnetic Anisotropy of a Single Atomic Spin Embedded in a Surface Molecular Network", Science **317**, 1199–1203 (2007).

[56] T. Balashov, T. Schuh, A. F. Takács, A. Ernst, S. Ostanin, J. Henk, I. Mertig, P. Bruno, T. Miyamachi, S. Suga, and W. Wulfhekel, "Magnetic Anisotropy and Magnetization Dynamics of Individual Atoms and Clusters of Fe and Co on Pt(111)", Phys. Rev. Lett. **102**, 257203 (2009).

[57] A. A. Khajetoorians, S. Lounis, B. Chilian, A. T. Costa, L. Zhou, D. L. Mills, J. Wiebe, and R. Wiesendanger, "Itinerant Nature of Atom-Magnetization Excitation by Tunneling Electrons", Phys. Rev. Lett. **106**, 037205 (2011).

[58] C. F. Hirjibehedin, C. P. Lutz, and A. J. Heinrich, "Spin Coupling in Engineered Atomic Structures", Science **312**, 1021–1024 (2006).

[59] X. Chen, Y.-S. Fu, S.-H. Ji, T. Zhang, P. Cheng, X.-C. Ma, X.-L. Zou, W.-H. Duan, J.-F. Jia, and Q.-K. Xue, "Probing Superexchange Interaction in Molecular Magnets by Spin-Flip Spectroscopy and Microscopy", Phys. Rev. Lett. **101**, 197208 (2008).

[60] Y.-S. Fu, T. Zhang, S.-H. Ji, X. Chen, X.-C. Ma, J.-F. Jia, and Q.-K. Xue, "Identifying Charge States of Molecules with Spin-Flip Spectroscopy", Phys. Rev. Lett. **103**, 257202 (2009).

[61] N. Tsukahara, K.-i. Noto, M. Ohara, S. Shiraki, N. Takagi, Y. Takata, J. Miyawaki, M. Taguchi, A. Chainani, S. Shin, and M. Kawai, "Adsorption-Induced Switching of Magnetic Anisotropy in a Single Iron(II) Phthalocyanine Molecule on an Oxidized Cu(110) Surface", Phys. Rev. Lett. **102**, 167203 (2009).

[62] H. Spiering, K. Boukheddaden, J. Linares, and F. Varret, "Total free energy of a spin-crossover molecular system", Phys. Rev. B **70**, 184106 (2004).

[63] G. Félix, W. Nicolazzi, L. Salmon, G. Molnár, M. Perrier, G. Maurin, J. Larionova, J. Long, Y. Guari, and A. Bousseksou, "Enhanced Cooperative Interactions at the Nanoscale in Spin-Crossover Materials with a First-Order Phase Transition", Phys. Rev. Lett. **110**, 235701 (2013).

[64] S. Ostrovsky, A. Palii, S. Decurtins, S.-X. Liu, and S. Klokishner, "Microscopic Approach to the Problem of Cooperative Spin Crossover in Polynuclear Cluster Compounds: Application to Tetranuclear Iron(II) Square Complexes", J. Phys. Chem. C **122**, 22150–22159 (2018).

[65] I. C. Berdiell, T. Hochdörffer, C. Desplanches, R. Kulmaczewski, N. Shahid, J. A. Wolny, S. L. Warriner, O. Cespedes, V. Schünemann, G. Chastanet, and M. A. Halcrow, "Supramolecular Iron Metallocubanes Exhibiting Site-Selective Thermal and Light-Induced Spin-Crossover", J. Am. Chem. Soc. **141**, 18759–18770 (2019).

[66] M. Steinert, B. Schneider, S. Dechert, S. Demeshko, and F. Meyer, "Spin-State Versatility in a Series of Fe_4 [2 × 2] Grid Complexes: Effects of Counteranions, Lattice Solvent, and Intramolecular Cooperativity", Inorg. Chem. **55**, 2363–2373 (2016).

[67] M. Arczyński, J. Stanek, B. Sieklucka, K. R. Dunbar, and D. Pinkowicz, "Site-Selective Photoswitching of Two Distinct Magnetic Chromophores in a Propeller-Like Molecule To Achieve Four Different Magnetic States", J. Am. Chem. Soc. **141**, 19067–19077 (2019).

[68] F. Milocco, F. d. Vries, I. M. A. Bartels, R. W. A. Havenith, J. Cirera, S. Demeshko, F. Meyer, and E. Otten, "Electronic Control of Spin-Crossover Properties in Four-Coordinate Bis(formazanate) Iron(II) Complexes", J. Am. Chem. Soc. **142**, 20170–20181 (2020).

[69] B. Schneider, S. Demeshko, S. Dechert, and F. Meyer, "Ein zweifach schaltender multistabiler Fe_4-Gitterkomplex mit stufenweisen Spin- und Redoxübergängen", Angew. Chem. **122**, 9461–9464 (2010).

[70] C. Wäckerlin, F. Donati, A. Singha, R. Baltic, S. Decurtins, S.-X. Liu, S. Rusponi, and J. Dreiser, "Excited Spin-State Trapping in Spin Crossover Complexes on Ferroelectric Substrates", J. Phys. Chem. C **122**, 8202–8208 (2018).

[71] S. Rohlf, M. Gruber, B. M. Flöser, J. Grunwald, S. Jarausch, F. Diekmann, M. Kalläne, T. Jasper-Toennies, A. Buchholz, W. Plass, R. Berndt, F. Tuczek, and K. Rossnagel, "Light-Induced Spin Crossover in an Fe(II) Low-Spin Complex Enabled by Surface Adsorption", J. Phys. Chem. Lett. **9**, 1491–1496 (2018).

[72] L. Kipgen, M. Bernien, S. Ossinger, F. Nickel, A. J. Britton, L. M. Arruda, H. Naggert, C. Luo, C. Lotze, H. Ryll, F. Radu, E. Schierle, E. Weschke, F. Tuczek, and W. Kuch, "Evolution of cooperativity in the spin transition of an iron(II) complex on a graphite surface", Nat. Commun. **9**, 2984 (2018).

[73] C. Fourmental, S. Mondal, R. Banerjee, A. Bellec, Y. Garreau, A. Coati, C. Chacon, Y. Girard, J. Lagoute, S. Rousset, M.-L. Boillot, T. Mallah, C. Enachescu, C. Barreteau, Y. J. Dappe, A. Smogunov, S. Narasimhan, and V. Repain, "Importance of Epitaxial Strain at a Spin-Crossover Molecule–Metal Interface", J. Phys. Chem. Lett. **10**, 4103–4109 (2019).

[74] S. Beniwal, S. Sarkar, F. Baier, B. Weber, P. A. Dowben, and A. Enders, "Site selective adsorption of the spin crossover complex $Fe(phen)_2(NCS)$ on Au(111)", J. Phys. Condens. Matter **32**, 324003 (2020).

[75] M. Bernien, D. Wiedemann, C. F. Hermanns, A. Krüger, D. Rolf, W. Kroener, P. Müller, A. Grohmann, and W. Kuch, "Spin Crossover in a Vacuum-Deposited Submonolayer of a Molecular Iron(II) Complex", J. Phys. Chem. Lett. **3**, 3431–3434 (2012).

[76] T. Palamarciuc, J. C. Oberg, F. El Hallak, C. F. Hirjibehedin, M. Serri, S. Heutz, J.-F. Létard, and P. Rosa, "Spin crossover materials evaporated under clean high vacuum and ultra-high vacuum conditions: from thin films to single molecules", J. Mater. Chem. **22**, 9690 (2012).

[77] B. Warner, J. C. Oberg, T. G. Gill, F. El Hallak, C. F. Hirjibehedin, M. Serri, S. Heutz, M.-A. Arrio, P. Sainctavit, M. Mannini, G. Poneti, R. Sessoli, and P. Rosa, "Temperature- And Light-Induced Spin Crossover Observed by X-Ray Spectroscopy on Isolated Fe(II) Complexes on Gold", J. Phys. Chem. Lett. **4**, 1546–1552 (2013).

[78] M. Bernien, H. Naggert, L. M. Arruda, L. Kipgen, F. Nickel, J. Miguel, C. F. Hermanns, A. Krüger, D. Krüger, E. Schierle, E. Weschke, F. Tuczek, and W. Kuch, "Highly Efficient Thermal and Light-Induced Spin-State Switching of an Fe(II) Complex in Direct Contact with a Solid Surface", ACS Nano **9**, 8960–8966 (2015).

[79] K. Bairagi, O. Iasco, A. Bellec, A. Kartsev, D. Li, J. Lagoute, C. Chacon, Y. Girard, S. Rousset, F. Miserque, Y. J. Dappe, A. Smogunov, C. Barreteau, M.-L. Boillot, T. Mallah, and V. Repain, "Molecular-scale dynamics of light-induced spin cross-over in a two-dimensional layer", Nat. Commun. **7**, 12212 (2016).

[80] L. Kipgen, M. Bernien, F. Nickel, H. Naggert, A. J. Britton, L. M. Arruda, E. Schierle, E. Weschke, F. Tuczek, and W. Kuch, "Soft-x-ray-induced spin-state switching of an adsorbed Fe(II) spin-crossover complex", J. Phys. Condens. Matter **29**, 394003 (2017).

[81] X. Zhang, P. S. Costa, J. Hooper, D. P. Miller, A. T. N'Diaye, S. Beniwal, X. Jiang, Y. Yin, P. Rosa, L. Routaboul, M. Gonidec, L. Poggini, P. Braunstein, B. Doudin, X. Xu, A. Enders, E. Zurek, and P. A. Dowben, "Locking and Unlocking the Molecular Spin Crossover Transition", Adv. Mater. **29**, 1702257 (2017).

[82] S. Karan, C. Hamann, H. Tang, A. R. Stefankiewicz, J.-M. Lehn, and R. Berndt, "Surface Trapping and STM Observation of Conformational Isomers of a Bis(Terpyridine) Ligand from Metallosupramolecular Grids", ChemPhysChem **16**, 1370–1373 (2015).

[83] S. Karan, T. G. Gopakumar, H. Jacob, S. Meyer, F. Tuczek, and R. Berndt, "Remotely Triggered Geometrical Isomerization of a Binuclear Complex", J. Am. Chem. Soc. **136**, 6163–6166 (2014).

[84] S. Ossinger, C. Näther, A. Buchholz, M. Schmidtmann, S. Mangelsen, R. Beckhaus, W. Plass, and F. Tuczek, "Spin Transition of an Iron(II) Organoborate Complex in Different Polymorphs and in Vacuum-Deposited Thin Films: Influence of Cooperativity", Inorg. Chem. **59**, 7966–7979 (2020).

[85] P. Gütlich and H. A. Goodwin, "Spin Crossover—An Overall Perspective", In: Gütlich, P., Goodwin, H. (eds) "Spin Crossover in Transition Metal Compounds I. Topics in Current Chemistry", vol. 233. Springer Berlin Heidelberg, 1–47 (2004).

[86] Y. Kim, K. Motobayashi, T. Frederiksen, H. Ueba, and M. Kawai, "Action spectroscopy for single-molecule reactions – Experiments and theory", Prog. Surf. Sci. **90**, 85–143 (2015).

[87] T. Jasper-Toennies, M. Gruber, S. Johannsen, T. Frederiksen, A. Garcia-Lekue, T. Jäkel, F. Roehricht, R. Herges, and R. Berndt, "Rotation of Ethoxy and Ethyl Moieties on a Molecular Platform on Au(111)", ACS Nano **14**, 3907–3916 (2020).

[88] G. Auböck and M. Chergui, "Sub-50-fs Photoinduced Spin Crossover in $[Fe(bpy)_3]^{2+}$", Nat. Chem. **7**, 629–633 (2015).

[89] M. Chergui and E. Collet, "Photoinduced Structural Dynamics of Molecular Systems Mapped by Time-Resolved X-ray Methods", Chem. Rev. **117**, 11025–11065 (2017).

[90] J. Liu, Y. Gao, T. Wang, Q. Xue, M. Hua, Y. Wang, L. Huang, and N. Lin, "Collective Spin Manipulation in Antiferroelastic Spin-Crossover Metallo-Supramolecular Chains", ACS Nano **14**, 11283–11293 (2020).

[91] B. C. Stipe, M. A. Rezaei, and W. Ho, "Coupling of Vibrational Excitation to the Rotational Motion of a Single Adsorbed Molecule", Phys. Rev. Lett. **81**, 1263–1266 (1998).

[92] J. Kügel, L. Klein, M. Leisegang, and M. Bode, "Analyzing and Tuning the Energetic Landscape of H_2Pc Tautomerization", J. Phys. Chem. C **121**, 28204–28210 (2017).

[93] J. Schaffert, M. C. Cottin, A. Sonntag, C. A. Bobisch, R. Möller, J.-P. Gauyacq, and N. Lorente, "Tunneling electron induced rotation of a copper phthalocyanine molecule on Cu(111)", Phys. Rev. B **88**, 075410 (2013).

[94] J. Homberg, A. Weismann, R. Berndt, and M. Gruber, "Inducing and Controlling Molecular Magnetism through Supramolecular Manipulation", ACS Nano **14**, 17387–17395 (2020).

[95] F. Neese, "The ORCA program system", WIREs Comput. Mol. Sci. **2**, 73–78 (2011).

[96] F. Neese, "Software update: the ORCA program system, version 4.0", WIREs Comput. Mol. Sci. **8**, e1327 (2017).

[97] A. D. Becke, "Density-functional thermochemistry. III. The role of exact exchange", J. Chem. Phys. **98**, 5648–5652 (1993).

[98] C. Lee, W. Yang, and R. G. Parr, "Development of the Colle-Salvetti correlation-energy formula into a functional of the electron density", Phys. Rev. B **37**, 785–789 (1988).

[99] P. J. Stephens, F. J. Devlin, C. F. Chabalowski, and M. J. Frisch, "Ab Initio Calculation of Vibrational Absorption and Circular Dichroism Spectra Using Density Functional Force Fields", J. Phys. Chem. **98**, 11623–11627 (1994).

[100] F. Weigend and R. Ahlrichs, "Balanced Basis Sets of Split Valence, Triple Zeta Valence and Quadruple Zeta Valence Quality for H to Rn: Design and Assessment of Accuracy", Phys. Chem. Chem. Phys. **7**, 3297–3305 (2005).

[101] F. Weigend, "Accurate Coulomb-fitting basis sets for H to Rn", Phys. Chem. Chem. Phys. **8**, 1057–1065 (2006).

[102] S. Grimme, J. Antony, S. Ehrlich, and H. Krieg, "A consistent and accurate ab initio parametrization of density functional dispersion correction (DFT-D) for the 94 elements H-Pu", J. Chem. Phys. **132**, 154104 (2010).

[103] S. Grimme, S. Ehrlich, and L. Goerigk, "Effect of the damping function in dispersion corrected density functional theory", J. Comput. Chem. **32**, 1456–1465 (2011).

[104] C. F. Macrae, P. R. Edgington, P. McCabe, E. Pidcock, G. P. Shields, R. Taylor, M. Towler, and J. v. d. Streek, "Mercury: visualization and analysis of crystal structures", J. Appl. Crystallogr. **39**, 453–457 (2006).

[105] C. F. Macrae, I. J. Bruno, J. A. Chisholm, P. R. Edgington, P. McCabe, E. Pidcock, L. Rodriguez-Monge, R. Taylor, J. v. d. Streek, and P. A. Wood, "Mercury CSD 2.0– new features for the visualization and investigation of crystal structures", J. Appl. Crystallogr. **41**, 466–470 (2008).

[106] "QuantumATK version S-2021.06, Synopsys QuantumATK, www.synopsys.com/silicon/quantumatk.html", (last accessed 2021-06-04).

[107] S. Smidstrup, T. Markussen, P. Vancraeyveld, J. Wellendorff, J. Schneider, T. Gunst, B. Verstichel, D. Stradi, P. A. Khomyakov, U. G. Vej-Hansen, M.-E. Lee, S. T. Chill, F. Rasmussen, G. Penazzi, F. Corsetti, A. Ojanperä, K. Jensen, M. L. N. Palsgaard, U. Martinez, A. Blom, M. Brandbyge, and K. Stokbro, "QuantumATK: An Integrated Platform of Electronic and Atomic-Scale Modelling Tools", J. Phys. Condens. Matter **32**, 015901 (2019).

[108] J. P. Perdew, K. Burke, and M. Ernzerhof, "Generalized Gradient Approximation Made Simple", Phys. Rev. Lett. **77**, 3865–3868 (1996).

[109] N. J. Tao, "Electron transport in molecular junctions", Nat. Nanotechnol. **1**, 173–181 (2006).

[110] F. Evers, R. Korytár, S. Tewari, and J. M. van Ruitenbeek, "Advances and challenges in single-molecule electron transport", Rev. Mod. Phys. **92**, 035001 (2020).

[111] S. Karan, C. García, M. Karolak, D. Jacob, N. Lorente, and R. Berndt, "Spin Control Induced by Molecular Charging in a Transport Junction", Nano Lett. **18**, 88–93 (2018).

[112] N. A. Pradhan, N. Liu, and W. Ho, "Vibronic Spectroscopy of Single C60 Molecules and Monolayers with the STM", J. Phys. Chem. B **109**, 8513–8518 (2005).

[113] X. H. Qiu, G. V. Nazin, and W. Ho, "Vibronic States in Single Molecule Electron Transport", Phys. Rev. Lett. **92**, 206102 (2004).

[114] A. Yu, S. Li, B. Dhital, H. P. Lu, and W. Ho, "Tunneling Electron Induced Charging and Light Emission of Single Panhematin Molecules", J. Phys. Chem. C **120**, 21099–21103 (2016).

[115] S. Fatayer, B. Schuler, W. Steurer, I. Scivetti, J. Repp, L. Gross, M. Persson, and G. Meyer, "Reorganization energy upon charging a single molecule on an insulator measured by atomic force microscopy", Nat. Nanotechnol. **13**, 376–380 (2018).

[116] N. Hauptmann, C. Hamann, H. Tang, and R. Berndt, "Switching and charging of a ruthenium dye on Ag(111)", Phys. Chem. Chem. Phys. **15**, 10326–10330 (2013).

[117] F. Matino, G. Schull, F. Köhler, S. Gabutti, M. Mayord, and R. Berndt, "Electronic decoupling of a cyclophane from a metal surface", PNAS **108**, 961–964 (2011).

[118] R. Dittmann and J. P. Strachan, "Redox-based memristive devices for new computing paradigm", APL Mater. **7**, 110903 (2019).

[119] S. Goswami, R. Pramanick, A. Patra, S. P. Rath, M. Foltin, A. Ariando, D. Thompson, T. Venkatesan, S. Goswami, and R. S. Williams, "Decision trees within a molecular memristor", Nature **597**, 51–56 (2021).

[120] G. Molnár, L. Salmon, W. Nicolazzi, F. Terki, and A. Bousseksou, "Emerging Properties and Applications of Spin Crossover Nanomaterials", J. Mater. Chem. C **2**, 1360 (2014).

[121] K. S. Kumar and M. Ruben, "Sublimable Spin-Crossover Complexes: From Spin-State Switching to Molecular Devices", Angew. Chem. Int. Ed. **60**, 7502–7521 (2021).

[122] P. E. Figgins and D. H. Busch, "Complexes of Iron(II), Cobalt(II) and Nickel(II) with Biacetyl-bis-methylimine, 2-Pyridinal-methylimine and 2,6-Pyridindial-bis-methylimine", J. Am. Chem. Soc. **82**, 820–824 (1960).

[123] D. Reinen, C. Friebel, and V. Propach, "High- und Low-Spin-Verhalten des Ni^{3+}-Ions in oktaedrischer Koordination. (A) NiF_6^{3-}-Polyeder", Z. Anorg. Allg. Chem. **408**, 187–204 (1974).

[124] Y. Garcia and P. Gütlich, "Thermal Spin Crossover in Mn(II), Mn(III), Cr(II) and Co(III) Coordination Compounds", In: "Spin Crossover in Transition Metal Compounds II. Topics in Current Chemistry", vol 234. Springer Berlin Heidelberg **234**, 49–62 (2004).

[125] H. A. Goodwin, "Spin Crossover in Cobalt(II) Systems", In: "Spin Crossover in Transition Metal Compounds II. Topics in Current Chemistry", vol 234, Springer Berlin Heidelberg **234**, 23–47 (2004).

[126] S. Hayami, Y. Komatsu, T. Shimizu, H. Kamihata, and Y. H. Lee, "Spin-crossover in cobalt(II) compounds containing terpyridine and its derivatives", Coord. Chem. Rev. **255**, 1981–1990 (2011).

[127] W. Kuch and M. Bernien, "Controlling the Magnetism of Adsorbed Metalexten-dashorganic Molecules", J. Phys. Condens. Matter **29**, 023001 (2017).

[128] S. Rohlf, J. Grunwald, M. Kalläne, J. Kähler, F. Diekmann, S. Ossinger, B. Flöser, F. Tuczek, K. Rossnagel, and M. Gruber, "Probing the Spin State of Spin-Crossover Complexes on Surfaces with Vacuum Ultraviolet Angle-Resolved Photoemission Spectroscopy", J. Phys. Chem. C **125**, 14105–14116 (2021).

[129] S. Thakur, E. Golias, I. Kumberg, K. Senthil Kumar, R. Hosseinifar, J. Torres-Rodríguez, L. Kipgen, C. Lotze, L. M. Arruda, C. Luo, F. Radu, M. Ruben, and W. Kuch, "Thermal- and Light-Induced Spin-Crossover Characteristics of a Functional Iron(II) Complex at Submonolayer Coverage on HOPG", J. Phys. Chem. C **125**, 13925–13932 (2021).

[130] T. G. Gopakumar, F. Matino, H. Naggert, A. Bannwarth, F. Tuczek, and R. Berndt, "Elektroneninduzierter Spin-Crossover von Einzelmolekülen in einer Doppellage auf Gold", Angew. Chem. **124**, 6367–6371 (2012).

[131] A. Pronschinske, R. C. Bruce, G. Lewis, Y. Chen, A. Calzolari, M. Buongiorno-Nardelli, D. A. Shultz, W. You, and D. B. Dougherty, "Iron(II) spin crossover films on Au(111): scanning probe microscopy and photoelectron spectroscopy", Chem. Commun. **49**, 10446–10452 (2013).

[132] M. G. Cowan, J. Olguín, S. Narayanaswamy, J. L. Tallon, and S. Brooker, "Reversible Switching of a Cobalt Complex by Thermal, Pressure, and Electrochemical Stimuli: Abrupt, Complete, Hysteretic Spin Crossover", J. Am. Chem. Soc. **134**, 2892–2894 (2012).

[133] M. G. Cowan and S. Brooker, "Nine non-symmetric pyrazine-pyridine imide-based complexes: reversible redox and isolation of $[M^{II/III}(pypzca)_2]^{0/+}$ when M = Co, Fe", Dalton Trans. **41**, 1465–1474 (2012).

[134] R. G. Miller, S. Narayanaswamy, S. M. Clark, P. Dera, G. B. Jameson, J. L. Tallon, and S. Brooker, "Pressure induced separation of phase-transition-triggered-abrupt vs. gradual components of spin crossover", Dalton Trans. **44**, 20843–20849 (2015).

[135] N. Fairley, V. Fernandez, M. Richard-Plouet, C. Guillot-Deudon, J. Walton, E. Smith, D. Flahaut, M. Greiner, M. Biesinger, S. Tougaard, D. Morgan, and J. Baltrusaitis, "Systematic and collaborative approach to problem solving using x-ray photoelectron spectroscopy", Applied Surface Science Advances **5**, 100112 (2021).

[136] Y. Tong, M. Kelaï, K. Bairagi, V. Repain, J. Lagoute, Y. Girard, S. Rousset, M.-L. Boillot, T. Mallah, C. Enachescu, and A. Bellec, "Voltage-Induced Bistability of Single Spin-Crossover Molecules in a Two-Dimensional Monolayer", J. Phys. Chem. Lett. **12**, 11029–11034 (2021).

[137] M. Kelai, V. Repain, A. Tauzin, W. Li, Y. Girard, J. Lagoute, S. Rousset, E. Otero, P. Sainctavit, M.-A. Arrio, M.-L. Boillot, T. Mallah, C. Enachescu, and A. Bellec, "Thermal Bistability of an Ultrathin Film of Iron(II) Spin-Crossover Molecules Directly Adsorbed on a Metal Surface", J. Phys. Chem. Lett. **12**, 6152–6158 (2021).

[138] F. Matino, G. Schull, U. Jana, F. Köhler, R. Berndt, and R. Herges, "Single azopyridine-substituted porphyrin molecules for configurational and electronic switching", Chem. Commun. **46**, 6780 (2010).

[139] R. Torres-Cavanillas, M. Morant-Giner, G. Escorcia-Ariza, J. Dugay, J. Canet-Ferrer, S. Tatay, S. Cardona-Serra, M. Giménez-Marqués, M. Galbiati, A. Forment-Aliaga, and E. Coronado, "Spin-crossover nanoparticles anchored on MoS_2 layers for heterostructures with tunable strain driven by thermal or light-induced spin switching", Nat. Chem. **13**, 1101–1109 (2021).

[140] C. Boix-Constant, V. García-López, E. Navarro-Moratalla, M. Clemente-León, J. L. Zafra, J. Casado, F. Guinea, S. Mañas-Valero, and E. Coronado, "Strain switching in van der waals heterostructures triggered by a spin-crossover metal–organic framework", Adv. Mater. **34**, 2110027 (2022).

[141] M. Gavara-Edo, R. Córdoba, F. J. Valverde-Muñoz, J. Herrero-Martín, J. A. Real, and E. Coronado, "Electrical sensing of the thermal and light-induced spin transition in robust contactless spin-crossover/graphene hybrid devices", Adv. Mater. **34**, 2202551 (2022).

[142] J. Dugay, M. Aarts, M. Giménez-Marqués, T. Kozlova, H. W. Zandbergen, E. Coronado, and H. S. J. van der Zant, "Phase transitions in spin-crossover thin films probed by graphene transport measurements", Nano Lett. **17**, 186–193 (2017).

[143] M. S. G. Ahlquist and P.-O. Norrby, "Dispersion and back-donation gives tetracoordinate $[Pd(PPh_3)_4]$", Angew. Chem. Int. Ed. **50**, 11794–11797 (2011).

[144] L. P. Wolters, R. Koekkoek, and F. M. Bickelhaupt, "Role of Steric Attraction and Bite-Angle Flexibility in Metal-Mediated C–H Bond Activation", ACS Catal. **5**, 5766–5775 (2015).

[145] L. Schweighauser, M. A. Strauss, S. Bellotto, and H. A. Wegner, "Anziehung oder Abstoßung? London-Dispersionswechselwirkungen kontrollieren Azobenzol-basierte molekulare Schalter", Angew. Chem. **127**, 13636–13639 (2015).

[146] C. L. Wagner, L. Tao, E. J. Thompson, T. A. Stich, J. Guo, J. C. Fettinger, L. A. Berben, R. D. Britt, S. Nagase, and P. P. Power, "Dispersion-force-assisted disproportionation: a stable two-coordinate copper(II) complex", Angew. Chem. **128**, 10600–10603 (2016).

[147] J. R. Reimers, M. J. Ford, S. M. Marcuccio, J. Ulstrup, and N. S. Hush, "Competition of van der waals and chemical forces on gold–sulfur surfaces and nanoparticles", Nat. Rev. Chem. **1**, 0017 (2017).

[148] J. N. Israelachvili, "Intermolecular and Surface Forces", Elsevier Science & Technology Books: Amsterdam, 704 (2011).

[149] J. Kuntze, R. Berndt, P. Jiang, H. Tang, A. Gourdon, and C. Joachim, "Conformations of a molecular wire adsorbed on a metal surface", Phys. Rev. B **65**, 233405 (2002).

[150] T. Jasper-Tönnies, I. Poltavsky, S. Ulrich, T. Moje, A. Tkatchenko, R. Herges, and R. Berndt, "Stability of functionalized platform molecules on Au(111)", J. Chem. Phys. **149**, 244705 (2018).

[151] A. Bayler, A. Schier, G. A. Bowmaker, and H. Schmidbaur, "Gold is Smaller than Silver. Crystal Structures of [Bis(trimesitylphosphine)gold(I)] and [Bis(trimesitylphosphine) silver(I)] Tetrafluoroborate", J. Am. Chem. Soc. **118**, 7006–7007 (1996).

[152] M. C. Gimeno, "The Chemistry of Gold, Gold-metal interactions and applications", In: "Modern Supramolecular Gold Chemistry", Wiley-VCH, edited by A. Laguna, 1–63 (2008).

[153] A. Droghetti, D. Alfè, and S. Sanvito, "Assessment of density functional theory for iron(II) molecules across the spin-crossover transition", J. Chem. Phys. **137**, 124303 (2012).

[154] S. Lebègue, S. Pillet, and J. G. Ángyán, "Modeling Spin-Crossover Compounds by Periodic DFT + U Approach", Phys. Rev. B **78**, 024433 (2008).

[155] M. Reiher, O. Salomon, and B. Artur Hess, "Reparameterization of Hybrid Functionals Based on Energy Differences of States of Different Multiplicity", Theor. Chem. Acc. **107**, 48–55 (2001).

[156] G. Prokopiou and L. Kronik, "Spin-State Energetics of Fe Complexes from an Optimally Tuned Range-Separated Hybrid Functional", Chem. Eur. J. **24**, 5173–5182 (2018).

[157] J. Heyd, G. E. Scuseria, and M. Ernzerhof, "Hybrid Functionals Based on a Screened Coulomb Potential", J. Chem. Phys. **118**, 8207–8215 (2003).

[158] J. Heyd, G. E. Scuseria, and M. Ernzerhof, "Erratum: Hybrid Functionals Based on a Screened Coulomb Potential", J. Chem. Phys. **118**, 8207 (2003).

[159] R. Otero, R. Miranda, and J. M. Gallego, "A Comparative Computational Study of the Adsorption of TCNQ and F4-TCNQ on the Coinage Metal Surfaces", ACS Omega **4**, 16906–16915 (2019).

[160] P. Pyykko and J. P. Desclaux, "Relativity and the periodic system of elements", Acc. Chem. Res. **12**, 276–281 (1979).

[161] N. Bartlett, "Relativistic effects and the chemistry of gold", Gold Bull. **31**, 22–25 (1998).

[162] R. H. M. Smit, C. Untiedt, A. I. Yanson, and J. M. van Ruitenbeek, "Common Origin for Surface Reconstruction and the Formation of Chains of Metal Atoms", Phys. Rev. Lett. **87**, 266102 (2001).

[163] S. Combettes, J. Lam, P. Benzo, A. Ponchet, M.-J. Casanove, F. Calvo, and M. Benoit, "How interface properties control the equilibrium shape of core–shell Fe–Au and Fe–Ag nanoparticles", Nanoscale **12**, 18079–18090 (2020).

[164] M. Gavara-Edo, F. J. Valverde-Muñoz, M. C. Muñoz, S. E. Moubtassim, F. Marques-Moros, J. Herrero-Martín, K. Znovjyak, M. Seredyuk, J. A. Real, and E. Coronado, "Design and processing as ultrathin films of a sublimable iron(II) spin crossover material exhibiting efficient and fast light-induced spin transition", Chem. Mater. **35**, 9591–9602 (2023).

[165] G. M. Sheldrick, "Crystal Structure Refinement with SHELXL", Acta Crystallogr. C Struct. Chem. **71**, 3–8 (2015).

[166] M. J. van Setten, M. Giantomassi, E. Bousquet, M. J. Verstraete, D. R. Hamann, X. Gonze, and G. .-. Rignanese, "The PseudoDojo: Training and grading a 85 element optimized norm-conserving pseudopotential table", Comput. Phys. Commun. **226**, 39–54 (2018).

[167] P. Gütlich, Y. Garcia, and H. A. Goodwin, "Spin crossover phenomena in Fe(II) complexes", Chem. Soc. Rev. **29**, 419–427 (2000).

[168] G. Molnár, S. Rat, L. Salmon, W. Nicolazzi, and A. Bousseksou, "Spin crossover nanomaterials: from fundamental concepts to devices", Adv. Mater. **30**, 1703862 (2018).

[169] A. Bellec, J. Lagoute, and V. Repain, "Molecular electronics: scanning tunneling microscopy and single-molecule devices", C. R. Chim. **21**, 1287–1299 (2018).

[170] S. Rat, K. Ridier, L. Vendier, G. Molnár, L. Salmon, and A. Bousseksou, "Solvatomorphism and structural-spin crossover property relationship in bis[hydrotris(1,2,4-triazol-1-yl)borate]iron(II)", CrystEngComm **19**, 3271–3280 (2017).

[171] V. Shalabaeva, S. Rat, M. D. Manrique-Juarez, A.-C. Bas, L. Vendier, L. Salmon, G. Molnár, and A. Bousseksou, "Vacuum deposition of high-quality thin films displaying spin transition near room temperature", J. Mater. Chem. C **5**, 4419–4425 (2017).

[172] M. Leisegang, J. Kügel, L. Klein, and M. Bode, "Analyzing the wave nature of hot electrons with a molecular nanoprobe", Nano Lett. **18**, 2165–2171 (2018).

[173] M. Ternes, "Spin excitations and correlations in scanning tunneling spectroscopy", New J. Phys. **17**, 063016 (2015).